Advances in Meteorology

Hydrological Hazards in a Changing Environment: Early Warning, Forecasting, and Impact Assessment

Guest Editors: Slavisa Trajkovic, Ozgur Kisi, Momcilo Markus, Hossein Tabari, Milan Gocic, and Shahaboddin Shamshirband

Hydrological Hazards in a Changing Environment: Early Warning, Forecasting, and Impact Assessment

Advances in Meteorology

Hydrological Hazards in a Changing Environment: Early Warning, Forecasting, and Impact Assessment

Guest Editors: Slavisa Trajkovic, Ozgur Kisi,
Momcilo Markus, Hossein Tabari, Milan Gocic,
and Shahaboddin Shamshirband

Editorial Board

Contents

Hindawi Publishing Corporation
Advances in Meteorology
Volume 2016, Article ID 2752091, 2 pages
http://dx.doi.org/10.1155/2016/2752091

Editorial

Hydrological Hazards in a Changing Environment: Early Warning, Forecasting, and Impact Assessment

Slavisa Trajkovic,[1] Ozgur Kisi,[2] Momcilo Markus,[3] Hossein Tabari,[4] Milan Gocic,[1] and Shahaboddin Shamshirband[5]

[1] *Faculty of Civil Engineering and Architecture, University of Niš, Aleksandra Medvedeva 14, 18000 Niš, Serbia*
[2] *Faculty of Architecture and Engineering, Canik Başarı University, Gürgenyatak Köyü, Canik, 55080 Samsun, Turkey*
[3] *University of Illinois at Urbana-Champaign, 2204 Griffith Drive, Champaign, IL 61820, USA*
[4] *Department of Civil Engineering, University of Leuven, Kasteelpark Arenberg 40, P.O. Box 2448, 3001 Leuven, Belgium*
[5] *Faculty of Computer Science and Information Technology, University of Malaya, 50603 Kuala Lumpur, Malaysia*

Correspondence should be addressed to Slavisa Trajkovic; slavisa@gaf.ni.ac.rs

Received 12 June 2016; Accepted 13 June 2016

Hydrological hazards of various types present a myriad of technical and public policy issues worldwide. Defined as extreme events associated with water occurrence, movement, and distribution, hydrological hazards include droughts and flooding and related events (e.g., landslides and river scour and deposition). Hydrological hazards and their impacts are associated with climate variability, demographic trends, land-cover change, and other causative factors and could be exasperated by global climate change. The increase in greenhouse gases in the atmosphere will continue leading to global warming and an intensification of the hydrological cycle, making hydrological extreme studies more complex and challenging.

Because of the immense impacts of hydrological hazards on society and its economies, it is important to consider novel approaches, techniques, or methods for the prediction, prevention, and mitigation of hydrological extremes. Given the complexity of the nonstationary hydrometeorological and hydroclimatological processes, it is critical to utilize recent technological developments and scientific knowledge to improve our understanding of hydrological hazards and our ability to cope with droughts and floods.

In this special issue, ten papers are collected that cover the hydrological hazards in a changing environment. This collection includes the following topics: regional flood/drought analysis, methodologies for the prediction and prevention of hydrological extremes, early warning and forecasting systems for hydrological extremes, case studies in different parts of the world, emerging technologies in data analysis, hydroinformatics, and climate informatics and effects of climate change and land-use/land-cover changes.

Flood hazard mapping of the Mert River Basin, Samsun, Turkey, was investigated using GIS and HEC-RAS in the paper by V. Demir and O. Kisi (2016). 3D hazard maps were obtained for the Q10, Q25, Q50, and Q100 floods. The flood maps demonstrated that some areas are highly affected by flooding resulting from a low return period (Q10) event.

B. S. Kim et al. (2016) identified drought characteristics by applying the threshold level method and projecting the drought risk of each administrative division in South Korea in the 21st century.

W. Yu et al. (2016) investigated the uncertainty propagation of a rainfall forecast into hydrological response with catchment scale through distributed rainfall-runoff modeling based on the forecasted ensemble rainfall of a numerical weather prediction (NWP) model. This study is carried out and verified using the largest flood event by typhoon "Talas" of 2011, Shingu River Basin, Japan.

N. Diodato et al. (2016) established thresholds in the power of rainstorms to discern the spatial patterns of a rainfall erosivity hazard in the Rhone region (eastern France). Climate fluctuations of rainfall erosivity revealed possible signals of increased storminess hazards across the region in recent times.

L. Tadić et al. (2016) analysed the small catchment area in the Croatian lowland with its hydrological characteristics in the period between 1981 and 2014 to define the significance of change in hydrological and meteorological parameters and water balance components.

H. Jia and D. Pan (2016) used the wavelet transform technique to analyse precipitation data for nearly 60 years (1954–2012) in the Yunnan Province of China. According to the main cycle of summer and the annual rainfall, precipitation of Yunnan is in the decreased oscillation period; local drought may also occur in the future.

N. Ožanić et al. (2016) investigated the possibility of implementing the early warning system (EWS) in a small-scale catchment in Croatia and developed the methodology for a hydrological prediction model based on an artificial neural network (ANN).

F. Vemado and A. J. P. Filho (2016) analysed the Metropolitan Area of São Paulo (MASP) heat island (HI) effect and its interaction with the local sea breeze (SB) inflow in rainfall amounts and deep convection.

M. Gocic et al. (2016) presented a spatial pattern of the precipitation concentration index (PCI) in Serbia. For the purpose of PCI prediction, three Support Vector Machine (SVM) models were developed and used.

S. Kolaković et al. (2016) analysed the exploitation of documented historical floods for achieving better flood defense at the catchment of the Tisza River (Hungary and Serbia).

Acknowledgments

As guest editors of this special issue, we would like to thank all the authors for their contributions to this volume. Special mention of thanks and appreciation is due to the international panel of reviewers for making their expertise available for evaluation of the manuscripts.

Slavisa Trajkovic
Ozgur Kisi
Momcilo Markus
Hossein Tabari
Milan Gocic
Shahaboddin Shamshirband

Hindawi Publishing Corporation
Advances in Meteorology
Volume 2016, Article ID 7912357, 11 pages
http://dx.doi.org/10.1155/2016/7912357

Research Article

Long-Term Precipitation Analysis and Estimation of Precipitation Concentration Index Using Three Support Vector Machine Methods

Milan Gocic,[1] Shahaboddin Shamshirband,[2] Zaidi Razak,[2] Dalibor Petković,[3] Sudheer Ch,[4] and Slavisa Trajkovic[1]

[1] *Faculty of Civil Engineering and Architecture, University of Nis, Aleksandra Medvedeva 14, 18000 Nis, Serbia*
[2] *Faculty of Computer Science and Information Technology, Department of Computer System and Technology, University of Malaya, 50603 Kuala Lumpur, Malaysia*
[3] *Faculty of Mechanical Engineering, Department for Mechatronics and Control, University of Nis, Aleksandra Medvedeva 14, 18000 Nis, Serbia*
[4] *Department of Civil Engineering, Indian Institute of Technology, Hauz Khas, New Delhi 110016, India*

Correspondence should be addressed to Milan Gocic; milan.gocic@gaf.ni.ac.rs

Received 27 October 2015; Revised 20 December 2015; Accepted 4 January 2016

Academic Editor: Stefano Dietrich

The monthly precipitation data from 29 stations in Serbia during the period of 1946–2012 were considered. Precipitation trends were calculated using linear regression method. Three CLINO periods (1961–1990, 1971–2000, and 1981–2010) in three subregions were analysed. The CLINO 1981–2010 period had a significant increasing trend. Spatial pattern of the precipitation concentration index (PCI) was presented. For the purpose of PCI prediction, three Support Vector Machine (SVM) models, namely, SVM coupled with the discrete wavelet transform (SVM-Wavelet), the firefly algorithm (SVM-FFA), and using the radial basis function (SVM-RBF), were developed and used. The estimation and prediction results of these models were compared with each other using three statistical indicators, that is, root mean square error, coefficient of determination, and coefficient of efficiency. The experimental results showed that an improvement in predictive accuracy and capability of generalization can be achieved by the SVM-Wavelet approach. Moreover, the results indicated the proposed SVM-Wavelet model can adequately predict the PCI.

1. Introduction

Precipitation is one of the important climatic variables due to its changes in the intensity and the amount affecting appearing of the hydrological hazards such as flood and drought [1]. Therefore, numerous studies on precipitation variability and development of statistical indices to evaluate the changes of precipitation have been undertaken [2–7]. In this study, the precipitation concentration index (PCI) is analysed. The PCI allows quantifying the relative distribution of precipitation patterns. It also provides a good presentation to the spatial variability of monthly precipitation [5, 8] and information on long-term total variability in the precipitation amount record [9, 10]. The PCI can be used as an indicator of hydrological hazard risks such as floods and droughts.

In this study, the prediction model of PCI is introduced using the soft computing method, namely, the Support Vector Machine (SVM). The SVM, one of the novel soft computing learning algorithms, has found wide application in the field of computing, hydrology, and environmental science [11–16]. Furthermore, it has been majorly applied in pattern recognition, forecasting, classification, and regression analysis [17–20]. The most commonly used kernels include linear, polynomial, and radial basis function (RBF), whose selection depends on the nature of the observed data [21]. Shamshirband et al. [22] used adaptive neurofuzzy inference system (ANFIS) and support vector regression (SVR) for precipitation estimation, while S. Chattopadhyay and G. Chattopadhyay [23], Nastos et al. [24], and Wu and Chau [25] applied artificial neural networks (ANNs). Chen et al. [26]

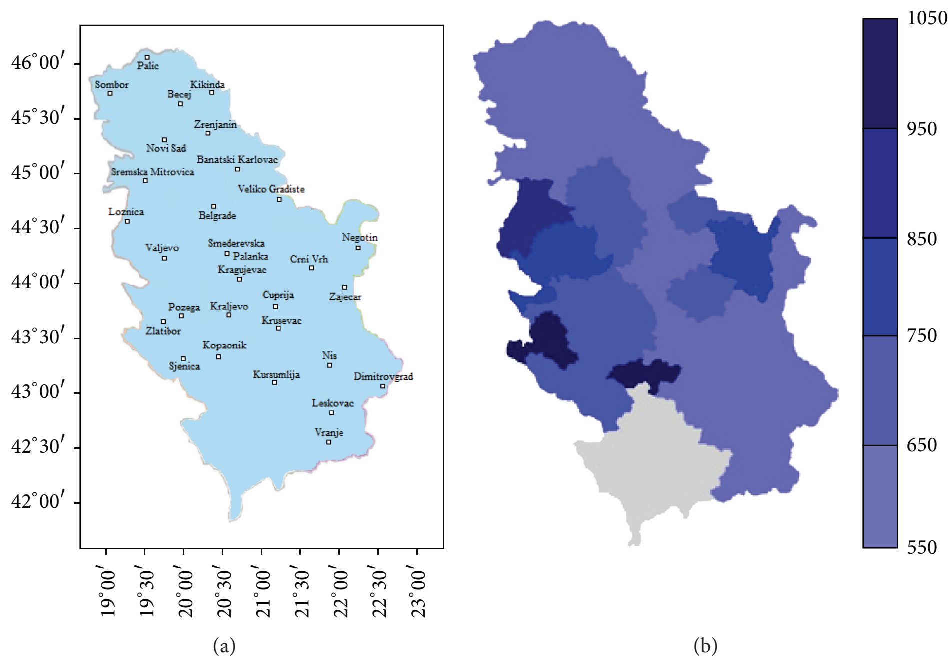

Figure 1: (a) Spatial distribution of the 29 meteorological stations in Serbia map; (b) spatial distribution of the mean annual precipitation in Serbia for the period of 1946–2012.

implemented SVM and multivariate analysis to project daily precipitation. Meyer et al. [27] compared four machine learning algorithms for their applicability in rainfall retrievals.

Metaheuristic optimization algorithms such as ant colony optimization (ACO), genetic algorithm (GA), particle swarm optimization (PSO), and cuckoo search (CS) have been applied in different fields of science [28–37]. These algorithms are based on the mechanism of selection of the fittest in biological systems. A more recent approach in biological inspired metaheuristic optimization algorithms is firefly algorithm (FFA) developed by Yang [38]. The FFA has been adjudged to be more efficient and robust in finding both local and global optima compared to other biological inspired optimization algorithms [39–43]. The prediction accuracy of the SVM model highly relies on proper determination of model parameters [44–47]. Although organized strategies for selecting parameters are important, model parameter alignment also needs to be made. In this study, the FFA is used for determination of SVM parameters, while the SVM was coupled with discrete wavelet transform.

Wavelet transform (WT) has a number of basis functions for selection that depends on the analysed signal. Wavelet analysis was used to decompose the time series of data into its various components, after which the decomposed components can be used as inputs for the SVM model. Over the past few years, this technique has become of enormous interest in engineering applications [48–51]. Nalley et al. [52] used discrete wavelet transform (DWT) to analyse trends in precipitation in Canada, while Hsu and Li [53] clustered spatial-temporal precipitation data using WT. Partal and Kucuk [54] analysed long-term precipitation trend using DWT in Turkey. Kisi and Cimen [55] applied wavelet-Support Vector Machine conjunction model for daily precipitation forecast and concluded the proposed model increases the forecast accuracy.

The objectives of the current study are as follows: (1) to provide presentation of the spatial variability of monthly precipitation and information on long-term total variability in the precipitation data using precipitation concentration index and (2) to construct, develop, and evaluate the results of SVM-Wavelet, SVM-FFA, and SVM-RBF for PCI prediction.

2. Materials and Methods

2.1. Study Area and Used Data. Monthly precipitation data were chosen from 29 meteorological stations in Serbia (Figure 1(a)) over the period of 1946–2012. Data were obtained from the Republic Hydro Meteorological Service of Serbia (http://www.hidmet.gov.rs/). There are no missing values in the data set.

According to Gocic and Trajkovic [56], precipitation increases with the altitude; that is, dry areas in the northeast part of Serbia have the precipitation below 600 mm, and the area along the valley of the South Morava to Vranje has the precipitation to 650 mm, while in the mountains precipitation may rise up to 1000 mm per year. The mean annual precipitation for the observed period for the whole country is 662.4 mm. The spatial distribution of the mean annual precipitation in Serbia for the analysed period is illustrated in Figure 1(b).

2.2. Methodology for Precipitation Analysis. The spatial distribution of the number of wet and dry years can be obtained

Table 1: Classification of PCI values.

PCI	Description
<10	Uniform precipitation distribution
11 to 15	Moderate precipitation distribution
16 to 20	Irregular distribution
>20	Strong irregularity of precipitation distribution

using a transformed annual precipitation departure z for each station as

$$z = \frac{x - \mu}{\sigma}, \tag{1}$$

where x is the annual precipitation, μ is the annual mean precipitation, and σ is the standard deviation of the annual precipitation. The dry year existed, where $z \leq -0.5$, and wet one existed if $z \geq 0.5$ [57].

Precipitation concentration index (PCI) [58] is calculated as follows:

$$\mathrm{PCI}_{\mathrm{annaul}} = \frac{\sum_{i=1}^{12} {p_i}^2}{\left(\sum_{i=1}^{12} p_i\right)^2} \cdot 100, \tag{2}$$

where p_i is the precipitation amount in month i. Classification of PCI values is shown in Table 1.

2.3. Soft Computing Methodologies

2.3.1. Support Vector Machine. Support Vector Machine (SVM) [59, 60] is based on machine learning theory to maximize predictive accuracy; that is,

$$\begin{aligned} \text{Minimize} \quad & R_{\mathrm{SVM}}\left(w, \xi^*\right) = \frac{1}{2}\|w\|^2 + C\sum_{i=1}^{n}\left(\xi_i + \xi_i^*\right) \\ \text{Subject to} \quad & d_i - w\varphi\left(x_i\right) + b_i \leq \varepsilon + \xi_i \\ & w\varphi\left(x_i\right) + b_i - d_i \leq \varepsilon + \xi_i \\ & \xi_i, \xi_i^* \geq 0, \quad i = 1, \ldots, l, \end{aligned} \tag{3}$$

where w is a normal vector, $(1/2)\|w\|^2$ is the regularization term, C is the error penalty factor, b is a bias, ε is the loss function, x_i is the input vector, d_i is the target value, l is the number of elements in the training data set, $\varphi(x_i)$ is a feature space, and ξ_i and ξ_i^* are upper and lower excess deviation.

The architecture of SVM is shown in Figure 2. The kernel function, that is, radial basis function (RBF) is denoted as

$$K\left(x_i, x_j\right) = \exp\left(-\gamma\left\|x_i - x_j\right\|^2\right), \tag{4}$$

where variables x_i and x_j are vectors in the input space and γ is the regularization parameter. Lagrange multipliers are presented as $\overline{\alpha}_i = \alpha_i - \alpha_i^*$.

The accuracy of prediction is based on the selection of three parameters, that is, γ, ε and C, whose values are determined using firefly algorithm.

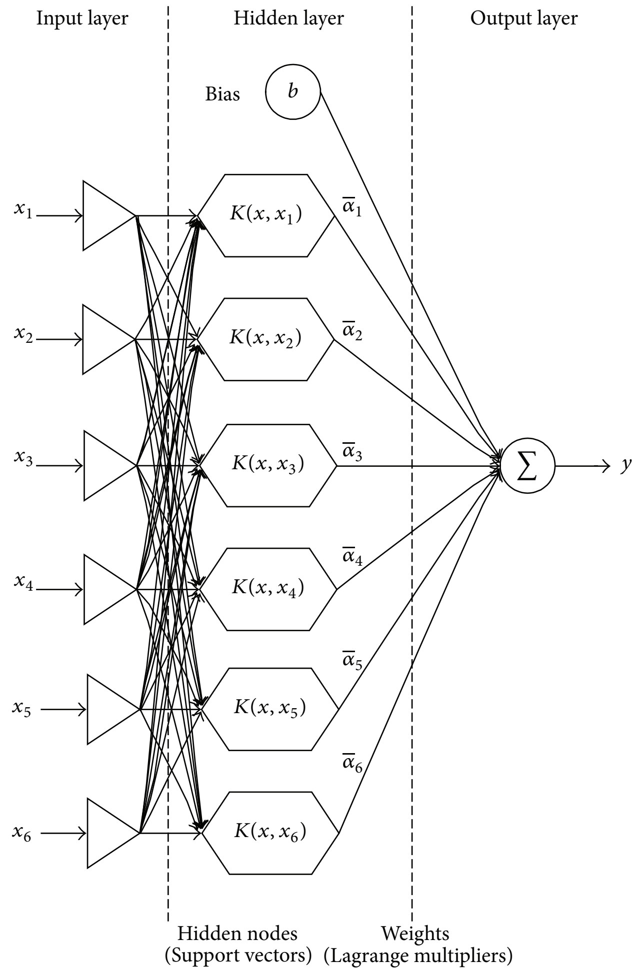

Figure 2: The network architecture of SVM.

2.3.2. Firefly Algorithm. The firefly algorithm (FFA) [38, 61, 62] is based on the behaviour of insect named firefly. The major issues in FFA development are the formulation of the objective function and the variation of the light intensity.

A firefly is a kind of insects that uses the principle of bioluminescence to attract mates or prey. The luminance produced by a firefly enables other fireflies to trail its path in searching of their prey. This concept of luminance production helps in the development of algorithms that solve optimization problems.

For example, in the optimal design problem involving maximization of objective function, the fitness function is proportional to the brightness or the amount of light emitted by the firefly. Therefore, decreasing in the light intensity due to distance between the fireflies will lead to variations of intensity and thereby lessen the attractiveness among them. The light intensity with varying distance can be represented as

$$I(r) = I_0 \exp\left(-\gamma r^2\right), \tag{5}$$

where I is the light intensity at distance r from a firefly, I_0 represents initial light intensity, that is, when $r = 0$, and γ is the light absorption coefficient. As firefly's attractiveness is proportional to the light intensity observed by adjacent fireflies, the attractiveness β at a distance r from the firefly can be represented as

$$\beta(r) = \beta_0 \exp\left(-\gamma r^2\right), \quad (6)$$

where β_0 represents the attractiveness at distance $r = 0$.

The Cartesian distance between any two fireflies i and j is given by

$$r_{ij} = \left\|x_i + x_j\right\| = \sqrt{\sum_{k=1}^{d}\left(x_{i,k} - x_{j,k}\right)}. \quad (7)$$

The movement of firefly i as attracted to another brighter firefly j and can be represented as

$$\Delta x_i = \beta_0 \exp\left(-\gamma r^2\right)\left(x_j - x_i\right) + \alpha\varepsilon_i, \quad (8)$$

where the first term in the equation is due to the attraction, the second term represents the randomization with α as randomization coefficient, and ε_i is the random number vector derived from a Gaussian distribution. The next movement of firefly i is updated as

$$x_i^{i+1} = x_i + \Delta x_i. \quad (9)$$

Steps in FFA development are presented in Figure 3.

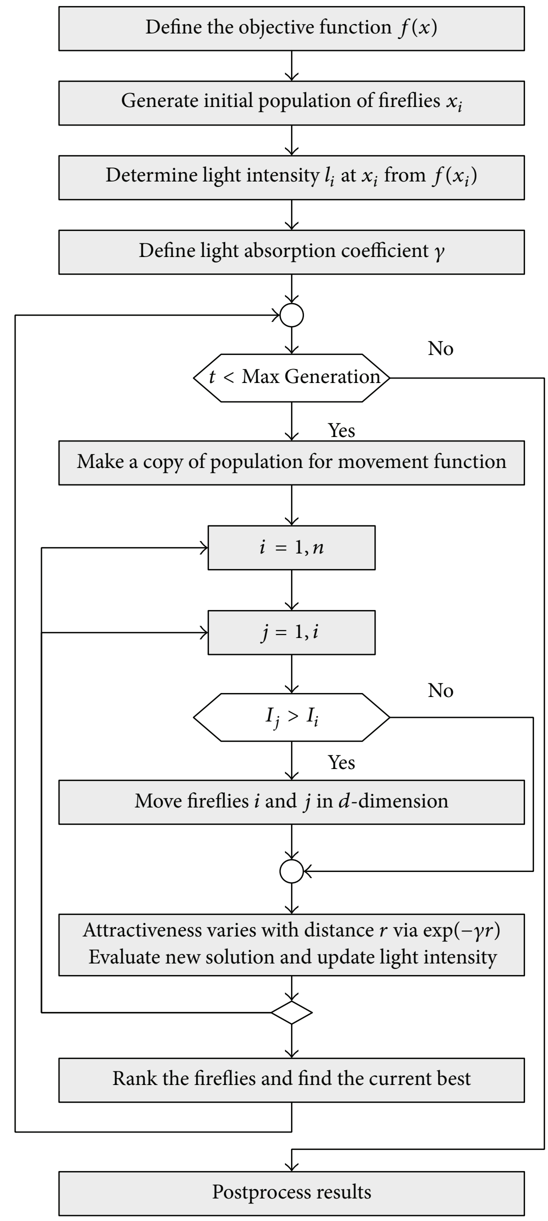

Figure 3: Flow chart of firefly algorithm.

2.3.3. Discrete Wavelet Transform. The wavelet transform (WT) represents a mathematical expression for decomposing a time series' frequency signal into different components. In this study, wavelet analysis was used to decompose the time series of precipitation data into various components, after which the decomposed components were used as inputs for the SVM model. Flow chart of discrete wavelet algorithm, that is, used to determine SVM parameters, is shown in Figure 4.

Continuous wavelet transform (CWT) of a signal $f(t)$ is a time-scale technique of signal processing that can be defined as the integral of all signals over the entire period multiplied by the scaled, shifted versions of the wavelet function $\psi(t)$, given mathematically as

$$W_x(a, b, \psi) = \frac{1}{\sqrt{a}} \int_{-\infty}^{\infty} f(t)\, \psi^*\left(\frac{t-a}{b}\right) dt, \quad (10)$$

where $\psi(t)$ is the mother wavelet function, a is the scale index parameter, that is, inverse of the frequency, and b is the time shifting parameter, also known as translation. The discrete wavelet transform (DWT) can be derived by discretizing (10), where the parameters a and b are given as follows:

$$\begin{aligned} a &= a_0^m, \\ b &= n a_0^m b_0, \end{aligned} \quad (11)$$

where the variables n and m are integers. Replacing a and b in (10) gives

$$W_x(m, n, \psi) = a_0^{-m/2} \int_{-\infty}^{\infty} f(t)\, \psi^*\left(a_0^{-m} t - n b_0\right) dt. \quad (12)$$

2.4. Evaluating Accuracy of Proposed Models. In this study, the following statistical indicators were applied to compare the developed SVM models:

(1) root mean square error (RMSE):

$$\text{RMSE} = \sqrt{\frac{\sum_{i=1}^{n}\left(P_i - O_i\right)^2}{n}}, \quad (13)$$

(2) coefficient of determination (R^2):

$$R^2 = \frac{\left[\sum_{i=1}^{n}\left(O_i - \overline{O_i}\right) \cdot \left(P_i - \overline{P_i}\right)\right]^2}{\sum_{i=1}^{n}\left(O_i - \overline{O_i}\right) \cdot \sum_{i=1}^{n}\left(P_i - \overline{P_i}\right)}, \quad (14)$$

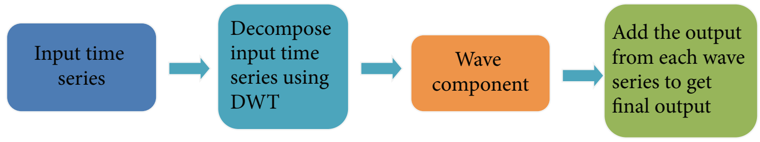

Figure 4: Flow chart of proposed discrete wavelet algorithm.

(3) coefficient of efficiency (EI):

$$\mathrm{EI} = 1 - \frac{\sum_{i=1}^{n} \left(P_i - O_i\right)^2}{\sum_{i=1}^{n} \left(P_i - \overline{P}_i\right)^2}, \tag{15}$$

where P_i and O_i are the experimental and predicted values of PCI index, respectively, and n is the size of test data.

3. Results and Discussion

3.1. Analysis of Precipitation Distribution. The number of dry and wet years is tabulated in Table 2. The most frequented number of dry years is in the north of Serbia, while the number of wet years is greater than the number of dry years in the west of country. The number of dry years is 20, while the number of wet years is 19 for whole Serbia.

According to Gocic and Trajkovic [56], three precipitation subregions were detected: (1) subregion R1 (12 stations) is located in the north part of the country with the precipitation ranging from 223 to 1051 mm and the average value of precipitation of 608.2 mm, (2) subregion R2 (7 stations) is the wettest one and includes stations in the west of country with the precipitation between 385 and 1282 mm and with the mean value of precipitation of 784.5 mm, and (3) subregion R3 (10 stations) in the east and south part of Serbia with precipitation between 302 and 1113 mm and the mean of precipitation of 623.3 mm.

The annual precipitation shows an increasing trend in Serbia during the period of 1946–2012 (stronger in R2 and R1). Three CLINO periods (1961–1990, 1971–2000, and 1981–2010) were illustrated in Figure 5. The CLINO period 1981–2010 shows a significant increasing trend at all subregions. The most precipitation falls in June and has the value of 80.8 mm in Serbia (41.15% of total precipitation in summer), which is directly connected with the intensive convection of colder and humid, usually maritime, air masses.

Precipitation distribution is determined using the PCI. Figure 6 illustrates the spatial distribution of PCI in Serbia. The minimum PCI values were detected in Zlatibor (10.43) and Pozega (10.83), while the maximum was in Negotin (12.49). The majority of the stations had the values between 11.12 in Sjenica and 11.94 in Banatski Karlovac.

Table 2: Number of dry and wet years for the synoptic stations used in the study.

Station name	Number of dry years	Number of wet years
(1) Banatski Karlovac	22	20
(2) Becej	22	19
(3) Belgrade	23	20
(4) Crni Vrh	20	22
(5) Cuprija	23	20
(6) Dimitrovgrad	19	19
(7) Kikinda	19	18
(8) Kopaonik	20	18
(9) Kragujevac	21	19
(10) Kraljevo	17	19
(11) Krusevac	20	17
(12) Kursumlija	19	19
(13) Leskovac	20	20
(14) Loznica	17	20
(15) Negotin	18	21
(16) Nis	19	20
(17) Novi Sad	25	21
(18) Palic	21	18
(19) Pozega	21	23
(20) Sjenica	22	18
(21) Sombor	19	17
(22) Smederevska Palanka	24	20
(23) Sremska Mitrovica	20	18
(24) Valjevo	22	22
(25) Veliko Gradiste	23	24
(26) Vranje	20	22
(27) Zajecar	21	20
(28) Zlatibor	22	24
(29) Zrenjanin	25	21

3.2. Performance Evaluation of Proposed SVM Models. Precipitation data was used to obtain six parameters such as annual total precipitation, mean winter precipitation amount, mean spring precipitation amount, mean summer precipitation amount, mean autumn precipitation amount, and mean of precipitation for vegetable period (April–September). For the experiments, 38 years (57% of data) was used to train samples and the subsequent 29 years (43% of data) served to test samples. Table 3 illustrates six variables using the following statistical indicators, that is, the minimum, maximum, median, mean, standard deviation, and skewness.

In this study, three SVM models, that is, SVM-Wavelet, SVM-RBF, and SVM-FFA, were analysed to predict the PCI index. The RBF was implemented as the kernel function to obtain three parameters, C, γ, and ε, whose selection

Table 3: Summary statistics for used data sets.

(a)

Variables	Training data set					
	Min (mm)	Max (mm)	Median (mm)	Mean (mm)	Standard deviation (mm)	Skewness
Annual total precipitation	503.2	914.6	648.8	659.7	90.2	0.56
Mean winter precipitation amount	36.4	248.1	130.5	141.0	43.5	0.07
Mean spring precipitation amount	99.9	247.1	169.0	166.9	38.8	0.01
Mean summer precipitation amount	80.6	335.3	203.9	198.0	59.1	−0.10
Mean autumn precipitation amount	63.9	266.1	148.3	153.8	50.1	0.58
Mean of precipitation for vegetable period (April–September)	203.9	516.1	369.7	369.2	77.3	−0.26

(b)

Variables	Testing data set					
	Min (mm)	Max (mm)	Median (mm)	Mean (mm)	Standard deviation (mm)	Skewness
Annual total precipitation	414.8	872.0	678.3	663.9	116.9	−0.26
Mean winter precipitation amount	46.7	216.4	131.3	141.2	43.5	0.11
Mean spring precipitation amount	101.4	273.3	166.0	166.0	39.5	0.60
Mean summer precipitation amount	82.0	304.8	210.8	194.1	63.8	−0.12
Mean autumn precipitation amount	53.2	301.6	156.3	164.1	56.8	0.27
Mean of precipitation for vegetable period (April–September)	233.6	572.1	366.7	371.6	87.5	0.38

directly influences prediction accuracy. Table 4 provides the optimal values of parameters for the proposed SVM models. Firefly algorithm founds optimal SVM parameters according to searching algorithm. For the SVM-Wavelet and SVM-RBF approaches the parameters are selected manually after several trial and error iterations.

To evaluate SVM model performance, calculated PCI was plotted against the predicted ones. Figure 7(a) presents the accuracy of developed SVM-Wavelet PCI predictive model, while Figures 7(b) and 7(c) present the accuracy of developed SVM-RBF and SVM-FFA PCI predictive models, respectively. The most of the points fall along the diagonal line for the SVM-Wavelet prediction model. It means the prediction results are in a very good agreement with the measured values for the SVM-Wavelet model. The confirmation of this is the high value for R^2 ($R^2 = 0.86$).

Figure 8 illustrates the spatial distribution of PCI in Serbia using three SVM methods, that is, SVM-Wavelet, SVM-FFA, and SVM-RBF. According to the obtained results, it can be concluded that the spatial distribution using values of SVM-Wavelet method is similar to the spatial distribution in Figure 6.

3.3. Performance Comparison of SVM Models. To illustrate the performance characteristics of the developed SVM models for PCI prediction, three SVM models' prediction accuracies were compared with each other. The statistical indicators such as RMSE, R^2, and EI were used for comparison. Table 5 summarizes the prediction results for test data sets since training error is not credible indicator for prediction potential of particular model. Results in Table 5 are obtained for the same number of runs and according to the multiple runs average results are calculated for each method. The same number of interactions is used in order to make the comparison fair and accurate. SVM-Wavelet produced better results than the other two approaches since wavelet algorithm

Table 4: User-defined parameters for SVM models.

SVM model	Used parameters		
	C	γ	ε
SVM-Wavelet	1.45	0.34	0.34
SVM-RBF	2.47	0.67	0.62
SVM-FFA	1.74	0.47	0.27

Table 5: Comparative performance statistics of the SVM-Wavelet, SVM-RBF, and SVM-FFA models for PCI prediction.

SVM model	Statistical indicator		
	RMSE	R^2	EI
SVM-Wavelet	0.14	0.86	0.86
SVM-RBF	0.19	0.74	0.74
SVM-FFA	0.15	0.84	0.84

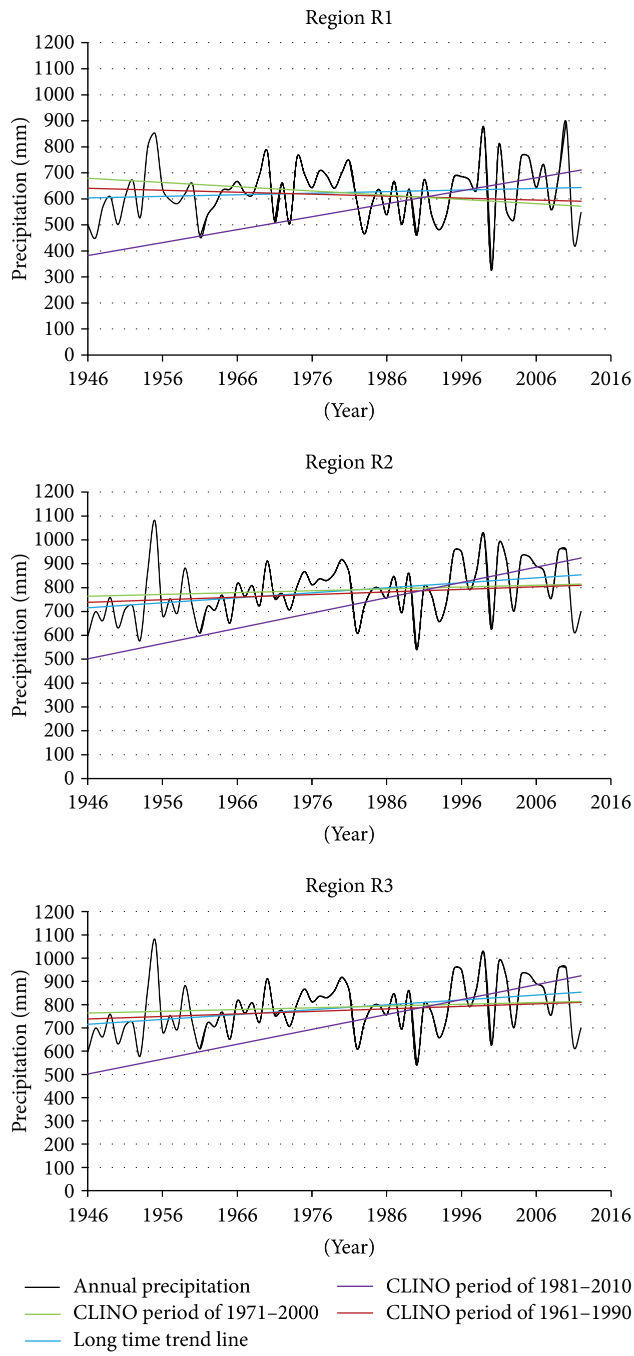

Figure 5: The trend of annual precipitation by regions.

decomposes nonlinear series in multiple linearized series in order to make it easier to regress.

The SVM-Wavelet model outperforms the SVM-RBF and the SVM-FFA models according to the obtained results. The predictions from the SVM models correlate highly with the actual PCI data.

4. Conclusion

The study carried out a systematic approach to create the SVM models for the PCI prediction such as SVM-Wavelet, SVM-RBF, and SVM-FFA. The proposed SVM-Wavelet model was obtained by combining two methods, that is, the SVM and the wavelet transform. The RBF was selected as the kernel function for the SVM, while the FFA was used to obtain the SVM parameters.

Each of these SVM approaches has some advantages and disadvantages. SVM-FFA has firefly searching algorithm in order to find optimal SVM parameters. Wavelet approach divides series into subgroups in order to make it more linear and at the end all groups are merged. SVM-RBF approach is the basic approach with manual estimation of SVM parameters. Therefore SMV-RBF results are not as good as the other two approaches as was presented.

A comparison of the SVM-Wavelet, the SVM-RBF, and the SVM-FFA was performed in order to assess the prediction accuracy. Accuracy results, measured in terms of RMSE, R^2, and EI, indicate that SVM-Wavelet predictions are superior to the SVM-RBF and the SVM-FFA.

The main advantages of the SVM schemes are as follows: computationally efficient and well-adaptable with optimization and adaptive techniques. The developed strategy is not only simple, but also reliable and may be easy to implement in real time applications using some interfacing cards for control of various parameters. This can be combined with expert systems and rough sets for other applications.

The further research will test the proposed soft computing methods in a different part of the world and different climate types to confirm the results. Also, some hybrid soft computing models will be applied to compare with the developed models presented in this study.

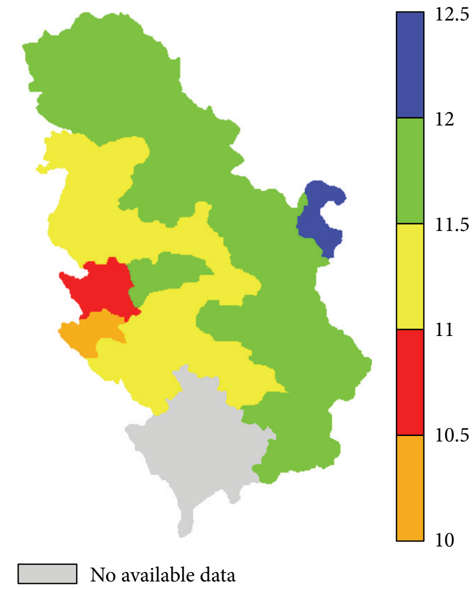

Figure 6: Spatial pattern of the precipitation concentration index.

Competing Interests

The authors declare that they have no competing interests.

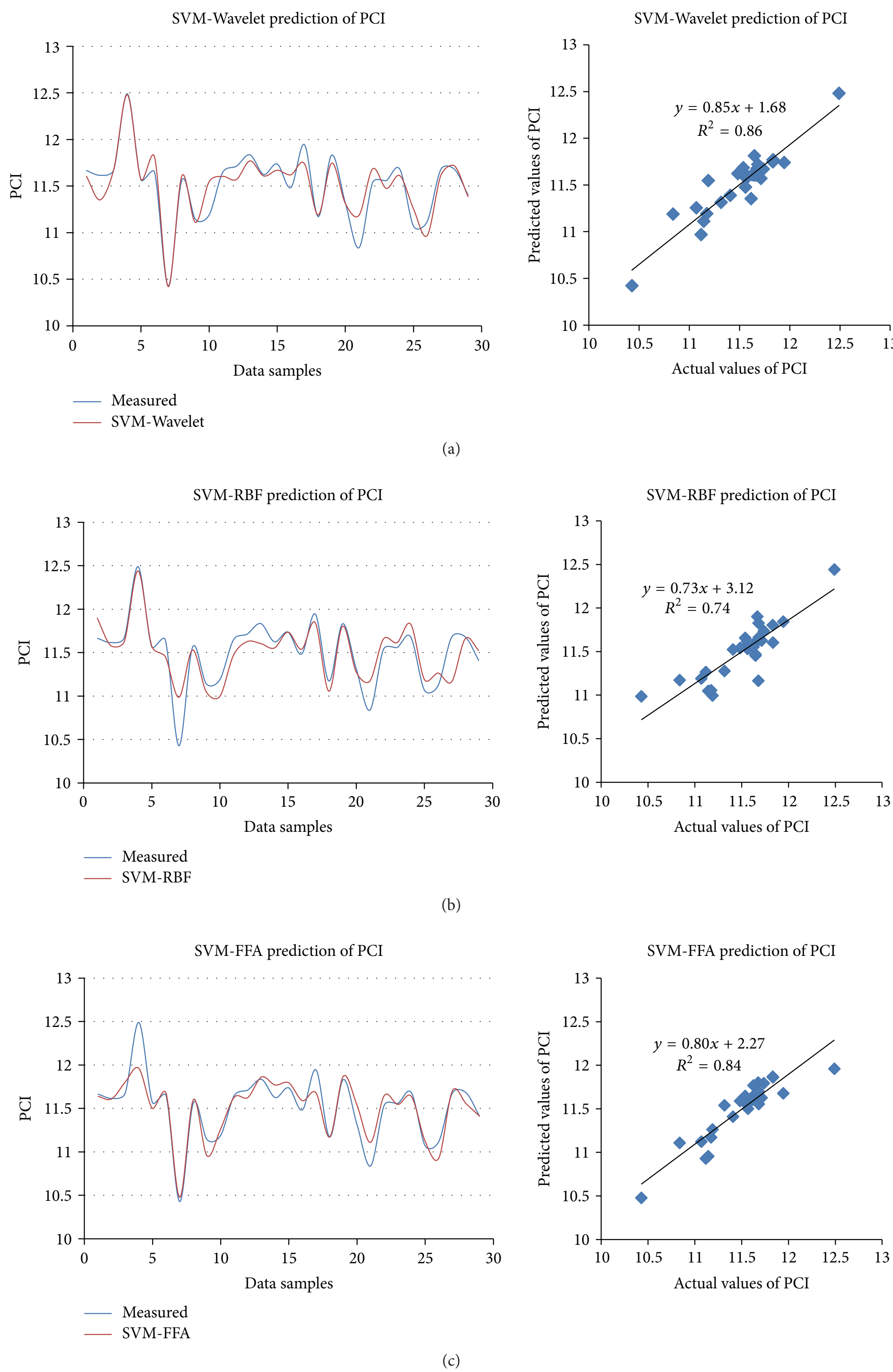

Figure 7: Scatter plots of actual and predicted values of PCI using (a) SVM-Wavelet, (b) SVM-RBF, and (c) SVM-FFA method.

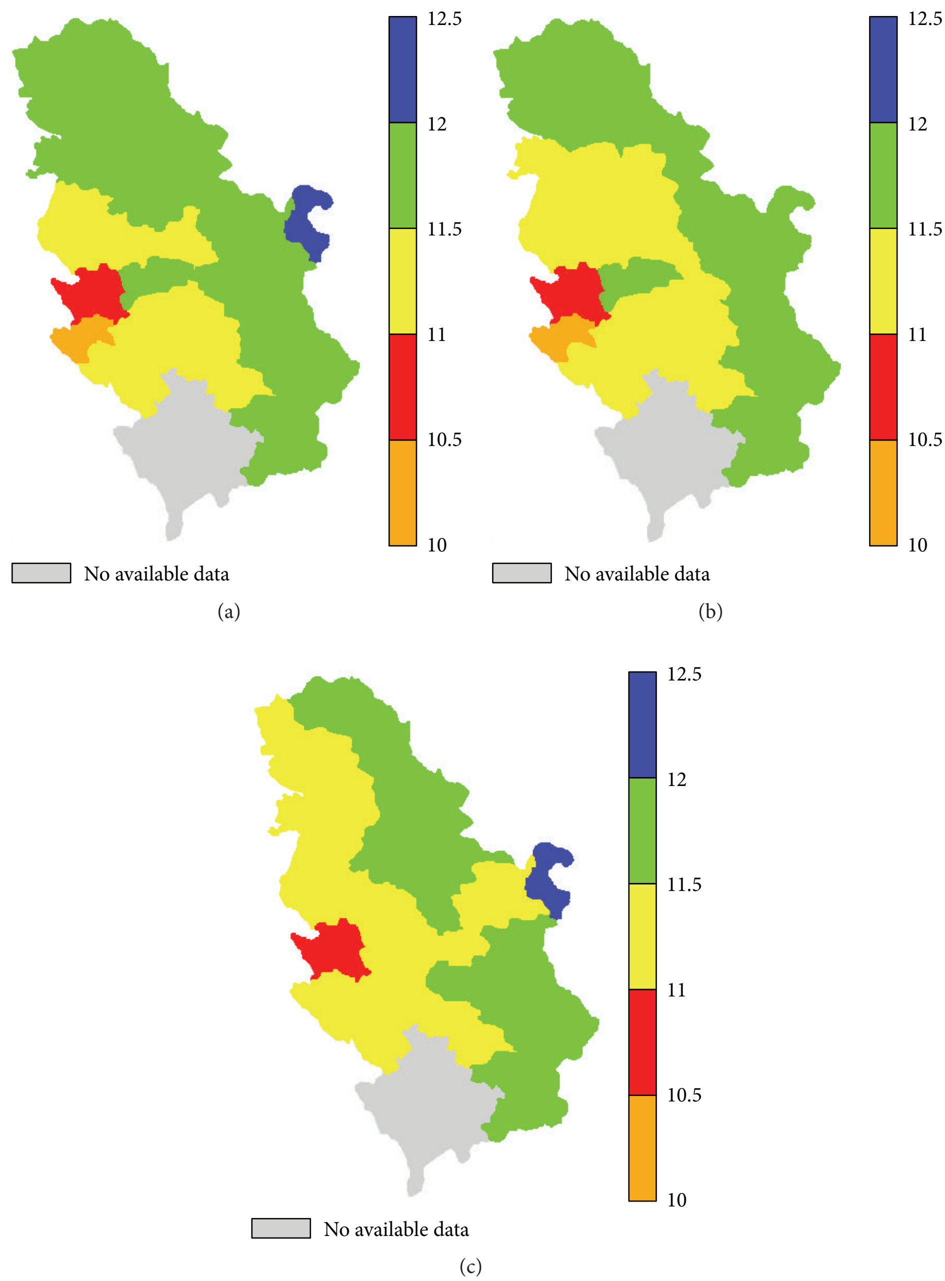

FIGURE 8: Spatial patterns of the PCI obtained using (a) SVM-Wavelet, (b) SVM-FFA, and (c) SVM-RBF method.

Acknowledgments

The study is supported by the Ministry of Education, Science and Technological Development, Republic of Serbia (Grant no. TR37003) and the ICT COST Action IC1408 Computationally Intensive Methods for the Robust Analysis of Non-Standard Data (CRoNoS). This research is supported by University of Malaya under UMRG grant (Project no. RP036A-15AET: Efficient Detection and Reporting of Flood Wastes using Wireless Sensor Network RP036B-15AET: Measurement of the Flood Waste Volume based on the Digital Image RP036C-15AET: Intelligent Estimation and Prediction of Flood Wastes).

References

[1] Y. Zhang, W. Cai, Q. Chen, Y. Yao, and K. Liu, "Analysis of changes in precipitation and drought in Aksu River Basin, Northwest China," *Advances in Meteorology*, vol. 2015, Article ID 215840, 15 pages, 2015.

[2] B. Alijani, J. O'Brien, and B. Yarnal, "Spatial analysis of precipitation intensity and concentration in Iran," *Theoretical and Applied Climatology*, vol. 94, no. 1-2, pp. 107–124, 2008.

[3] H. Feidas, C. Noulopoulou, T. Makrogiannis, and E. Bora-Senta, "Trend analysis of precipitation time series in Greece and their relationship with circulation using surface and satellite data:

1955–2001," *Theoretical and Applied Climatology*, vol. 87, no. 1–4, pp. 155–177, 2007.

[4] G. Buttafuoco, T. Caloiero, and R. Coscarelli, "Spatial and temporal patterns of the mean annual precipitation at decadal time scale in southern Italy (Calabria region)," *Theoretical and Applied Climatology*, vol. 105, no. 3, pp. 431–444, 2011.

[5] R. Coscarelli and T. Caloiero, "Analysis of daily and monthly rainfall concentration in Southern Italy (Calabria region)," *Journal of Hydrology*, vol. 416-417, pp. 145–156, 2012.

[6] W. Shi, X. Yu, W. Liao, Y. Wang, and B. Jia, "Spatial and temporal variability of daily precipitation concentration in the Lancang River basin, China," *Journal of Hydrology*, vol. 495, pp. 197–207, 2013.

[7] Q. Zhang, P. Sun, V. P. Singh, and X. Chen, "Spatialtemporal precipitation changes (1956–2000) and their implications for agriculture in China," *Global and Planetary Change*, vol. 82-83, pp. 86–95, 2012.

[8] T. Raziei, I. Bordi, and L. S. Pereira, "A precipitation-based regionalization for Western Iran and regional drought variability," *Hydrology and Earth System Sciences*, vol. 12, no. 6, pp. 1309–1321, 2008.

[9] M. De Luis, J. C. González-Hidalgo, M. Brunetti, and L. A. Longares, "Precipitation concentration changes in Spain 1946–2005," *Natural Hazards and Earth System Science*, vol. 11, no. 5, pp. 1259–1265, 2011.

[10] D. S. Martins, T. Raziei, A. A. Paulo, and L. S. Pereira, "Spatial and temporal variability of precipitation and drought in Portugal," *Natural Hazards and Earth System Science*, vol. 12, no. 5, pp. 1493–1501, 2012.

[11] W.-Z. Lu and W.-J. Wang, "Potential assessment of the 'support vector machine' method in forecasting ambient air pollutant trends," *Chemosphere*, vol. 59, no. 5, pp. 693–701, 2005.

[12] T. Asefa, M. Kemblowski, M. McKee, and A. Khalil, "Multi-time scale stream flow predictions: the support vector machines approach," *Journal of Hydrology*, vol. 318, no. 1–4, pp. 7–16, 2006.

[13] P. Jain, J. M. Garibaldi, and J. D. Hirst, "Supervised machine learning algorithms for protein structure classification," *Computational Biology and Chemistry*, vol. 33, no. 3, pp. 216–223, 2009.

[14] Y. Ji and S. Sun, "Multitask multiclass support vector machines: model and experiments," *Pattern Recognition*, vol. 46, no. 3, pp. 914–924, 2013.

[15] S. Sun, "A survey of multi-view machine learning," *Neural Computing and Applications*, vol. 23, no. 7-8, pp. 2031–2038, 2013.

[16] B. Zheng, S. W. Myint, P. S. Thenkabail, and R. M. Aggarwal, "A support vector machine to identify irrigated crop types using time-series Landsat NDVI data," *International Journal of Applied Earth Observation and Geoinformation*, vol. 34, no. 1, pp. 103–112, 2015.

[17] J. Alonso, A. Villa, and A. Bahamonde, "Improved estimation of bovine weight trajectories using support vector machine classification," *Computers and Electronics in Agriculture*, vol. 110, pp. 36–41, 2015.

[18] M. Fu, Y. Tian, and F. Wu, "Step-wise support vector machines for classification of overlapping samples," *Neurocomputing*, vol. 155, pp. 159–166, 2015.

[19] F. Kaytez, M. C. Taplamacioglu, E. Cam, and F. Hardalac, "Forecasting electricity consumption: a comparison of regression analysis, neural networks and least squares support vector machines," *International Journal of Electrical Power and Energy Systems*, vol. 67, pp. 431–438, 2015.

[20] S. G. Kim, Y. G. No, and P. H. Seong, "Prediction of severe accident occurrence time using support vector machines," *Nuclear Engineering and Technology*, vol. 47, no. 1, pp. 74–84, 2015.

[21] R. Zhang and W. Wang, "Facilitating the applications of support vector machine by using a new kernel," *Expert Systems with Applications*, vol. 38, no. 11, pp. 14225–14230, 2011.

[22] S. Shamshirband, M. Gocić, D. Petković et al., "Soft-computing methodologies for precipitation estimation: a case study," *IEEE Journal of Selected Topics in Applied Earth Observations and Remote Sensing*, vol. 8, no. 3, pp. 1353–1358, 2015.

[23] S. Chattopadhyay and G. Chattopadhyay, "Identification of the best hidden layer size for three-layered neural net in predicting monsoon rainfall in India," *Journal of Hydroinformatics*, vol. 10, no. 2, pp. 181–188, 2008.

[24] P. T. Nastos, K. P. Moustris, I. K. Larissi, and A. G. Paliatsos, "Rain intensity forecast using artificial neural networks in Athens, Greece," *Atmospheric Research*, vol. 119, pp. 153–160, 2013.

[25] C. L. Wu and K. W. Chau, "Prediction of rainfall time series using modular soft computing methods," *Engineering Applications of Artificial Intelligence*, vol. 26, no. 3, pp. 997–1007, 2013.

[26] S.-T. Chen, P.-S. Yu, and Y.-H. Tang, "Statistical downscaling of daily precipitation using support vector machines and multivariate analysis," *Journal of Hydrology*, vol. 385, no. 1–4, pp. 13–22, 2010.

[27] H. Meyer, M. Kühnlein, T. Appelhans, and T. Nauss, "Comparison of four machine learning algorithms for their applicability in satellite-based optical rainfall retrievals," *Atmospheric Research*, vol. 169, pp. 424–433, 2016.

[28] J. S. Angelo, H. S. Bernardino, and H. J. C. Barbosa, "Ant colony approaches for multiobjective structural optimization problems with a cardinality constraint," *Advances in Engineering Software*, vol. 80, pp. 101–115, 2015.

[29] E. Assareh, M. A. Behrang, M. R. Assari, and A. Ghanbarzadeh, "Application of PSO (particle swarm optimization) and GA (genetic algorithm) techniques on demand estimation of oil in Iran," *Energy*, vol. 35, no. 12, pp. 5223–5229, 2010.

[30] M. Dorigo, G. Di Caro, and L. M. Gambardella, "Ant algorithms for discrete optimization," *Artificial Life*, vol. 5, no. 2, pp. 137–172, 1999.

[31] M. Dorigo and T. Stützle, "The ant colony optimization metaheuristic: algorithms, applications, and advances," in *Handbook of Metaheuristics*, vol. 57 of *International Series in Operations Research & Management Science*, pp. 250–285, Springer, Berlin, Germany, 2003.

[32] X.-S. Yang and S. Deb, "Cuckoo search: recent advances and applications," *Neural Computing and Applications*, vol. 24, no. 1, pp. 169–174, 2014.

[33] Y. Bao, Z. Hu, and T. Xiong, "A PSO and pattern search based memetic algorithm for SVMs parameters optimization," *Neurocomputing*, vol. 117, pp. 98–106, 2013.

[34] M. Basu, "Modified particle swarm optimization for nonconvex economic dispatch problems," *International Journal of Electrical Power and Energy Systems*, vol. 69, pp. 304–312, 2015.

[35] Z. Beheshti, S. M. Shamsuddin, and S. Hasan, "Memetic binary particle swarm optimization for discrete optimization problems," *Information Sciences*, vol. 299, pp. 58–84, 2015.

[36] M. Kumar and T. K. Rawat, "Optimal design of FIR fractional order differentiator using cuckoo search algorithm," *Expert Systems with Applications*, vol. 42, no. 7, pp. 3433–3449, 2015.

[37] A. Teske, R. Falcon, and A. Nayak, "Efficient detection of faulty nodes with cuckoo search in t-diagnosable systems," *Applied Soft Computing Journal*, vol. 29, pp. 52–64, 2015.

[38] X.-S. Yang, "Firefly algorithms for multimodal optimization," in *Stochastic Algorithms: Foundations and Applications: 5th International Symposium, SAGA 2009, Sapporo, Japan, October 26–28, 2009. Proceedings*, vol. 5792 of *Lecture Notes in Computer Science*, pp. 169–178, Springer, Berlin, Germany, 2009.

[39] I. Fister, I. Fister Jr., X.-S. Yang, and J. Brest, "A comprehensive review of firefly algorithms," *Swarm and Evolutionary Computation*, vol. 13, pp. 34–46, 2013.

[40] X.-S. Yang, "Multiobjective firefly algorithm for continuous optimization," *Engineering with Computers*, vol. 29, no. 2, pp. 175–184, 2013.

[41] C. Sudheer, S. K. Sohani, D. Kumar et al., "A support vector machine-firefly algorithm based forecasting model to determine malaria transmission," *Neurocomputing*, vol. 129, pp. 279–288, 2014.

[42] T. Kanimozhi and K. Latha, "An integrated approach to region based image retrieval using firefly algorithm and support vector machine," *Neurocomputing*, vol. 151, no. 3, pp. 1099–1111, 2015.

[43] S.-U.-R. Massan, A. I. Wagan, M. M. Shaikh, and R. Abro, "Wind turbine micrositing by using the firefly algorithm," *Applied Soft Computing*, vol. 27, pp. 450–456, 2015.

[44] S. Rajasekaran, S. Gayathri, and T.-L. Lee, "Support vector regression methodology for storm surge predictions," *Ocean Engineering*, vol. 35, no. 16, pp. 1578–1587, 2008.

[45] K.-P. Wu and S.-D. Wang, "Choosing the kernel parameters for support vector machines by the inter-cluster distance in the feature space," *Pattern Recognition*, vol. 42, no. 5, pp. 710–717, 2009.

[46] H. Yang, K. Huang, I. King, and M. R. Lyu, "Localized support vector regression for time series prediction," *Neurocomputing*, vol. 72, no. 10-12, pp. 2659–2669, 2009.

[47] Z. Ramedani, M. Omid, A. Keyhani, S. Shamshirband, and B. Khoshnevisan, "Potential of radial basis function based support vector regression for global solar radiation prediction," *Renewable and Sustainable Energy Reviews*, vol. 39, pp. 1005–1011, 2014.

[48] J. Adamowski and H. F. Chan, "A wavelet neural network conjunction model for groundwater level forecasting," *Journal of Hydrology*, vol. 407, no. 1–4, pp. 28–40, 2011.

[49] A. M. Kalteh, "Monthly river flow forecasting using artificial neural network and support vector regression models coupled with wavelet transform," *Computers & Geosciences*, vol. 54, pp. 1–8, 2013.

[50] A. Araghi, M. Mousavi Baygi, J. Adamowski, J. Malard, D. Nalley, and S. M. Hasheminia, "Using wavelet transforms to estimate surface temperature trends and dominant periodicities in Iran based on gridded reanalysis data," *Atmospheric Research*, vol. 155, pp. 52–72, 2015.

[51] S. Li, P. Wang, and L. Goel, "Short-term load forecasting by wavelet transform and evolutionary extreme learning machine," *Electric Power Systems Research*, vol. 122, pp. 96–103, 2015.

[52] D. Nalley, J. Adamowski, and B. Khalil, "Using discrete wavelet transforms to analyze trends in streamflow and precipitation in Quebec and Ontario (1954—2008)," *Journal of Hydrology*, vol. 475, pp. 204–228, 2012.

[53] K.-C. Hsu and S.-T. Li, "Clustering spatial-temporal precipitation data using wavelet transform and self-organizing map neural network," *Advances in Water Resources*, vol. 33, no. 2, pp. 190–200, 2010.

[54] T. Partal and M. Kucuk, "Long-term trend analysis using discrete wavelet components of annual precipitations measurements in Marmara region (Turkey)," *Physics and Chemistry of the Earth, Parts A/B/C*, vol. 31, no. 18, pp. 1189–1200, 2006.

[55] O. Kisi and M. Cimen, "Precipitation forecasting by using wavelet-support vector machine conjunction model," *Engineering Applications of Artificial Intelligence*, vol. 25, no. 4, pp. 783–792, 2012.

[56] M. Gocic and S. Trajkovic, "Spatio-temporal patterns of precipitation in Serbia," *Theoretical and Applied Climatology*, vol. 117, no. 3-4, pp. 419–431, 2014.

[57] J. D. Pnevmatikos and B. D. Katsoulis, "The changing rainfall regime in Greece and its impact on climatological means," *Meteorological Applications*, vol. 13, no. 4, pp. 331–345, 2006.

[58] J. E. Oliver, "Monthly precipitation distribution: a comparative index," *Professional Geographer*, vol. 32, no. 3, pp. 300–309, 1980.

[59] V. N. Vapnik, *Statistical Learning Theory*, Wiley-Interscience, New York, NY, USA, 1998.

[60] V. N. Vapnik, *The Nature of Statistical Learning Theory*, Springer, New York, NY, USA, 2000.

[61] X.-S. Yang, "Firefly algorithm, stochastic test functions and design optimisation," *International Journal of Bio-Inspired Computation*, vol. 2, no. 2, pp. 78–84, 2010.

[62] X. S. Yang and X. He, "Firefly algorithm: recent advances and applications," *International Journal of Swarm Intelligence*, vol. 1, no. 1, pp. 36–50, 2013.

Hindawi Publishing Corporation
Advances in Meteorology
Volume 2016, Article ID 2317252, 9 pages
http://dx.doi.org/10.1155/2016/2317252

Research Article

Exploitation of Documented Historical Floods for Achieving Better Flood Defense

Slobodan Kolaković,[1] Julius Fabian,[2] Sándor Kovács,[3] Ljubomir Budinski,[1] and Matija Stipić[1]

[1] *Department of Civil Engineering, Faculty of Technical Sciences, University of Novi Sad, Trg Dositeja Obradovica 6, 21000 Novi Sad, Serbia*
[2] *Department of Hydraulic, Water Resources and Environmental Engineering, Faculty of Civil Engineering Subotica, University of Novi Sad, Kozaracka 2/a, 24000 Subotica, Serbia*
[3] *Central Tisza Regional Directorate of Water Management, Boldog Sandor Istvan korut 4, Szolnok 5000, Hungary*

Correspondence should be addressed to Julius Fabian; julius@gf.uns.ac.rs

Received 2 October 2015; Revised 30 January 2016; Accepted 1 February 2016

Academic Editor: Ozgur Kisi

Establishing Base Flood Elevation for a stream network corresponding to a big catchment is feasible by interdisciplinary approach, involving stochastic hydrology, river hydraulics, and computer aided simulations. A numerical model calibrated by historical floods has been exploited in this study. The short presentation of the catchment of the Tisza River in this paper is followed by the overview of historical floods which hit the region in the documented period of 130 years. Several well documented historical floods provided opportunity for the calibration of the chosen numerical model. Once established, the model could be used for investigation of different extreme flood scenarios and to establish the Base Flood Elevation. The calibration has shown that the coefficient of friction in case of the Tisza River is dependent both on the actual water level and on the preceding flood events. The effect of flood plain maintenance as well as the activation of six potential detention ponds on flood mitigation has been examined. Furthermore, the expected maximum water levels have also been determined for the case if the ever observed biggest 1888 flood hit the region again. The investigated cases of flood superposition highlighted the impact of tributary Maros on flood mitigation along the Tisza River.

1. Introduction

According to the concept of flood defense relying on the Base Flood Elevation corresponding to the design flood of a given recurrence interval, the expected maximum water levels need to be determined all along the river. It is not a clear task, since the BFE depends on many factors, among others on the actual condition of the tributary network in the considered catchment. Producing a suitable solution tool—a flow analysis numerical model—requires interdisciplinary approach exploiting statistical hydrology, river hydraulics, and computer science. In case of large catchments the numerical model may become complex due to the big number of tributaries involved, all having specific flow conditions [1–5]. High velocities and low discharges are characteristic to the upstream tributaries [1] and low velocities and high discharges are typical to the river sections in lowlands [4, 5].

A flow analysis software package known by acronym HEC-RAS has been adopted in this study by the authors. It is capable of accounting for a wide variety of conditions and influences. However, it needs to be calibrated for the conditions of extreme floods which are unique in many aspects [6, 7]. Not any flood event is suitable for calibration purposes, since all aspects of extreme floods need to be revealed by the chosen floods [8].

Once the model is set up properly, it can be used to simulate different possible flood scenarios having specific chance of occurrence [2, 9], imposing certain level of threat to the community. The model produces information regarding maximum water levels along the reaches, corresponding to the modeled extreme flood event. Exhaustive investigation of scenarios corresponding to well-documented historical floods finds out the expected highest peak water levels, in consequence, the safest solution. This approach—applicable to any catchment—is presented in this paper through the example of the Tisza River.

The catchment of the Tisza River is chosen by reason, since due to its size and characteristics it exhibits a number of special conditions which might influence the expected maximum water levels (inhomogeneous hydrological conditions over the subcatchments, intensive change of the river bed due to erosion/deposition, superposition of flood waves coming from tributaries, and so on). The catchment of the Tisza River having area of 157.200 km^2 is considered to be the most important tributary of the Danube River. Approximately 30% of the total catchment area of the Tisza River spreads in the Hungarian lowlands, while the rest 70% is in the territory of Slovakia, Ukraine, Romania, and Serbia. In terms of elevations, 46% of the catchment is below 200 MSL (related to the Baltic Sea), 34% is between 200 and 500 MSL, and the remaining 20% is located between 500 and 1600 MSL. The annual drainage exceeds 1500 mm in the highest parts of the catchment, while it remains below 28 mm in the lowlands, producing discharge from 50 l/s to 0.8 l/s per square km of the catchment.

The shape of the catchment is almost circular having diameter of 460 km in the north–south direction and 520 km in the east–west direction. Extreme climate conditions over the catchment, the relative contribution of individual tributaries (Upper-Tisza, Tur, Szamos, Kraszna, Lonyai Canal, Bodrog, Sajo-Hernad, Eger-Creek, Lasko-Creek, Zagyva, Koros, Maros, Aranka, and Bega) to the total flow of the Tisza River, extremely low bed slope of the section stretching in the Hungarian lowlands, significant amount of sediment carried by the river, and the existing water training works altogether make the Tisza River one of the most variegated rivers in the region, producing extreme floods as well as extreme low flow periods. As a result, 1919, 1941, 1970, 1980, and 1998 were plentiful in water. Contrarily, 1921, 1943, 1961, 1973, 1990, and 1994 were short in water.

There is no other river in Europe which encountered so radical reduction in length by regulation works (from 1398.9 km to 945.8 km). The flow is restricted by embankments almost along its whole length, while three dams built in the recent five decades radically changed the mid- and low-flow regimes. On the one hand, the mentioned regulation works along with the deforestation of the catchment increased the runoff and the peak flood discharges. On the other hand, the increased water demand of the industry and of the agriculture further reduced the low discharges during the dry periods.

For the ongoing radical anthropogenic impacts on the flow regime of the river during the last century and due to the risks involved, this study targets extreme flood events. Past floods can be employed for calibration of a suitable numerical model, used later as a tool for predicting the possible outcome of extreme flood scenarios. This opportunity has been investigated by this study.

2. Methods and Materials

2.1. Overview of Historical Floods in the Catchment of the Tisza River. The basic parameters of a flood wave are its volume, peak discharge, and duration. Actually, the hydrograph of the flood wave provides the most information. The peak water level caused by the flood wave—depending on the location and time of interest—is rather consequence than basic parameter of the flood. Table 1 shows the peak water levels of the observed historical floods at four river stations along the Tisza River together with the corresponding intermittent periods.

The 1885 flood is of exceptional importance, not only for its volume, but for the fact it was the last extreme flood before regulation works along the Tisza River commenced. Meander cutoffs and restriction of the river by levees increased the peaks of successive floods. The 1879 flood destroyed more than 93% of buildings in Szeged and claimed 151 lives. The flood peak in 1888 was the absolute maximum until 1919, while it is still not overpassed at Dombrad. Following the accomplishment of the regulation works, the 1895 flood—even though moderate compared to the earlier ones—caused significant damage. The 1919 flood was distinctive in sense of threatening public security all along the river. Following the 1932 flood the practice of watercourse-restricting measures in flood control was abandoned. The flood in 1940 was associated with ice. In 1941 three floods occurred, one in January-February, the second in March-April, and the third in September-October. More moderate floods were characteristics of 1942. The following significant flood happened in 1964. The biggest flood ever—in terms of both peak discharge and duration—happened in 1970. It lasted 125 days, 65 settlements have been evacuated, and 43000 people have been engaged in flood defense. The following flood in 1979 produced peak level at Szolnok just 5 cm below the earlier maximum. In 1991 and in 2000 the earlier highest level (detected in 1970) was exceeded by 1.5 m, an increment not experienced for about a century. Proceeded by an early spring flood significant flood happened in fall 1998. The flood in 1999 was triggered by snowmelt and by the changes in the river bed during the last three decades. This flood was extraordinary in terms of peak level, velocity, and duration, exceeding the corresponding values of the 1970 flood. Leaking of dikes in 1100 locations was discovered (and treated), intervention in cases of 127 boils was needed, and creeping of embankment face in 26 cases has been registered. 2001 was not easier at all. 2005 and 2006 produced a flood lasting through the winter to the spring, supported by snowmelt and intensive rainfall in April. The 2010 flood was triggered by extraordinary rains, bringing six times more precipitation than average to the watershed.

Not only are the main parameters of the flood events informative; looking at the details of their genesis is even more instructive. In case of the Tisza River, in general, floods occur mostly at spring in the period of March–May. Floods are least probable in September. In addition to the extreme meteorological conditions, excessive floods are triggered by late snowmelts accompanied with heavy spring rainfalls, or by coincidence of tributary peak discharges, and by restricting the flood plain by embankments.

2.2. The Modeled Stream Network of the Tisza River. The modeled section of the Tisza River between Kiskore and Titel is 403 km long, including 7 tributaries and 13 reaches.

Table 1: Basic characteristics of excessive and record breaking floods in the Tisza catchment.

Vasarosnameny				Tokaj				Szolnok				Szeged			
Year	Peak level (cm)	Intermittent period (year)	Intermittent period, record breaking floods (year)	Year	Peak level (cm)	Intermittent period (year)	Intermittent period, record breaking floods (year)	Year	Peak level (cm)	Intermittent period (year)	Intermittent period, record breaking floods (year)	Year	Peak level (cm)	Intermittent period (year)	Intermittent period, record breaking floods (year)
1888	**900**			**1888**	**872**			**1888**	**818**			**1888**	**847**		
1895	840	7		1895	815	7		**1895**	**827**	7	7	1889	805	1	
1915	830	10		1915	825	20		1915	808	20		**1895**	**884**	6	7
1919	850	4		1919	860	4		**1919**	**884**	4	24	1913	802	8	
1932	848	13		1924	802	5		1924	846	5		**1919**	**916**	6	20
1940	802	8		1932	856	8		**1932**	**894**	8	13	1924	872	5	
1947	885	7		1940	818	8		1940	880	8		**1932**	**923**	8	13
1962	816	15		1941	800	1		1941	856	0		1940	847	8	
1964	850	2		1964	857	23		1953	801	12		1941	855	1	
1968	800	4		1967	831	3		1962	836	9		1962	820	21	
1970	**912**	2	82	1970	858	3		1964	853	2		*1970*	*960*	8	38
1974	848	4		**1979**	**880**	9	91	1966	855	2		1974	804	4	
1978	870	4		1980	837	1		1967	881	1		1979	842	5	
1979	853	1		1981	805	1		**1970**	**909**	3	38	1981	873	2	
1981	834	2		1998	872	17		1974	840	0		1999	817	18	
1985	831	4		**1999**	**894**	1	20	1977	880	3		2000	930	1	
1993	876	8		*2000*	*928*	1	1	1979	904	2					
1995	843	2		2001	847	1		1980	873	1					
1998	**923**	3	28					1981	885	1					
1999	830	1						1998	897	17					
2000	882	1						**1999**	**974**	1	29				
2001	*941*	1	3					*2000*	*1041*	1	1				
								2001	836	1					

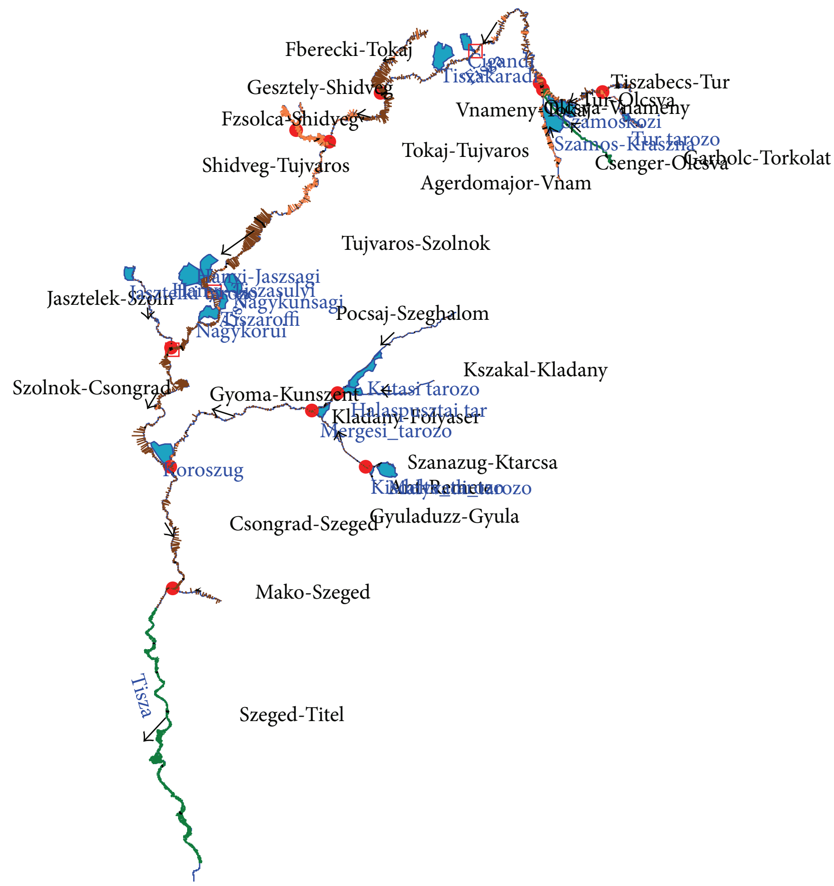

Figure 1: Stream network of the Tisza River.

The total length of the streams involved exceeds 762 km. Bathymetry is defined by around 1200 cross sections. 62 bridges, 1 inline structure, 5 lateral structures, and 12 already existing flood reducing detention ponds are incorporated into the model, Figure 1. Eight out of twelve detention ponds have gate controlled in/outlets, particularly:

(i) Five on the Tisza River: the Beregi, Cigandi, Nagykunsagi, Hanyi-Tiszasulyi, and Tiszaroffi.

(ii) One on the Szamos: the Szamos-Krasznai.

(iii) One on the Fekete-Koros: the Malyvadi.

(iv) One in the junction of the Fekete Koros and the Feher-Koros: the Kisdelta detention pond.

2.3. The HEC-RAS Model. Computer aided analysis of well-documented, reliable, historical flood data is the most instructive and straightforward way of learning about floods and predicting the most likely consequences [6]. The River Analysis System software—known by acronym as HEC-RAS—developed in the Hydrologic Engineering Center by the US Army Corps of Engineers has been adopted for this study by the authors [10, 11]. The HEC-RAS software is capable of simulating 1D steady and unsteady flow in a system of natural and constructed channels, producing as a result the corresponding water surface profiles and the related data.

The general principles of modeling unsteady flow in systems of open channels in the HEC-RAS environment are given in [3, 5, 12, 13]. Unsteady flow routing using HEC-RAS is provided by numerical solution of the continuity and momentum equations. The derivation of the governing equations is presented in [10] by Liggett. The most successful and accepted procedure for solving the one-dimensional unsteady flow equations is the four-point implicit scheme, also known as the box scheme. The software package can handle hydraulic structures like bridges, barrages, culverts, overflow weirs, floodgates, bottom stages, bottom sills, side overflows and gates, static reservoirs, pump stations, and water intakes. Example of application in a complex flood control project is given by [7]. Extended description of the software is given in [11].

2.4. Calibration and Verification of the Model. Calibration is feasible by adjusting the global parameters of the model—in most of the cases Manning's coefficient of friction, eventually the loss coefficients of expansion/contraction [2, 8, 9]—providing successful reproduction of a well-documented past real flood event. Initial values of friction coefficient were estimated by digital aerial orthophotography and in situ surveys, while the final values—separately for the main channel and for the flood plain—were determined by calibration using historical flow data. Calibration is a straightforward procedure in cases of rather frequent floods. However, detailed

Table 2: Manning's coefficient of friction.

Year	Main channel	Flood plain
1979	0,0286	0,0309
1998	0,0285	0,0420

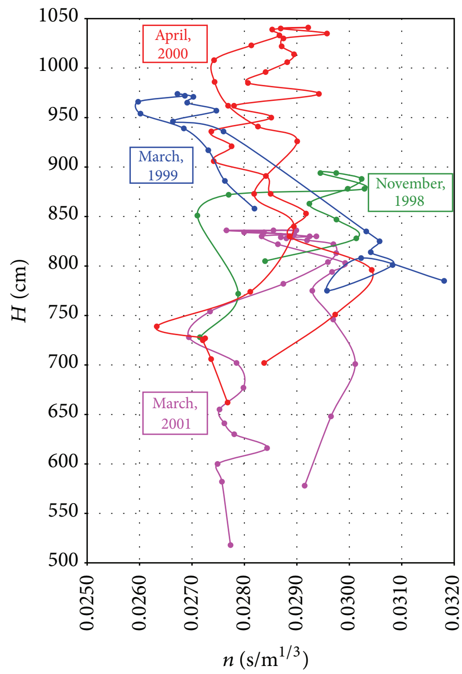

Figure 2: Variation of Manning's coefficient of friction by water level, main bed at Szolnok.

data for extreme floods are seldom available, making them valued.

Flow measurements during flood recession in 1998 were carried out from bridges and boats. Comparison of the 1998 measurement with an earlier one in 1979 produced results shown in Table 2.

The data show almost unchanged characteristics in case of the main channel; however, flow conditions in the flood plain are significantly deteriorated during the corresponding two decades causing reduction in flow capacity up to 300 m^3/s.

Successive measurements in 1998, 1999, 2000, and 2001 produced results shown in Figures 2 and 3 for the main bed and for the flood plain, respectively. The graphs reveal change in friction depending on the time of observation and on the actual water level. Variation of friction coefficient from 0.026 to 0.032 is observed in the main bed and from 0.025 to 0.048 in the flood plain. Increase in friction is due to the development of plant cover in the watercourse. Passing a flood wave often triggers decrease in friction as cutting a passage through an upsilted river section cleans the waterway.

Calibration of the Tisza River model was achieved making use of almost 50 time series comprising of hourly detected water levels at standard measuring posts, and water level readings of dam keepers. In the calibration process default values, 0.3 and 0.1, have been adopted for the expansion and contraction coefficients, respectively. Manning's coefficients

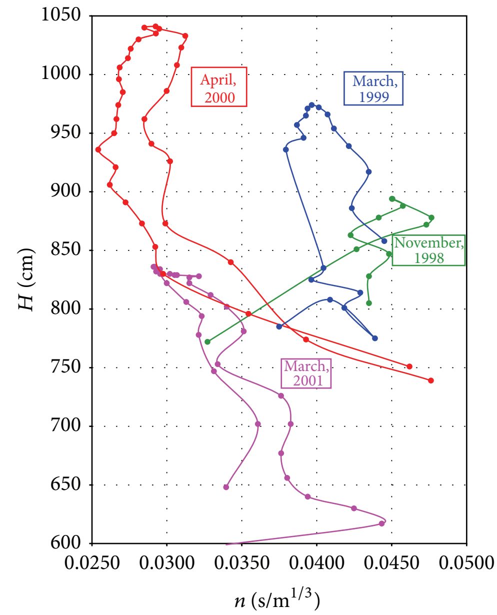

Figure 3: Variation of Manning's coefficient of friction by water level, flood plain at Szolnok.

for the main channel and for the flood plain were determined separately in each cross section. Figures 2 and 3 demonstrate an attempt to establish water level dependant Manning's coefficient; however, it could be achieved for short river sections only.

The blue line in Figure 4 represents the calculated peak water levels, while the red dots are the observed maximum water levels corresponding to the 2006 flood. The maximum difference between the calculated and observed water levels in the river section between Tiszabecs and Titel was 5 cm, which may be considered as very good agreement.

3. Application of the Model

Along the Hungarian section of the Tisza River, peak flow levels have overpassed the Base Flood Elevation during the 2000 flood, at some locations even by 80 cm. Flood protection by endless increasing in the height of the dikes is unfeasible. Alternative solution is reaching the goal by flood plain interventions and by employing detention storages along the river to reduce the peak water levels. Six detention ponds—the Szamos-Krasznakoz, Cigand, Hany-Tiszasuly, Nagykoru, Nagykunsag, and Tiszaroff—have been assigned for this purpose. The first case study is aimed at checking the expected efficiency of flood plain maintenance and activation of detention storages in flood defense.

The second case study investigates if the 1888 extreme flood applied to the current condition of the watercourse could pass nowadays without causing disaster.

At last, flood superposition scenarios have been studied in the third case study by the means of the calibrated model.

3.1. Flood Plain Maintenance, Detention Storages. The influence of flood plain maintenance and the impact of detention

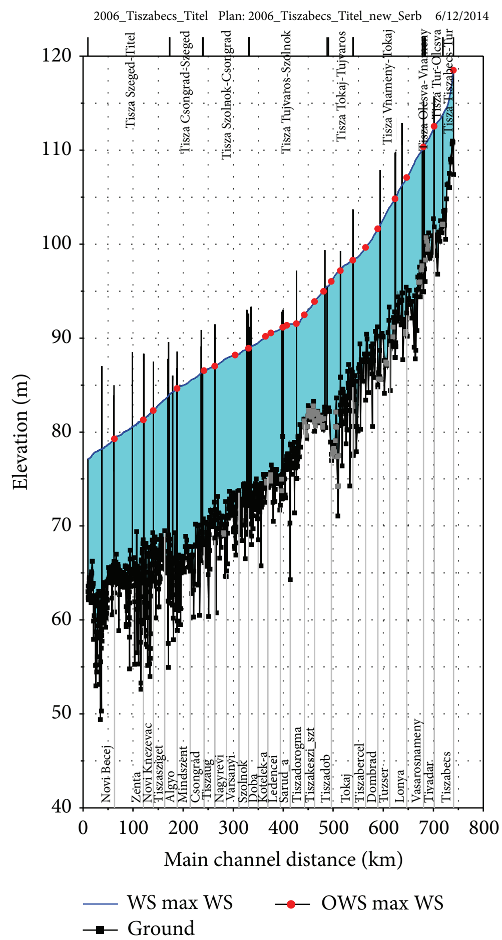

FIGURE 4: Verification of the calibrated parameters against the observed water levels of the 2006 flood.

ponds on flood mitigation have been investigated by the calibrated model: Cases

(a) with flood plain maintenance, without detention ponds activated,

(b) with detention ponds activated, without flood plain maintenance,

(c) with flood plain maintenance, with detention ponds activated

have been considered. The data of the 2000 flood have been exploited in this study for good reason; it was record breaking in terms of maximum water levels even at five locations, Tokaj, Tiszafured, Tiszabo, Szolnok, and Csongrad, Table 3.

The results are shown in Figure 5, where Δz (cm) denotes water level difference due to a particular intervention, compared to the peak water levels expected for the current condition of the river bed; x is river station (km). The light green line represents case (a), the blue line corresponds to case (b), and the dark green line shows the joint effect of both interventions, case (c). The increase of peak water levels in the downstream section ($x < 220$ km) caused by flood plain maintenance is successfully compensated by the effect of detention ponds. With both measures applied, the maximum water levels could be reduced up to 160 cm.

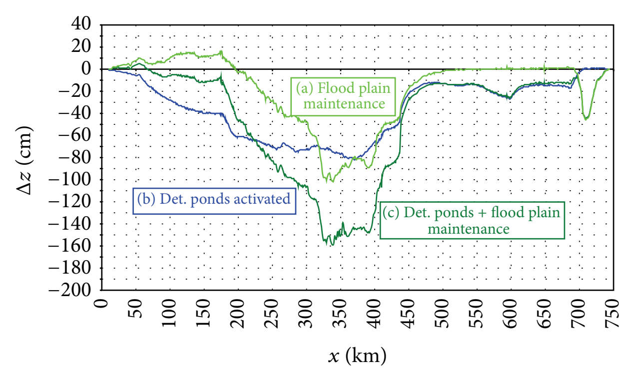

FIGURE 5: Calculated effects of flood plain maintenance and activation of detention ponds on the peak water levels in case of the 2000 flood.

Further improvement in terms of maximum water levels might be achieved using more sophisticated techniques in activation of the eight gate-controlled detention ponds [14]. Calculation results are similar for the 2006 flood as well.

3.2. Application of the 1888 Flood to the Current Condition of the Watercourse. The 1888 flood was so severe that the corresponding maximum water level detected at Dombrad

Table 3: Overview of peak flood levels.

Year	TIVA-DAR	VASAROS-NAMENY	ZAHONY	DOMBRAD	TOKAJ	TISZA-FURED	TISZABO	SZOLNOK	CSONG-RAD	SZEGED
1888	753	900	751	890	872	742		818	834	847
1895							866	827	867	884
1912	790									
1919							919	882	929	916
1925										
1932						750	921	894		923
1933										
1947	848									
1967						765				
1970	865	912				773	935	909	935	961
1979					880	788	949			
1998	964	923								
1999					894	835	1023	974		
2000					928	881	1080	1041	994	
2001	1014	941	758							
2006									1033	1009
Number of record-breaking peaks following the 1888 flood	6	4	2	1	4	7	7	7	6	6

is still not overpassed. In addition, it has occurred in case of watercourse unrestricted by dikes. Even more, extreme water levels over 800 cm lasted more than 14 days in the Vasarosnameny region. For the sake of comparison it is interesting to note that none of the recent floods (1998, 2001) exhibited peak water levels lasting longer than 3.5 days.

This simulation is meant to check if the 1888 flood could pass nowadays without causing trouble. The observed stage hydrograph of the 1888 flood has been set as upstream boundary condition. Stage hydrograph of the 2000 flood has been applied to the outlets of the tributaries and to the most downstream cross section of the Tisza River. The results of simulation compared to the consequences of the 2000 flood are shown in Figure 6. It clearly demonstrates that if the 1888 flood happened nowadays, it would have caused up to 80 cm higher peak levels than the 2000 flood did. Between Tiszalok and Tiszaug peak water levels would over pass the BFE up to 180 cm and they would last over 25 days! It is interesting to notice that, with flood plain maintenance carried out and all planned detention storages accomplished, most of the Hungarian section of the Tisza River could pass the 1888 extreme historical flood.

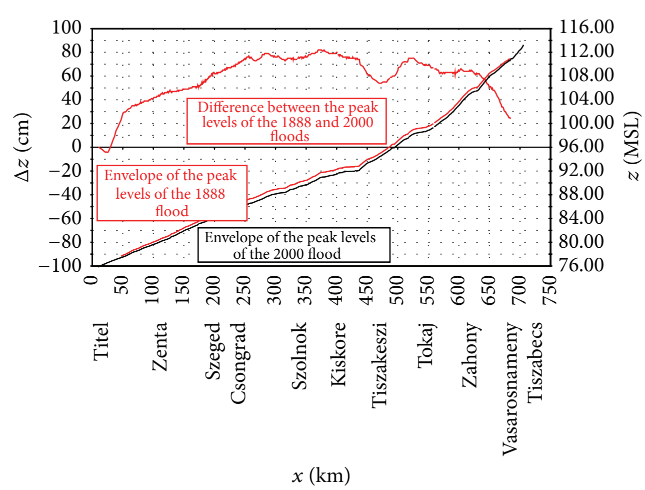

Figure 6: The expected maximum water levels of the 1888 flood calculated with the current condition of the watercourse, compared to the observed maximum water levels of the 2000 flood.

4. Superposition of Floods

A particular flood event on the Tisza River is significantly influenced by the

(i) intensity and duration of floods corresponding to each tributary,

(ii) timing of flood waves of tributaries in relation to the flood wave of the Tisza River.

Wide variety of flood wave superposition is possible producing different outcome in terms of peak levels and peak discharges. Of course, each of these specific combinations has its own chance of occurrence. Some of them—having

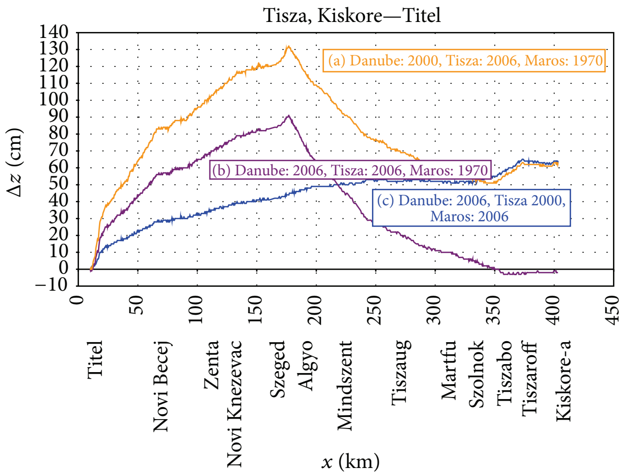

FIGURE 7: The calculated peak water levels for different flood superposition scenarios.

higher practical significance in planning flood defense—are investigated described as follows:

(a) Orange curve in Figure 7: the 2000 year flood is applied to the Danube, the 2006 flood to the Tisza, and the 1970 flood to the Maros.

(b) Purple curve in Figure 7: The 2006 year flood is applied to the Danube and to the Tisza, and the 1970 flood to the Maros.

(c) Blue curve in Figure 7: The 2006 year flood is applied to the Danube, the 2000 flood to the Tisza, and the 2006 flow hydrograph to the Maros.

In Figure 7 the envelope of peak water levels corresponding to the 2006 flood is the reference to which the levels of the investigated cases are compared.

Since the 2006 hydrograph of the Maros was not excessive, peaking at Szeged did not happen, case (c). As the 1970 flood of the Maros was extreme if it happened again, it would have caused excessive peak water levels, at Szeged, up to 130 cm higher than the reference peak level produced by the 2006 flood, cases (a) and (b).

This example highlights the need for stochastic approach in flood analysis in order to get insight into the probability of extreme flood scenarios. In combination with a well calibrated, reliable model, powerful tool in search for the most effective solutions in flood defense could be established.

5. Conclusions

Flood routing is a multidisciplinary complex task. In addition, conditions in a specific catchment are continuously changing partly due to anthropological influences, partly due to natural processes. Numerical models seem to be the only tool which can tackle the problem. If they are to be used for simulation of extreme floods, their calibration with well documented, historical flood data is inevitable. This approach ensures that all particular conditions specific to extreme floods (stochastic character of the event, significant flood plain flow, and inundation storage) reveal themselves.

Modeling different scenarios is currently the most suitable approach to investigate the effects of different flood control approaches; in this paper the influence of flood plain maintenance and exploitation of detention storages have been investigated with good results. Possible superposition of different flood-augmenting influences requires probabilistic approach to flood analysis. Therefore, numerical models combined with statistical hydrology seem to be the most suitable tool for flood prognosis.

The Base Flood Elevation corresponding to the design flood of a given recurrence interval may not be once and forever established, since the bathymetry of the reaches is continuously changing due to the erosion/deposition processes. In addition, seasonal variations are caused by cyclical changes in vegetation. Furthermore, hydrological events are of stochastic character. For that, a design flood of a chosen probability may come about in huge number of scenarios, each producing particular BFE at the location of interest. Therefore, BFE ensuring identical safety over the whole catchment is achievable by establishing the envelope of maximum BFEs coming from different flood scenarios. The envelope of BFEs is attainable by computer aided simulations only, combined with statistical hydrology or by exploiting data of extreme historical floods.

Conflict of Interests

The authors declare that there is no conflict of interests regarding the publication of this paper.

Acknowledgments

This work has been carried out using data provided by the Directorate for Water Management of Lower Tisza District, Szolnok, and by the Directorate for Water Management of Middle Tisza District, Szeged.

References

[1] K. W. Chau, "Application of the Preissmann scheme on flood propagation in river systems in difficult terrain," in *Hydrology in Mountainous Regions. I—Hydrological Measurements; the Water Cycle*, IAHS Publications No. 193, IAHS Press, 1990.

[2] S. L. Dingman and K. P. Sharma, "Statistical development and validation of discharge equations for natural channels," *Journal of Hydrology*, vol. 199, no. 1-2, pp. 13–35, 1997.

[3] R. L. Barkau, *UNET One—Dimensional Unsteady Flow through a Full Network of Open Channels User's Manual*, US Army Corps of Engineers, Hydrologic Engineering Center, Davis, Calif, USA, 1997.

[4] D. W. Knight and K. Shiono, "Channel and floodplain hydraulics," in *Floodplain Processes*, M. G. Anderson, D. E. Walling, and P. D. Bates, Eds., John Wiley & Sons, New York, NY, USA, 1996.

[5] D. W. Knight, K. Shiono, and J. Pirt, "Prediction of depth mean velocity and discharge in natural rivers with overbank flow," in *Proceedings of International Conference on Hydraulic and Environmental Modeling of Coastal, Estuarine and River Waters*,

R. A. Falconer, P. Goodwin, and R. G. S. Matthew, Eds., pp. 419–428, Gower Technical, University of Bradford, September 1989.

[6] S. Kovács, "Modeling the River Tisza by using one-dimension hydro-dynamic model," in *Proceedings of the 3rd International Symposium on Flood Defense*, Nijmengen, The Netherlands, May 2005.

[7] S. Kovács and P. Hegedüs, "Using HEC-RAS for complex flood control project," in *Proceedings of the FMA Annual Conference*, Sacramento, Calif, USA, September 2005.

[8] F. Pappenberger, K. Beven, M. Horritt, and S. Blazkova, "Uncertainty in the calibration of effective roughness parameters in HEC-RAS using inundation and downstream level observations," *Journal of Hydrology*, vol. 302, no. 1–4, pp. 46–69, 2005.

[9] G. Kuczera and M. Mroczkowski, "Assessment of hydrologic parameter uncertainty and the worth of multiresponse data," *Water Resources Research*, vol. 34, no. 6, pp. 1481–1489, 1998.

[10] J. A. Liggett, "Basic equations of unsteady flow," in *Unsteady Flow in Open Channels*, K. Mahmood and V. Yevjevich, Eds., vol. 1, chapter 2, Water Resources Publications, Fort Collins, Colo, USA, 1975.

[11] Haestad Methods, *Floodplain Modeling Using HEC-RAS*, Haestad Press, Waterbury, CT, USA, 2003.

[12] C. A. J. Fletcher, *Computational Techniques for Fluid Dynamics*, vol. I, Springer, Berlin, Germany, 1991.

[13] A. Chadwick and J. Morfett, *Hydraulics in Civil and Environmental Engineering*, Spon, London, UK, 1999.

[14] T. Haktanir, H. Citakoglu, and N. Acanal, "Fifteen-stage operation of gated spillways for flood routing management through artificial reservoirs," *Hydrological Sciences Journal*, vol. 58, no. 5, pp. 1013–1031, 2013.

Hindawi Publishing Corporation
Advances in Meteorology
Volume 2016, Article ID 4891015, 9 pages
http://dx.doi.org/10.1155/2016/4891015

Research Article

Flood Hazard Mapping by Using Geographic Information System and Hydraulic Model: Mert River, Samsun, Turkey

Vahdettin Demir and Ozgur Kisi

Civil Engineering Department, Canik Basari University, Samsun, Turkey

Correspondence should be addressed to Ozgur Kisi; okisi@basari.edu.tr

Received 2 October 2015; Revised 19 December 2015; Accepted 22 December 2015

Academic Editor: Francesco Viola

In this study, flood hazard maps were prepared for the Mert River Basin, Samsun, Turkey, by using GIS and Hydrologic Engineering Centers River Analysis System (HEC-RAS). In this river basin, human life losses and a significant amount of property damages were experienced in 2012 flood. The preparation of flood risk maps employed in the study includes the following steps: (1) digitization of topographical data and preparation of digital elevation model using ArcGIS, (2) simulation of flood lows of different return periods using a hydraulic model (HEC-RAS), and (3) preparation of flood risk maps by integrating the results of (1) and (2).

1. Introduction

Flooding, as a major natural disaster, affects many parts of the world including developed countries. Due to this natural disaster, billions of dollars in infrastructure and property damages and hundreds of human lives are lost each year. These hazards and losses can be prevented and reduced by providing reliable information to the public about the flood risk through flood inundation maps [1]. Flood inundation maps are very essential for municipal planning, emergency action plans, flood insurance rates, and ecological studies [2]. Samsun is the largest and densely populated in the north of Turkey. This area is almost under threat of flooding in each year. In this region, the main reason of devastating flood is the influence of the Mert River especially during March, April, and July and due to seasonal rainfall which eventually makes the district vulnerable to flooding. In addition, the human based constructions and the collapse of water retaining structures are among the main causes of flooding.

Geographic Information Systems (GIS) are successfully used to visualize the extent of flooding and also to analyze the flood maps to produce flood damage estimation maps and flood risk map [3–5]. The GIS must be used together with a hydraulic method to estimate flood profile with a given return period. After 1970, Hydrologic Engineering Centers River Analysis System (HEC-RAS) software developed by United States Army Corps of Engineers (USACE) is widely used in Europe and America. In our country, it was first applied on Bartin River in 1998 by Yazıcılar and Önder [6]. GIS and HEC-RAS models were successfully used for obtaining flood maps of Waller River in Texas [7], Ohio Swan River Basin [3], Atrato River in Colombia [8], Vistula River in Warsaw, Poland [4], Gordon River in France [9], northwest of Colombia [8], mid-eastern Dhaka in Bangladesh [10], and Onaville in Haiti [11]. Çelik et al. analysed the 2004 flood of Kozdere Stream in Istanbul using HEC-RAS and GIS [12]. Sole et al. produced risk maps of Basilicata region (Italy) by acquiring water surface profiles according to different repetition flow in the main distributary (30, 200, and 500 years) [5]. Masood and Takeuchi used HEC-RAS and GIS for assessing flood hazard, vulnerability, and risk of mid-eastern Dhaka [10]. They obtained inundation map for flood of 100-year return period. Sarhadi et al. obtained flood inundation maps of ungauged rivers in southeastern Iran by using HEC-RAS and GIS [13]. Heimhuber et al. used HEC-RAS and GIS to perform one-dimensional, unsteady-flow simulations of design floods in the Ravine Lan Couline, which is the major drainage channel of the area [11]. To the knowledge of the authors, the HEC-RAS and GIS methods were not previously applied to Mert River Basin. Due to its proximity to numerous homes, businesses, and industrial area, the location of Mert River's flood plain is of great interest to city planners,

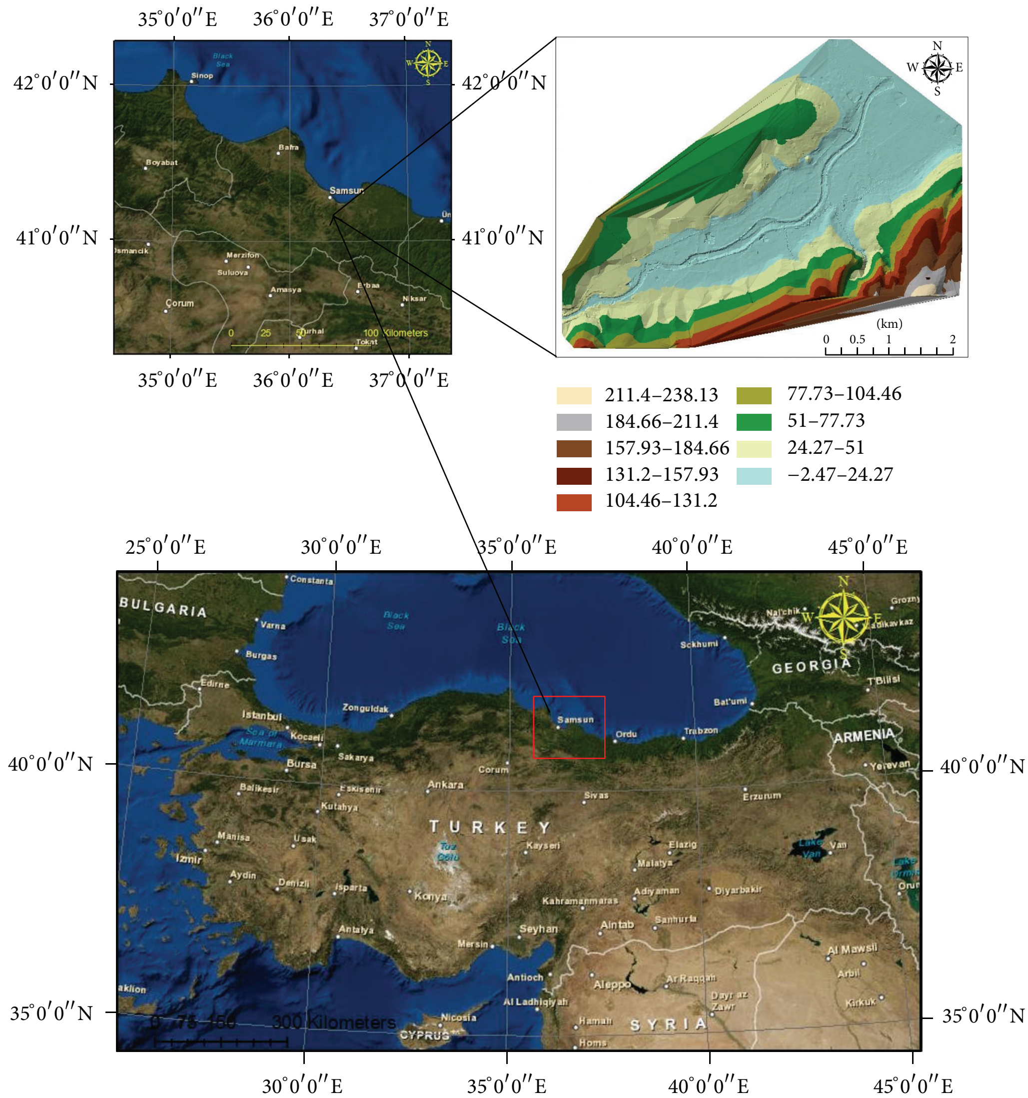

Figure 1: The location of the study area in Turkey.

developers, and property owners. To the knowledge of the authors, the GIS and HEC-RAS were not previously applied to this area where devastating floods happened.

The aim of this study is to obtain flood hazard maps of the Mert River Basin using GIS and HEC-RAS for floods of different return periods (10, 25, 50, 100, and 1000). First, topographical data were digitized and digital elevation model was prepared using ArcGIS. Then, flood flows of different return periods were simulated using a hydraulic model (HEC-RAS). Finally, flood risk maps were obtained by integrating the results of ArcGIS and HEC-RAS. The obtained flood map for 10-year return period was also tested by 2012 flood in which 12 people lost their lives.

2. Study Area

Mert River is located in the center of Samsun. Geographic location of the study area is between Latitude 41.279 and Longitude 36.352. Samsun is the largest city in the Central Black Sea Region of Turkey. This district faces devastating floods which have a destructive effect on humans, buildings, and substructure systems. The Mert River which is about 8 kilometers long flows into the Black Sea. Mert River was selected for this study because it had a great loss of life and property in the recent floods (e.g., July 3, 2012). This river has five highway bridges and one pedestrian bridge. First, second, and third bridges of this river are located in the Black Sea coastline and provide ease of transport between cities. The study area is shown in Figure 1.

2.1. Methodology. In the present study, flood hazard maps were obtained by using HEC-RAS, HEC-GeoRAS, and ArcGIS. The methodology for developing a flood hazard map can be explained by the following three phases: (i) preparing digital elevation model using ArcGIS, (ii) simulation of flood flows of different return periods using HEC-RAS hydraulic model, and (iii) preparing flood risk maps by integrating phases (i) and (ii). The flow chart of the methodology is

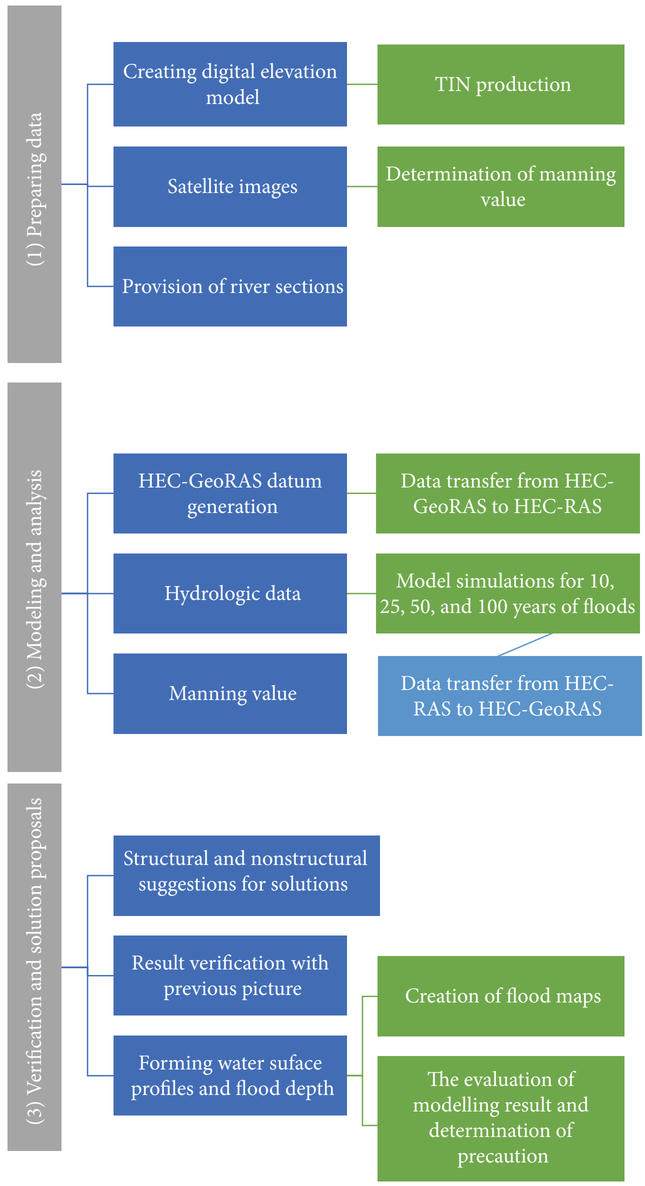

Figure 2: Flow chart of methodology.

illustrated in Figure 2. Next, brief information is provided for the HEC-RAS and HEC-GeoRAS. Detailed information for these methods can be obtained from related literature [14, 15].

2.2. HEC-RAS Model. HEC-RAS, a hydraulic model developed by the USACE, is extensively applied in calculating the hydraulic characteristics of rivers [16, 17]. It is an integrated program and uses the following energy equation for calculating water surface profiles [14, 18]:

$$Y_2 + Z_2 + \frac{\alpha_2 V_2^2}{2g} = Y_1 + Z_1 + \frac{\alpha_1 V_1^2}{2g} + h_e, \qquad (1)$$

where Y, Z, V, α, h_e, and g represent water depth, channel elevation, average velocity, velocity weighting coefficient, energy head loss, and gravitational acceleration; and subscripts 1 and 2, respectively, show cross sections 1 and 2.

This program provides user to input data, data correction, to receive output display and analysis. HEC-RAS model needs details of river cross sections and upstream flow rate. The water depth and mean velocity are calculated for a given cross section using the energy conservation equation [14].

HEC-RAS calculates the water levels' variation along the channel and the water level values are overlaid on a digital elevation model (DEM) of the area to get the extent and flood depth using GIS [19]. Spatial data like cross section, river reach, stream network, flow paths, and others have been obtained using HEC-GeoRAS (Arc-GIS extension) and these data then transferred to HEC-RAS [15].

2.3. HEC-GeoRAS Model (GIS). HEC-GeoRAS is developed for the treatment of geographic data with the HEC-RAS and is working on an extension to ArcGIS (module). Other supplemental information with geometric data files is obtained

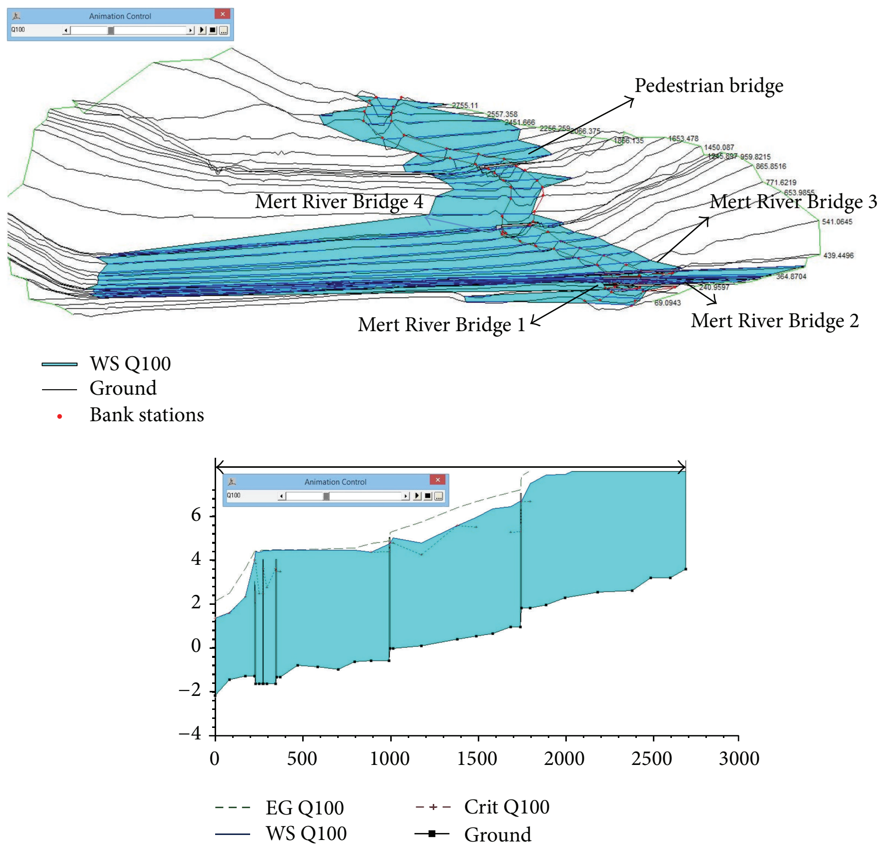

FIGURE 3: Water surface profile for the Q100 flood.

from the Digital Terrain Models. This module can convert the format of HEC-RAS software and can read the obtained format. After analyzing the data with HEC-RAS, water surface profiles, water level, and water velocity can be obtained. The results obtained from hydraulic model can be converted to GIS format by using HEC-GeoRAS and thus flood mapping and flood depth map can be obtained [20].

The mixture of processing topographical information and other GIS data in ArcMap utilizing GeoRAS provides us with the capacity to create and export a geometry file to be investigated by RAS. The created geometry document holds information on river, catchment, and station cross section cut lines, bank stations, flow path. It achieves lengths for left and right overbanks and channel and roughness coefficients and furthermore can contain blocked obstructions. The results of RAS reproduction, for example, river profiles, can be sent specifically to a GIS environment, where they can be analyzed further by the assistance of the GeoRAS toolbar. A particularly arranged GIS information exchange document (∗. sdf) is utilized to perform the GIS data import and export between RAS and ArcMap [21].

3. Application and Results

In this study, HEC-RAS 4.10 was utilized for hydraulic analysis and ArcGIS 10.2 was used for mapping. First, 3D model of study area was prepared utilizing ArcGIS. Digital Elevation Model (DEM) was produced by 1/1000 scale topographical contour lines. Then, topographic data obtained from ArcGIS were transferred to HEC-RAS via Hec-GeoRAS module. Flood values of different return periods (10, 25, 50, and 100 years) and Manning roughness coefficient values were also entered into the HEC-RAS program for calculating water level for each cross section. Finally, the hydraulic analysis results were entered into the ArcGIS via Hec-GeoRAS module and flood hazard maps were obtained for each return period.

Manning roughness coefficients of 0.022, 0.026, and 0.045 were used for concrete, bush-wooded, and woodland river banks and 0.03 was utilized for the river base. Flood values of diverse return periods and annual instant maximum flows were obtained from the Turkish General Directorate of State Hydraulic Works. All these values are reported in Table 1. Table 2 gives the annual instant maximum flows of Mert River. As can be clearly seen from Table 2 a flood (near Q10, flood of ten-year return period) was seen in the studied area in 2012 and loss of life and property occurred.

Flood simulations were conducted using hydrodynamic program for the floods of 10, 15, 50, and 100 return periods. As an example, water surface profiles for the Q100 flood and the location of the bridges on Mert River are shown in Figure 3. Bridges were numbered according to their proximity to the

Table 1: Flood values of different return periods of Mert River.

Return period	5	10	25	50	100	500	1000	10000
Flood (m^3/s)	508	641.8	839.7	1011.6	1207.6	1709.5	2028.5	3139.5

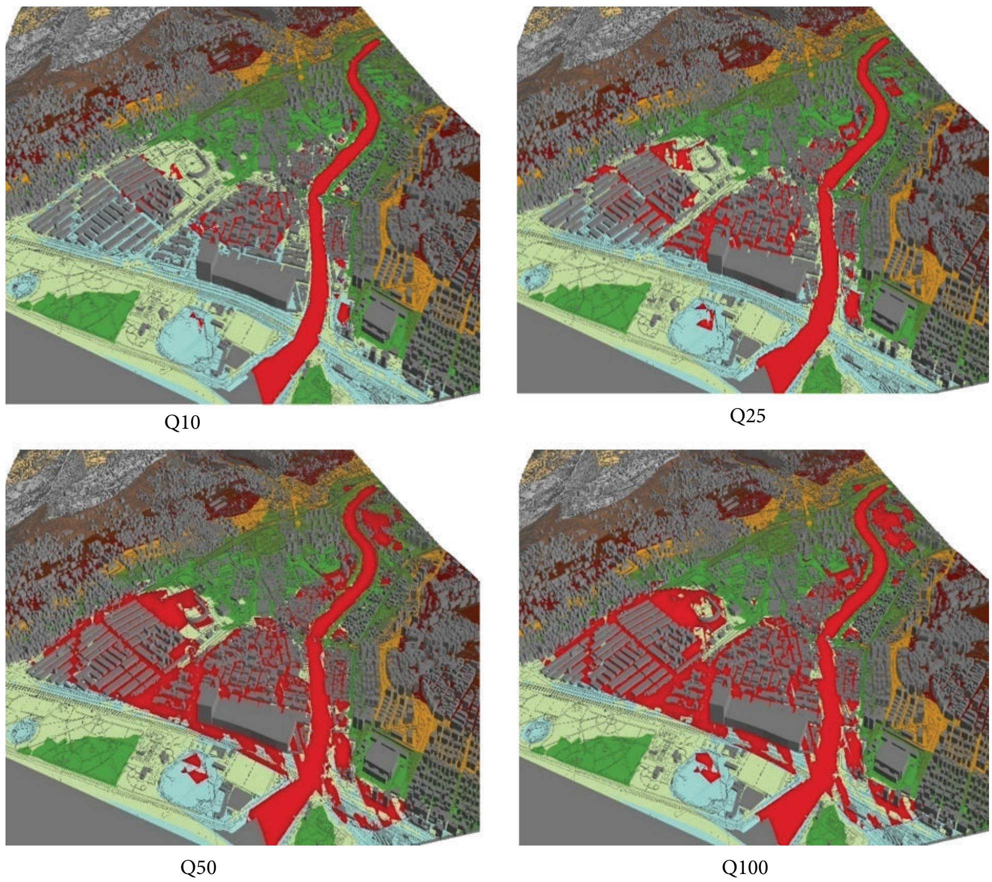

Figure 4: 3D hazard maps of the Mert River obtained for the Q10, Q25, Q50, and Q100 floods.

Table 2: Annual instant maximum flows of Mert River.

Year	2007	2008	2009	2010	2011	2012	2013
Flow (m^3/s)	158	102	66.3	87.1	73	570	66.1

Black Sea. Mert River flows into the sea after Mert River Bridge 1. It is clear from the figure that the last three bridges stay under water in the case of Q100 flood. 3D hazard maps of the Mert River acquired for the Q10, Q25, Q50, and Q100 floods are illustrated in Figure 4. As obviously seen from the figure, there are residential and industrial areas in the studied region which are significantly affected by flood disaster.

Flood depths for each return period were illustrated in Figure 5. The maps clearly demonstrates that when Q10 flood happens, the maximum depth is 6.2 m and affected area is approximately 30% (according to the urban area) in the downstream of the Mert River and the maximum depth and flooded area, respectively, increase to 7.6 m and 60% in the case of Q100 flood. This indicates the flatness of the study area. Concerning the quantity of affected residential area, 650 housings were affected by the 10-year event. This increases to 780, 840, and 960 housings in the case of Q25, Q50, and Q100 floods, respectively.

2012 flood where loss of life and property occurred was also simulated in the present study. Flood hazard map and a photograph indicating a flood instant are outlined in Figure 6. It is clear from the figure that the influenced area is approximately 30% like the Q10 flood. The greatest hazards occur on the right side of the river which is mostly covered by industrial area. The flood magnitude alters a little on the left side of the river and the water reaches just a small number of houses near the river bank. It is clear from the hazard map prepared according to the 2012 flood which appeared in Figure 6 that the maximum depth is around 1 and 1.9 m in the residential area. A flooded building demonstrates that the water level in this area increased to 1–1.5 m when 2012 flood occurred. 619 housings were affected by the 2012 flood. This indicates that the simulation results obtained in this study correspond to the real flood hazard.

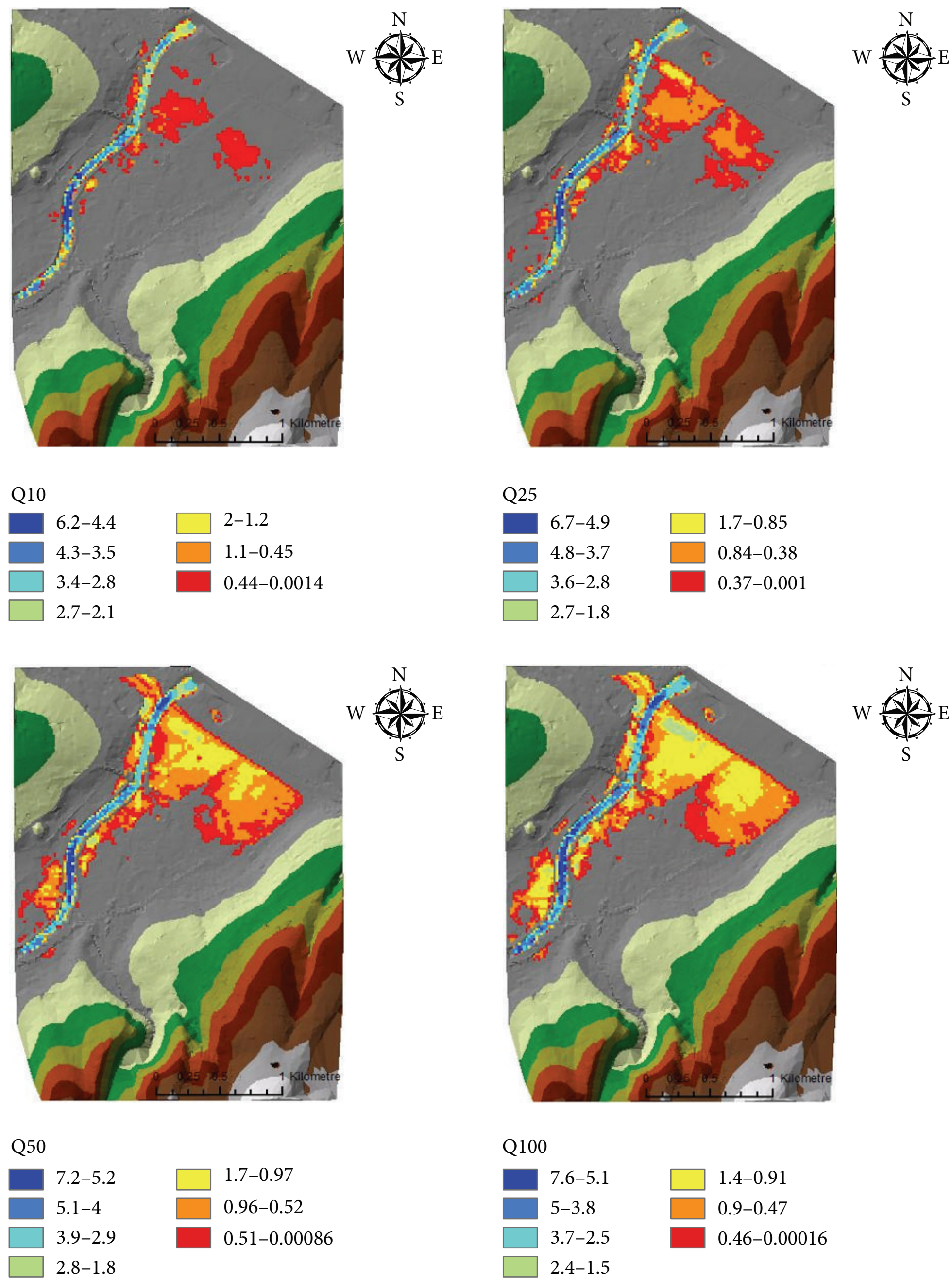

FIGURE 5: Water elevation maps of the studied area for the Q10, Q25, Q50, and Q100 floods.

Flood of July 3, 2012, demonstrated that some areas (traffic roads and buildings surrounding the Mert River) are highly affected even though they have a low recurrence period (close to Q10). The flooded area is located in downstream of Mert River and includes industrial region and residential buildings. It ought to be noticed that the buildings are placed near watercourses. All these indicate a deficient urban planning which results in occupation of river and/or natural flooding areas [22].

The analyzed cross sections of Mert River and flooded area in the case of 2012 flood are represented in Figure 7. The flood impact additionally appeared for the selected section (red line) in this figure (see Figure 7(a)). Figure 7(b) shows the prevention of flood by adding levee and regulation of river bottom. Dotted line in cross section indicates the swell height of the flood.

For the duration of an intense storm, real-time analysis includes using observed rainfall or gauged stage upstream as input for hydrologic modeling, utilizing output flow rates to hydraulic modeling, and finally mapping the output (flood hazard mapping) by a GIS program. Then, this information is utilized to manage flood warning activities such as voidances and road closures. However, the stream velocities are usually too great during a flood to make the flood hazard mapping

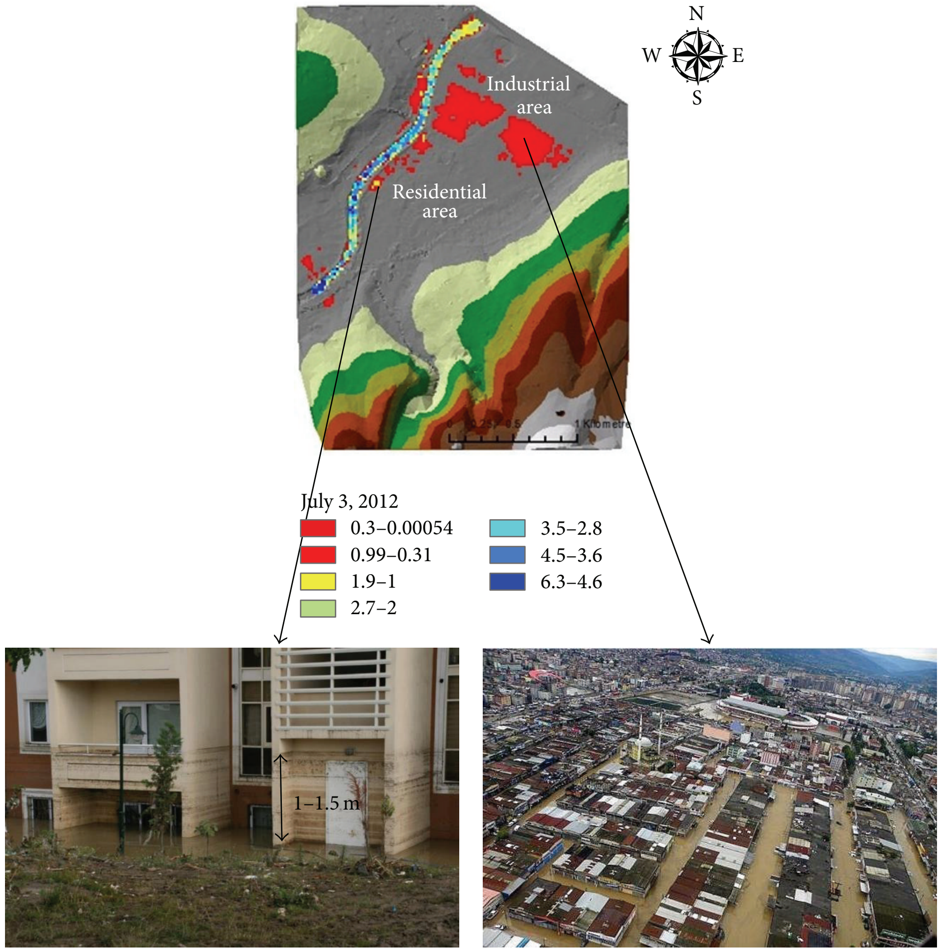

Figure 6: Flood hazard map and a photograph indicating the flood instants in industrial and residential area for the flood of July 3, 2012 [1, 24–26].

practical. For solving this problem, the flood hazard mapping procedures employed in this study may be utilized to prepare a series of flood hazard maps taking into account diverse return periods. In the duration of an intense storm, the flood warning controller can choose the most appropriate digital flood hazard map that corresponds most closely to the real-time measured stream flow [23].

Numerous existing flood hazard maps require revision since they are outdated. The flood hazard mapping outlined in this study saves time and money versus traditional flood hazard delineation on paper maps. By this way, flood hazard maps can be regularly updated as variations in hydrologic and hydraulic conditions warrant [23].

4. Conclusions

Flood hazard mapping of Mert River Basin, Samsun, Turkey, was investigated using GIS and HEC-RAS in this study. 3D hazard maps were obtained for the Q10, Q25, Q50, and Q100 floods. The flood maps demonstrated that some areas are highly affected from flood for low return period (Q10) event. Through Q10 flood, the maximum depth reached 6.2 m and affected area was approximately 30% in the downstream of the Mert River. In addition, 650 housing were affected by this flood. All these indicated an insufficient urban planning in this area. Significant floods occurred for the 100-year return period on the downstream of the Mert River and three bridges out of five remained under flood. Flood hazard map of the 2012 flood where human life losses and a significant amount of property damages were experienced was additionally prepared utilizing GIS and HEC-RAS programs. The simulation results of the Q10 and 2012 floods were compared with each other and similarity was found between them. The studied area generally covers industrial and residential areas. It was seen that floods can be prevented in this region by adding levee and regulation of river bottom. Otherwise, the majority of this flooded area ought to be forested and/or kept as park area.

Conflict of Interests

The authors declare that there is no conflict of interests regarding the publication of this paper.

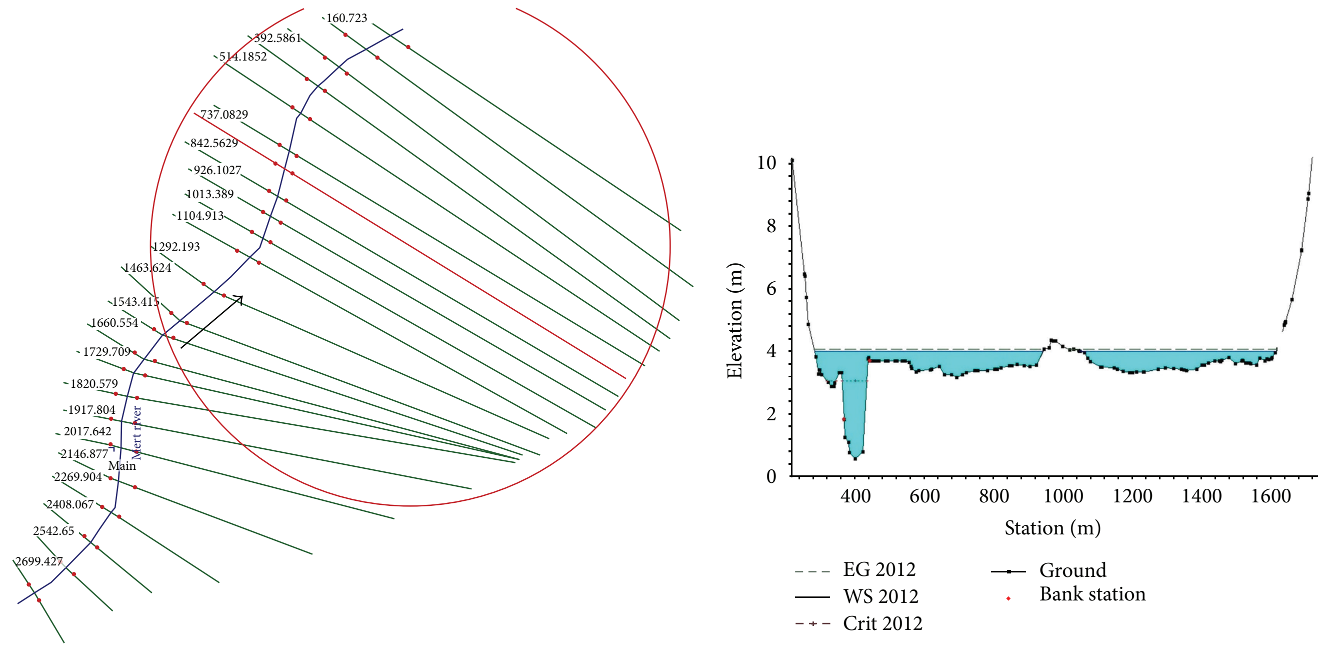

(a)

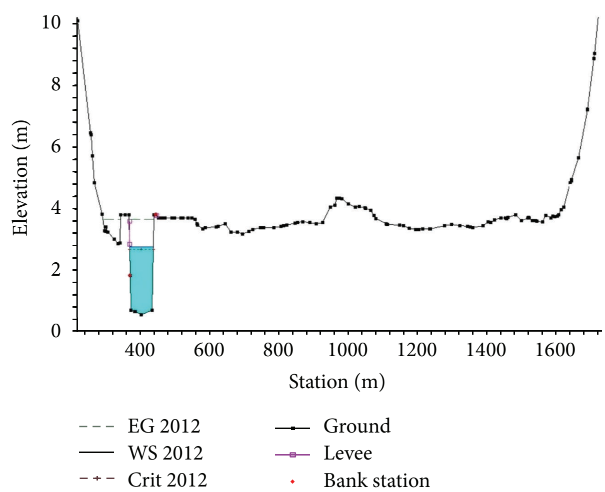

(b)

Figure 7: The analyzed cross sections of Mert River and flooded area in the case of 2012 flood: (a) flood effect for the selected section; (b) prevention of flood by adding levee and regulation of river bottom.

Acknowledgment

This study was supported by Turkish Academy of Sciences (TUBA).

References

[1] V. Demir, *Mert River (SAMSUN/TURKEY) the Flood Maps Determining the Help of Geographic Information Systems*, Canik Basari University Institute of Natural Sciences, Samsun, Turkey, 2015.

[2] C. Goodell and C. Warren, "Flood inundation mapping using HEC-RAS," *Obras y Proyectos*, pp. 18–23, 2006.

[3] J. J. Wiles and N. S. Levine, "A combined GIS and HEC model for the analysis of the effect of urbanization on flooding; the Swan Creek watershed, Ohio," *Environmental & Engineering Geoscience*, vol. 8, no. 1, pp. 47–61, 2002.

[4] M. Gutry-Korycka, A. Magnuszewski, J. Suchozebrski, W. Jaworski, M. Marcinkowski, and M. Szydlowski, "Numerical estimation of flood zones in the Vistula River valley, Warsaw, Poland," in *Climate Variability and Change—Hydrological Impacts*, pp. 191–195, IAHS-AISH Publication, 2006.

[5] A. Sole, L. Giosa, and V. Copertino, "Risk flood areas, a study case: Basilicata region," in *River Basin Management IV*, vol. 1, pp. 213–228, WIT Press, Southampton, UK, 2007.

[6] F. Yazıcılar and H. Önder, "Taşkın Yatakları Planlamasında HEC-RAS Bilgisayar Programı ile Su Yüzü Profili Hesaplanması-Bartın Nehrinde Bir Uygulama," in *Su Mühendisliği Problemleri Semineri*, Muğla, Turkey, September 1998.

[7] E. C. Tate, D. R. Maidment, F. Olivera, and D. J. Anderson, “Creating a terrain model for floodplain mapping,” *Journal of Hydrologic Engineering*, vol. 7, no. 2, pp. 100–108, 2002.

[8] S. Mosquera-Machado and S. Ahmad, “Flood hazard assessment of Atrato River in Colombia,” *Water Resources Management*, vol. 21, no. 3, pp. 591–609, 2007.

[9] N. A. Sheffer, M. Rico, Y. Enzel, G. Benito, and T. Grodek, “The Palaeoflood record of the Gardon River, France: a comparison with the extreme 2002 flood event,” *Geomorphology*, vol. 98, no. 1-2, pp. 71–83, 2008.

[10] M. Masood and K. Takeuchi, “Assessment of flood hazard, vulnerability and risk of mid-eastern Dhaka using DEM and 1D hydrodynamic model,” *Natural Hazards*, vol. 61, no. 2, pp. 757–770, 2012.

[11] V. Heimhuber, J.-C. Hannemann, and W. Rieger, “Flood risk management in remote and impoverished areas—a case study of Onaville, Haiti,” *Water*, vol. 7, no. 7, pp. 3832–3860, 2015.

[12] H. E. Çelik, G. Coskun, H. K. Cigizoglu, N. Ağıralioğlu, A. Aydin, and A. I. Esin, “The analysis of 2004 flood on Kozdere Stream in Istanbul,” *Natural Hazards*, vol. 63, no. 2, pp. 461–477, 2012.

[13] A. Sarhadi, S. Soltani, and R. Modarres, “Probabilistic flood inundation mapping of ungauged rivers: linking GIS techniques and frequency analysis,” *Journal of Hydrology*, vol. 458-459, pp. 68–86, 2012.

[14] C. Fan, C.-H. Ko, and W.-S. Wang, “An innovative modeling approach using Qual2K and HEC-RAS integration to assess the impact of tidal effect on River Water quality simulation,” *Journal of Environmental Management*, vol. 90, no. 5, pp. 1824–1832, 2009.

[15] A. A. Baky, A. M. Zaman, and A. U. Khan, “Managing flood flows for crop production risk management with hydraulic and GIS modeling: case study of agricultural areas in Shariatpur,” *APCBEE Procedia*, vol. 1, pp. 318–324, 2012.

[16] E. C. Carson, “Hydrologic modeling of flood conveyance and impacts of historic overbank sedimentation on West Fork Black’s Fork, Uinta Mountains, northeastern Utah, USA,” *Geomorphology*, vol. 75, no. 3-4, pp. 368–383, 2006.

[17] F. Pappenberger, K. Beven, M. Horritt, and S. Blazkova, “Uncertainty in the calibration of effective roughness parameters in HEC-RAS using inundation and downstream level observations,” *Journal of Hydrology*, vol. 302, no. 1–4, pp. 46–69, 2005.

[18] G. Brunner and V. Bonner, *HEC River Analysis System (HEC-RAS)*, US Army Corps of Engineers Institude for Water Resources Hydrologic Engineering Center, Davis, Calif, USA, 2010.

[19] D. K. Gautam and R. G. Kharbuja, “Flood hazard mapping of bagmati river in kathmandu valley using geo-informatics tools,” *Journal of Hydrology and Meteorology*, vol. 3, no. 2677, pp. 1–9, 2006.

[20] HEC-GeoRAS, *HEC-GeoRAS GIS Tools for Support of HEC-RAS using ARCGIS*, HEC-GeoRAS, 2009.

[21] A. Haghizadeh, L. Teang Shui, M. Mirzaei, and H. Memarian, “Incorporation of GIS based program intohydraulic model for water level modeling on river basin,” *Journal of Water Resource and Protection*, vol. 4, pp. 25–31, 2012.

[22] F. V. Silva, N. B. Bonumá, and P. K. Uda, “Flood mapping in urban area using HEC-RAS model supported by GIS,” in *Proceedings of the 6th International Conference on Flood Management (ICFM6 ’14)*, São Paulo, Brazil, September 2014.

[23] E. Tate and D. Maidment, “Floodplain mapping using HEC-RAS and ArcView GIS,” CRWR Online Report 99-1, Center for Research in Water Resources, 1999.

[24] Samsunda-sel-felaketi-on-raporu-aciklandi-2012-07-08, 2012, http://www.ensonhaber.com/samsunda-sel-felaketi-on-raporu-aciklandi-2012-07-08.html.

[25] NTV, “Samsunda-sel-9-can aldi, 2012,” 2012, http://www.ntv.com.tr/galeri/turkiye/samsunda-sel-9-can-aldi,Qz9WsxxiRU-uFyoEQ6BtJHg/.

[26] 2012, http://www.samsunmimar.org/dosyalar/134218056132631.doc.

Hindawi Publishing Corporation
Advances in Meteorology
Volume 2016, Article ID 4148710, 23 pages
http://dx.doi.org/10.1155/2016/4148710

Research Article

Projection in Future Drought Hazard of South Korea Based on RCP Climate Change Scenario 8.5 Using SPEI

Byung Sik Kim,[1] In Gi Chang,[1] Jang Hyun Sung,[2] and Hae Jin Han[3]

[1] *Department of Urban & Environmental Disaster Prevention, School of Disaster Prevention, Kangwon National University, 345 Jungang-ro, Samcheck-si, Gangwon-do, Republic of Korea*
[2] *Ministry of Land, Infrastructure and Transport, Geum River Flood Control Office, No. 551, Gongju-si, Chungcheongnam-do, Republic of Korea*
[3] *Korea Environment Institute, 370 Sicheong-daero, Sejong-si, Republic of Korea*

Correspondence should be addressed to Jang Hyun Sung; jhsung1@korea.kr

Received 19 July 2015; Revised 8 October 2015; Accepted 29 October 2015

Academic Editor: Milan Gocic

The Standardized Precipitation Evapotranspiration Index (SPEI) analysis was conducted using monthly precipitation data and temperature data on a 12.5 km × 12.5 km resolution based on a Representative Concentration Pathways (RCP) 8.5 climate change scenario, and the characteristics of drought were identified by the threshold. In addition, the changes in drought severity and intensity were projected using the threshold based on the run-length concept and frequency analysis. As a result of the analysis, the probability density function of the total drought and maximum drought intensity moved the upper tail for the upcoming years, and the average drought intensity was also projected to become stronger in the future than in the present to the right side. Through this, it could be projected that the drought scale and frequency and the drought intensity will become severer over South Korea because of future climate change.

1. Introduction

Based on the recent research efforts on climate change, it is projected that South Korea will be one of the countries exposed to the risk of extreme natural disasters, such as heavy rainfall and drought, because of climate change. Since the announcement of the Fourth Assessment Report (AR4) of the Intergovernmental Panel on Climate Change (IPCC), climate change impact assessments have been carried out in South Korea using climate projection data [1–4]. To assess the extreme climate mostly represented by extreme precipitation, drought, and flood, various analyses were applied to a regional climate model or data using statistical downscaling [5–7]. The application results generally project that the probability distribution of extreme precipitation will move to the upper tail and that the drought severity and frequency will increase [8].

The drought starts from meteorological drought and leads to agricultural drought, hydrological drought, and socioeconomic drought; they are monitored or projected using various drought indexes depending on each purpose [9, 10]. Among meteorological drought indexes, Standardized Precipitation Index (SPI) [11] is frequently used because of its simple requirements [12]. The evaluation and projection using SPI of meteorological drought indexes have been actively conducted for South Korea [8, 13]. However, there are some limitations in the assessment of droughts that employs the meteorological drought index because of the multivariate characteristics of droughts. Thus, to consider multivariate drought, an integrated index dealing with various variables, such as runoff, soil moisture, and evapotranspiration, as well as precipitation, has been proposed and applied [14, 15]. Standardized Precipitation Evapotranspiration Index (SPEI) [16], which considers the demand (evapotranspiration) as well as the supply (precipitation), was suggested, and the meteorological drought is assessed in a more physical manner than SPI.

As it is difficult to define when the drought started and ended, previous researches assessed the risk of drought in an indirect way by conducting the frequency analysis of the

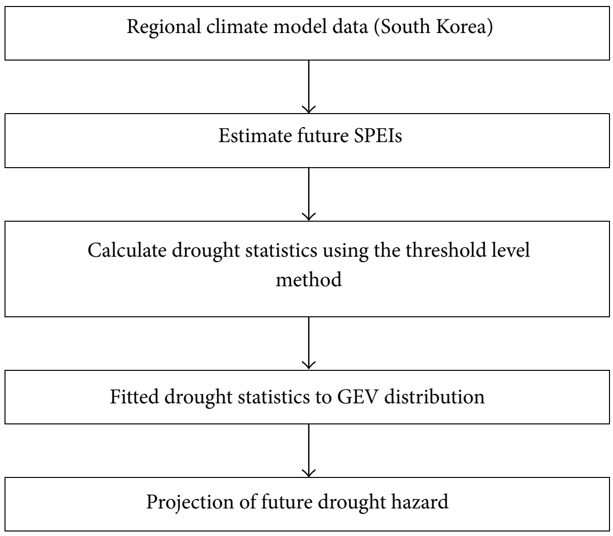

Figure 1: Procedure of this study.

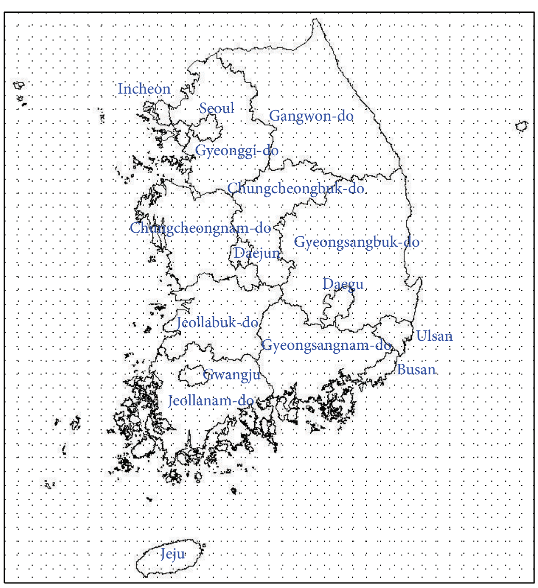

Figure 2: Location map including RCM grid and administrative division.

drought indexes [10, 17]. Mishra and Singh [18] calculated the drought index for each nonexceedance probability by fitting the SPI value to an EV-1 (Extreme Value Type-1) distribution. Lee and Kim [17] derived drought severity-duration-frequency curves by fitting the annual minimum SPI to probability distribution as a random variable. Mishra and Singh [18] developed severity-area-frequency (SAF) curves for annual droughts by climate change. Most researches in the field considered only the annual minimum value and temporary severity of the drought. However, as the drought is multiscale, the analysis of important variables, such as the magnitude, intensity, and duration of the drought, must be conducted. This study aimed to project future SPEI using RCP8.5 projection data. Since 2014, South Korea has been

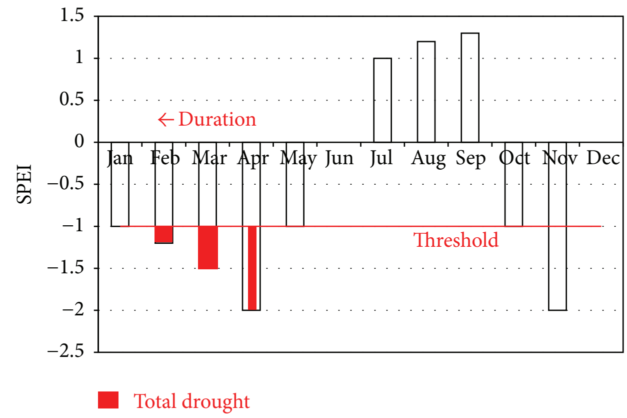

Figure 3: Definition of total drought, maximum drought intensity, and drought magnitude.

suffering from extreme drought; thus, this study projected change in extreme droughts under extreme scenarios. In addition, the drought characteristics by the threshold level to the projected SPEI were identified. This study also projected the drought risk of each administrative division of South Korea in the 21st century by fitting the drought characteristics to the Generalized Extreme Value (GEV) distribution.

2. Theoretical Background and Study Area

2.1. SPEI and Threshold Level. Because SPI does not consider the variables related to temperature, it has a limitation of being unable to consider the change in demand, such as the change in water budget, like the precipitation and evapotranspiration by climate variation. However, SPEI is similar to SPI but can reflect the effect of not only the variability in precipitation but also the variability of evapotranspiration. Thus, this study used SPEI. SPEI is the difference between the random month i and PET obtained by using the precipitation and the Thornthwaite equation [19, 20], as shown in

$$D_i = P_i - \mathrm{PET}_i \tag{1}$$

which is synthesized in each time scale like

$$D_n^k = \sum_{i=0}^{k-1} P_{n-i} - \mathrm{PET}_{n-i}. \tag{2}$$

Here, k is the time scale of synthesis, and n is the month used for calculation. The total drought, maximum drought intensity, and drought magnitude were calculated using SPEI (Figure 3). Negative SPEIs mean the dry condition; a drought event is defined when the SPEI is continuously negative and reaches a value of "–1.0" or less [16]. Thus, it is assumed that "–1.0" is the threshold level and that the drought starts in the level lower than "–1.0" in monthly SPEI. The aggregate of SPEI while one drought event lasts was defined as total drought, and the maximum SPEI during the drought was defined as maximum drought intensity. The drought magnitude was obtained by dividing the total drought by drought duration. The aggregate of SPEI while one drought

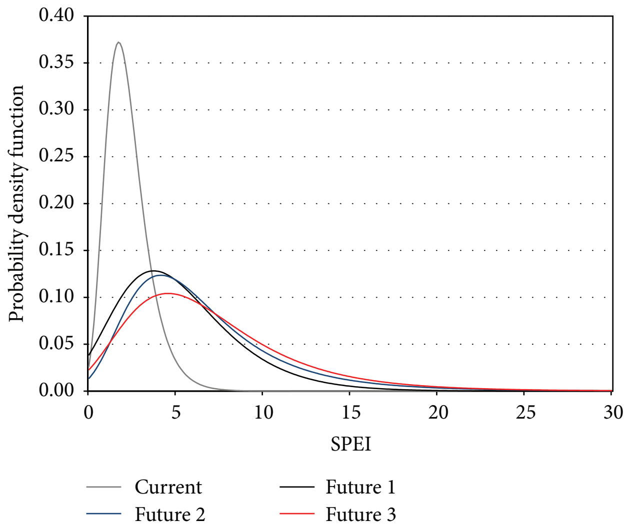

(a) Gangwon-do

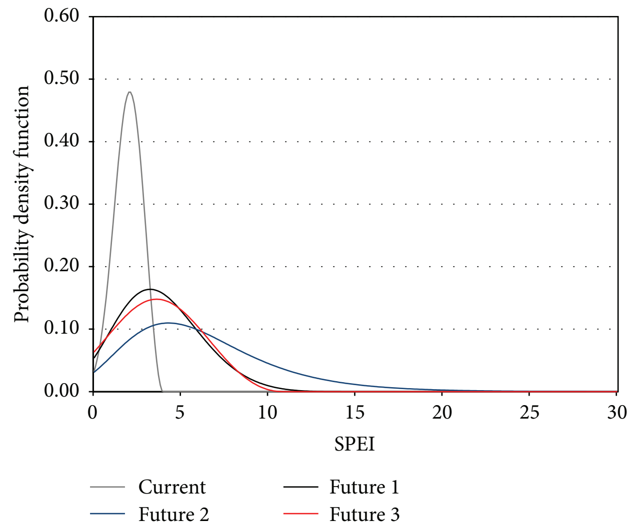

(b) Gyeonggi-do

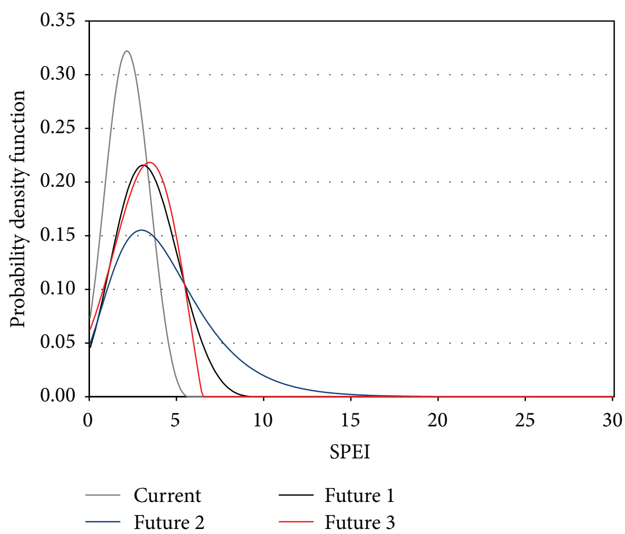

(c) Gyeongsangnam-do

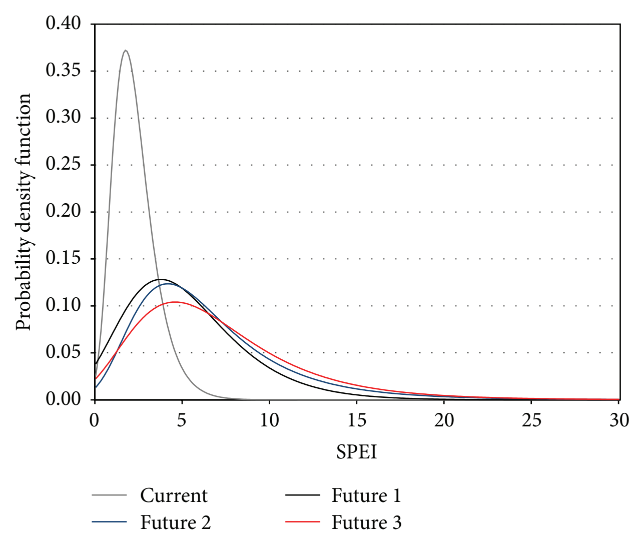

(d) Gyeongsangbuk-do

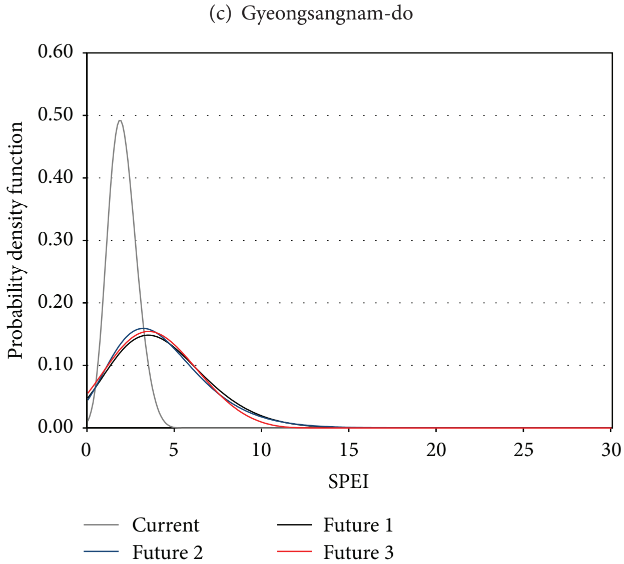

(e) Jeollanam-do

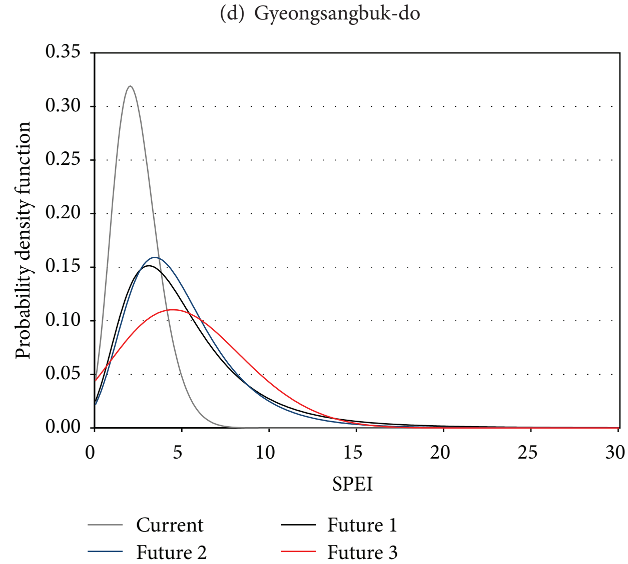

(f) Jeollabuk-do

FIGURE 4: Continued.

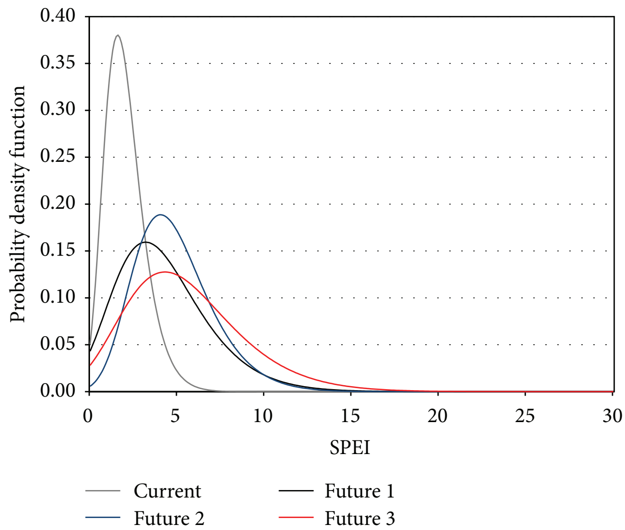

(g) Chungcheongnam-do

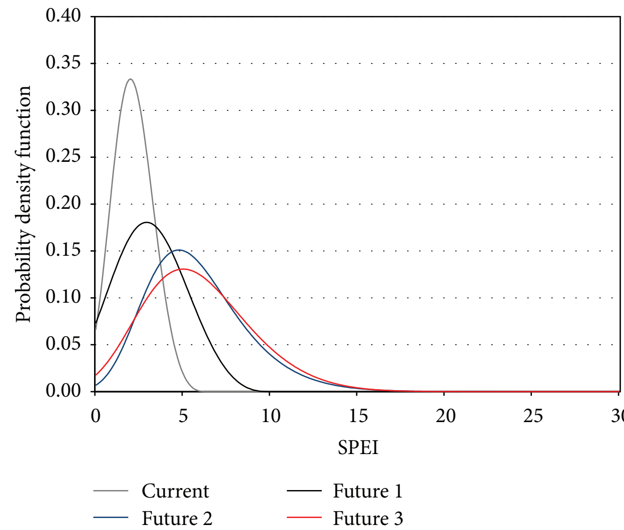

(h) Chungcheongbuk-do

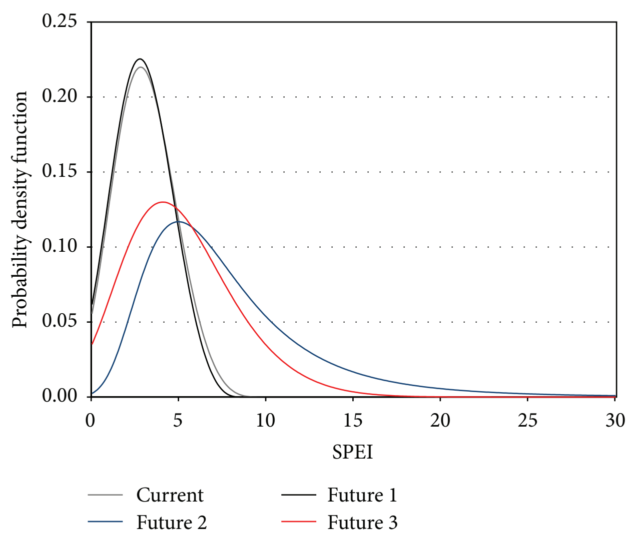

(i) Jeju

Figure 4: GEV PDF projection of total drought according to administrative division.

event lasts was defined as total drought, and the maximum SPEI during the drought was defined as maximum drought intensity. The drought magnitude was obtained by dividing the total drought by drought duration.

2.2. Methodology. Figure 1 shows the research procedure in this study. First, this study projected the SPEI of South Korea in the future by collecting the grid data of the HadGEM3-RA—the representative regional climate model provided by the Korea Meteorological Administration (KMA). The climate of South Korea is composed of four seasons: spring, summer, autumn, and winter. South Korea's winter is influenced by the Siberian air mass, while its summer is hot and humid because of the maritime Pacific high and monsoon. With this, South Korea has been suffering extreme drought recently. By applying the threshold level to future SPEI monthly time series, the drought characteristics were calculated, and the changes of the risk for future drought characteristics were projected using frequency analysis. The HadGEM3-RA [21] used in this study is a regional climate model produced from the global atmosphere-ocean combination model scenario (HadGEM2-AO, resolution: 135 km^2) based on Representative Concentration Pathways (RCP) (Figure 2).

3. Results and Discussion

3.1. Results. Figures 4–6 show the projection of the Probability Density Function (PDF) of the GEV distribution in current climate and future climate for total drought, maximum drought intensity, and drought magnitude. This study takes the absolute value of total drought, maximum

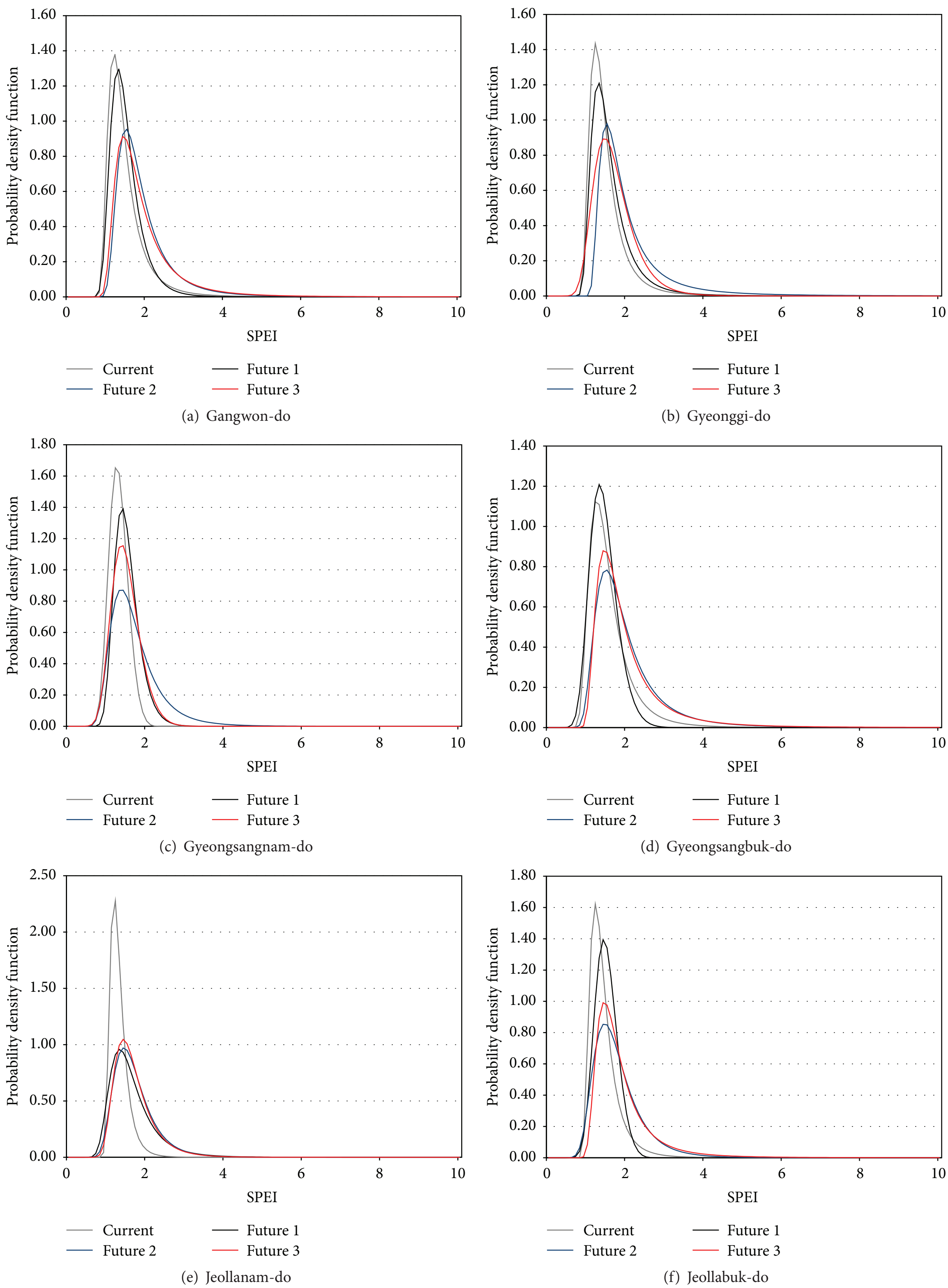

Figure 5: Continued.

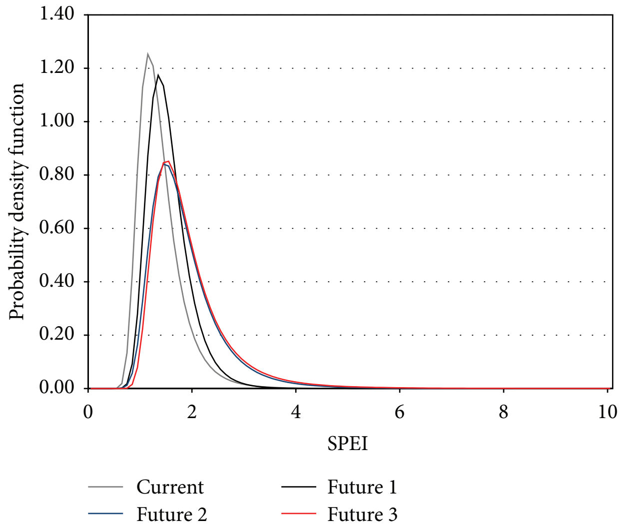

(g) Chungcheongnam-do

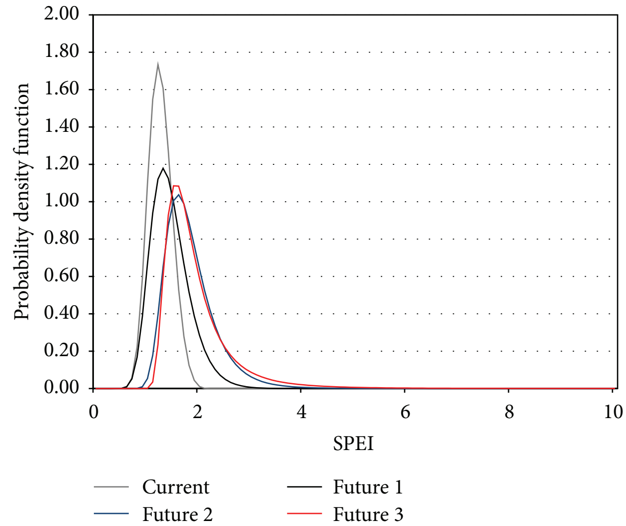

(h) Chungcheongbuk-do

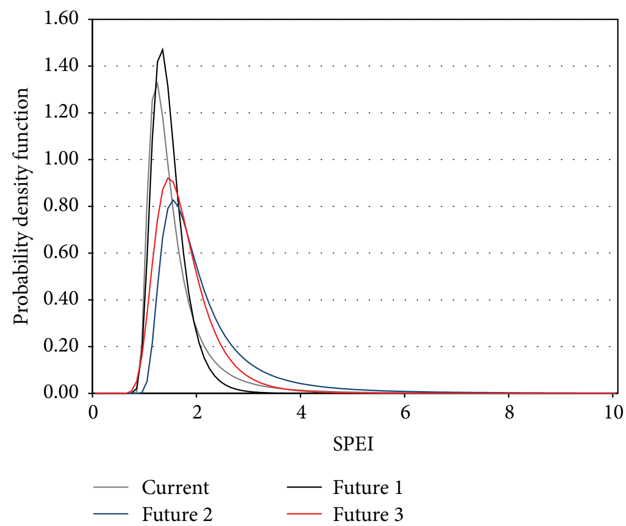

(i) Jeju

Figure 5: GEV PDF projection of maximum drought intensity according to administrative division.

drought intensity, and drought magnitude; these absolute values follow GEV Type II (Frechet) having right tail. Thus, we fitted drought statistics to GEV distribution regardless of goodness-of-fit test.

In this study, the period from 1980 to 2005 is referred to as current climate, from 2011 to 2040 as Future 1, from 2041 to 2070 as Future 2, and from 2071 to 2100 as Future 3. It was projected that the PDF of total drought GEV distribution will generally show a continuously increasing location and scale parameters in the future. If the shape parameter becomes smaller, the upper tail of the GEV distribution at the upper tail becomes thicker. This means the extreme event occurs more frequently. In addition, the shape parameter of some regions was smaller in the middle part of the 21st century than the later part of the said century. Therefore, the frequency of total drought occurrence on a larger scale was higher in the middle part of the 21st century. This phenomenon of reversal was identified in Gyeonggi-do, Gyeongsangnam-do, Jeollanam-do, and Jeju-do, and this phenomenon is considered to have been caused by more average precipitation in the middle part of the 21st century.

The maximum drought intensity relates to temporary maximum intensity or maximum severity during the drought period; for example, the SPEI of the month when the drought was the severest in a year, and it is the random variable that was used most frequently so far in the risk assessment using drought index. Figure 5 shows the PDF of the maximum drought intensity in the current and future climates, and according to this figure, the location and scale parameters grew increasingly larger in the future. In all regions, the drought of comparatively stronger intensity than the maximum drought intensity in the current climate

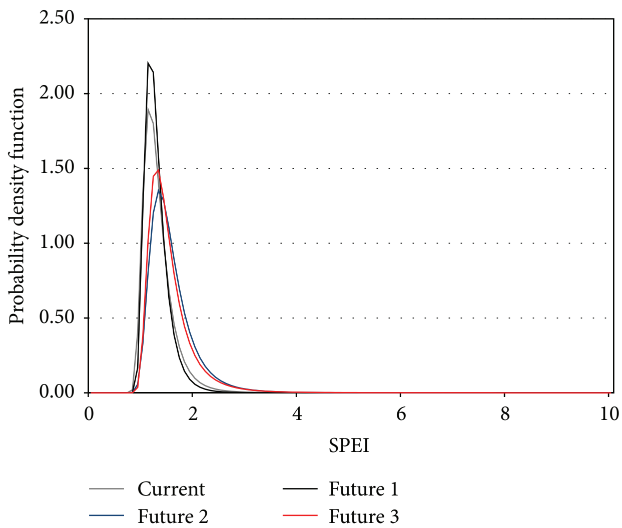

(a) Gangwon-do

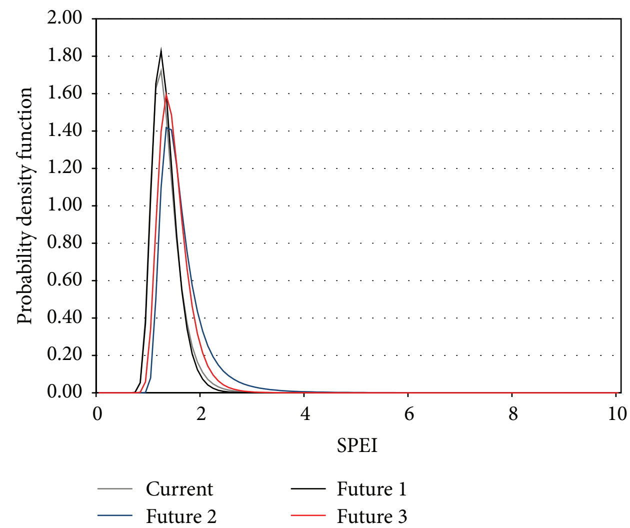

(b) Gyeonggi-do

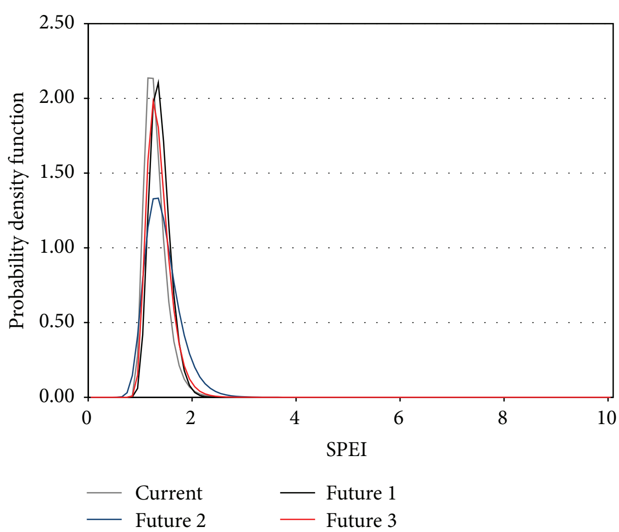

(c) Gyeongsangnam-do

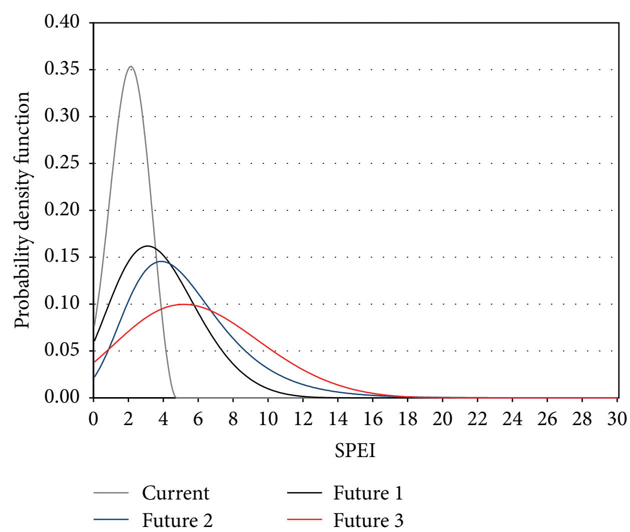

(d) Gyeongsangbuk-do

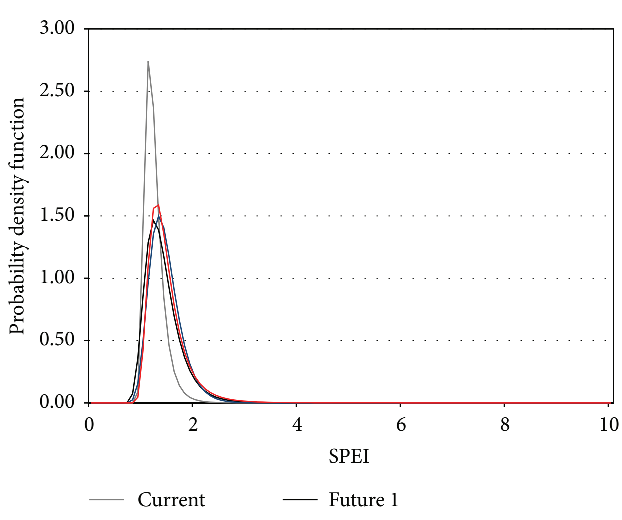

(e) Jeollanam-do

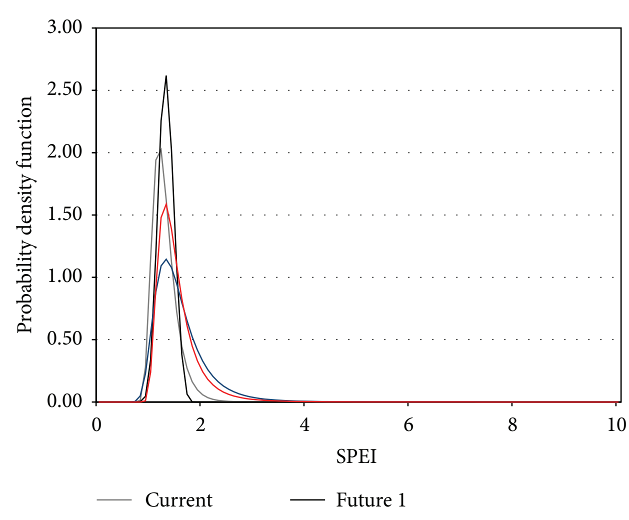

(f) Jeollabuk-do

Figure 6: Continued.

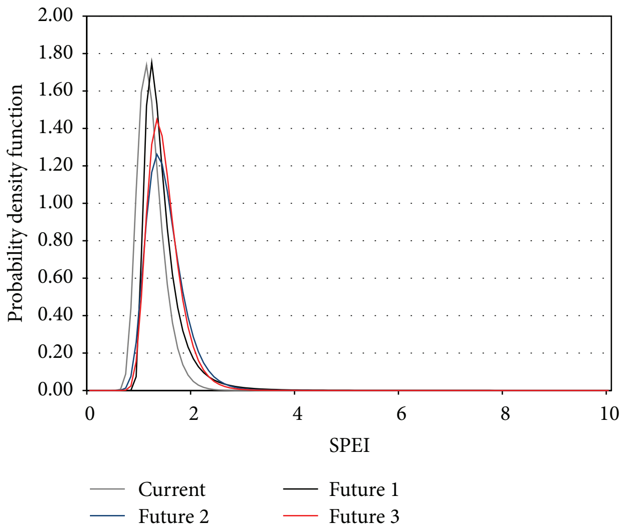

(g) Chungcheongnam-do

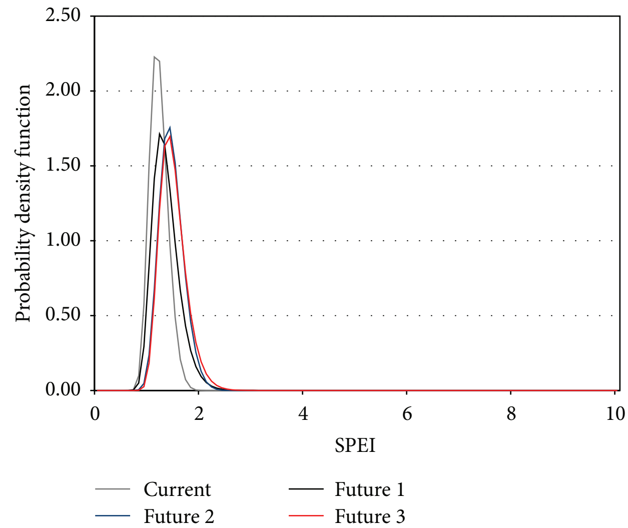

(h) Chungcheongbuk-do

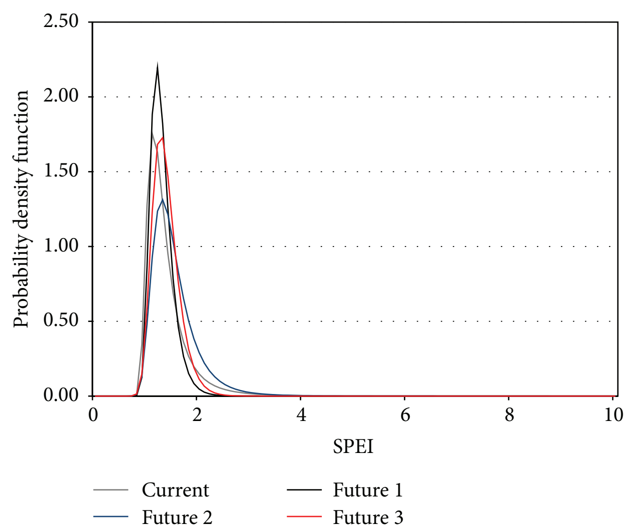

(i) Jeju

Figure 6: GEV PDF projection of drought magnitude according to administrative division.

was projected. This result corresponds with previous studies [22–24]. According to the analysis result, the average and variation of the maximum drought intensity are increasing, which indicates that the average of the drought having strong intensity will further increase in the future and that the droughts of much stronger intensity will occur among the droughts of strong intensity, and droughts of much weaker intensity will occur among the droughts of weaker intensity. The special trend of the shape parameter related to the occurrence frequency was not identified, but the drought intensity in Gyeonggi-do, Gyeongsangnam-do, and Jeju-do was stronger in the middle part of the 21st century than the later part of the said century. The total drought in Jeollanam-do Province showed more reversal phenomena in the middle part of the 21st century than in the later part of the said century; however, the maximum drought intensity showed no significant difference between the middle and later parts of the 21st century, which means that many total droughts will occur in Jeollanam-do Province in the middle part of the 21st century, but they will have no considerably strong intensity.

Similar to this, as the maximum drought intensity, the location and scale parameters of the drought magnitude (obtained by dividing the total drought by duration) were becoming increasingly larger in the future, and the shape parameter was projected to increase to more than its level in the current climate in all locations except Jeju-do. The drought magnitude (the same concept as precipitation intensity) relates to the intensity for unit time. It is generally projected that the intensity of the precipitation will become increasingly stronger in the future; the drought intensity was also projected to become stronger in the future. The magnitude of the total drought in Gangwon-do, Gyeongsangbuk-do, Jeollabuk-do, Chungcheongnam-do, and Chungcheongbuk-do was projected to become

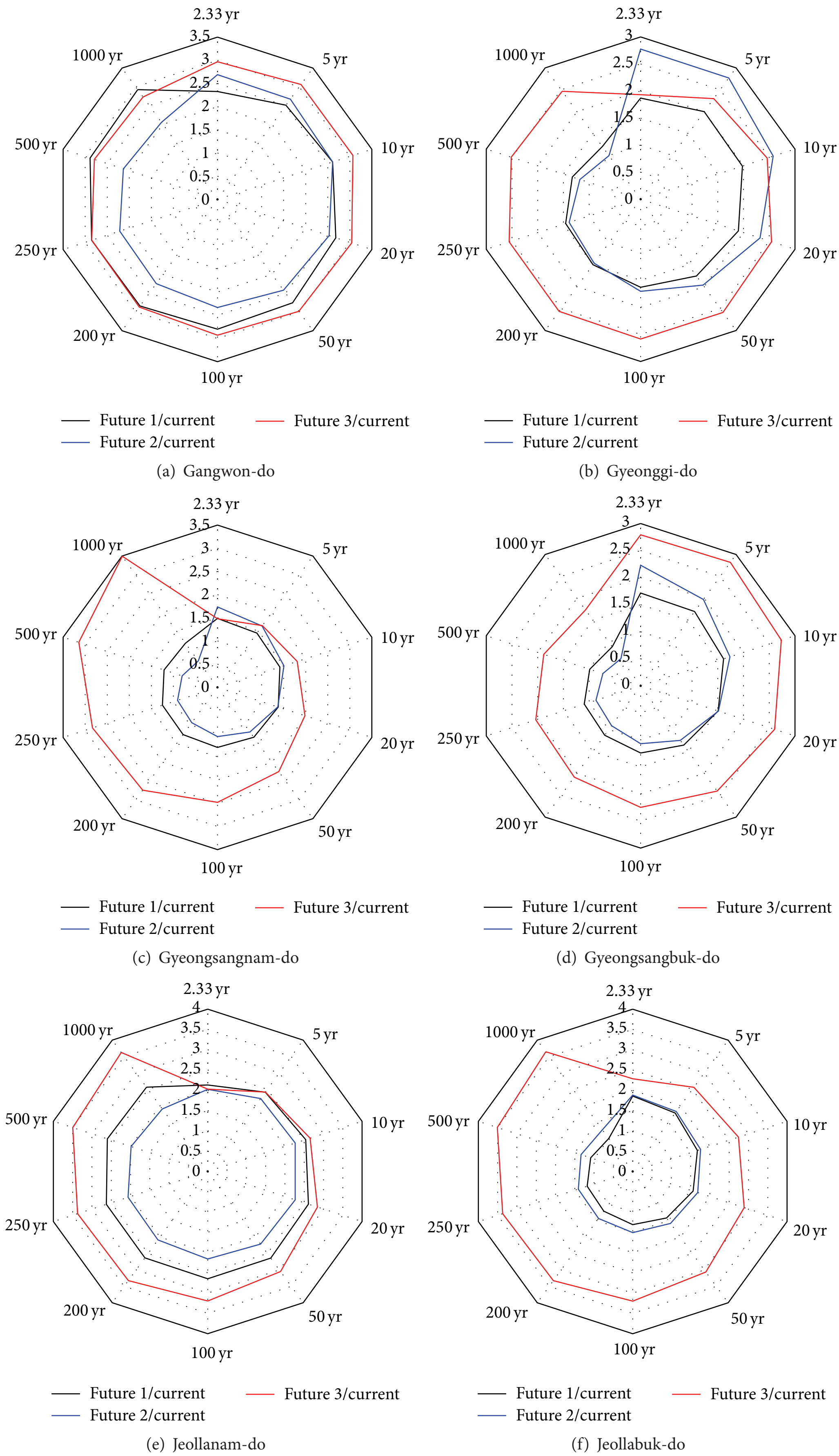

(a) Gangwon-do

(b) Gyeonggi-do

(c) Gyeongsangnam-do

(d) Gyeongsangbuk-do

(e) Jeollanam-do

(f) Jeollabuk-do

FIGURE 7: Continued.

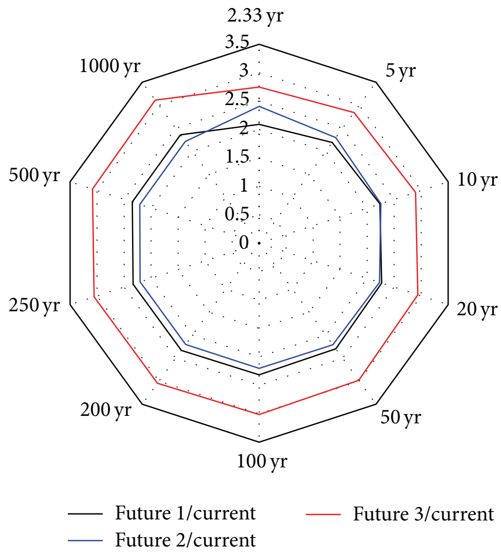

(g) Chungcheongnam-do

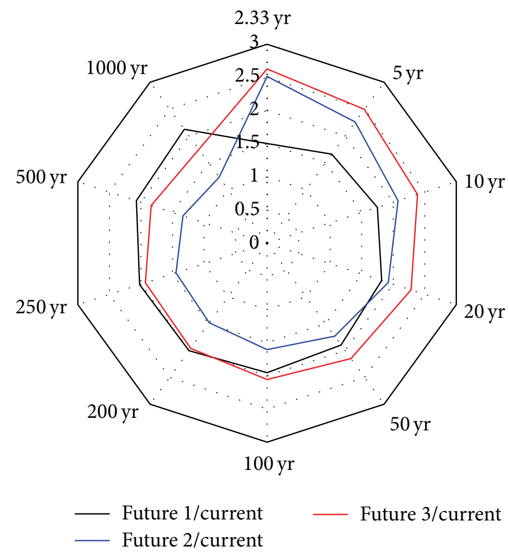

(h) Chungcheongbuk-do

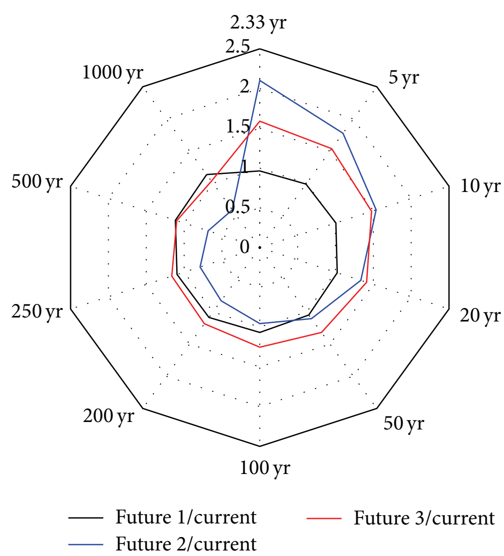

(i) Jeju

FIGURE 7: Ratio of total drought in the future climate to the current climate.

increasingly larger in the future, but the drought magnitude in Gangwon-do, Gyeongsangbuk-do, Jeollabuk-do, and Chungcheongnam-do was comparatively smaller in the later part than the middle part of the 21st century, which indicates that the number of dry days in the relevant regions will increase or the under-anomaly of the precipitation will continue for a longer period (Figure 6).

Figure 7 shows the rate of increase of total drought in each administrative division in the future climate compared to the current climate according to recurrence period. The possibility of total drought of the later part of the 21st century was projected to be high in Gyeonggi-do, Gyeongsangnam-do, Jeollanam-do, Jeollabuk-do, and Chungcheongnam-do and that of the first part of the 21st century in Gangwon-do and Chungcheongbuk-do was projected to be high as well but only in some recurrence periods. In general, however, the total drought showed the trend of a higher increase in the future climate than in the current climate. The rate of increase became increasingly larger in the future, and it was projected (based on a 100-year frequency) that the rate will increase about three times from the current climate in Gyeongsangnam-do, Jeollanam-do, and Jeollabuk-do.

Figure 8 shows the rate of increase of drought intensity in the future climate compared with the current climate in each administrative division according to recurrence period. Because of its great randomness through the use of the annual lowest SPEI, the rate of increase in future climate compared with the current climate did not show a significant trend other than the total drought; however, in Gyeonggi-do, Gyeongsangnam-do, and Jeju-do, the maximum drought intensity was projected to be stronger in the later part of the 21st century, and in Gangwon-do and Chungcheongnam-do,

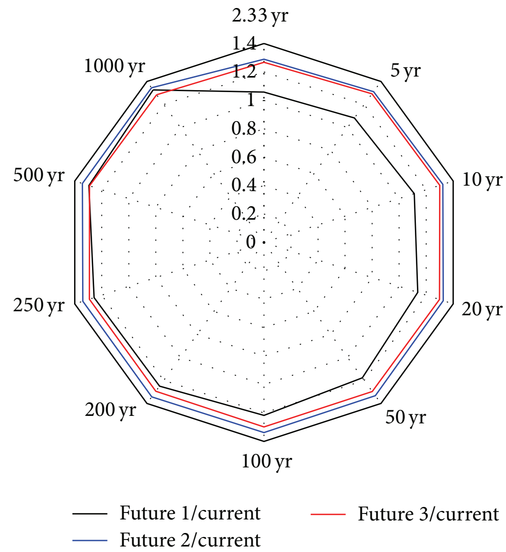

(a) Gangwon-do

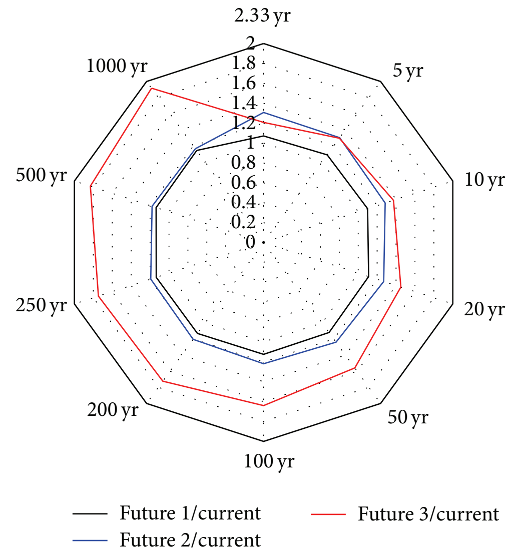

(b) Gyeonggi-do

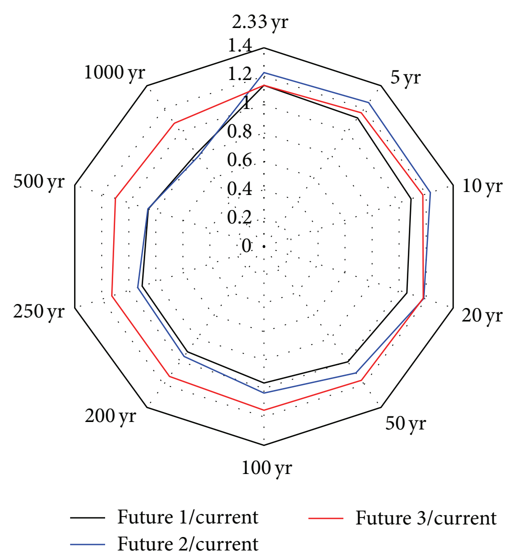

(c) Gyeongsangnam-do

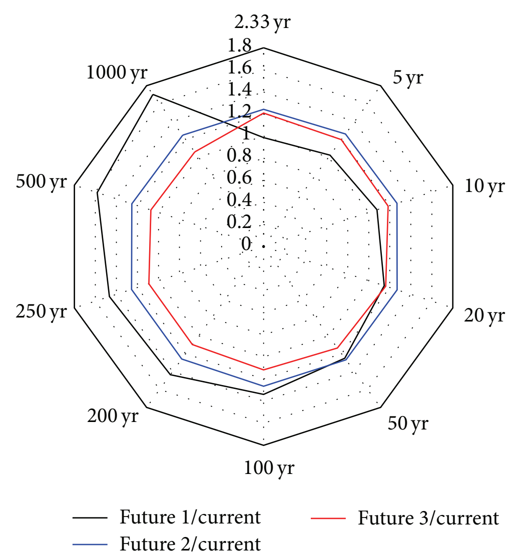

(d) Gyeongsangbuk-do

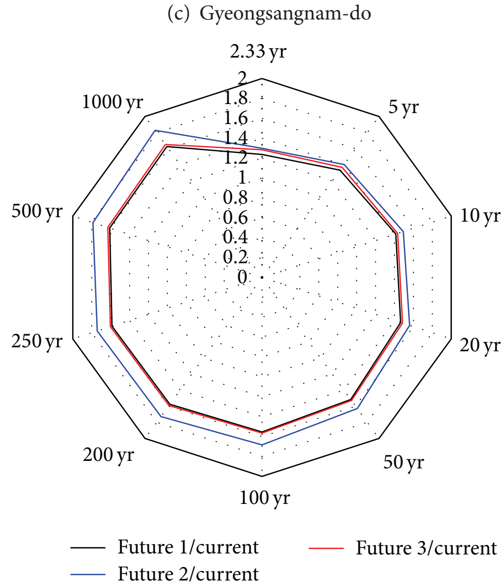

(e) Jeollanam-do

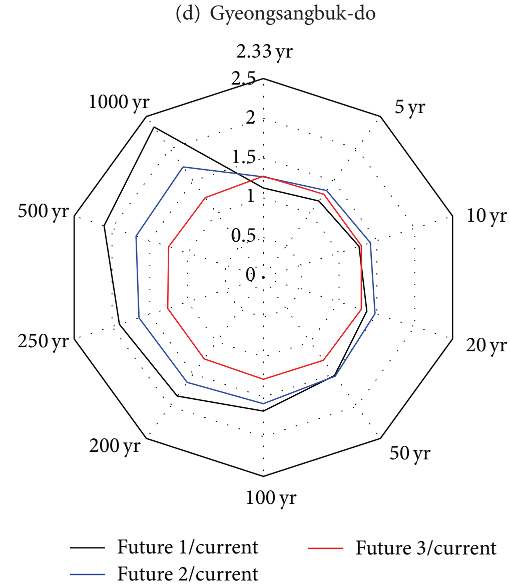

(f) Jeollabuk-do

Figure 8: Continued.

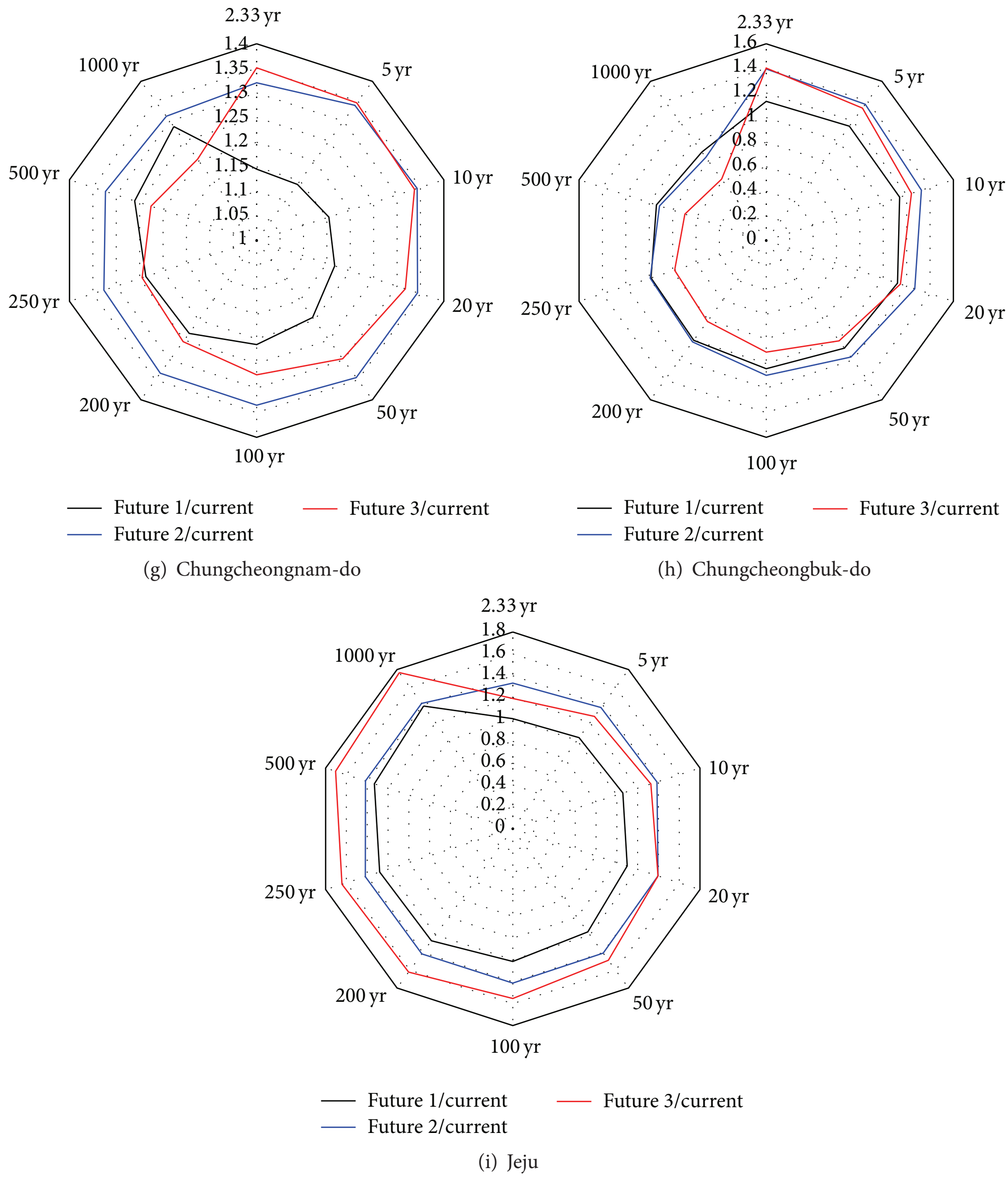

Figure 8: Ratio of maximum drought intensity in the future climate to the current climate.

the maximum drought intensity was projected to be stronger in the middle part of the 21st century. In general, it was projected that the maximum drought intensity will become stronger in the future than the present, but the opposite trend was identified in Chungcheongbuk-do Province.

Figure 9 shows the drought magnitude in the future compared with the current in each administrative division according to recurrence period. In Gangwon-do, Gyeongsangnam-do, Jeollanam-do, Chungcheongnam-do, and Chungcheongbuk-do, the drought magnitude was projected to be larger in the middle than the later part of the 21st century, and in Gangwon-do and Jeju-do, the drought magnitude was projected to be larger in the later part than the middle part of the 21st century. Based on a 100-year frequency, the drought magnitude was projected to increase about 1.8 times from the present in Jeollanam-do Province in the middle part of the 21st century. The climate model is known to have better estimation capability for the temperature than the precipitation. In view of that, the variable that shows an increasingly dramatic trend of increase in the future is the temperature. SPEI is the drought index that considers the difference between precipitation and evapotranspiration, with evapotranspiration as the function of temperature. The stronger drought magnitude in the middle part than the later part of the 21st century indicates that there is a considerably small level of precipitation in the middle part of the 21st century regardless of the increase of evapotranspiration.

3.2. The Result of the Change in the Threshold Level. The drought size in the current and future climates was calculated while changing the drought standard, that is, the threshold level, to "−1" and "−1.5" (Figure 10). The total drought in "−1"

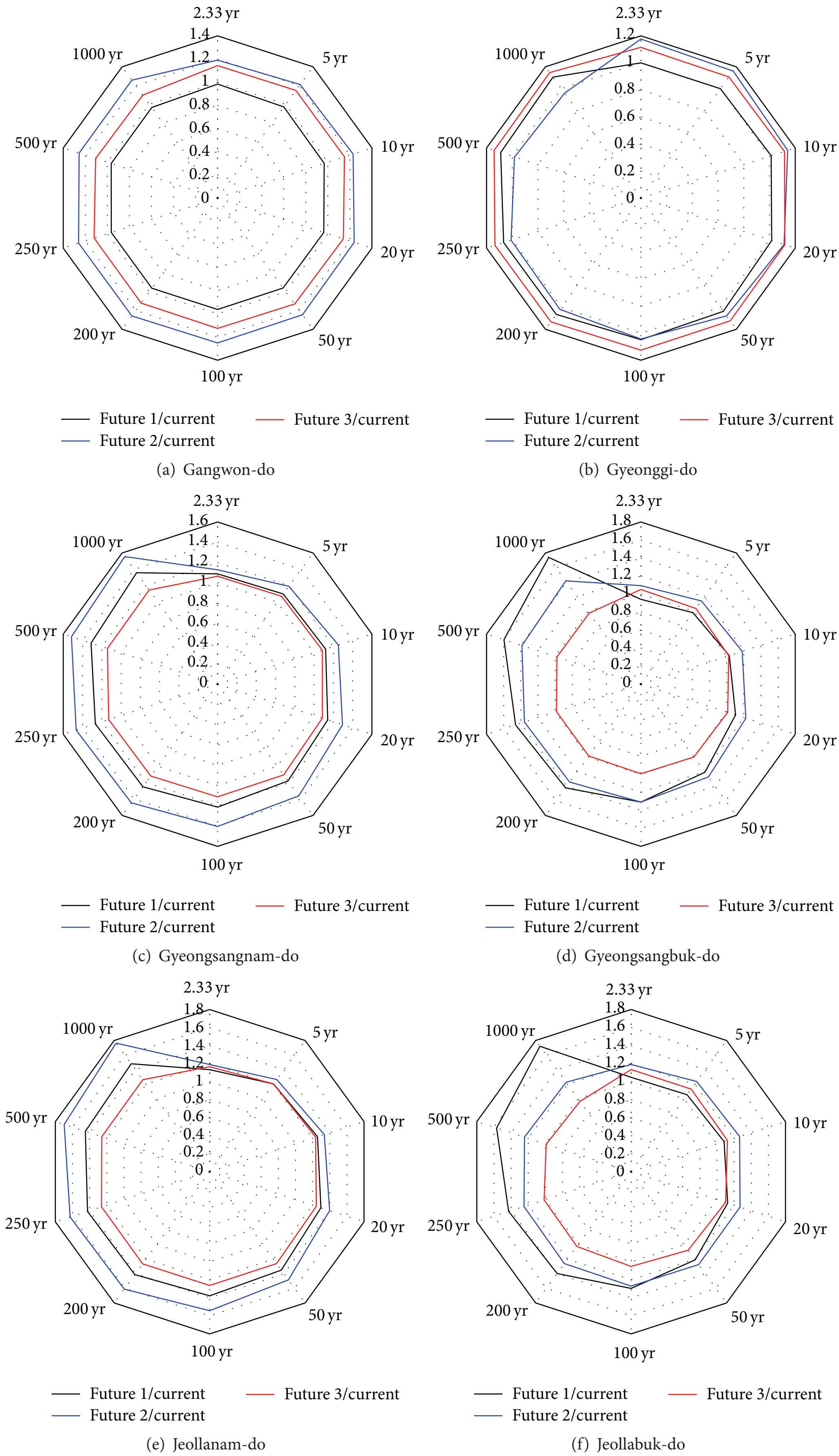

(a) Gangwon-do

(b) Gyeonggi-do

(c) Gyeongsangnam-do

(d) Gyeongsangbuk-do

(e) Jeollanam-do

(f) Jeollabuk-do

FIGURE 9: Continued.

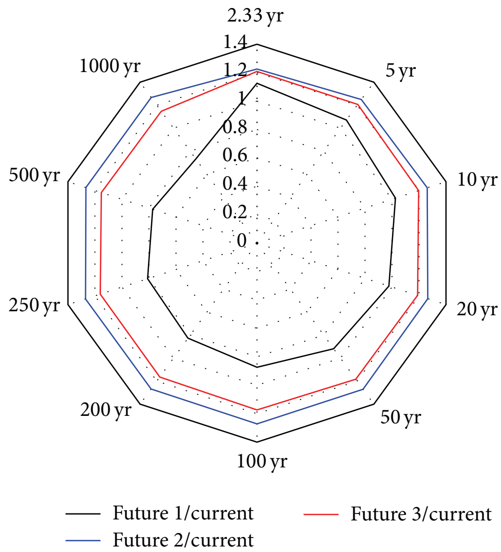

(g) Chungcheongnam-do

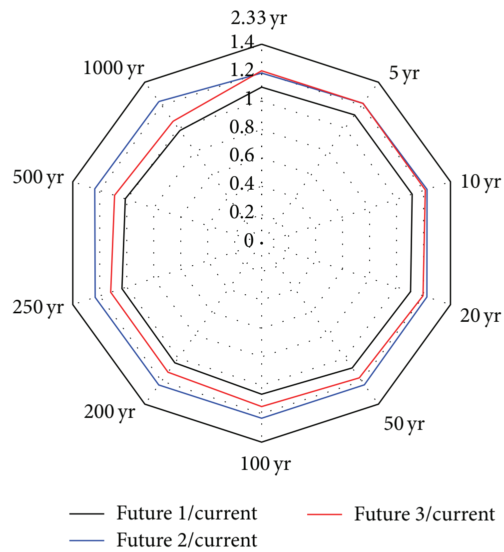

(h) Chungcheongbuk-do

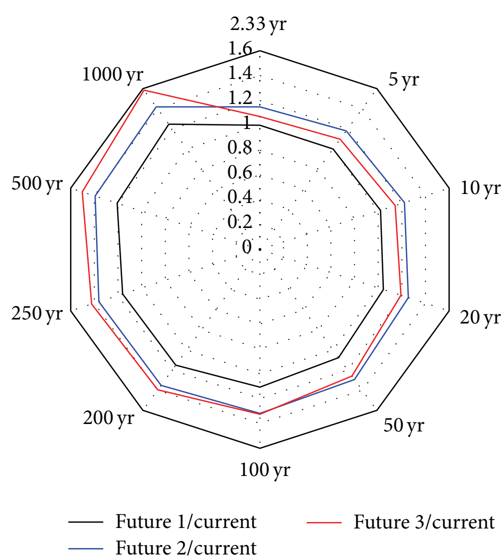

(i) Jeju

Figure 9: Ratio of drought magnitude in the future climate to the current climate.

was becoming increasingly larger in the future (Figure 10). However, the total drought in Gangwon-do, Gyeonggi-do, Jeollanam-do, Chungcheongbuk-do, and Jeju-do was larger in the middle part than the later part of the 21st century. The extreme total drought below "–1.5" also showed the trend of becoming increasingly larger in the future; however, the total drought in Gangwon-do, Gyeonggi-do, and Jeju-do was larger in the middle part than the later part of the 21st century, and the total drought in Jeollanam-do Province remained in a similar level from the first part to the later part of the 21st century.

The maximum drought intensity below "–1" of the SPEI was becoming stronger and stronger in the future (Figure 11). However, the maximum drought intensity in Gangwon-do, Gyeonggi-do, Gyeongsangnam-do, Jeollanam-do, Jeollabuk-do, Chungcheongbuk-do, and Chungcheongnam-do was stronger in the middle part than the later part of the 21st century. The maximum drought intensity below "–1.5" also showed the trend of becoming increasingly stronger in the future, but the maximum drought intensity in Gangwon-do, Gyeonggi-do, Gyeongsangnam-do, Jeollanam-do, and Jeju-do was projected to be stronger in the middle part than the later part of the 21st century.

The drought magnitude below "–1" of the SPEI was becoming increasingly larger in the future even though the extent is comparatively less than the total drought and maximum drought intensity (Figure 12). However, it was projected that the drought magnitude of similar magnitude will continue from the current climate to the first part of the 21st century in Gangwon-do, Gyeonggi-do,

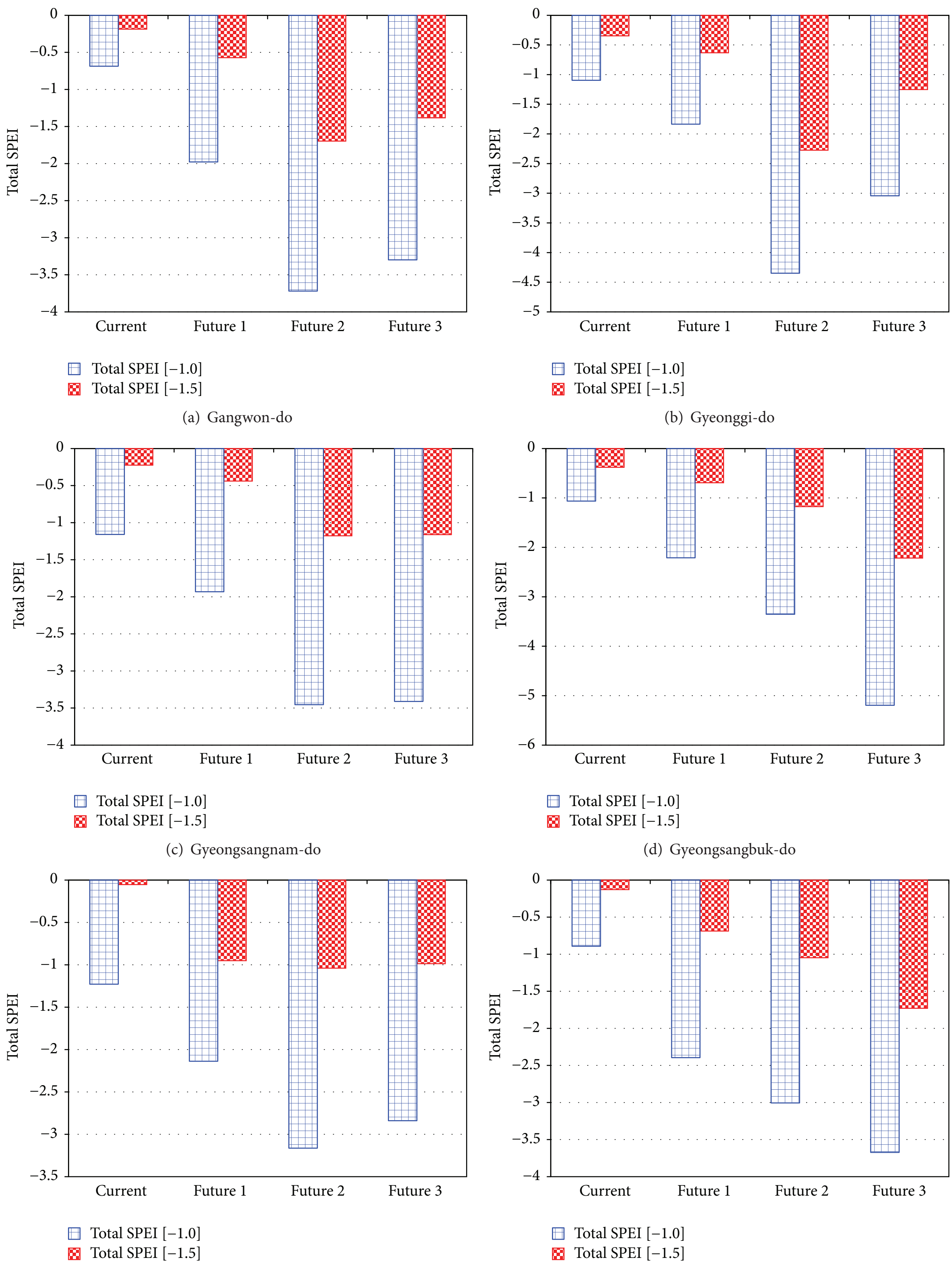

(a) Gangwon-do
(b) Gyeonggi-do
(c) Gyeongsangnam-do
(d) Gyeongsangbuk-do
(e) Jeollanam-do
(f) Jeollabuk-do

FIGURE 10: Continued.

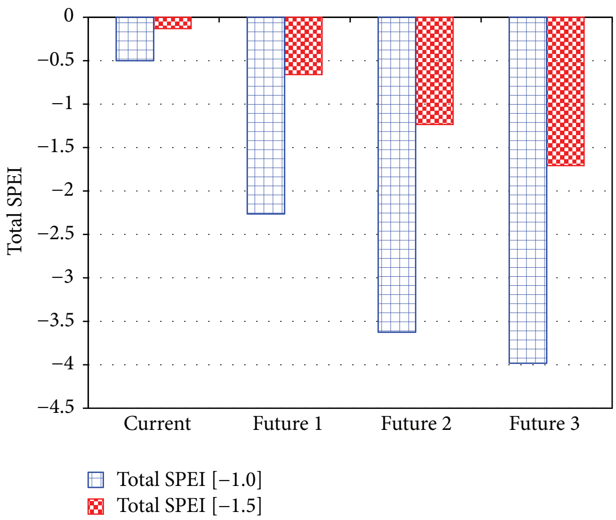

(g) Chungcheongnam-do

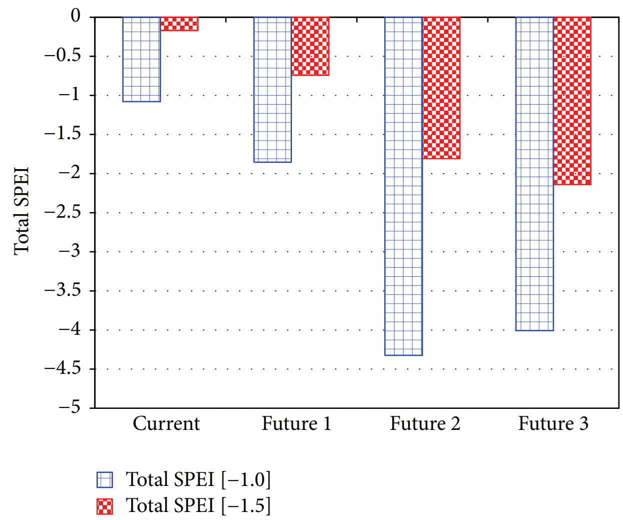

(h) Chungcheongbuk-do

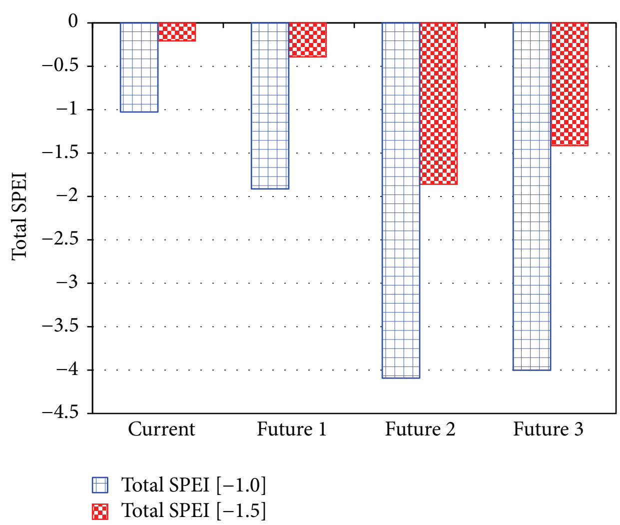

(i) Jeju

Figure 10: Change in total drought in the current and future climates.

and Jeollanam-do and that the drought magnitude in Gangwon-do, Gyeonggi-do, Gyeongsangnam-do, Jeollanam-do, Jeollabuk-do, Chungcheongnam-do, Chungcheongbuk-do, and Jeollabuk-do was projected to become larger in the middle part than the later part of the 21st century. The drought magnitude below "1.5" also showed the trend of becoming increasingly larger in the future; however, the drought magnitude in Gangwon-do, Gyeonggi-do, Gyeongsangnam-do, and Jeju-do was projected to become larger in the middle part than the later part of the 21st century.

The drought duration in each drought period was calculated (Figure 13). The drought duration below "–1" was 0.76 months/year in the current climate, but drought duration was projected to become increasingly longer in the future and extreme drought to last for longer than 2.50 months/year (Figure 12). The calculation of the drought duration below "1.5" showed similar results. The drought duration was 0.13 months/year in the current climate, but the drought duration was projected to become increasingly longer in the future and extreme drought to last for longer than 1.10 months/year (Figure 12). In general, in Gyeongsangbuk-do Province, the drought below "–1" is expected to last for longer than three months in the later part of the 21st century and the severer drought below "–1.5" is expected to last for about two months. In Chungcheongbuk-do Province, it was projected that the drought below "–1" will last for about three months in the middle part of the 21st century, but with the duration expected to decrease in the later part of the 21st century.

4. Conclusions

This study aimed to identify the drought characteristics by applying the threshold level method and projected

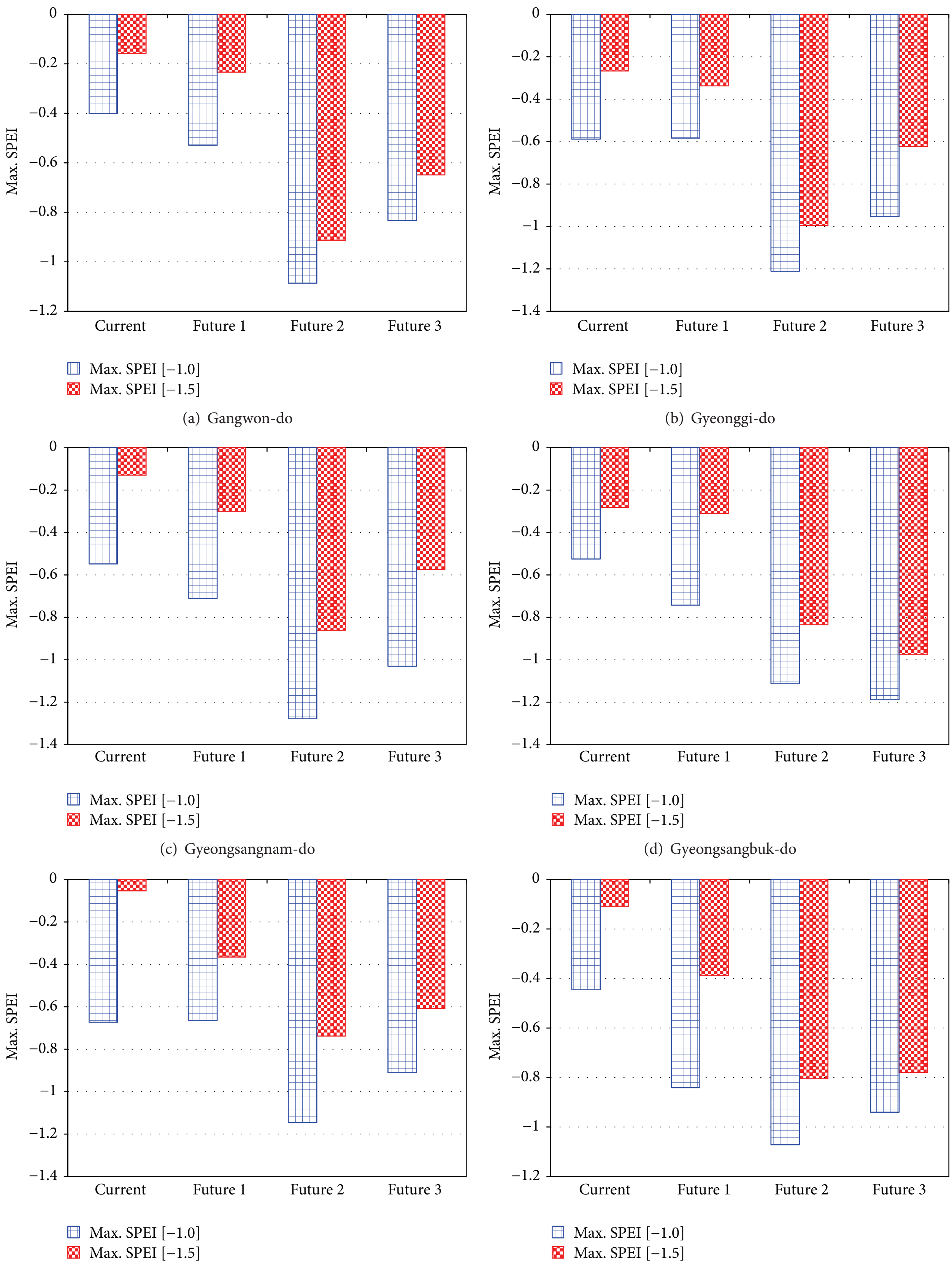

(a) Gangwon-do

(b) Gyeonggi-do

(c) Gyeongsangnam-do

(d) Gyeongsangbuk-do

(e) Jeollanam-do

(f) Jeollabuk-do

FIGURE 11: Continued.

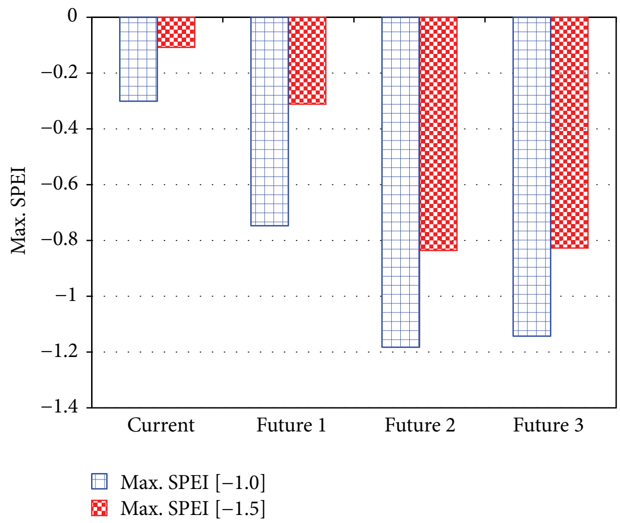

(g) Chungcheongnam-do

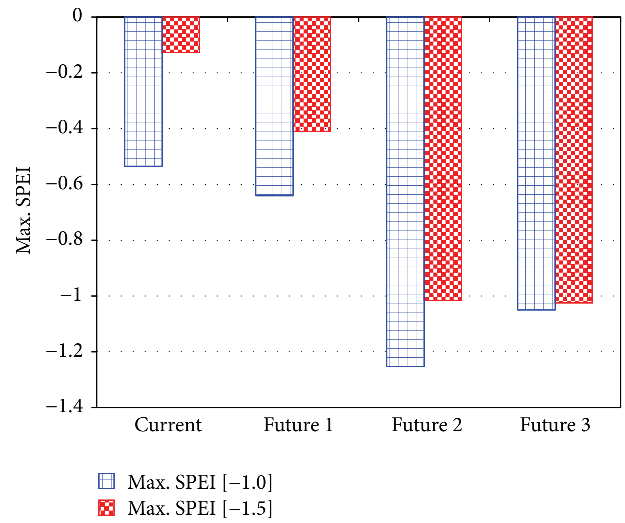

(h) Chungcheongbuk-do

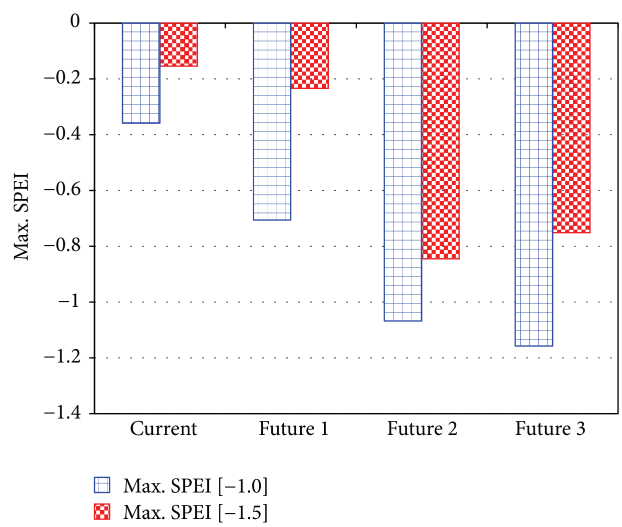

(i) Jeju

Figure 11: Change in maximum drought intensity in the current and future climates.

the drought risk of each administrative division in South Korea in the 21st century by fitting the identified drought characteristics to GEV distribution. The result of the analysis about the total drought, maximum drought intensity, and drought magnitude showed that the PDF of the total drought and maximum drought intensity was moving further and further to the upper tail part, and the drought of stronger intensity was also projected to occur more frequently in the future than the current in the right side of the GEV distribution.

The total volume of the mild drought was projected to increase from the current 0.97/year to 3.72/year in the later part of the 21st century, and the total volume of the severe drought was projected to increase from the current 0.20/year to 1.55/year in the later part of the 21st century. The maximum drought intensity of the mild drought was projected to increase from the current 0.49/year to 1.02/year in the later part of the 21st century, and the maximum drought intensity of the severe drought was projected to increase from the current 0.15/year to 0.76/year in the later part of the 21st century. The average drought intensity of the mild drought was projected to increase from the current 0.45/year to 0.87/year in the later part of the 21st century, and the average drought intensity of the severe drought was projected to increase from the current 0.14/year to 0.65/year in the later part of the 21st century. As a result of drought duration calculation, the duration of the mild drought was 0.76 months/year in the current climate, but it was projected to become increasingly longer in the future and to last for longer than 2.50 months/year in the future climate. As a result of calculating severe drought duration, the drought duration was 0.13 months/year in the current climate, but it

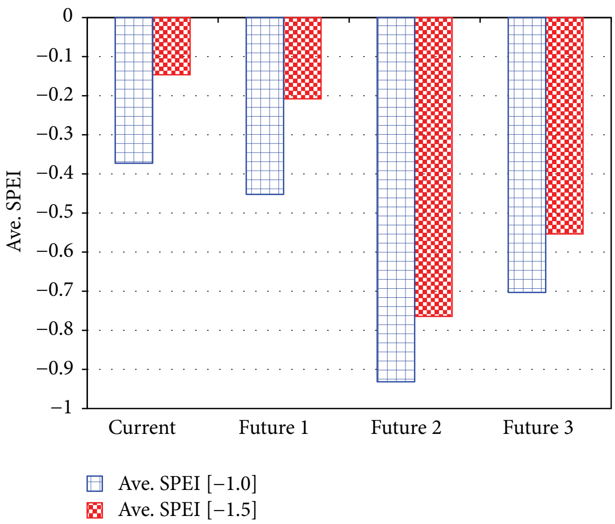

(a) Gangwon-do

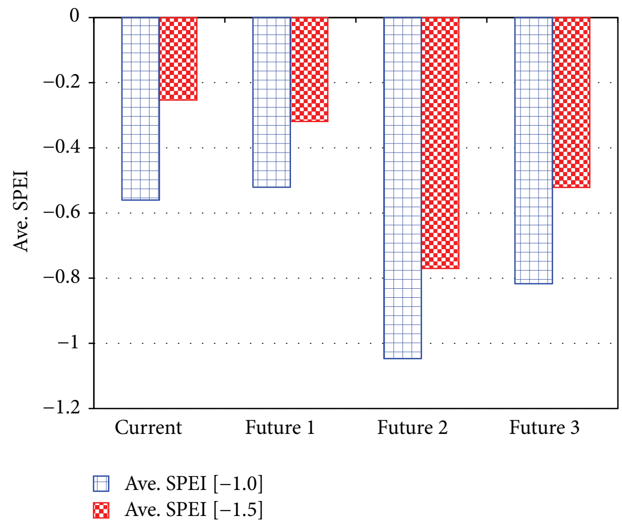

(b) Gyeonggi-do

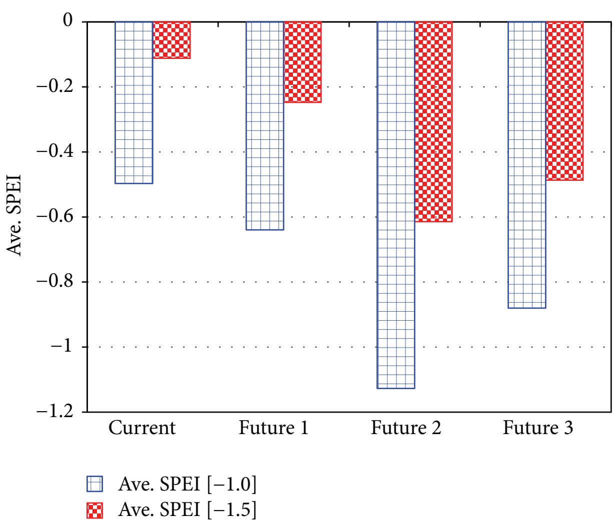

(c) Gyeongsangnam-do

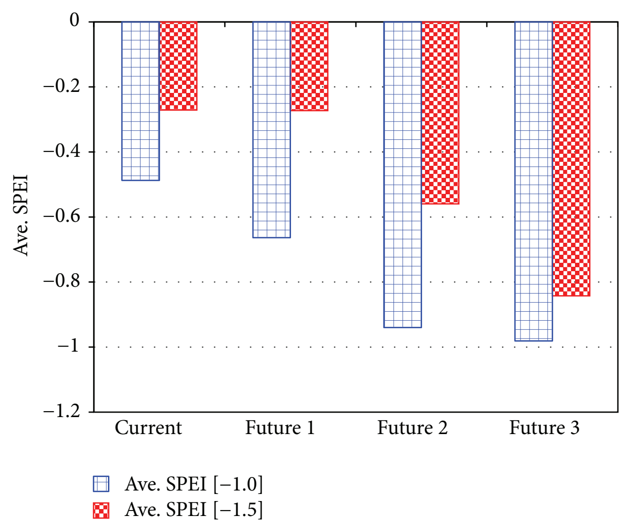

(d) Gyeongsangbuk-do

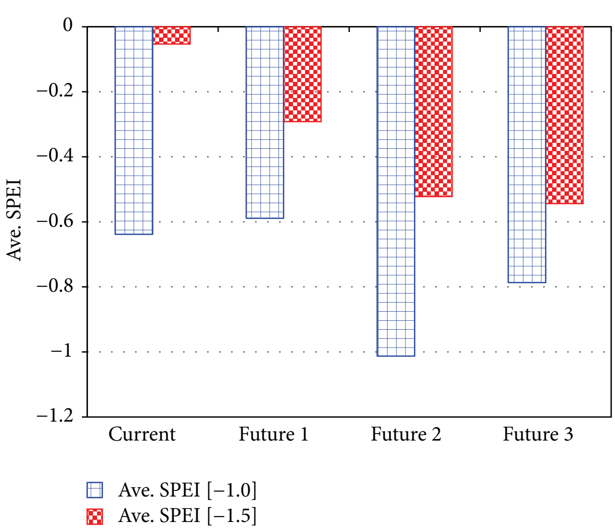

(e) Jeollanam-do

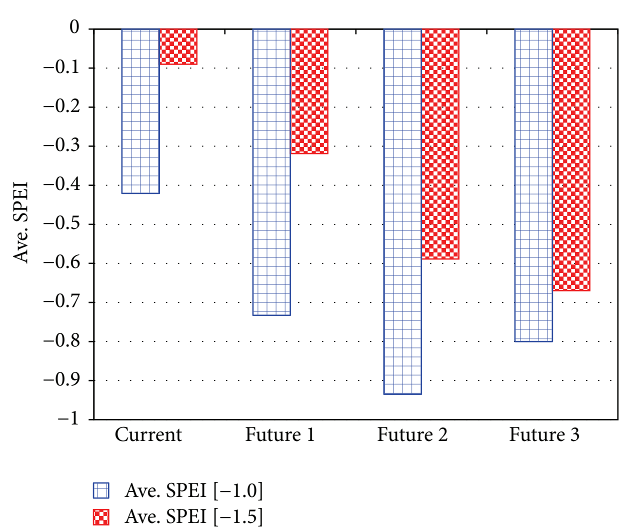

(f) Jeollabuk-do

Figure 12: Continued.

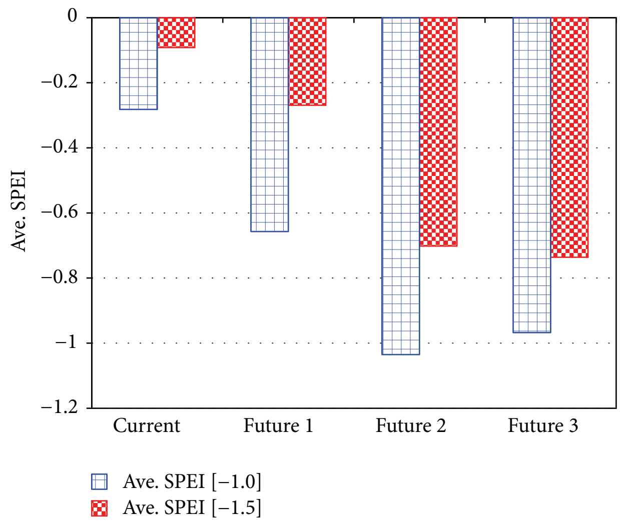

(g) Chungcheongnam-do

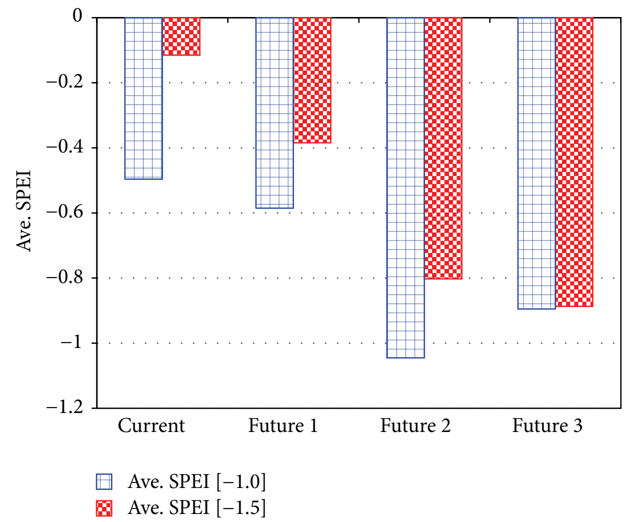

(h) Chungcheongbuk-do

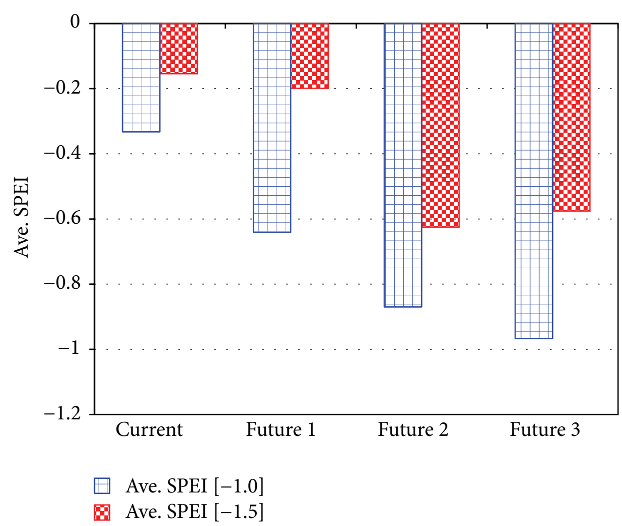

(i) Jeju

Figure 12: Change in drought magnitude in the current and future climates.

was projected to become increasingly longer in the future and to last for longer than 1.10 months/year in the future climate.

Drought magnitude and duration are key variables. With this, according to the extent of human needs, the drought magnitude also needs to take into consideration separately the maximum drought intensity, drought magnitude, and total drought. In the health-welfare area, for example, the maximum drought intensity among drought features will be the most useful in preventing drought damage (high temperature and dryness) to people belonging to the vulnerable class, and the drought magnitude—with the same concept as precipitation intensity—can provide useful information to the designers of water supply facilities. Because the total drought includes the concept of drought duration, it can provide useful information during the process of drought transition from agricultural to hydrological and socioeconomic drought. There is a significance in projecting future drought on the basis of the extreme climate. Because this study has a limitation to employ a single scenario, future studies should attempt to quantify uncertainties in the combination of multiple scenarios.

Conflict of Interests

The authors declare that there is no conflict of interests regarding the publication of this paper.

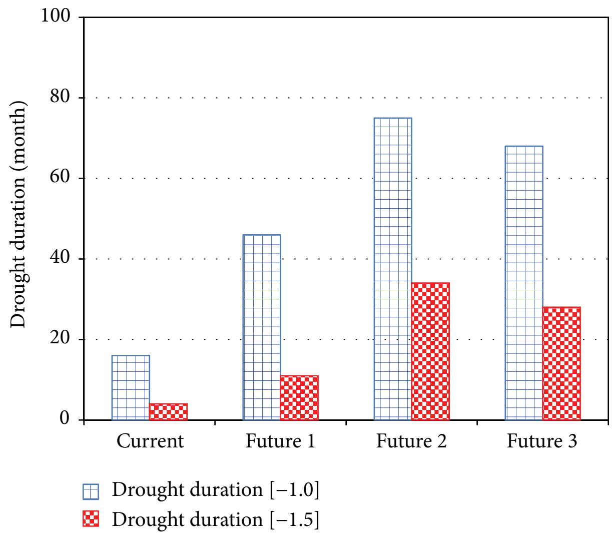

(a) Gangwon-do

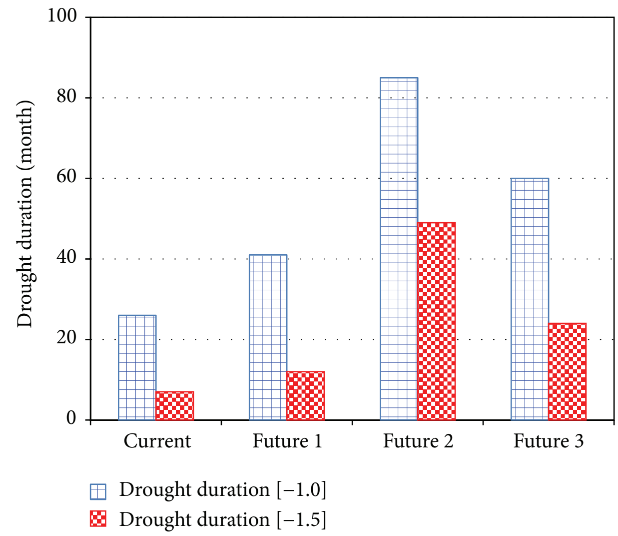

(b) Gyeonggi-do

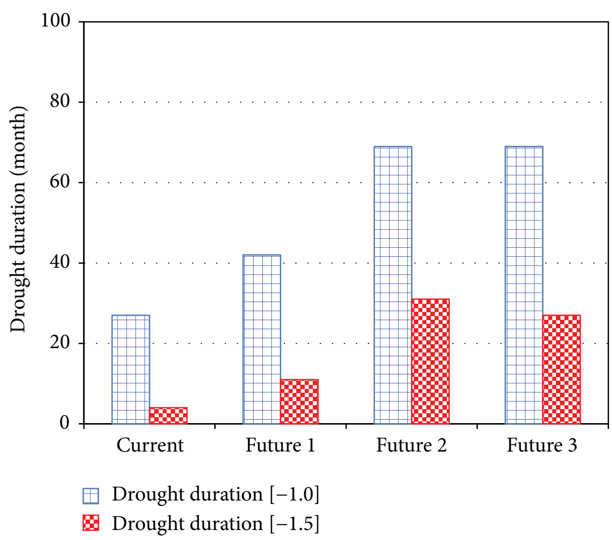

(c) Gyeongsangnam-do

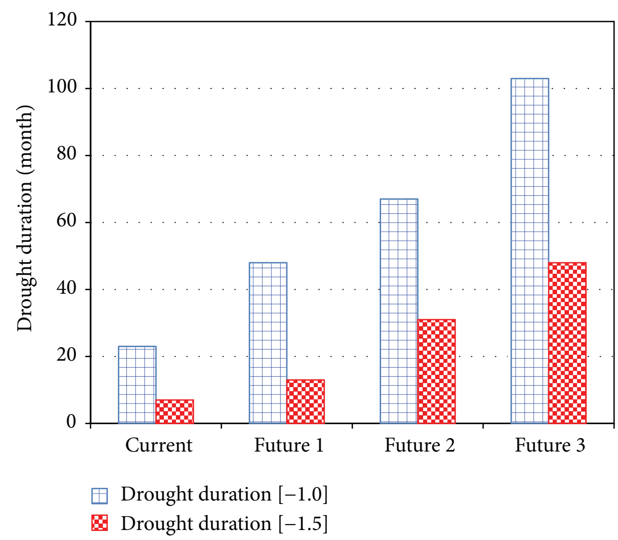

(d) Gyeongsangbuk-do

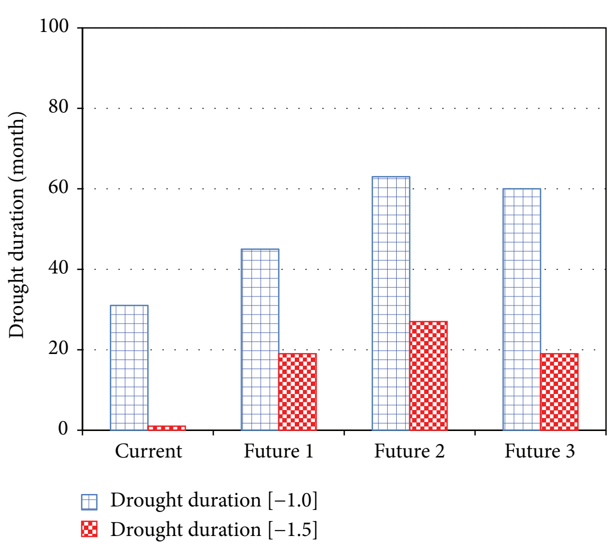

(e) Jeollanam-do

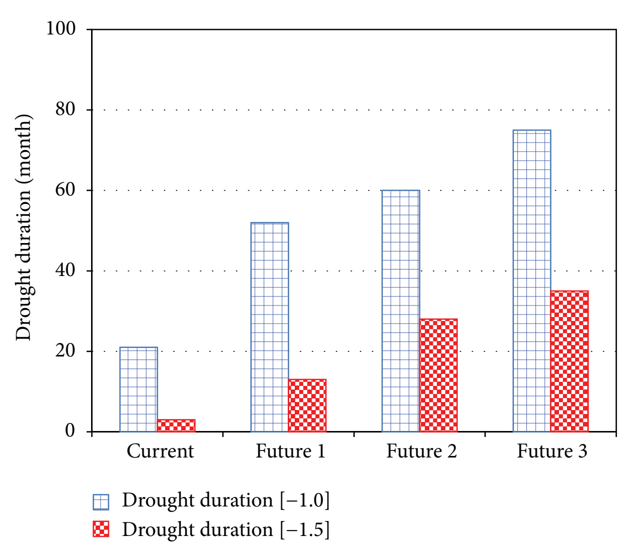

(f) Jeollabuk-do

Figure 13: Continued.

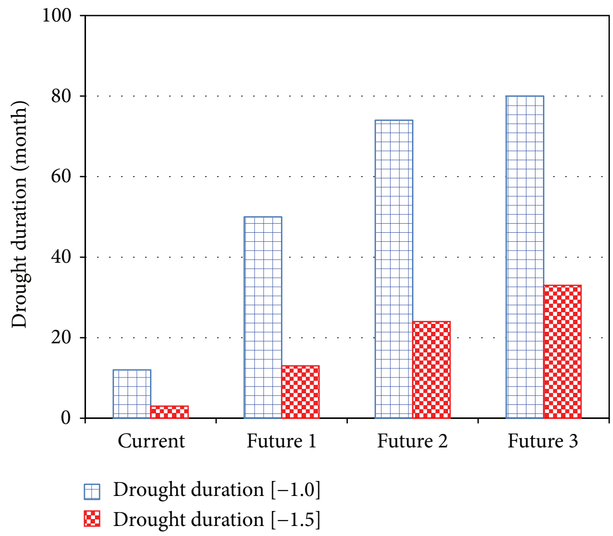

(g) Chungcheongnam-do

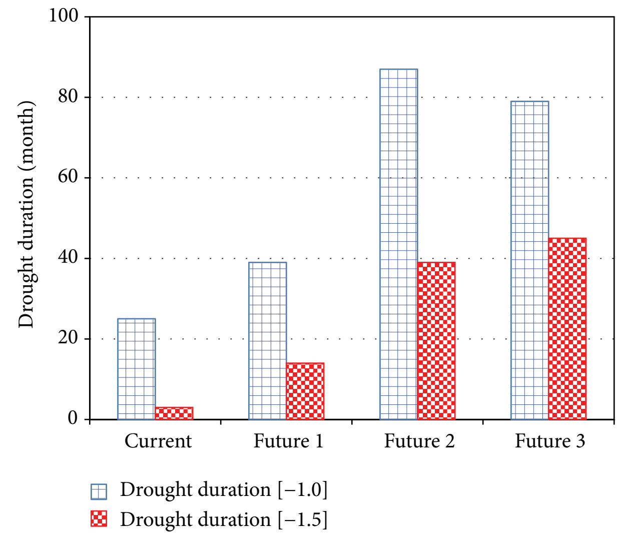

(h) Chungcheongbuk-do

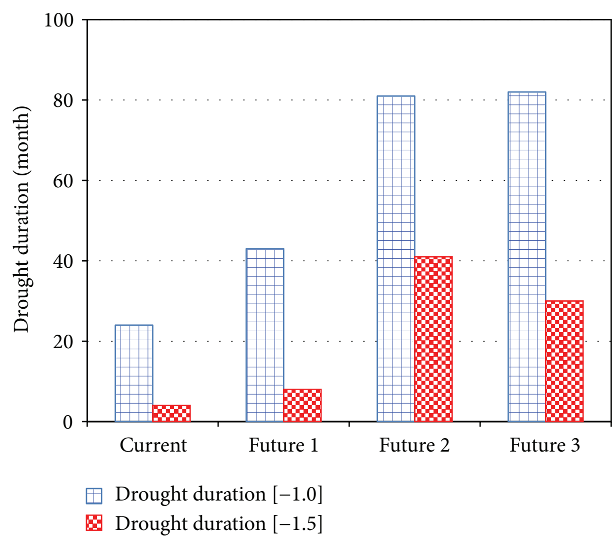

(i) Jeju

FIGURE 13: Change in drought duration in the current and future climates.

Acknowledgment

This study was supported by the 2011 Research Grant from Kangwon National University.

References

[1] B. S. Kim, H. S. Kim, B. H. Seoh, and N. W. Kim, "Impact of climate change on water resources in Yongdam Dam Basin, Korea," *Stochastic Environmental Research and Risk Assessment*, vol. 21, no. 4, pp. 355–373, 2007.

[2] B.-S. Kim, B.-K. Kim, and H.-H. Kwon, "Assessment of the impact of climate change on the flow regime of the Han River basin using indicators of hydrologic alteration," *Hydrological Processes*, vol. 25, no. 5, pp. 691–704, 2011.

[3] D.-H. Bae, I.-W. Jung, and D. P. Lettenmaier, "Hydrologic uncertainties in climate change from IPCC AR4 GCM simulations of the Chungju Basin, Korea," *Journal of Hydrology*, vol. 401, no. 1-2, pp. 90–105, 2011.

[4] I. W. Jung, D. H. Bae, and B. J. Lee, "Possible change in Korean streamflow seasonality based on multi-model climate projections," *Hydrological Processes*, vol. 27, no. 7, pp. 1033–1045, 2013.

[5] K.-O. Boo, W.-T. Kwon, J.-H. Oh, and H.-J. Baek, "Response of global warming on regional climate change over Korea: an experiment with the MM5 model," *Geophysical Research Letters*, vol. 31, no. 21, Article ID L21206, 2004.

[6] K.-O. Boo, W.-T. Kwon, and H.-J. Baek, "Change of extreme events of temperature and precipitation over Korea using regional projection of future climate change," *Geophysical Research Letters*, vol. 33, no. 1, Article ID L01701, 2006.

[7] E.-S. Im, J.-B. Ahn, A. R. Remedio, and W.-T. Kwon, "Sensitivity of the regional climate of East/Southeast Asia to convective parameterizations in the RegCM3 modelling system. Part 1:

focus on the Korean peninsula," *International Journal of Climatology*, vol. 28, no. 14, pp. 1861–1877, 2008.

[8] B. Kim, J. H. Sung, B. H. Lee, and D. J. Kim, "Evaluation on the impact of extreme droughts in South Korea using the SPEI and RCP8.5 climate change scenario," *Journal of Korean Society of Hazard Mitigation*, vol. 13, no. 2, pp. 97–109, 2013.

[9] D. A. Wilhite and M. H. Glantz, "Understanding the drought phenomenon: the role of definitions," *Water International*, vol. 10, no. 3, pp. 111–120, 1985.

[10] A. K. Mishra and V. P. Singh, "A review of drought concepts," *Journal of Hydrology*, vol. 391, no. 1-2, pp. 202–216, 2010.

[11] T. B. McKee, N. J. Doesken, and J. Kieist, "The relationship of drought frequency and duration to time scales," in *Proceedings of the 8th Conference of Applied Climatology*, pp. 179–184, American Chemical Society, Anaheim, Calif, USA, January 1993.

[12] C. J. Kim, M. J. Park, and J. H. Lee, "Analysis of climate change impacts on the spatial and frequency patterns of drought using a potential drought hazard mapping approach," *International Journal of Climatology*, vol. 34, no. 1, pp. 61–80, 2014.

[13] S.-K. Min, W.-T. Kwon, E.-H. Park, and Y. Choi, "Spatial and temporal comparisons of droughts over Korea with East Asia," *International Journal of Climatology*, vol. 23, no. 2, pp. 223–233, 2003.

[14] M. Gocic and S. Trajkovic, "Water surplus variability index as an indicator of drought," *Journal of Hydrologic Engineering*, vol. 20, no. 2, Article ID 04014038, 2015.

[15] D. Rajsekhar, V. P. Singh, and A. K. Mishra, "Multivariate drought index: an information theory based approach for integrated drought assessment," *Journal of Hydrology*, vol. 526, pp. 164–182, 2015.

[16] S. M. Vicente-Serrano, S. Beguería, and J. I. López-Moreno, "A multiscalar drought index sensitive to global warming: the standardized precipitation evapotranspiration index," *Journal of Climate*, vol. 23, no. 7, pp. 1696–1718, 2010.

[17] J.-H. Lee and C.-J. Kim, "Derivation of drought severity-duration-frequency curves using drought frequency analysis," *Journal of Korea Water Resources Association*, vol. 44, no. 11, pp. 889–902, 2011 (Korean).

[18] A. K. Mishra and V. P. Singh, "Analysis of drought severity-area-frequency curves using a general circulation model and scenario uncertainty," *Journal of Geophysical Research: Atmospheres*, vol. 114, no. 6, Article ID D06120, 2009.

[19] C. W. Thornthwaite, "An approach toward a rational classification of climate," *Geographical Review*, vol. 38, no. 1, pp. 55–94, 1948.

[20] C. W. Thornthwaite and J. R. Mather, *The Water Balance*, vol. 8, no. 1 of *Publications in Climatology*, Thornthwaite & Associates, Centerton, NJ, USA, 1955.

[21] NIMR, *Report on Climate Change Scenarios for IPCC AR5*, National Institute of Meteorological Research, Seoul, Republic of Korea, 2011.

[22] H. Douville, F. Chauvin, S. Planton, J.-F. Royer, D. Salas-Mélia, and S. Tyteca, "Sensitivity of the hydrological cycle to increasing amounts of greenhouse gases and aerosols," *Climate Dynamics*, vol. 20, no. 1, pp. 45–68, 2002.

[23] T. P. Barnett, J. C. Adam, and D. P. Lettenmaier, "Potential impacts of a warming climate on water availability in snow-dominated regions," *Nature*, vol. 438, no. 7066, pp. 303–309, 2005.

[24] E. J. Burke, S. J. Brown, and N. Christidis, "Modeling the recent evolution of global drought and projections for the twenty-first century with the Hadley Centre climate model," *Journal of Hydrometeorology*, vol. 7, no. 5, pp. 1113–1125, 2006.

Hindawi Publishing Corporation
Advances in Meteorology
Volume 2016, Article ID 1384302, 17 pages
http://dx.doi.org/10.1155/2016/1384302

Research Article

Impact Assessment of Uncertainty Propagation of Ensemble NWP Rainfall to Flood Forecasting with Catchment Scale

Wansik Yu,[1] Eiichi Nakakita,[1] Sunmin Kim,[2] and Kosei Yamaguchi[1]

[1] *Disaster Prevention Research Institute, Kyoto University, Kyoto 611-0011, Japan*
[2] *Department of Civil and Earth Resources Engineering, Kyoto University, Kyoto 615-8540, Japan*

Correspondence should be addressed to Wansik Yu; yuwansik@gmail.com

Received 14 September 2015; Revised 15 November 2015; Accepted 15 November 2015

Academic Editor: Milan Gocic

The common approach to quantifying the precipitation forecast uncertainty is ensemble simulations where a numerical weather prediction (NWP) model is run for a number of cases with slightly different initial conditions. In practice, the spread of ensemble members in terms of flood discharge is used as a measure of forecast uncertainty due to uncertain precipitation forecasts. This study presents the uncertainty propagation of rainfall forecast into hydrological response with catchment scale through distributed rainfall-runoff modeling based on the forecasted ensemble rainfall of NWP model. At first, forecast rainfall error based on the BIAS is compared with flood forecast error to assess the error propagation. Second, the variability of flood forecast uncertainty according to catchment scale is discussed using ensemble spread. Then we also assess the flood forecast uncertainty with catchment scale using an estimation regression equation between ensemble rainfall BIAS and discharge BIAS. Finally, the flood forecast uncertainty with RMSE using specific discharge in catchment scale is discussed. Our study is carried out and verified using the largest flood event by typhoon "Talas" of 2011 over the 33 subcatchments of Shingu river basin (2,360 km^2), which is located in the Kii Peninsula, Japan.

1. Introduction

Recent advances in weather measurement and forecasting have created opportunities to improve streamflow forecasts. It is possible to combine high-resolution numerical weather prediction (NWP) data directly into streamflow forecast systems in order to obtain an extended lead time. The accuracy of weather forecasts has steadily improved over the years, but recent researches represented that direct application of outputs from the NWP model into the hydrological domain can result in considerable bias and uncertainty that are propagated into hydrological domains [1, 2].

One of the biggest sources of uncertainty in the application of streamflow forecasting comes from forecasted rainfall. The grid size in NWP models is often larger than the subcatchment size in hydrological models, which results in the forecast rainfall data not being at the appropriate resolution required for flood forecasting. In addition, even small errors in the location of weather systems by NWP models may result in forecast rainfall for the catchment concerned being significantly wrong [3, 4]. These biases and uncertainties of rainfall forecast may be amplified when cascaded through the hydrological system, and small uncertainties in rainfall forecast may translate into larger errors in flood forecasting. As an example, Komma et al. [5] showed that an uncertainty range of 70% in terms of NWP rainfall translated into an uncertainty range of 200% in terms of runoff for a lead time of 48 hours. They presented this to the nonlinearity of the catchment responses, but uncertainties such as forecast rainfall, parameter, and structure of a hydrologic model may contribute to the amplification of the uncertainty in terms of flood forecasting. Xuan et al. [6] also highlighted that although the QPF from NWP model could generally catch the rainfall pattern, the uncertainties of rainfall at the scale of model grid to the catchment were always significant.

It is difficult to understand the full range and interaction of uncertainties in flood forecasting. And the different types of uncertainty will vary with lead time of the forecasts, and with the magnitude of the event and catchment characteristics. Vivoni et al. [7] addressed the propagation of radar rainfall nowcasting errors to flood forecasts in the context of distributed hydrological simulations. However, they used the radar rainfall measurements to quantify how increases in nowcasting errors to flood forecast with lead time, whereas our approach applies the ensemble NWP rainfall into the flood forecasts to assess the error and uncertainty propagation with the catchment scale. And the variability of runoff predictions by rainfall uncertainty differs for different case studies and thus no general trend is apparent [8–10]. This study is carried out under the assumption that model parameters and structure errors do not contribute to uncertainty of flood forecasting to remove the focus from forecast rainfall error. As a result, a distributed hydrologic model is considered to be the appropriate tool to assess rainfall forecast quality and to understand how uncertainty in the rainfall forecasts field may propagate throughout the watershed. Further, the integration of the rainfall forecast into runoff simulation at multiple locations in a catchment allows the investigation of the effects of catchment scale on the propagation of rainfall forecast uncertainties in the streamflow forecasting.

The main objective of this study is to assess the error and uncertainty propagation due to NWP rainfall uncertainty on hydrological response through a distributed hydrologic model depending on catchment scale. In the context of flood forecasts, it is important to assess the forecast rainfall uncertainty in terms of the effect on runoff. And uncertainties based on spatial scale are also important by means of the information for real-time flood forecast and the possible amount of flow to the reservoir and exceeding its capacity to optimize the water volume to be released. Therefore, the coupled use of NWP rainfall output and hydrologic flood forecasting requires an assessment of uncertainty through hydrological response.

The research question is as follows: How does ensemble NWP rainfall error translate into flood forecasting, and how does flood forecast uncertainty propagate as a function of catchment scale dependency? To our knowledge, there exists research about rainfall uncertainty's direct propagation into the hydrological domain, but the spatial scale dependency of uncertainty propagation of ensemble NWP rainfall into hydrological predictions has not been addressed. First, we compared forecast rainfall error based on the BIAS, which is used to measure error amplification, to flood forecast error driven by ensemble NWP forecast outputs to assess error propagation. Second, we discussed the variability of flood forecast uncertainty according to catchment scale using ensemble spread, which is driven by ensemble NWP rainfall through a distributed hydrologic model. We also assessed flood forecast uncertainty, which is under the condition that ensemble NWP rainfall has not BIAS compared with observed radar rainfall and catchment scale using an estimation regression equation between ensemble NWP rainfall and discharge based on the BIAS. Finally, we assessed flood forecast uncertainty with RMSE using specific discharge in catchment scale. Note that we focused not only on the quantitative error propagation of rainfall forecast into flood forecast but also the variability of flood forecast uncertainty with catchment scale.

This paper has been organized in the following way. After the Introduction, Section 2 introduces the design of meteorological experiment for the Typhoon Talas event and describes the target area and a hydrologic model, and Section 3 addresses the results of uncertainty propagation of NWP Rainfall Forecast to Flood Forecast with catchment scale. Finally, we summarize our major conclusions in Section 4.

2. Data and Methodology

2.1. Meteorological Data. In Japan, an operational one-week ensemble prediction model from JMA was developed to provide probabilistic information of 51 ensemble members with a horizontal resolution of 60 km, and it used to be applied for hydrological applications (e.g., prior and optimized release discharge for dam operation) [11]. However, operational short-term (1-2 days) ensemble prediction with much finer resolution has not yet been developed. For that reason, studies on ensemble forecast systems that are composed of 11 members (1 unperturbed and 10 perturbed member) with a horizontal resolution of 10 km and 2 km, the latter nested inside the former with a 6-hour lag, have been conducted by the Meteorological Research Institute (MRI) of JMA for the 2011 Typhoon Talas event.

Both 10 km and 2 km resolution systems used the JMA Nonhydrostatic Model (NHM) as the forecast model [12, 13]. Whereas the 10 km resolution forecast adopted the cloud microphysical process and Kain-Fritsch convective scheme, the 2 km resolution forecast did not use a convective scheme because of its cloud resolving resolutions. The coarse resolution system of 10 km had a domain of 361 × 289 grid points with 50 vertical levels and forecasted up to 36 hours in advance. For initial and lateral boundary conditions, 10 km used the analysis from the JMA nonhydrostatic 4DVAR (JNoVA) data assimilation system [14] and the forecasts of JMA's high-resolution (TL959L60) global spectral model (GSM). The control run (cntl) is the forecast with a nonperturbed analysis, and the 10 perturbed forecasts were generated from JMA's 1-week global EPS (WEP) for the initial and boundary perturbations. The fine-resolution 2 km system was conducted from the downscale forecast of 10 km resolution systems. This system had a domain of 350 × 350 grid points with 60 vertical levels and forecasted up to 30 hours in advance. The domain of the two ensemble systems with 10 km and 2 km horizontal resolution are illustrated in Figure 1(a). The initial and boundary conditions for each member at 2 km were interpolated from the forecasts on the corresponding member at 10 km resolution with a 6-hour lag. 10 km started running at 21 JST every day, and 2 km began 6 hours later. Figure 1(b) shows a schematic of forecast runs with 10 km and 2 km resolution.

In this study, we introduced the results of ensemble prediction with a 2 km horizontal resolution due to the viewpoints of high resolution and better predictability of weather phenomena and used 4 sets of ensemble prediction outputs with 30 hours forecast time to assess rainfall forecast uncertainty and to understand how uncertainty in the rainfall forecast may propagate throughout the watershed (Table 1).

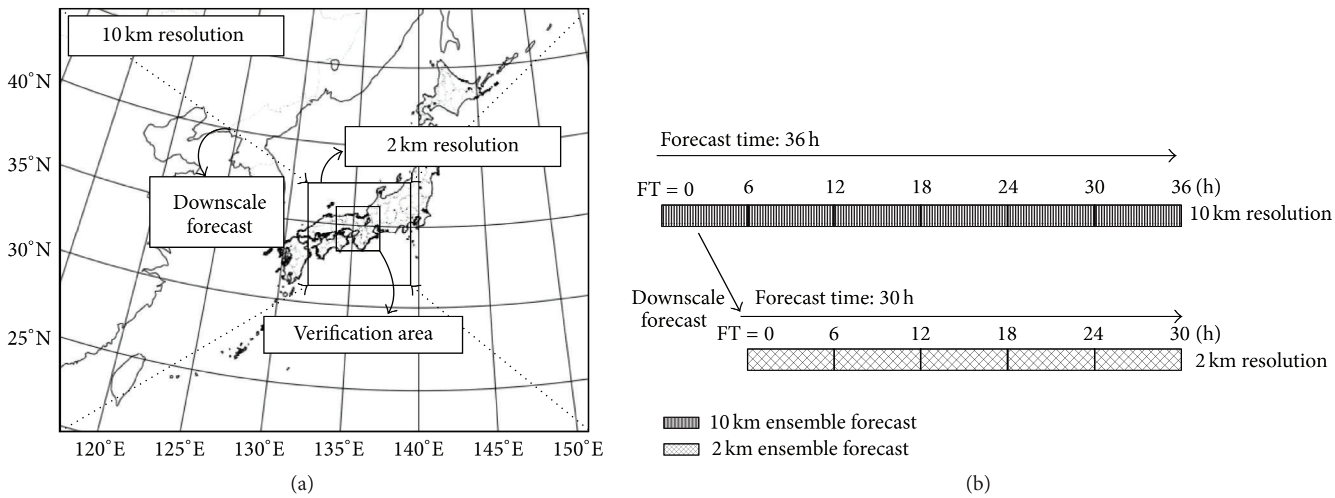

Figure 1: (a) Forecast domains of 10 km and 2 km horizontal resolution. (b) Schematic of forecast runs with 10 km and 2 km horizontal resolution. The rectangle inside 2 km domain denotes the spatial verification area for Kinki region.

Table 1: Four forecast sets with 30 hours' forecast time and 2 km horizontal resolution used in the study. Each forecast is overlapped with 6 hours.

Forecast period	First forecast	2011/09/01 03:00–09/02 09:00 JST
	Second forecast	2011/09/02 03:00–09/03 09:00 JST
	Third forecast	2011/09/03 03:00–09/04 09:00 JST
	Fourth forecast	2011/09/04 03:00–09/05 09:00 JST

And the ensemble NWP rainfall forecast in this study is verified spatially against the Ministry of Land, Infrastructure, Transport and Tourism (MLIT) C-band composite radar data (radius of quantitative observation range: 120 km, 1 km mesh and 5 min resolution). Since the first installation of C-band radar in Japan in 1976, the radars have installed all parts of Japan gradually. Now 26 C-band radars cover and monitor rainfall of all Japan. It is important to provide information of river and basin rapidly to relevant authorities and people in order to protect human life and property from disaster. MLIT C-band radar provides wide observation range and is useful for large river flood-management tool in observing the seasonal rain front or typhoons.

2.2. Target Area and a Hydrologic Model. The Shingu river basin was selected as the target area to assess rainfall forecast uncertainty into streamflow forecast with spatial scale. The Shingu river basin is located in the Kii Peninsula of the Kinki area, Japan, and covers an area of 2,360 km^2. The average elevation of the study site is 644.6 m, and the slope is steep; this basin is a mountainous area. The five dams, Futatsuno, Kazeya, Komori, Nanairo, and Ikehara, are located upstream. The left and right sides of the Shing river basin exhibit different characteristics. The left side is the Totsukawa basin, and the right side is the Kitayamakawa basin. Their characteristics are completely different. The elevation of Totsukawa is higher than that of Kitayamakawa. And Kitayamakawa

Table 2: Subcatchment area at gauged and ungauged points.

Catchment	Area (km^2)	Catchment	Area (km^2)
1	92.2	18	141.56
2	165.99	19	347.35
3	279.78	20	429.07
4	150.56	21	94.23
5	444.04	22 (Nanairo dam)	529.49
6	54.24	23 (Komori dam)	633.22
7	533.73	24	700.49
8	105.72	25	1090.92
9 (Kazeya dam)	656.08	26	56.68
10	65.97	27	65.20
11	766.19	28	1268.03
12	65.04	29	783.85
13	130.74	30	2091.38
14 (Futatsuno dam)	1012.15	31	110.92
15	112.13	32	2212.24
16	72.65	33 (Ouga station)	2245.56
17 (Ikehara dam)	203.27		

has a lower level in the channel. We divided the Shingu river basin into 33 subcatchments from 54.24 to 2245 km^2 (Figure 2, Table 2), including 6 gauged (5 dams and 1 gauge station) and 27 ungauged locations, for the assessment of uncertainty of ensemble NWP rainfall into flood forecast with catchment scale. At first, we divided the Shingu river basin into 6 subcatchments including the 5 dams and 1 gauge station, which have the observed discharge data. Then we also divided the Shingu river basin into 33 subcatchments from 54.24 to 2245 km^2 by considering the channel junction of tributaries using the drainage networks of digital elevation model (DEM). Segond [9] specified the catchment into small (<100 km^2), medium (100–2000 km^2), and large (>2000 km^2) catchments. However, the standard of catchment scale differs

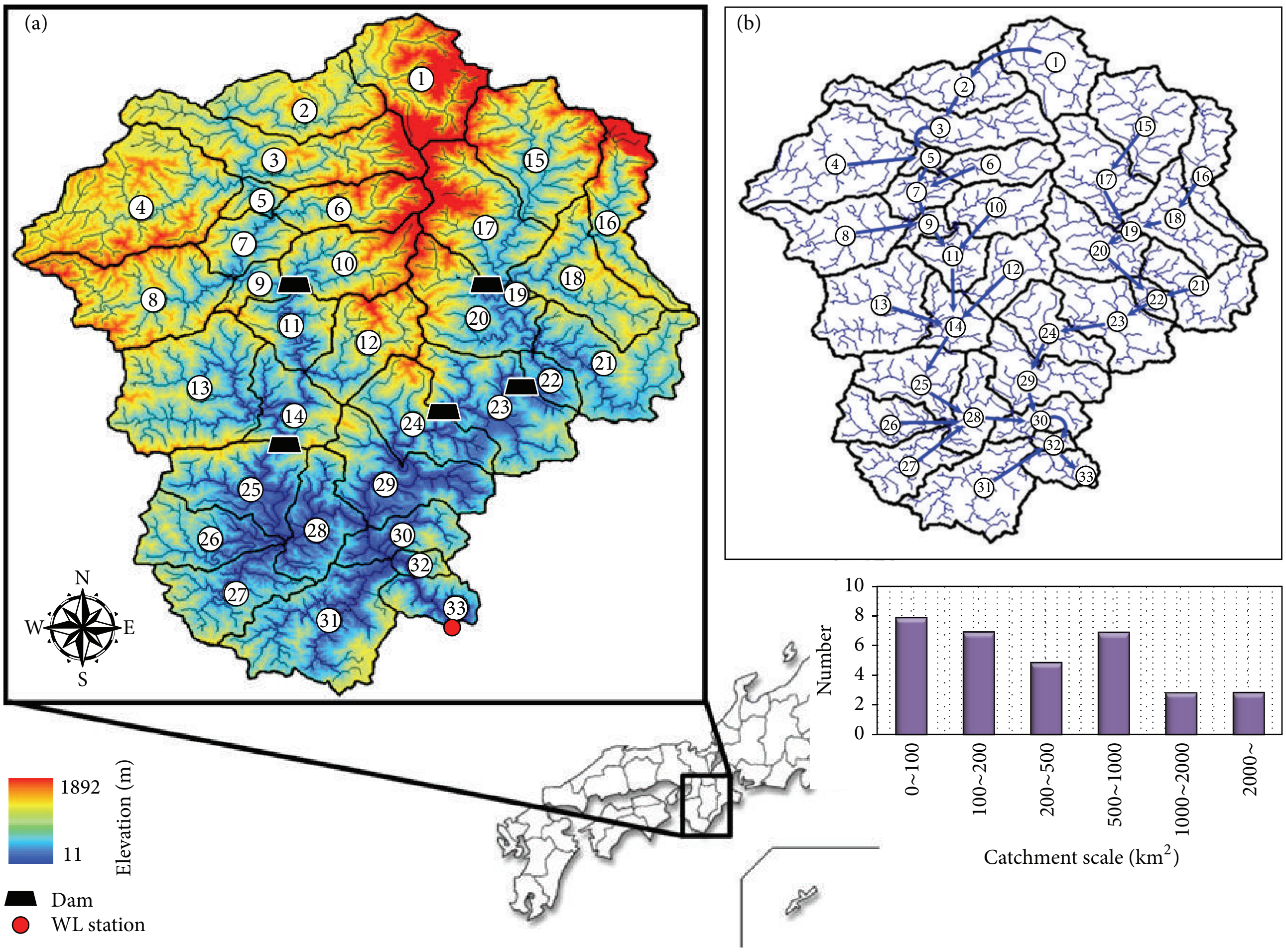

FIGURE 2: (a) 33 subcatchments including 6 gauged (5 dams and 1 gauge station) and 27 ungauged locations and (b) connections with flow directions.

for different case studies, and the Shingu river basin covers an area of 2,360 km^2; thus, we specified 33 subcatchments into 3 types, small catchment (<200 km^2), medium catchment (200~1000 km^2), and large catchment (>1000 km^2) to evaluate the variability with catchment scale. We also divided catchment characteristics into 2 types, mountainous area (>800 m) and flat area (<800 m) considering average elevation (800 m) of the 33 subcatchments.

We used a spatially distributed hydrologic model, based on one-dimensional kinematic wave method for subsurface and surface flow (hereafter, KWMSS) with a conceptual stage-discharge relationship [15]. Figure 3 is a conceptualization of spatial flow movement and flow process in hillslope elements of KWMSS. The rainfall-runoff transformation conducted by KWMSS is based on the assumption that each hillslope element is covered with a permeable soil layer. This soil layer consists of a capillary layer and a noncapillary layer. In these conceptual soil layers, slow and quick flow are simulated as unsaturated Darcy flow and saturated Darcy flow, respectively, and overland flow occurs if water depth, h [m], exceeds soil water capacity:

$$q = \begin{cases} v_c d_c \left(\dfrac{h}{d_c}\right)^{\beta}, & 0 \le h \le d_c \\ v_c d_c + v_a \left(h - d_c\right), & d_c \le h \le d_s \\ v_c d_c + v_a \left(h - d_c\right) + \alpha \left(h - d_s\right)^m, & d_s \le h, \end{cases} \quad (1)$$

$$\frac{\partial h}{\partial t} + \frac{\partial q}{\partial x} = r(x,t), \quad (2)$$

where $v_c = k_c i$ [m/s], $v_a = k_a i$ [m/s], $k_c = k_a/\beta$ [m/s], $\alpha = i^{1/2}/n$ [$m^{1/3}s^{-1}$], $m = 5/3$, i is the slope gradient, k_c [m/s] is the hydraulic conductivity of the capillary soil layer, k_a [m/s] is the hydraulic conductivity of the noncapillary soil layer, n [$m^{-1/3}s$] is the roughness coefficient, d_s [m] is the water depth corresponding to the water content, and d_c [m] is the water depth corresponding to maximum water content in the capillary pore. The flow rate of each hillslope element q [m^2/s] is calculated by (1) and combined with the continuity equation for channel routing by (2). Many studies have applied this hydrologic model in a variety of hydrologic applications and have shown that this rainfall-runoff model was effective, robust, and flexible [16–18].

Table 3: Optimized parameter values from multicalibration using SCE-UA optimization method.

Parameter	Description	Optimal values
n	Roughness coefficient [$\mathrm{m}^{-1/3}\mathrm{s}$]	0.1284
d_c	Depth of the unsaturated soil layer [m]	0.2369
d_s	Depth of the saturated soil layer [m]	0.1442
k_a	Hydraulic conductivity of the saturated soil layer [m/s]	0.0150
β	Nonlinear exponent constant for the unsaturated soil layer [−]	3.7898

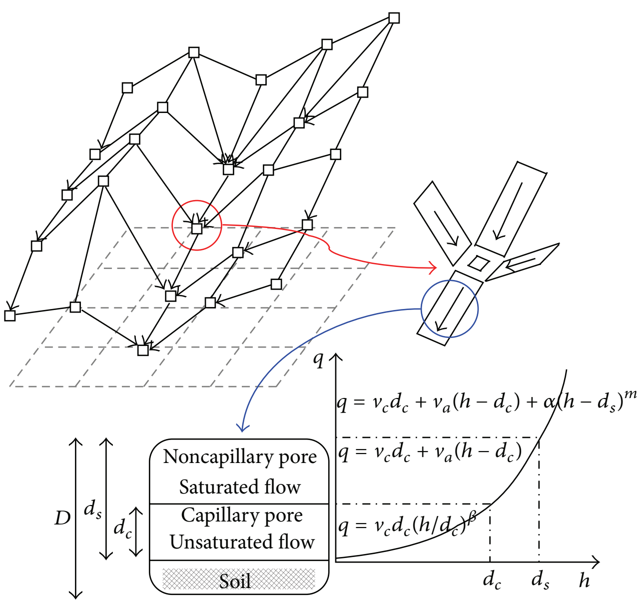

Figure 3: Conceptualization of spatial flow movement and flow process in hillslope elements; the arrows indicate element models for calculating hydrological variables, such as water flux.

There was no observed discharge data in subcatchments, except in 5 dams and 1 gauge station. For that reason, the parameter optimization of the hydrologic model was conducted using the Ministry of Land, Infrastructure, Transport and Tourism (MLIT) C-band composite radar data, which has high spatial-temporal resolution to capture the spatial variability of rainfall. However, in spite of the high-resolution accuracy of radar data, parameterization associated with soil parameters of hydrological model remains uncertain due to impossibility of direct observation and use of the soil parameters (i.e., discordance between soil properties and model parameters). Therefore, we assumed that parameters of hydrologic model in Table 3 are spatially homogenous over the 33 subcatchments. The Shuffled Complex Evolution (SCE) global optimization method [19] was used for the parameter optimization of the hydrologic model using MLIT composite radar rainfall to acquire the reference data of the 33 subcatchments. The SCE-UA, one of the computer-based automatic optimization algorithms, is a single-objective optimization method designed to handle high parameter dimensionality encountered in calibration of a nonlinear hydrologic simulation model. Basically, this scheme is based on the following three concepts: (1) combination of simplex procedure using the concepts of a controlled random search approach; (2) competitive evolution; and (3) complex shuffling. The integration of these steps makes the SCE-UA effective, robust, and flexible. In this study, the SCE-UA optimization method was modified to minimize the objective function between observed inflows and simulated results for all 5 dams and 1 gauge station at the same time (Equation (3)). The hydrologic model used here provides output variable of the discharge at the outlet of interest that our target is to find the near-optimal parameter values. We selected objective function using the root mean square error (RMSE). Table 3 summarizes the optimized parameter values from multicalibration using SCE-UA optimization method, and Figure 4 shows the results of multicalibration using the SCE-UA optimization method and minimizing the objective function of 6 observation points:

$$\text{Minimize OF} = \sum_{\text{Basin}=1}^{6} \text{RMSE}_{\text{Basin}}. \tag{3}$$

Observed radar data and its simulated discharge were used as reference data to compare the ensemble NWP rainfall forecast and flood forecast for the assessment of uncertainty propagation in 33 subcatchments. Although the simulated discharge from observed radar rainfall does not specifically represent the true discharge, the simulated discharge from the observed radar data is nevertheless set as reference data for comparison with the discharge from ensemble prediction data.

2.3. Skill Score Descriptions. To evaluate the accuracy of the ensemble forecast in terms of areal rainfall intensity, we calculated two error indexes. The first is the normalized root mean square error (RMSE), which is normalized by the mean value of the observations during the each forecast period (30 hours). The second is the log ratio bias, which a relative error and provides information about the total amount of rainfall. A log ratio bias value of zero indicates a perfect forecast; positive and negative values indicate underestimated and overestimated forecasts, respectively:

$$\begin{gathered}\text{Nor. RMSE} = \frac{\sqrt{(1/N)\sum_{t=1}^{N}(O_t - F_t)^2}}{\overline{O}},\\ \text{log ratio BIAS} = \log\frac{\sum_{t=1}^{N} O_t}{\sum_{t=1}^{N} F_t},\end{gathered} \tag{4}$$

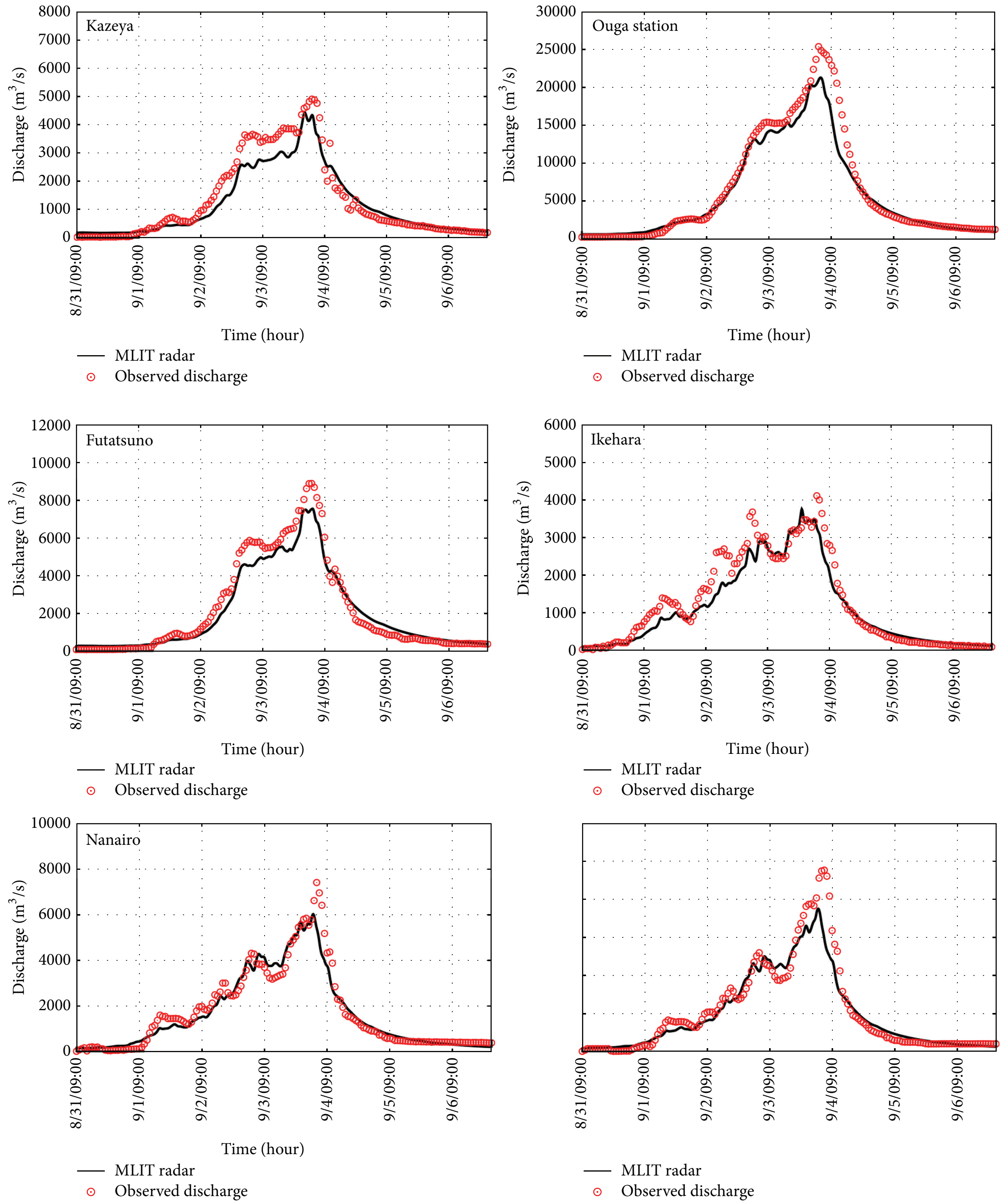

Figure 4: Multicalibration using SCE optimization method and minimizing the objective function of 6 observation points.

where N is forecast time (30 hours) in each period and O_t and F_t are the observed and forecasted rainfall at time t.

For the spatial verification of ensemble NWP rainfall, the rainfall forecasts have been verified spatially against the MLIT C-band composite radar data. The ensemble forecast was expressed as probabilities of exceeding selected rainfall thresholds (1.0 and 5.0 mm/h). A contingency table can be constructed with a spatial comparison, in which each area with more than selected rainfall threshold is defined as "yes," and other areas are defined as "no" for both forecasted and observed rainfall fields. In this study, two indexes are considered for spatial verification of ensemble forecast in the Kinki region (Figure 1). First index is critical success index (CSI), which is also called the "threat score" and its range is 0 to 1, with a value of 1 indicating a perfect forecast. It takes into account both false alarms and missed events. And second one is BIAS, which has range with 0 to ∞. CSI and BIAS are given by

$$\mathrm{CSI} = \frac{\text{hits}}{\text{hits} + \text{misses} + \text{false alarms}},$$
$$\mathrm{BIAS} = \frac{\text{hits} + \text{false alarms}}{\text{hits} + \text{misses}}, \tag{5}$$

where hits are the number of correct forecasts over the threshold (i.e., rainfall is forecast and also observed), and misses are the number of times rainfall is not forecast but is observed. False alarms are the number of times rainfall is forecast but is not observed.

Rainfall forecast error of ensemble outputs from the NWP model is compared with the flood forecast error driven by those rainfall forecasts to assess the uncertainty propagation. It is important, however, to quantify uncertainty propagation from rainfall forecast to flood forecast using statistical measures that appropriately capture forecast deviations. For this reason, the BIAS was used to compare the mean conditions in the forecast and observation in terms of rainfall and flood forecast and to measure error amplification. Note that the BIAS of the basin-mean rainfall is directly compared with the discharge BIAS, and the BIAS is used for an average value of 30 hours of forecast time of rainfall and flood forecast results. Furthermore, the results are classified according to the forecast period of ensemble rainfall from the NWP model:

$$\mathrm{BIAS}_i = \frac{\sum_{t=1}^{N} F_{i,t}}{\sum_{t=1}^{N} O_t}, \tag{6}$$

where N is the forecast time of each forecast period (30 hours); O_t and F_t are the observed and forecasted rainfall and discharge at time t, respectively; and i is each ensemble forecast (11 ensemble members).

For the evaluation of the variability of flood forecast uncertainty according to catchment scale, the mean value of the coefficient of variation (CV), which is a normalized measure of dispersion of a probability distribution or frequency distribution, was used (Equation (7)). It is defined as the ratio of the standard deviation to the mean. The absolute value of the CV is sometimes known as relative standard deviation (RSD), which is expressed as a percentage. The coefficient of variation determines the risk:

$$\text{Ave. CV}_i = \frac{\sum_{t=1}^{N} (\sigma_{i,t}/\mu_{i,t})}{N}, \tag{7}$$

where N is the forecast time of each forecast period (30 hours), and $\sigma_{i,t}$ and $\mu_{i,t}$ are the standard deviation to the mean value of the flood forecast at each ensemble i and time t, respectively.

3. Results and Discussion

3.1. Rainfall Verification. For the purpose of temporal verification of QPF with ensemble NWP rainfall during the Talas event, the areal rainfall intensity of ensemble forecasts is compared with the Automated Meteorological Data Acquisition System (AMeDAS) over the Shingu river basin. For comparison, the observed rainfall of AMeDAS (18 stations, 10 min step) is interpolated using the Thiessen polygon spatial distribution method.

Figure 5 shows areal rainfall of ensemble forecast over the Shingu river basin in the form of box plots plotted from 0 to 24 hours forecast time of ensemble forecast excluding overlapped forecast time (from 25 to 30 hours) compared with the areal rainfall of AMeDAS. In the 1st and 2nd forecast periods, the control run (unperturbed member) and ensemble (perturbed members) forecasts produced a suitable areal rainfall compared with the AMeDAS rainfall, but as shown in the 3rd forecast result, the control run forecast was not well matched and did not produce the rainfall intensity because the spatial pattern of rain cells moved to the north-eastern part of Kii peninsula quickly by that the MSM failed to correctly forecast, as mentioned in the Introduction. On the other hand, the upper range of the ensemble forecast was able to produce considerable rainfall intensity, and the amounts of maximum rainfall intensity are also similar to AMeDAS rainfall. In 4th forecast period, the reason why rainfall intensities are overestimated can be explained by the fact that the last spatial rainfall pattern of the 3rd forecast moved to the north-eastern part of the Kii peninsula; however, it started the forecast again from the Kii peninsula in the 4th forecast. For this reason, rainfall intensities were very high in the 4th forecast period compared with AMeDAS.

In the index of normalized RMSE, the control run and ensemble mean have similar values from 1st to 3rd forecast period, but the best index of the ensemble spread could provide good value as compared with the deterministic control run. In the 4th forecast period, as mentioned above, the index of the control run and ensemble spread is relatively large, but the best index of the ensemble is estimated at 0.89 (the control run is 3.85). In the index of the log ratio bias, the best index of ensemble spread could cover zero value (perfect forecast), whereas the control run forecast was underestimated for the 1st, 2nd, and 3rd forecasts and overestimated for the 4th forecast period.

Figure 6 shows the results of Critical Success Index (CSI) and BIAS in a comparison of radar data and ensemble forecasts with selected rainfall thresholds (1.0 and 5.0 mm/h) during the 1st, 2nd, 3rd, and 4th forecast periods. In the 1st forecast period of CSI with 1.0 mm/h threshold value, ensemble spread could provide better results than deterministic control run after 17 hours' forecast time, whereas the CSI of control run is close to the ensemble mean value. In the 2nd forecast period, although the CSI of control run are better than ensemble mean, the best index of the ensemble spread outperformed the control run. In the 3rd forecast period, as stated above, the spatial pattern of rain cells moved to the north-eastern part of Kii peninsula quickly, so the CSI

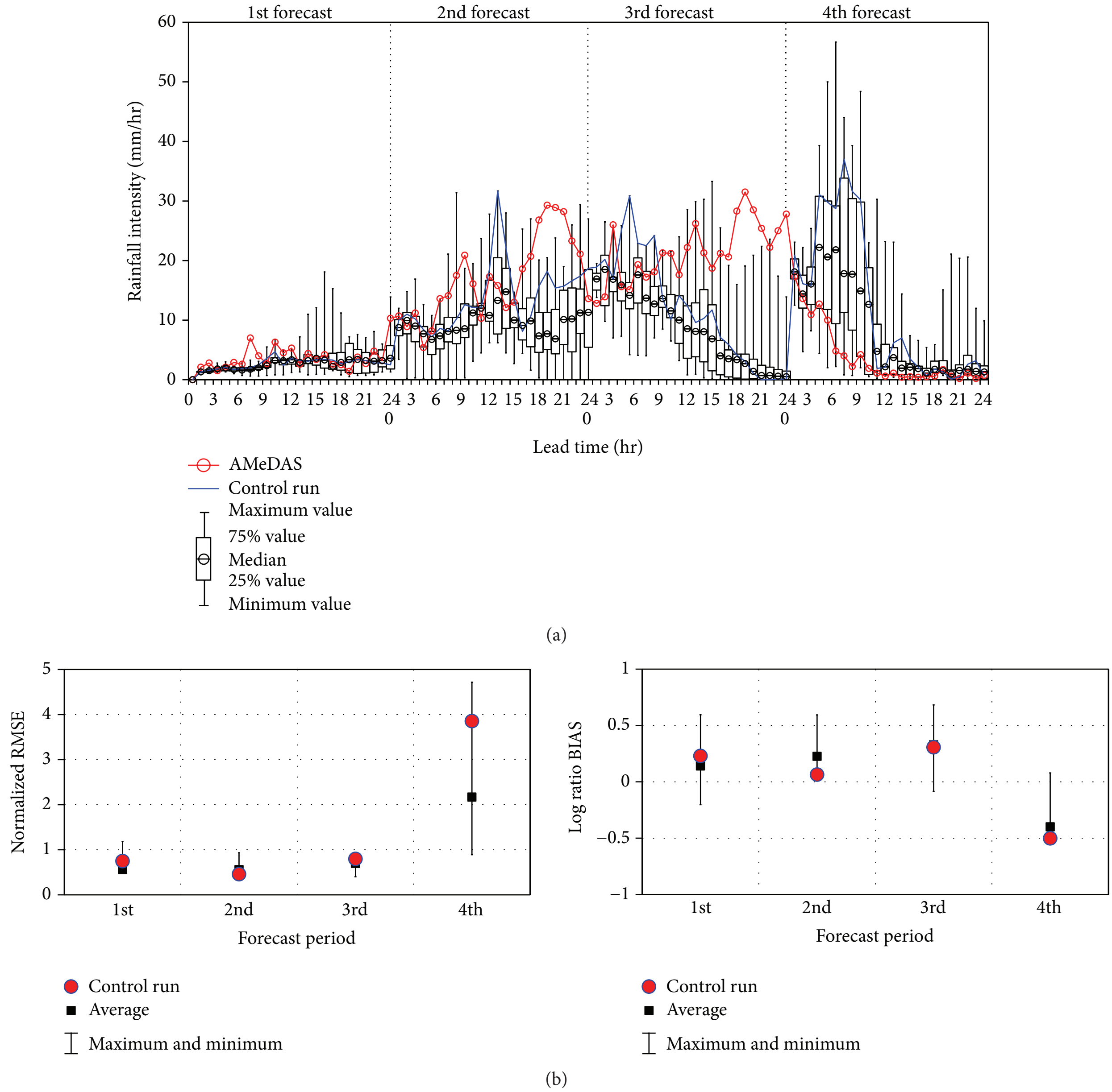

Figure 5: (a) Ensemble areal rainfall forecast over the Shingu river basin in the form of box plots plotted from 0 to 24 hr forecast time, excluding overlapped forecast time (from 25 to 30 hr) for the overall comparison for the Typhoon Talas. (b) Verification results of areal rainfall with normalized RMSE and log ratio bias for Typhoon Talas. Red circles and black squares mean the indexes of the control run and the mean value of ensemble forecast, respectively. The lower and upper bounds of the black lines correspond to the minimum and maximum values, respectively.

of control run decreased as lead time increased, whereas the best value of ensemble spread could provide the better result than the control run. In the 4th forecast period, the control run was close to the ensemble mean, and ensemble spread could cover the control run. In the 3rd forecast period with 1.0 and 5.0 mm/h threshold value, the BIAS decreased quickly as lead time increased. However, the best values of the ensemble spread could maintain higher forecast accuracy compared to the control run forecast. It showed that ensemble forecasts have an advantage in terms of spatial accuracy, although lower value of ensemble forecasts exists in each forecast period as lead time increases.

3.2. Uncertainty Propagation of NWP Rainfall Forecast to Flood Forecast. We conducted the ensemble flood forecasts of 33 subcatchments in the Shingu river basin for an assessment of the ensemble flood forecast driven by ensemble NWP rainfall. Simulated discharges from the observed radar rainfall were used as the initial condition for the ensemble flood forecast in each forecast period. Figure 7 shows the results of the 30 hours' ensemble flood forecast from first to fourth forecast periods over the 33 subcatchments for Typhoon Talas event. Figure 5 illustrates a complete set of the forecasted discharge for the ensemble range (grey curve), the ensemble mean (red curve), and observed radar discharge

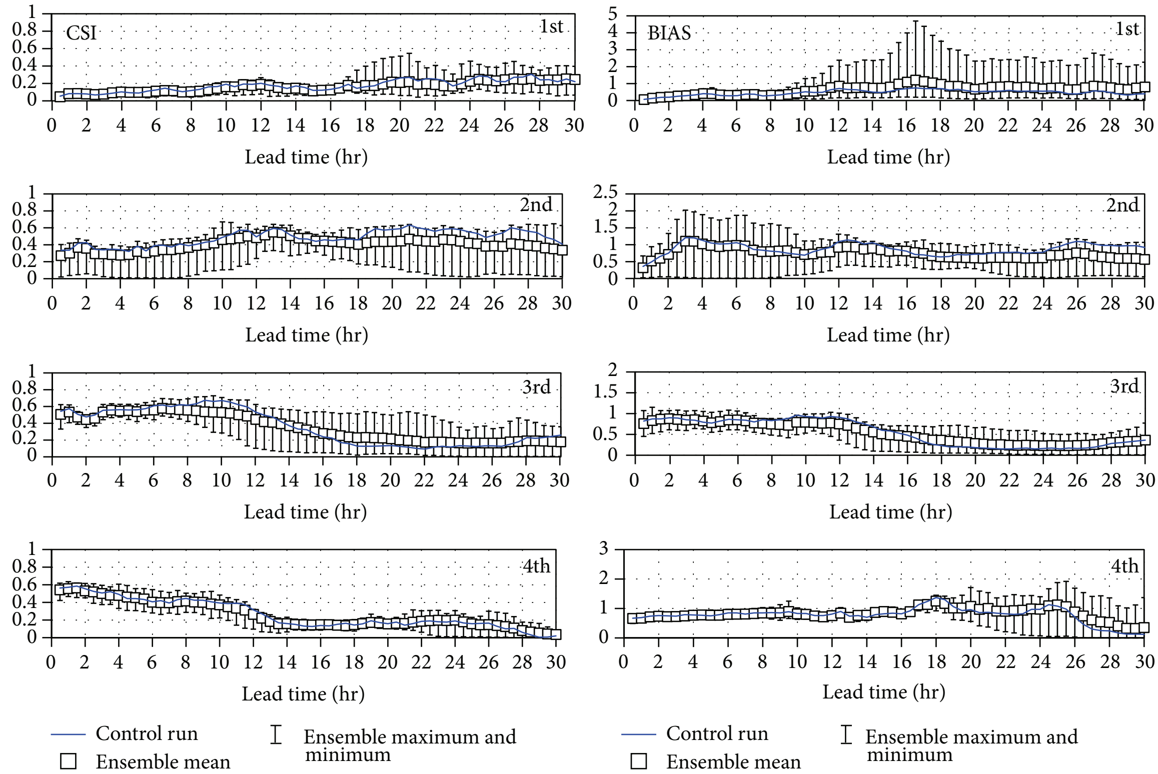

(a) CSI and BIAS with 1 mm/h threshold value

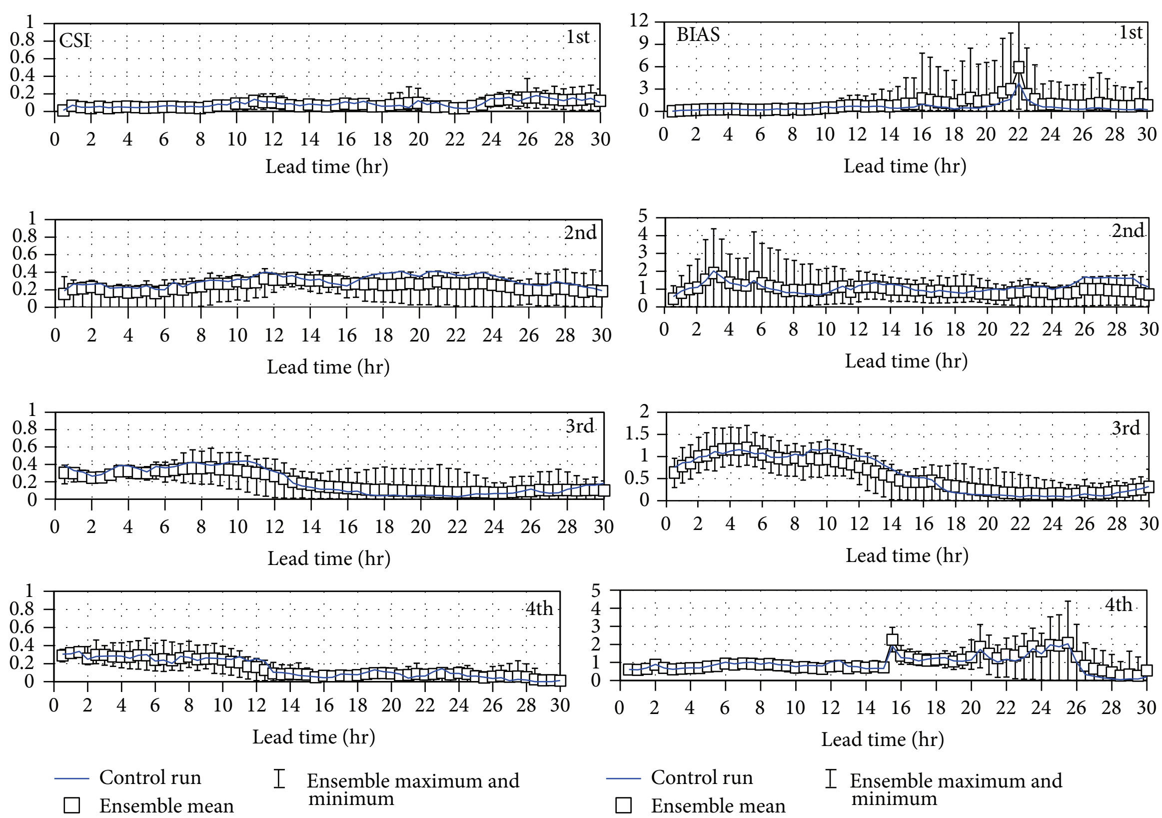

(b) CSI and BIAS with 5 mm/h threshold value

FIGURE 6: Spatial rainfall verification using CSI and BIAS with threshold values in verification area of Figure 1.

data of 33 subcatchment outlet points (bold black curve). Through Figure 5, the ensemble rainfall from NWP model from the first to the fourth forecasts produced a suitable discharge, but average ensemble values were lower than the observed radar discharge of the 2nd forecast period over the 33 subcatchments, caused by the underestimation of the rainfall forecast. In the 3rd forecast period of peak discharge, the average ensemble rainfall was typically lower than the observed discharge, caused by the spatial shift of ensemble NWP rainfall from the correct spatial position. The majority of ensemble members were also lower than the observed discharge, but a few ensemble members exceeded the observed radar discharge and were close to the observed discharge. In the 4th forecast period, the ensemble forecasts were well matched to observed radar discharge and were overestimated because the overestimation in rainfall forecast triggered a runoff overestimation. From the results of ensemble flood forecast over the 33 subcatchments, flood forecasts driven by ensemble outputs produced suitable results but showed that in general it has a large proportion of under- and overpredictions at low lead times and exhibit a negative bias at longer lead times.

Figure 8 presents a comparison of rainfall and flood forecast errors from the first to the fourth forecast periods with linear regression equations based on a statistical measure, the BIAS, for 33 subcatchments of the Shingu river basin represented in Figure 2. Through Figure 8, rainfall forecast errors lead to proportional flood forecast errors with linear regression equations. The discharge BIAS varies based on the same rainfall BIAS, so the discharge BIAS is different based on catchment scale. For small catchments, rainfall errors from forecast location error occur sensitively due to rainfall pixels of NWP model, which does not cover the small catchment exactly. For larger catchments, many rainfall pixels contribute to the rainfall forecast error propagation in the flood forecast. Therefore, the variability of flood forecast uncertainty according to catchment scale should be investigated.

3.3. Flood Forecast Uncertainty with Catchment Scale. As mentioned above, the Shingu river basin is divided into 33 subcatchments from 54.24 to 2245 km^2, including 6 gauged and 27 ungauged locations, for the assessment of uncertainty of ensemble NWP rainfall into flood forecast with catchment scale. The Shingu river basin has 3 types (small, medium, and large catchments) and 2 characteristics (mountainous and flat area) for evaluation of the variability with catchment scale.

Figure 9 shows the flood forecast variability expressed by coefficient of variation using ensemble spread of the flood forecasting with catchment scale and characteristic. Each CV value refers to the average value from the first to the fourth forecast periods and shows CV values for 3 types of the small (red point), medium (blue point), and large (grey point) catchments and 2 characteristics of mountainous (large point) and flat (small point) area for evaluation of the variability with catchment scale. It is evident from Figure 9 that the coefficient of variation in medium and large catchments is close to 0.25, and this is maintained as the catchment increases. For small catchments, however, there is a larger variability than for medium and large catchments, and small catchments have a high coefficient of variation (>0.3). This result suggests that uncertainty variability occurs sensitively and diversely at the same time in different catchments, and small catchments have more sensitive variability in uncertainty. Therefore, flood forecasting in small catchment requires care due to the large variability of uncertainty. On the other hand, in medium and large catchments, there is less uncertainty than with small catchments, and the coefficient of variation converges into a uniform value.

Flood forecast uncertainty focuses on the discharge uncertainty with catchment scale and was assessed when rainfall BIAS was 1, using an estimated linear regression equation between each ensemble rainfall BIAS and discharge BIAS of 33 subcatchments. Figure 10 compares the rainfall BIAS of ensemble members and discharge BIAS driven by those rainfall forecasts in each subcatchment and linear regression equation. From Figure 8, the relationship between rainfall forecast errors and flood forecast errors is proportional in ensemble members to the linear regression equation and is different with catchment scale. And as a result of separation of the forecast BIAS by each subcatchment, we obtain 132 linear regression equations for 33 subcatchments and 4 forecast periods. Then we calculate the discharge BIAS when rainfall BIAS is 1 using a linear regression equation for each subcatchment to focus on the discharge BIAS with catchment scale.

Figure 11 represents the discharge BIAS. It is assumed that rainfall forecast has no error compared to observed radar rainfall (rainfall BIAS is 1 using the linear regression equation) with catchment scale and characteristic. Figure 11 shows that there is a discharge BIAS in all of small, medium, and large catchments even though rainfall forecast has no errors compared to observed radar rainfall. This is due to the spatial variability of rainfall, even though basin-mean rainfall is similar to the observed radar rainfall. As an example, Lee et al. [20] showed that input uncertainty is due to spatial variability of rainfall on catchment responses in rainfall-runoff modeling. As stated above, however, we focused not only on the quantitative error propagation of rainfall forecast into flood forecast but also on the variability of flood forecast uncertainty with catchment scale. The discharge BIAS in medium and large catchments has properties similar to those of the coefficient of variation in Figure 9. The small catchments indicate large variability of discharge BIAS.

Figure 12 represents the flood forecast uncertainty with root mean square error (RMSE) using specific discharge (discharge/catchment scale) of outlets with catchment scale. Figure 12 demonstrates properties similar to those resulting from the coefficient of variation and BIAS in Figures 9 and 11, respectively. In medium catchments, however, there are two types of characteristics in forecast uncertainty variability. In mountainous areas, discharge RMSE is less than that in flat areas, and this characteristic is also seen in Totsukawa and Kitayamaka, the left and right sides of the Shingu river basin, respectively.

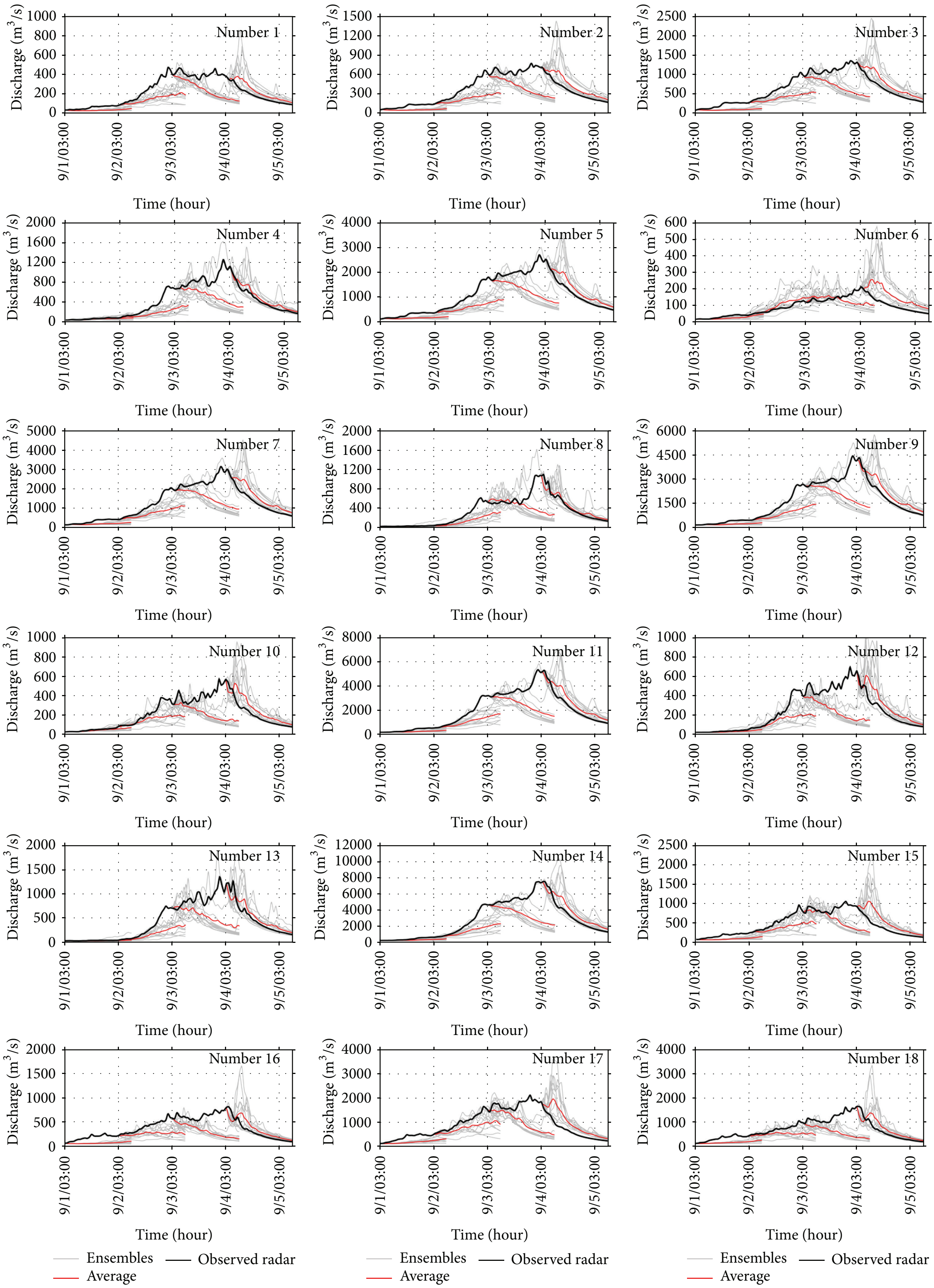

Figure 7: Continued.

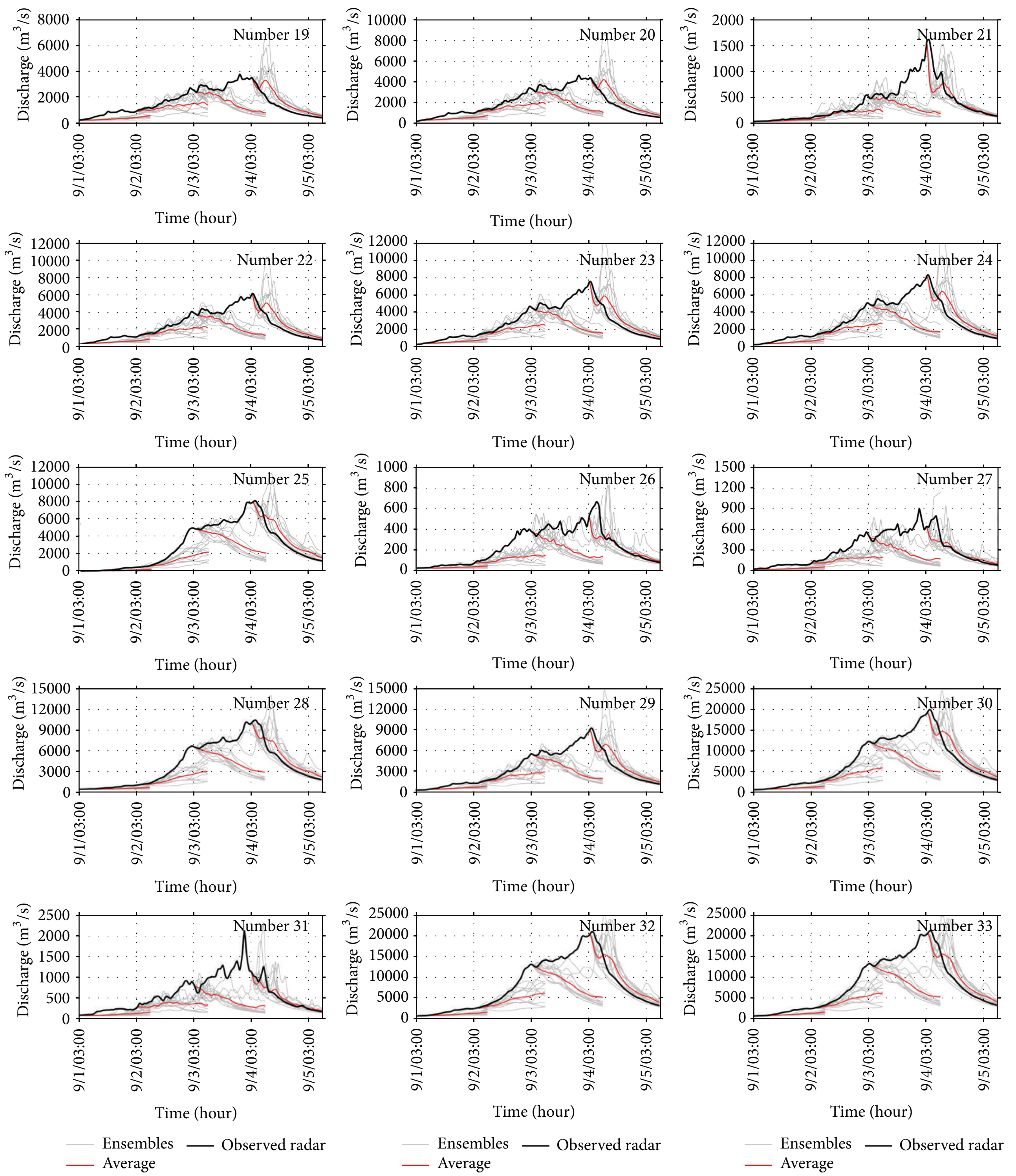

Figure 7: Flood forecast results in over 33 subcatchments. Grey line represents the each forecasted discharge driven by 11 ensemble NWP rainfall. Red curve illustrates the ensemble average results. Black line represents the observed radar discharge of 33 subcatchments.

4. Concluding Remarks

Forecast uncertainty of NWP models is usually assumed to represent the largest source of uncertainty on flood forecasts. However, there are in fact many sources of uncertainties in the flood forecasts which could also be significant, for example, the corrections and downscaling mentioned above and spatial and temporal uncertainties as input into the hydrological simulations including data assimilation. And the different types of uncertainty will vary with lead time

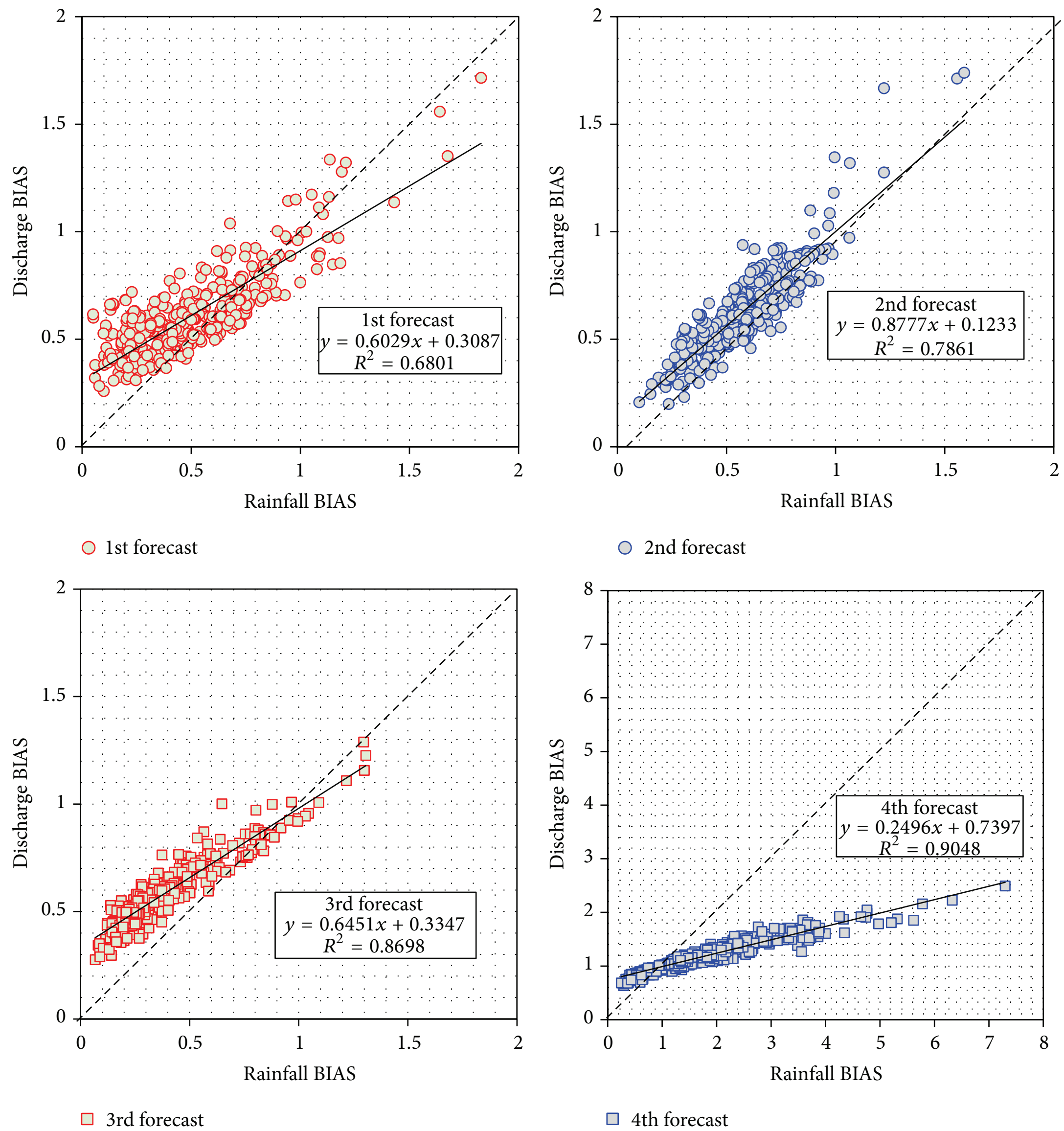

FIGURE 8: Propagation of rainfall forecast errors to flood forecast errors from the first to the fourth forecast periods.

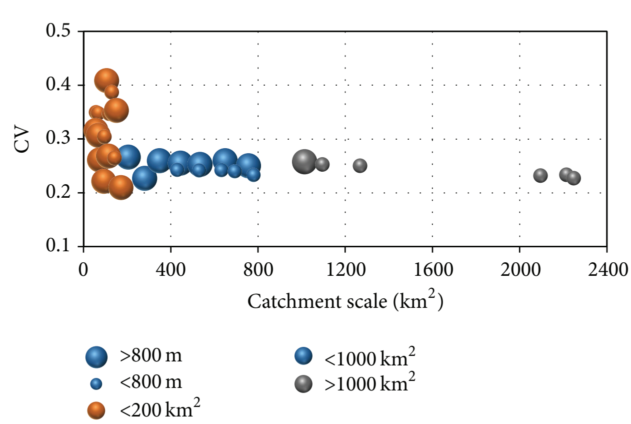

FIGURE 9: Flood forecast variability expressed by coefficient of variation with catchment scale and characteristic. Red, blue, and gray points represent the small catchment (<200 km^2), medium catchment (200~1000 km^2), and large catchment (>1000 km^2), respectively. And we also divided catchment characteristics into 2 types, mountainous area (>800 m, big point) and flat area (<800 m, small point) considering average elevation (800 m) of the 33 subcatchments.

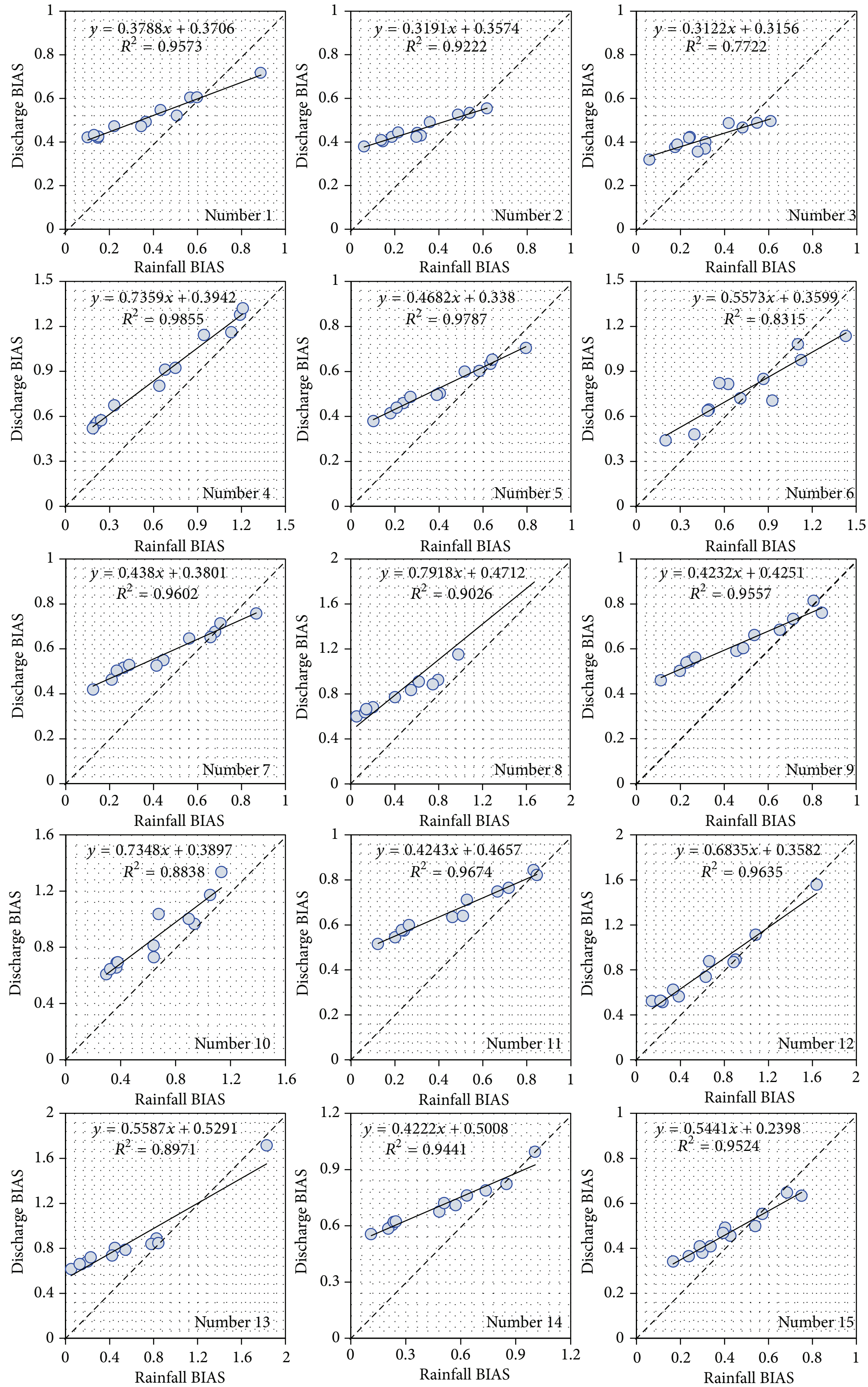

Figure 10: Continued.

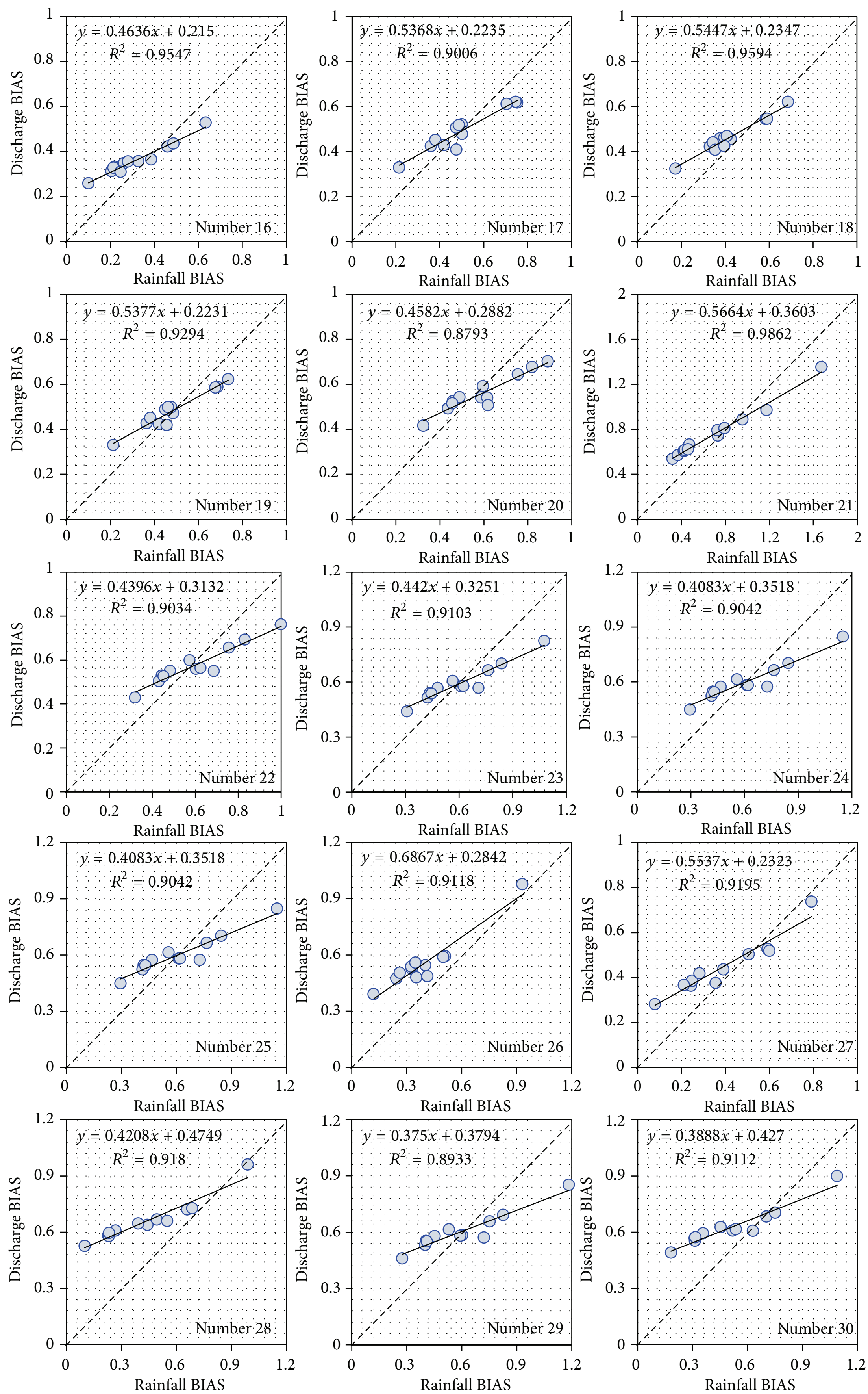

Figure 10: Continued.

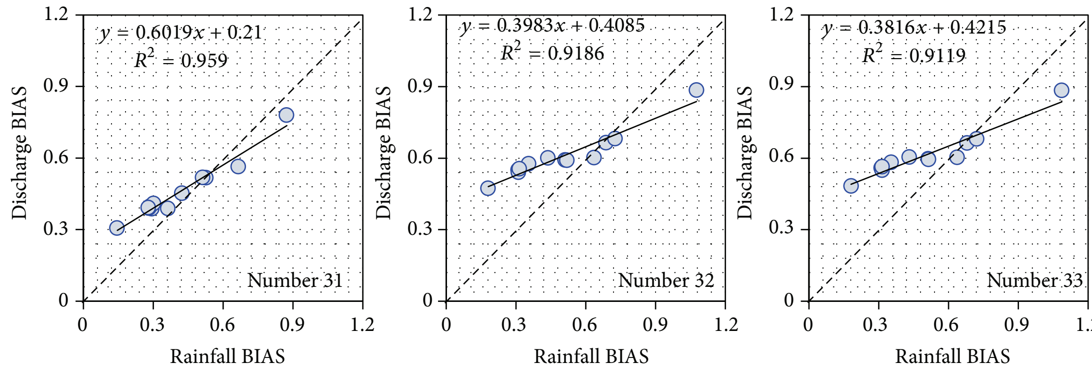

FIGURE 10: Comparison of rainfall and discharge BIAS of ensemble members in each subcatchment and linear regression equation.

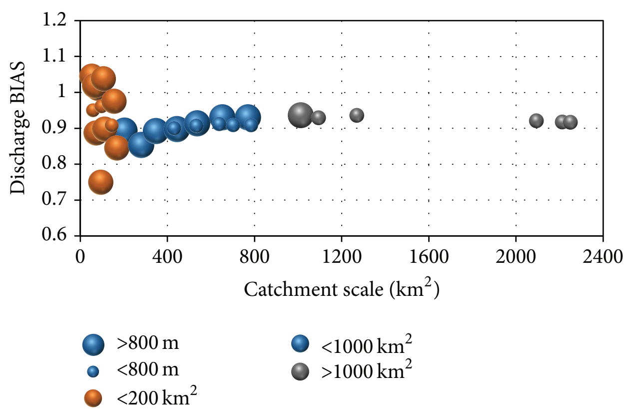

FIGURE 11: Flood forecast variability expressed by BIAS with catchment scale and characteristic. Red, blue, and gray points represent the small catchment (<200 km^2), medium catchment (200~1000 km^2), and large catchment (>1000 km^2), respectively. And we also divided catchment characteristics into 2 types, mountainous area (>800 m, big point) and flat area (<800 m, small point) considering average elevation (800 m) of the 33 subcatchments.

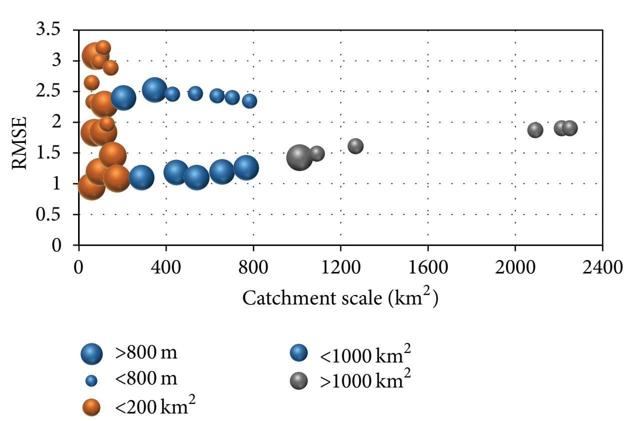

FIGURE 12: Flood forecast variability expressed by RMSE with catchment scale and characteristic. Red, blue, and gray points represent the small catchment (<200 km^2), medium catchment (200~1000 km^2), and large catchment (>1000 km^2), respectively. And we also divided catchment characteristics into 2 types, mountainous area (>800 m, big point) and flat area (<800 m, small point) considering average elevation (800 m) of the 33 subcatchments.

of the forecasts and with the magnitude of the event and catchment characteristics. Ensemble flood forecasting by ensemble NWP rainfall is specifically designed to capture the uncertainty, by representing a set of possible future states of the atmosphere. This uncertainty can then be cascaded through flood forecasting systems to produce an uncertain or probabilistic prediction of flooding. In many cases, the potential of flood forecasting is described alongside cautious notes regarding variability, uncertainty, communication of ensemble information, need for decision support, and problems of using short time series [9]. Therefore, it is important to assess the forecast rainfall uncertainty in terms of the effect on runoff, and uncertainties based on spatial scale are also important for the information of real-time flood forecast.

The main objective of this study is to investigate the error and uncertainty propagation due to NWP rainfall uncertainty on hydrological response through a distributed hydrologic model depending on catchment scale. First, we conducted the ensemble flood forecasts of 33 subcatchments in the Shingu river basin for an assessment of the ensemble flood forecast driven by ensemble NWP rainfall and compared forecast rainfall error based on the BIAS, which is used to measure error amplification, to flood forecast error driven by ensemble NWP forecast outputs to assess error propagation. Second, we discussed the variability of flood forecast uncertainty according to catchment scale using ensemble spread by ensemble NWP rainfall through a distributed hydrologic model. Finally, we assessed the flood forecast uncertainty using an estimation regression equation between ensemble NWP rainfall and discharge based on the BIAS and also assessed the flood forecast uncertainty with RMSE using specific discharge in catchment scale.

From the results, the ensemble flood forecast over the 33 subcatchments and flood forecasts driven by ensemble outputs produced suitable results but showed that in general it has a large proportion of under- and overpredictions at low lead times and exhibit a negative bias at longer lead times. And this study demonstrates that uncertainty variability occurs sensitively and diversely at the same time in different catchments, and small catchments have sensitive variability of uncertainty. General findings from this study are the fact that smaller catchments demonstrate a larger uncertainty in the flood forecast. Therefore, flood forecasting in small catchment should be careful due to the large variability of uncertainty. On the other hand, in medium and large catchments, there is less uncertainty than in small catchments as would be expected due to the smoothing effects of modeling a larger catchment. The ensemble forecasts are specifically designed to capture the uncertainty in NWPs, by representing a set of possible future states of the atmosphere. This uncertainty can then be cascaded through flood forecasting systems to produce an uncertain or probabilistic prediction of flooding. In order to use ensemble forecasts of NWP model for flood forecasts effectively, it is important to establish methodologies to analyze ensemble flood forecasts. To reduce the uncertainty of rainfall and flood forecasts, the bias correction and/or hybrid products with radar-based prediction are required to achieve more reliable hydrologic predictions; bias correction and blending method for accuracy improvement was addressed in Yu et al. [21]. In further research, we need to verify the applicability through a number of case studies, and we expect it to be used in hydrological applications such as real-time flood forecasting for warning system and optimized release discharge for dam operation.

Conflict of Interests

The authors declare that there is no conflict of interests regarding the publication of this paper.

Acknowledgments

This study was partly supported by the subproject of the field 3 on Next Generation Supercomputer Project, "Prediction of Heavy Rainfalls by a Cloud-Resolving NWP System," and was based on data from the Ministry of Land, Infrastructure, Transport and Tourism (MLIT) and J-POWER Co. Ltd., Japan. The authors are grateful for their support.

References

[1] L. Ferraris, R. Rudari, and F. Siccardi, "The uncertainty in the prediction of flash floods in the northern Mediterranean environment," *Journal of Hydrometeorology*, vol. 3, no. 6, pp. 714–727, 2002.

[2] L. Cuo, T. C. Pagano, and Q. J. Wang, "A review of quantitative precipitation forecasts and their use in short- to medium-range streamflow forecasting," *Journal of Hydrometeorology*, vol. 12, no. 5, pp. 713–728, 2011.

[3] C. P. Leahy, S. Srikanthan, G. Amirthanathan, and S. Sooriyakumaran, "Objective assessment and communication of uncertainty in flood warnings," in *Proceedings of the Extended Abstracts of Presentations at the 5th Victorian Flood Management Conference*, October 2007.

[4] E. E. Ebert, "Ability of a poor man's ensemble to predict the probability and distribution of precipitation," *Monthly Weather Review*, vol. 129, no. 10, pp. 2461–2480, 2001.

[5] J. Komma, C. Reszler, G. Blöschl, and T. Haiden, "Ensemble prediction of floods—catchment non-linearity and forecast probabilities," *Natural Hazards and Earth System Science*, vol. 7, pp. 431–444, 2007.

[6] Y. Xuan, I. D. Cluckie, and Y. Wang, "Uncertainty analysis of hydrological ensemble forecasts in a distributed model utilising short-range rainfall prediction," *Hydrology and Earth System Sciences*, vol. 13, no. 3, pp. 293–303, 2009.

[7] E. R. Vivoni, D. Entekhabi, and R. N. Hoffman, "Error propagation of radar rainfall nowcasting fields through a fully distributed flood forecasting model," *Journal of Applied Meteorology and Climatology*, vol. 46, no. 6, pp. 932–940, 2007.

[8] J. D. Michaud and S. Sorooshian, "Effect of rainfall-sampling errors on simulations of desert flash floods," *Water Resources Research*, vol. 30, no. 10, pp. 2765–2775, 1994.

[9] M. L. Segond, *Stochastic modelling of space-time rainfall and the significance of Spatial data for flood runoff generation [Ph.D. dissertation]*, Department of Civil and Environmental Engineering, Imperial College London, London, UK, 2006.

[10] H. L. Cloke and F. Pappenberger, "Ensemble flood forecasting: a review," *Journal of Hydrology*, vol. 375, no. 3-4, pp. 613–626, 2009.

[11] T. Matsubara, S. Kasahara, Y. Shimada, E. Nakakita, K. Tsuchida, and N. Takada, "Study on applicability of information of typhoons and GSM for dam operation," *Annual Journal of Hydraulic Engineering*, vol. 69, no. 4, pp. 367–372, 2013.

[12] K. Saito, T. Fujita, Y. Yamada et al., "The operational JMA nonhydrostatic mesoscale model," *Monthly Weather Review*, vol. 134, no. 4, pp. 1266–1298, 2006.

[13] K. Saito, "The JMA nonhydrostatic model and its applications to operation and research," in *Atmospheric Model Applications*, I. Yucel, Ed., chapter 5, pp. 85–110, InTech, Rijeka, Croatia, 2012.

[14] Y. Honda and K. Sawada, "A new 4D-Var for mesoscale analysis at the Japan meteorological agency," *CAS/JSC WGNE Research Activities in Atmospheric and Oceanic Modelling*, vol. 38, pp. 01.7–01.8, 2008.

[15] Y. Tachikawa, G. Nagatani, and K. Takara, "Development of stage-discharge relationship equation incorporating saturated-unsaturated flow mechanism," *Annual Journal of Hydraulic Engineering*, vol. 48, pp. 7–12, 2004.

[16] T. Sayama, Y. Tachikawa, K. Takara, and Y. Ichikawa, "Development of a real-time distributed flood prediction system in a flow regulated river basin," in *Proceedings of the 3rd Asia Pacific Association of Hydrology and Water Resources Conference (APHW '06)*, Bangkok, Thailand, October 2006.

[17] S. Kim, Y. Tachikawa, T. Sayama, and K. Takara, "Ensemble flood forecasting with stochastic radar image extrapolation and a distributed hydrologic model," *Hydrological Processes*, vol. 23, no. 4, pp. 597–611, 2009.

[18] W. Yu, E. Nakakita, and K. Yamaguchi, "Assessment of probabilistic flood Forecasting using ensemble NWP rainfall with 30hr forecast time during typhoon events," *Advances in River Engineering*, vol. 19, pp. 235–240, 2013.

[19] Q. Duan, S. Sorooshian, and V. K. Gupta, "Optimal use of the SCE-UA global optimization method for calibrating watershed models," *Journal of Hydrology*, vol. 158, no. 3-4, pp. 265–284, 1994.

[20] G. Lee, Y. Tachikawa, and K. Takara, "Assessment of prediction uncertainty under scale-dependant condition of rainfall runoff modeling," *Annuals of Disaster Prevention Research Institute, Kyoto University*, vol. 51, pp. 29–50, 2008.

[21] W. Yu, E. Nakakita, S. Kim, and K. Yamaguchi, "Improvement of rainfall and flood forecasts by blending ensemble NWP rainfall with radar prediction considering orographic rainfall," *Journal of Hydrology*, 2015.

Hindawi Publishing Corporation
Advances in Meteorology
Volume 2016, Article ID 7626505, 9 pages
http://dx.doi.org/10.1155/2016/7626505

Research Article

Modelling the Rainfall Erosivity of the Rhone Region (Southeastern France) Associated with Climate Variability and Storminess

Nazzareno Diodato,[1,2] Gianni Bellocchi,[1,3] Nunzio Romano,[4] and Francesco M. Guadagno[2]

[1] *Met European Research Observatory, Via Monte Pino snc, 82100 Benevento, Italy*
[2] *Department of Sciences and Technology, University of Sannio, Via Pont'Arsa 11, 82100 Benevento, Italy*
[3] *Grassland Ecosystem Research Unit, French National Institute of Agricultural Research, 5 chemin de Beaulieu, 63039 Clermont-Ferrand, France*
[4] *Department of Agriculture, AFBE Division, University of Napoli Federico II, Via Università 100, 80138 Naples, Italy*

Correspondence should be addressed to Nazzareno Diodato; scodalabdiodato@gmail.com

Received 2 June 2015; Revised 4 August 2015; Accepted 6 August 2015

Academic Editor: Sergio M. Vicente-Serrano

Changes in the spatial and temporal patterns of extreme rainfall may have important effects on the magnitude and timing of rainfall erosivity, which in turn lead to even severe soil degradation phenomena. The Mediterranean belt is characterized by strong climatic variability and specific seasonal features, where dry periods are often interrupted by pulsing storms. Identifying the thresholds associated with extreme rainfall events is among the most important challenges for this region. To discern the spatial patterns of rainfall erosivity hazard in the Rhone region (eastern France), this study establishes thresholds in the power of rainstorms. An indicator Kriging approach was employed for computing probability maps of the annual rainfall erosivity exceeding the threshold of 1800 MJ mm ha^{-1} h^{-1}, the latter being twice greater than the standard deviation. The interdecadal spatial patterns of hazard were assessed for recent decades (1991–2010) and the precedents ones (1961–1990). Climate fluctuations of rainfall erosivity revealed possible signals of increased storminess hazard across the region in recent times. We also discussed changes in the rainfall erosivity hazard forcing as related to climatic changes in daily rain rate, especially in autumn when the erosivity is likely affected by more intense storminess occurring across the southern part of the Rhone region.

1. Introduction

Environmental systems are generally in a state of dynamic equilibrium with external driving forces [1]. However, the recurrence of extreme climate events such as storms and floods can accelerate soil loss (sediment transport) in regional catchments. In this context, the identification of enhanced interdecadal climate signals may demonstrate the existence and help understanding the role of abrupt environmental changes over relatively long time periods [2–5]. Understanding how climate forcing affects region-wide responses is crucial for the purpose of erosion and sediment modelling and the reconstruction of hydrogeomorphological hazards [6, 7]. It also provides a new perspective to the study of landscape conservation and climate change, especially in highly dynamic systems (such as agricultural systems). Practical decision-making for protection from time-distributed extreme events often involves using environmental process models, also linked to temporal GIS (Geographical Information System). This is particularly true in subregional basins of Mediterranean Europe, which are characterised by hydrogeomorphological processes often dominated by extreme rainfall events and related rainfall erosivity, grouped in some particularly stormy years according to climate variability [7–11]. The maps of rainfall erosivity in Figure 1 give a spatial overview of the erosion risk in the Northern Hemisphere (Figure 1(a)), with focus on Europe (Figure 1(b)). The current availability of rainfall erosivity data worldwide provides a first

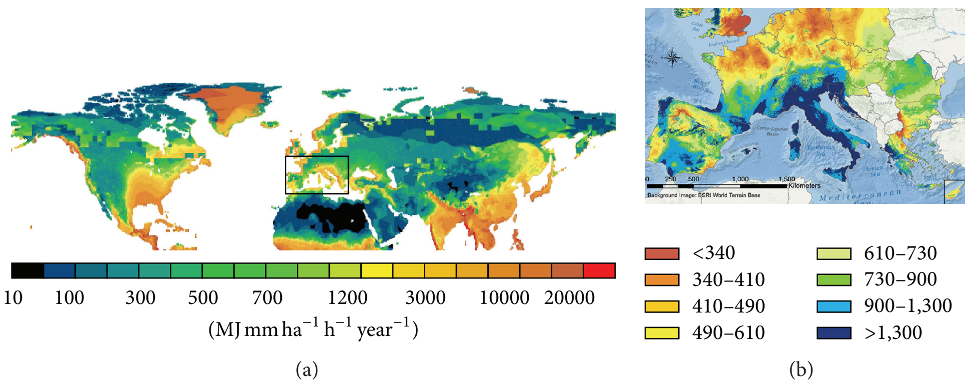

Figure 1: (a) Distribution of long-term mean of the rainfall erosivity (1961–1990) at five-arc-minute resolution (adapted from Naipal et al. [56]) for the Northern Hemisphere, (b) with detailed focus (0.1-arc-minute resolution) on Europe as arranged from European erosivity dataset for the period 2002–2011 [46].

and approximate basis for establishing which regions suffer most from rainfall erosivity and storminess, which requires further exploration and modelling at smaller spatial scales.

Societal infrastructures are becoming more sensitive to weather and climate extremes, which would be exacerbated by climate variability [12–14]. This has triggered a set of studies to determine the change in the probability of heavy precipitations at both global [12, 15, 16], and regional-subregional scales [17–20]. In spite of these efforts, still isolated researches are available documenting to which extent past storm-climatic variability has actually affected the dynamics of rainfall erosivity and landscape responses. Kundzewicz [21] prospected a greater variability of stormflow throughout the globe, both at seasonal and daily scales, coupled with an increase in the frequency of flash floods and rainfall erosivity, especially at mid- to high-latitudes.

The focus of this study is the Rhone river basin (RRB), in southeastern France [22]. This basin is particularly injured by erosivity and floods, which involve surface responses to precipitation events such as the relationship between rainfall-runoff responses and flood-routing mechanisms [23]. Heavy precipitation in the Rhone basin can be attributed to either convective or nonconvective processes or to a combination of them both [24, 25]. Large amounts of precipitation can accumulate over several day-long periods when one or several frontal perturbations slow down and then are enhanced by the relief of the Massif Central and the Alps. The occurrence of exceptionally heavy rainfall events and associated floods and sediment and organic carbon fluxes in many European areas during recent decades [26, 27] motivated us to study long-term changes in the forcing of storm erosivity in the Rhone region. In mainland France, in particular, flash floods and accelerated soil erosion represent the most destructive natural hazards, having caused billions of Euros in damage over the last two decades [26]. Severe flooding events between 1993 and 2003 in the Rhone catchments of Switzerland and France also caused loss of life [28, 29]. In recent times, damaging hydrological events occurred in the Rhone basin showing a climatic shift towards more erratic spatial and temporal distribution of extreme rainfalls, in the form of large-scale pulsing storms [30]. The catastrophic flash flood event of 8-9 September 2002 in the Gardon gorge of France (Gardon river ends into the Rhone at Comps, 43.85 latitude north and 4.61 longitude east) was particularly remarkable for its spatial extent with rain amounts greater than 200 mm in 24 h over 5500 km^2 [31].

This paper explores the feasibility to quantify the relative contribution of rainfall erosivity to the long-term annual and seasonal precipitations falling across the RRB. The major aim of the present study is to develop and evaluate an approach to (i) explain the interdecadal variability of rainfall erosivity and readily available climate data and (ii) recognize seasonal precipitations associated with different seasonal storm types. We hypothesized that the autumn rainfall pattern is an important component of the annual erosivity amount.

2. Environmental Setting and Modelling

2.1. Study Area. The Rhone river watershed covers a surface area of about 98000 km^2, shared by France (92%) and Switzerland. The Rhone river (813 km long) overpasses from north to south the Rhone region originating in the Swiss Alps (Rhone Glacier, 1765 m a.s.l.) and runs through southeastern France for 550 km before entering the Mediterranen Sea. The river is bordered by about 16 million people (~1.2 million in Switzerland). With ~20% of France's agriculture and industry and ~50% of France's tourism activity (after the Rhone-Mediterranean and Corsica Water Agency, through http://www.eaurmc.fr/), the area is identified as of prominent economic importance, the gross domestic product exceeding US$ 52000 million in total [32]. Roughly 70% of the surface water withdrawn in the basin is used for agricultural purposes, while domestic use and industry both use about 15%. Some other uses of the water are hydropower in the Alps, cooling French thermal and nuclear reactors, recreation, and navigation between Lyon (France) and the Mediterranen Sea [33]. The Rhone river contributes 69% of the total sediment export for France, whereas its drainage area represents only 23% of the total area [27]. The basin is placed in a core area with the highest 95th percentiles of June–November daily rainfalls in Europe [30]. The high yearly and seasonal

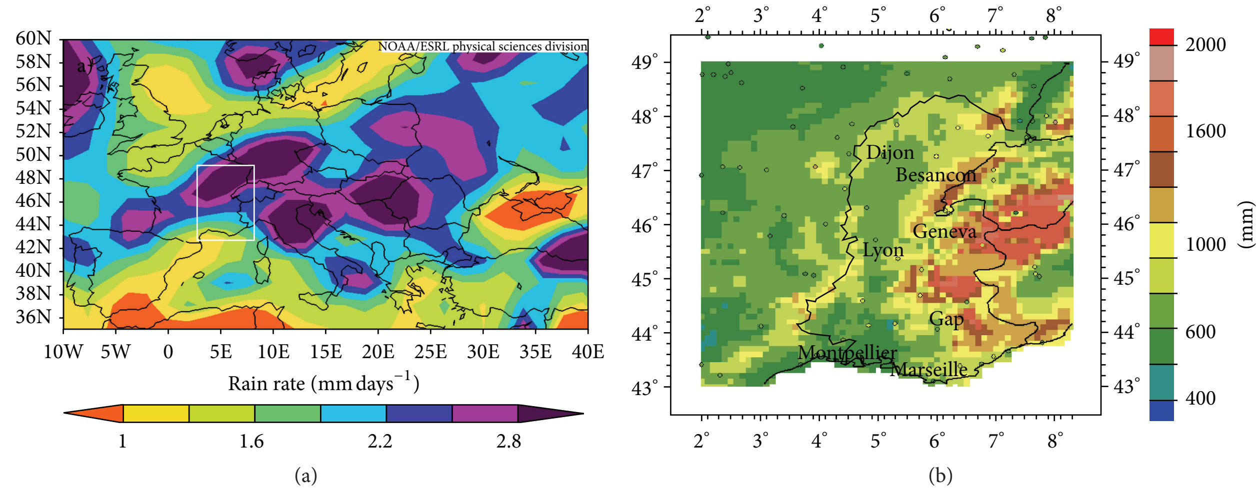

Figure 2: (a) Setting of the study area crossed by annual precipitation rates (1948–2014) via NOAA-ESRL NCEO Reanalysis, (b) with relative zoom of annual mean precipitation of Rhone region, as arranged from LocClim (http://www.fao.org/nr/climpag/pub/en0201_en.asp) via Inverse Distance Weighting with rainfall-elevation extrapolation.

variability of precipitation is mainly the result of the synoptic circulation that advects air masses of different origins (Mediterranean, maritime, polar maritime, and subtropical). However, most dynamic effects are modulated with more recurrence by the Mediterranean and Atlantic Sea. Air masses allow high storage of humidity representing the main energy supply for thunderstorms, which in turn are triggered by outbreaks of warm Mediterranean Sea and Atlantic maritime air in the middle troposphere [34].

The eastern areas and the mountains receive the highest annual precipitation amounts (1400–2000 mm on average, Figure 2). Eastern areas have summer storms of continental influence, whereas cold winter temperatures occur in the Savona valley. The southern part of the Rhone region has a typical Mediterranean climate, with hot and dry summers and rainfall mostly occurring in spring and autumn. The total average annual precipitation has a value of approximately 600 mm yr^{-1} in the north-south transect valley, but rainfall can become intense in September and October in the Cevennes Range (1600 m a.s.l.), located in the southeast of the basin. The maximum values of 600–700 mm observed on 8-9 September 2002 in the Gard gorge are among the highest daily records in the region [31].

2.2. Precipitation Hazard Types. Cyclones build up in three principal areas of the northern Mediterranean Basin: the Gulf of Genoa, the Aegean Sea, and the Black Sea. Generally, subsynoptic scale precipitation systems are produced and triggered by the passage of remnant north Atlantic synoptic fronts and their interaction with local topography [35]. However, the highest frequency on intense cyclones with maximum circulation exceeding 7×10^7 m^2 s^{-1} and a liftime of a least 24 h occurred in the Mediterranean area, with the core across central Italy [36]. These circulation types are characterized by warm and cold air sequences, with rainfall conditions mainly depending on evolving air mass. Other factors determining rainfall conditions are the wind direction at 500 hPa, the trajectory of the low pressure system, the orography, the distance from the sea of each specific area of interest, and surface roughness [37]. Their impact on rainfall is related to the intensity of the cold air intrusion, as well as to the depth of the associated sub-low-pressure system. The most hazardous precipitation events can occur associated with these subsynoptic scale systems. They include flash floods and floods that may have, however, different seasonal regimes (Figures 3(a) and 3(b)).

The period of occurrence of flood situations (especially those driven by convective rainfalls) may serve to identify periods during which extreme rainfall amounts occur. For the area of interest, the flash floods show a bimodal summer-late autumn distribution (one peak is usually noted in July and a second peak in October [38]), while floods have a typical autumn regime. The interweaving of these hydrological regimes is important because they are driven by the rainfall erosivity types that play a fundamental role in determining the intensity of these damaging floods phenomena. On the other hand, they may be useful for reconstructing rainfall erosivity in the past, when no detailed records of rainfall data are available.

Floods are common in the RRB and are known as "extraordinary flooding" or intermediate floods which, for their disruption activity, are particularly hazardous events [31]. Intermediate floods are events with duration of less than 24 hours and the maximum precipitation is usually recorded in less than six hours, with accumulated rainfall usually greater than 200 mm [39].

2.3. Experimental Data in Rainfall Erosivity. In order to evaluate storminess in both spatial and temporal domains and to provide evidence of a likely correspondence between trends in storminess and extreme rainfall, the rainfall erosivity factor is computed for decadal and longer periods, based

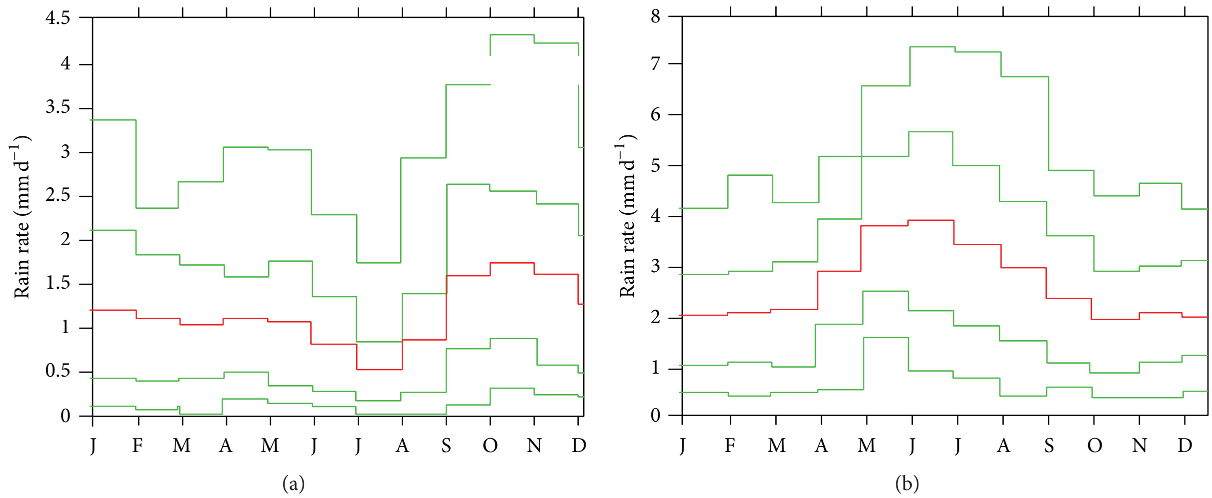

Figure 3: Mean monthly rain rates (red line) with the 25th and the 95th percentile (green lines) for (a) lower and (b) upper Rhone river basin (data arranged from NCEP Reanalysis provided via KNMI-Climate Explorer for the period 1961–2010 [57]).

on concepts by Diodato and Bellocchi [40], who derived the following relation for France [41]:

$$R_{\mathrm{DREMM}} = \alpha \cdot \sqrt{P_{(\max)\mathrm{Oct}}} + \left(P_{\mathrm{prc}\,95(\mathrm{M-O})}\right)^{\eta}, \quad (1)$$

where R_{DREMM} (MJ mm ha^{-1} h^{-1} y^{-1}) is the estimated long-terrm (10-year or longer periods) mean rainfall erosivity, $P_{\mathrm{prc}\,95(\mathrm{M-O})}$ (mm) is the 95th percentile of the monthly rainfall from May (M) to October (O) over each decade, $P_{(\max)\mathrm{Oct}}$ (mm) is the maximum monthly rainfall in October over the decade, α is a scale parameter, and $\eta = 2.459 - 0.02266 \cdot \mathrm{Lat} - 0.004777 \cdot \mathrm{Long}$ (where Lat and Long are latitude and longitude in degrees, taken at the centre of each grid point).

To estimate rainfall erosivity, 100 rainfall grid points covering the studied area were generated (using Kriging interpolation via ESRI—ArcGIS Geostatistical Analyst Extension [42]) based on the GPCC V6 Monthly Land-Surface Precipitation from Rain-Gauges, built on GTS-based and Historic Data with resolution of 0.5° [33] and supplied by Climate Research Unit at the University of East Anglia, United Kingdom (http://badc.nerc.ac.uk/data/cru).

2.4. Exceedance Probability Maps of Rainfall Erosivity. The nonparametric ordinary Kriging method known as indicator Kriging [43] was used to compute the probability maps of the annual rainfall erosivity being greater than a threshold. Compared to parametric approaches, indicator Kriging has the advantage of being less affected by the presence of outliers. The ordinary indicator Kriging (OIK) estimator for the rainfall erosivity is a linear combination of $i(s_\alpha; z_k)$ observations in the neighbourhood s_o:

$$\left[\mathrm{Prob}\left(Z\left(s_o\right) > z_k \mid (n)\right)\right]_{\mathrm{OIK}}^{*} = \sum_{\alpha=1}^{n} \lambda_{\alpha,k}\left(s_o; z_k\right) \cdot i\left(s_\alpha; z_k\right), \quad (2)$$

where λ_α are weighting factors calculated by solving the Kriging simultaneous equation system [40]. In order to assess changes in the rainfall forcing as related to climate changes, the probability maps of mean annual rainfall erosivity discussed in this study were generated for the periods 1961–1990 and 1991–2010 and assembled using ArcGIS platform 9.1 release of the ESRI (http://www.esri.com/software/arcgis).

3. Results and Discussion

3.1. Model Assumptions and Evaluation. In (1), monthly rainfall quantiles and the geographical control are modelled together to account for temporal and spatial dependencies of rainfall erosivity. Equation (1) is subject to the assumption that a large quantile value (95th percentile) of the monthly precipitation distribution over one or more decades is capable of delivering high values of rainfall erosivity, causative of extreme hydrological events. In this way, cumulated occurrence and magnitude of these events per decade(s) are controlled by the combination of climatic and hydrologic factors that the modelled R-factor helps to reveal. This is in agreement with the results referred by Hydrate database [26], which revealed the predominant role played by rainfall erosivity in explaining extreme events (Figure 4(b)). Based on this understanding, in (1) captures extreme rainfall events by percentiles statistics across the months from May to October, representing rainfall erosivity through a power-law function with an exponent (η) varying geographically. The scale parameter $\alpha = 24$ is a conversion factor that can be conveniently assumed constant over time and space. Its value is the same as that estimated at continental scale [40], which was used as initial value and did not change over the calibration process. The varying exponent not only provides a parsimonious description but also is a generic mechanism of the process that serves to either attenuate or enhance rainfall erosivity depending on site-specific climate conditions. In general, geographic location is known to be an important

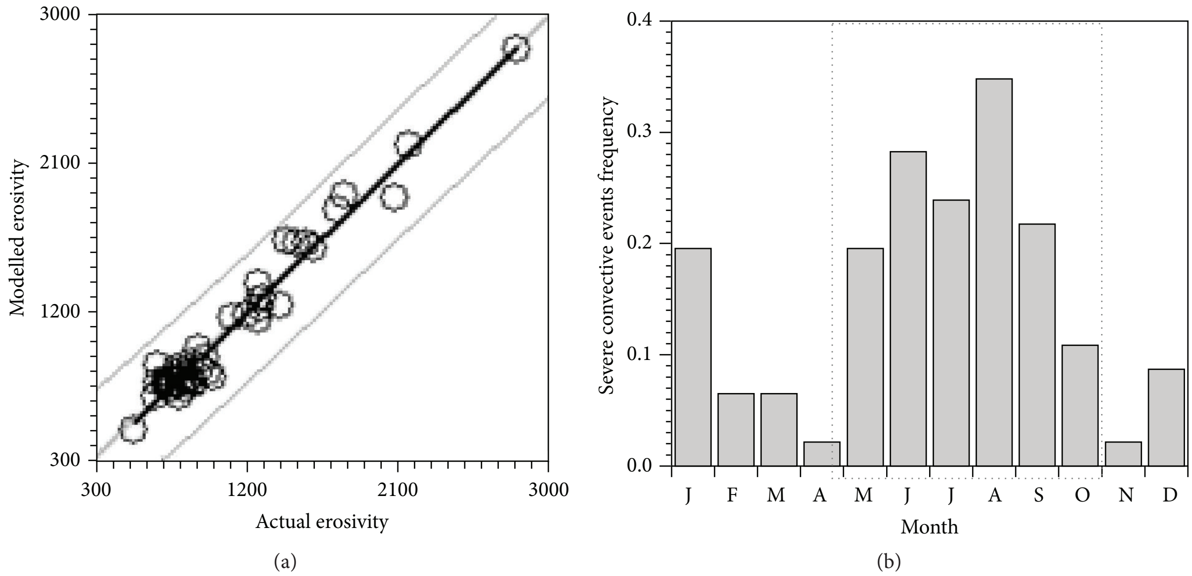

FIGURE 4: (a) Scatterplot between modelled (equation (1)) and actual ((*R*)USLE)-based rainfall erosivity. The black line is the interpolating line; the bold grey line denotes the 1 : 1 line; grey curves are 0.99 confidence limits of the interpolating line. (b) Monthly regime of severe convective events frequency estimated over 1957–2002 in Europe [58].

input property for rainfall erosivity models because the location, and then the climate zone, accommodates a broad range of conditions related to the occurrence of abundant and intense precipitation (e.g., [44]). We assumed that the exponent η may continuously vary with latitude and longitude, as a shape term to modulate the percentile statistic that pulls out seasonal rainfall erosivity between May and October. In the warm season, in fact, cumulonimbus can be accompanied by high rain variability and intensity, thus releasing a large amount of energy through sparse or localized short phenomena, generally with duration of 0.5 to 3 hours [45]. Considering the relatively low temporal resolution of the model (decadal and multidecadal timescales), adjusting the rainfall erosivity response for changes in elevation was not used in (1).

The performance of (1) was assessed against actual ((*R*)USLE)-based rainfall erosivity data from a set of sites and periods in mainland France [41]: Bennwihr (48.15 N, 7.32 E), 1966–1994; Brive-la-Gaillarde (45.15 N, 1.53 E), 1951–1970; Clermont-Ferrand (45.80 N, 3.10 E), 1951–1970; Dijon (47.30 N, 5.10 E), 1951–1970; Gap (44.57 N, 6.07), 1951–1970; Horbourg-Wihr (48.10 N, 7.40 E), 1951–1970; Hunspach (48.95 N, 7.95 E), 1976–1994; Montpellier (43.60 N., 3.90 E), 1961–1990; Orléans (47.90 N, 1.90 E), 1951–1970; Paris (48.80 N, 2.50 E), 1951–1970; Rennes (48.10 N, 1.69 W), 1951–1970; Rouen (49.40 N., 1.20 E), 1959–1988; Stenay (49.50 N, 5.20 E), 1950–2000; Toulouse (44.80 N, 0.70 W), 1951–1970; Valence (44.95 N, 4.90 E), 1951–1970. Overall, the mean absolute error was 91 MJ mm ha^{-1} h^{-1} y^{-1}, the modelling efficiency was equal to 0.98, and the regression line was in close proximity to the identity line (Figure 4(a)).

3.2. Temporal Analysis of Rainfall Erosivity with GIS. For the southwestern part of the basin (between Lyon and Montpellier) and for the period 1961–1990, Figure 5(a) shows the map of rainfall erosivity exceeding the threshold value of 1800 MJ mm h^{-1} ha^{-1} y^{-1}. The threshold 1800 MJ mm h^{-1} ha^{-1} y^{-1} was based upon two standard deviations added to the mean. This threshold does not reflect the maximum values of the rainfall erosivity found in some European stations (exceeding 2000 up to >6000 MJ mm h^{-1} ha^{-1} y^{-1} [46]) but is above the threshold values considered in previous studies (e.g., 1000 and 1500 MJ mm h^{-1} ha^{-1} y^{-1} [47]). When the period 1991–2010 was examined, erosivity exceeding 1800 MJ mm h^{-1} ha^{-1} y^{-1} extended until the eastern limits of the basin, the northern part not being affected (Figure 5(b)).

These phases generated an erosivity band crossing large southern lands of the Rhone region, plus main rainfall aggressiveness cells, among Aosta (Italy), Sion, and Geneva (Switzerland).

During the most recent phase of warming (1991–2010), new hydrological processes kicked off further power northwards, from the Mediterranean coast towards the inland areas. This suggests pulsing of extreme rainfall events that occurred over parts of the region. As shown in the work by Diodato et al. [48], an increase in extreme rainfall events in the Mediterranean region drives changes in rainfall erosivity and, in turn, an increased hazard in soil erosion and flash flooding usually more often occurring in relatively smaller catchments. These storminess and rainfall extremes are common in the fall season when they produce floods and flash floods, with the same regime as recorded by the FLASH European database [27].

3.3. Seasonal Hazard and Extreme Rainfall Events. To detect whether the rainfall power expands across the Rhone region depending on a particular season, we analysed the 95th

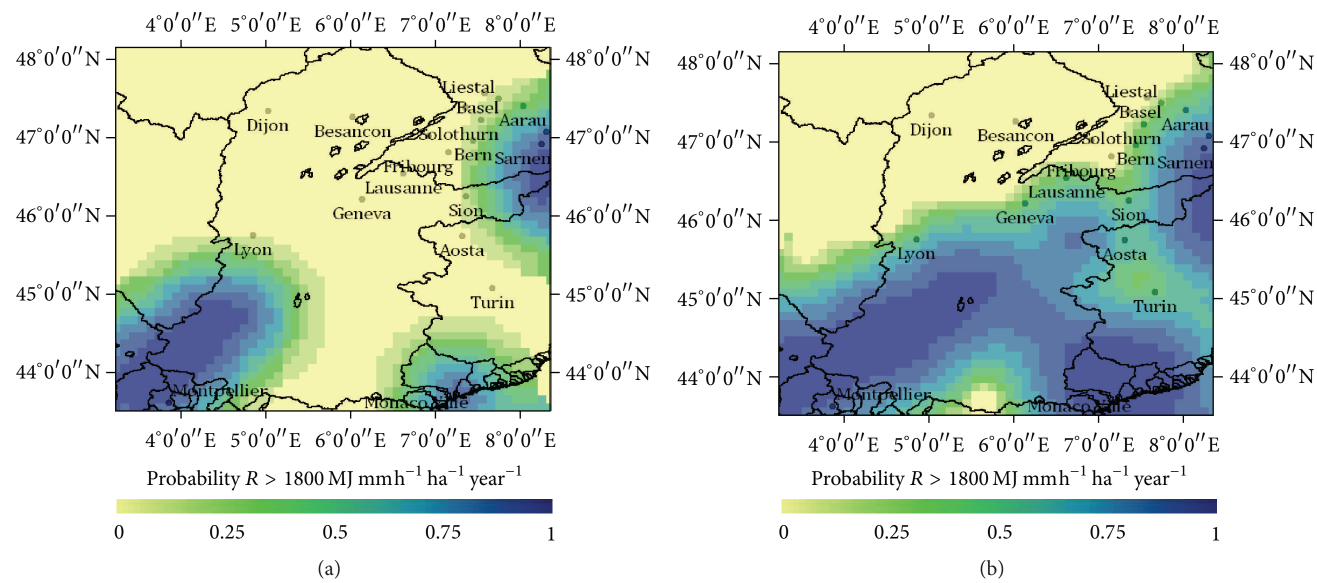

FIGURE 5: Indicator Kriging maps with probability that rainfall erosivity (R) exceeds 1800 MJ mm h^{-1} ha^{-1} y^{-1}, for the periods 1961–1990 (a) and 1991–2010 (b).

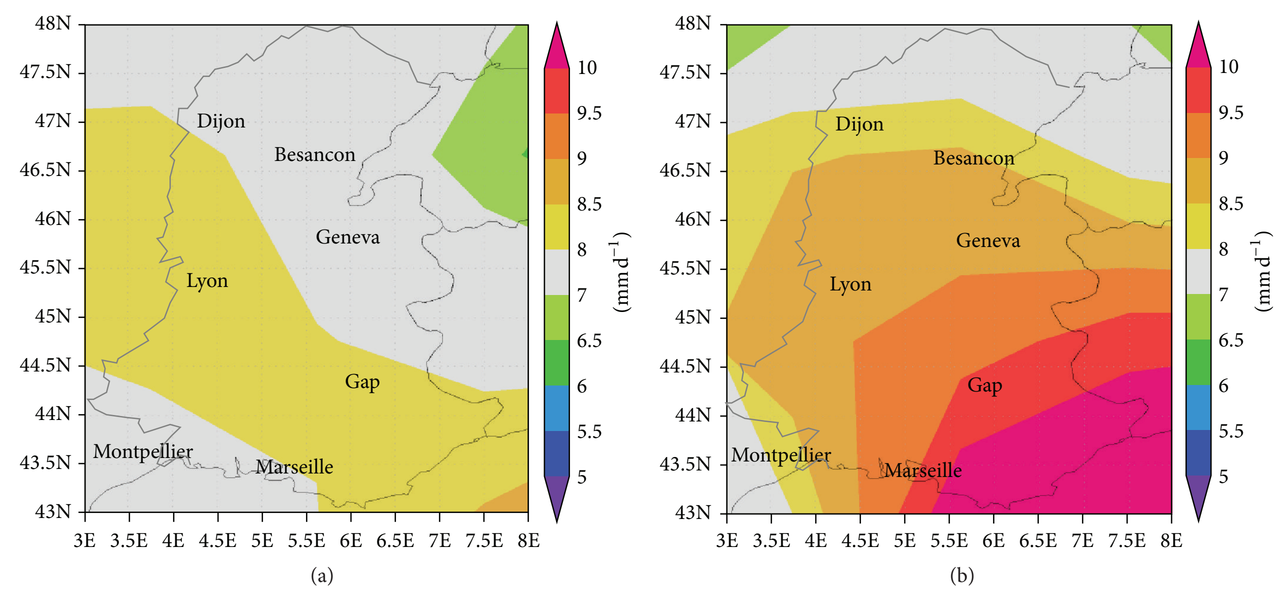

FIGURE 6: Spatial pattern of autumn daily rain rate 95th percentile across Rhone region for the periods 1951–1990 (a) and 1991–2013 (b). Data were arranged from NCEP/NCAR Reanalysis via Climate Explorer [57].

percentile of daily rain rate data from NCEP Reanalysis. It is therefore evident that autumn was the season with the highest rate of increase in the daily rainfall percentiles. This situation is clearly depicted in Figure 6 that compares the recent decades (1991–2013, Figure 6(b)) with the baseline climatology of the period 1951–1990 (Figure 6(a)). A remarkable increase in extreme rain rates in the past decades across the same area where rainfall erosivity was enhanced is worth noting (see Figure 5(b)).

Typically, the erosivity associated with the intensification of rain rates is the result of precipitations in the form of localized rainstorms (yet torrential), which are more frequent in summer and autumn. However, wet spring also brings additional runoff from rainfall but also provides antecedent conditions for summer flooding. In this case, not only heavy precipitation events but also moderate rain depths are of interest, because they provide favourable conditions (typical of local-scale storms) for floods occurring in heat period (June–October). For instance, the Cévennes-Vivarais region in the westernmost parts of the Rhone basin (on the border with the beginning of the Massif Central) has been especially affected by storms that caused floods on October 1995 [31].

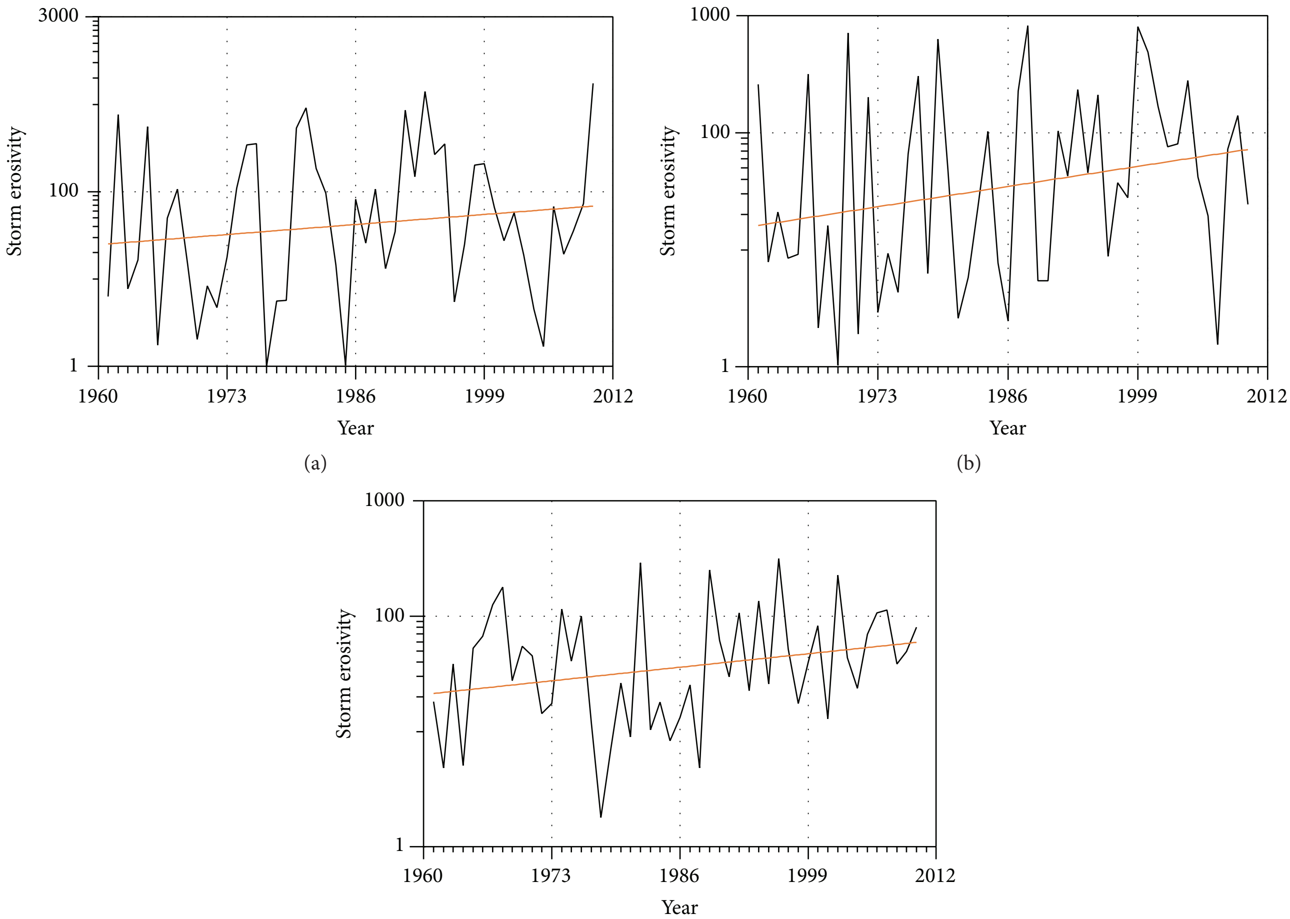

(a)

(b)

(c)

FIGURE 7: Temporal pattern of monthly storm erosivity at Lyon station for the months of September (a), October (b), and November (c) over the period 1961–2010, estimated with the model of Diodato [59]. Power trend with orange lines is also overlapped.

In the Aude (between the Massif Central and the eastern Pyrenees), during the flood event of 12-13 November 1999, the area receiving more than 200 mm in 48 hours extended more than 150 km in length and about 50 km in width [49]. The Gard precipitation event (8-9 September 2002) was an exceptional one due to the intensity of the event, with maximum precipitation around 600–700 mm in 24 hours (from 1200 UTC on 8 September) near Alès [49, 50]. This event released more than 7000 MJ mm h^{-1} ha^{-1} d^{-1} energy (i.e., three times more than in one mean year). These results show that sediment exports depend not only on the water flows but also on specific environmental factors [51, 52]: evidently, the Mediterranean climate with severe but short storms in summer and autumn leads to more significant peaks in sediment flux compared with the temperate oceanic climate basins where rainfall events are generally characterized by a lower intensity and a longer duration.

It was also estimated that the material flood damage recorded in the European continent in 2002 had been higher than in any single year before [21]. At the beginning of December 2003, one of the biggest floods over at least the previous 150 yrs. was recorded in the Rhone river [53]. This extreme rainfall event resulted in one of the century's most significant floods in the Aude region and produced remarkable flash floods in some catchments. Amongst them, small ungauged catchments are recognized as the most vulnerable to storms driven by high daily rain intensity [54].

In the months of September, October, and November, flash floods are expected to increase around Lyon, where storm erosivity is rising (Figures 7(a), 7(b), and 7(c)). September and November, however, present an increase in peaks too, whereas October is affected by a more complex temporal pattern (for this month, only mean values are reported to increase). From these results, it emerges that storminess has been increasing in the recent warming period as caused by more frequent intensive autumnal storms. This is in line with the findings of Meusburger et al. [55] in Switzerland, where in recent times the monthly rainfall erosivity has been significantly increasing in the months between May to October.

4. Conclusions

Hydrological forcing and climate processes are known to lead to complex responses in river basins. For the Rhone basin, characteristic of French Mediterranean and Alpine environments, this work has analyzed a rainfall erosivity simulation as obtained with mesoscale indicator geostatistics-based empirical model. This was done in an attempt to understand the sensitivity of the basin response (rainfall erosivity) to storminess (disturbing force) and to detect its temporal variability. The model allowed assessing erosivity changes at interdecadal time scales and revealed that the long-term trend is increasing. Since increased rainfall variability in response to climate change is a possibility in many regions, the effects of potential changes need to be addressed in the perspective of adapting to climate change. This is of considerable interest at present as the need to assess the impact of real or perceived climate change is vital in order to take correct environmental actions.

Conflict of Interests

The authors declare that there is no conflict of interests regarding the publication of this paper.

References

[1] C. Kosmas, M. Kirkby, and N. Geeson, *The Medalus Project: Mediterranean Desertification and Land Use*, European Union, Brussels, Belgium, 1999.

[2] H. A. Viles and A. S. Goudie, "Interannual, decadal and multidecadal scale climatic variability and geomorphology," *Earth-Science Reviews*, vol. 61, no. 1-2, pp. 105–131, 2003.

[3] N. Diodato, M. Ceccarelli, and G. Bellocchi, "Decadal and century-long changes in the reconstruction of erosive rainfall anomalies in a mediterranean fluvial basin," *Earth Surface Processes and Landforms*, vol. 33, no. 13, pp. 2078–2093, 2008.

[4] T. Swierczynski, A. Brauer, and S. Lauterbach, "A 1600 yr seasonally resolved record of decadal-scale flood variability from the Austrian Pre-Alps," *Geology*, vol. 40, pp. 1047–1050, 2012.

[5] B.-T. Pan, H.-P. Geng, X.-F. Hu, R.-H. Sun, and C. Wang, "The topographic controls on the decadal-scale erosion rates in Qilian Shan Mountains, N.W. China," *Earth and Planetary Science Letters*, vol. 292, no. 1-2, pp. 148–157, 2010.

[6] M. A. Palecki, J. R. Angel, and S. E. Hollinger, "Storm precipitation in the United States. Part I. Meteorological characteristics," *Journal of Applied Meteorology*, vol. 44, no. 6, pp. 933–946, 2005.

[7] M. Mulligan, "Modelling the geomorphological impact of climatic variability and extreme events in a semi-arid environment," *Geomorphology*, vol. 24, no. 1, pp. 59–78, 1998.

[8] J. M. Hooke and J. M. Mant, "Geomorphological impacts of a flood event on ephemeral channels in SE Spain," *Geomorphology*, vol. 34, no. 3-4, pp. 163–180, 2000.

[9] P. D'Odorico, J. Yoo, and T. M. Over, "An assessment of ENSO-induced patterns of rainfall erosivity in the Southwestern United States," *Journal of Climate*, vol. 14, no. 21, pp. 4230–4242, 2001.

[10] R. Coppus and A. C. Imeson, "Extreme events controlling erosion and sediment transport in a semi-arid sub-Andean valley," *Earth Surface Processes and Landforms*, vol. 27, no. 13, pp. 1365–1375, 2002.

[11] M. C. Ramos and M. Mulligan, "Impacts of climate variability and extreme events on soil hydrological processes," *Geophysical Research*, vol. 5, pp. 92–115, 2003.

[12] D. R. Easterling, G. A. Meehl, C. Parmesan, S. A. Changnon, T. R. Karl, and L. O. Mearns, "Climate extremes: observations, modeling, and impacts," *Science*, vol. 289, no. 5487, pp. 2068–2074, 2000.

[13] K. E. Trenberth, A. Dai, R. M. Rasmussen, and D. B. Parsons, "The changing character of precipitation," *Bulletin of the American Meteorological Society*, vol. 84, no. 9, pp. 1205–1161, 2003.

[14] J. P. Nunes and M. A. Nearing, "Modelling impacts of climatic change," in *Handbook of Erosion Modelling*, pp. 289–312, Wiley-Blackwell, Oxford, UK, 2011.

[15] R. G. Jones, M. Noguer, D. C. Hassell et al., *Generating High Resolution Climate Change Scenarios Using PRECIS*, Met Office Hadley Centre, Exeter, UK, 2004.

[16] S. Curtis, T. W. Crawford, and S. A. Lecce, "A comparison of TRMM to other basin-scale estimates of rainfall during the 1999 Hurricane Floyd flood," *Natural Hazards*, vol. 43, no. 2, pp. 187–198, 2007.

[17] P. Zhai, X. Zhang, H. Wan, and X. Pan, "Trends in total precipitation and frequency of daily precipitation extremes over China," *Journal of Climate*, vol. 18, no. 7, pp. 1096–1108, 2005.

[18] S. Beguería and S. M. Vicente-Serrano, "Mapping the hazard of extreme rainfall by peaks-over-threshold extreme value analysis and spatial regression techniques," *Journal of Applied Meteorology and Climatology*, vol. 45, no. 1, pp. 108–124, 2006.

[19] S. K. Aryal, B. C. Bate, E. P. Campbell, Y. Li, M. J. Palmer, and N. R. Viney, "Characterizing and modeling temporal and spatial trends in rainfall extremes," *Journal of Hydrometeorology*, vol. 10, no. 1, pp. 241–253, 2009.

[20] E. J. Becker, E. H. Berbery, and R. W. Higgins, "Understanding the characteristics of daily precipitation over the United States using the north American regional reanalysis," *Journal of Climate*, vol. 22, no. 23, pp. 6268–6286, 2009.

[21] Z. W. Kundzewicz, "Is the frequency and intensity of flooding changing in Europe?" in *Extreme Weather Events and Public Health Responses*, pp. 25–32, Springer, Berlin, Germany, 2005.

[22] J.-M. Olivier, G. Carrel, N. Lamouroux et al., "The Rhône river basin," in *Rivers of Europe*, pp. 247–296, Academic Press, London, UK, 2009.

[23] S. M. Jessup and A. T. DeGaetano, "A statistical comparison of the properties of flash flooding and nonflooding precipitation events in portions of New York and Pennsylvania," *Weather and Forecasting*, vol. 23, no. 1, pp. 114–130, 2008.

[24] S. Anquetin, F. Miniscloux, J. D. Creutin, S. Cosma, and S. Anquetin, "Numerical simulation of orographic rain," *Journal of Geophysical Research*, vol. 108, p. 8386, 2003.

[25] V. Ducrocq, D. Ricard, J.-P. Lafore, and F. Orain, "Storm-scale numerical rainfall prediction for five precipitating events over France—on the importance of the initial humidity field," *Weather and Forecasting*, vol. 17, no. 6, pp. 1236–1256, 2002.

[26] E. Gaume, V. Bain, P. Bernardara et al., "A compilation of data on European flash floods," *Journal of Hydrology*, vol. 367, no. 1-2, pp. 70–78, 2009.

[27] M. C. Llasat, M. Llasat-Botija, M. A. Prat et al., "High-impact floods and flash floods in Mediterranean countries: the FLASH preliminary database," *Advances in Geosciences*, vol. 23, pp. 47–55, 2010.

[28] J.-P. Bravard, "Impacts of climate change on the management of upland waters: the Rhone river case," in *Proceedings of the 5th Biennial Rosenberg International Forum on Water Policy*, Banff, Canada, September 2006.

[29] G. Arnaud-Fassetta, L. Astrade, E. Bardou et al., "Fluvial geomorphology and flood-risk management," *Géomorphologie: Relief, Processus, Environnement*, vol. 2, pp. 109–128, 2009.

[30] N. Diodato and G. Bellocchi, "Multiscale modelling of rainstorm-induced historical intermediate floods (June-November) in the Rhone River Basin," *Natural Hazards*, vol. 65, no. 3, pp. 1465–1479, 2013.

[31] G. Delrieu, V. Ducrocq, E. Gaume et al., "The catastrophic flash-flood event of 8-9 September 2002 in the Gard Region, France: a first case study for the Cévennes-Vivarais Mediterranean hydrometeorological observatory," *Journal of Hydrometeorology*, vol. 6, no. 1, pp. 34–52, 2005.

[32] K. Tockner, V. Bremerich, and I. Jentschke, "European map of the spatial extent and environmental state of riverine flood-plains and deltaic areas," in *Deliverable 4.14 of the EU-FP7 Project REFRESH—Adaptive Strategies to Mitigate the Impacts of Climate Change on European Freshwater Ecosystems*, 2014, http://www.refresh.ucl.ac.uk/webfm_send/2410.

[33] A. Houston, "The Rhone river region," Transboundary Waters, 2012, http://www.caee.utexas.edu/prof/mckinney/ce397/Topics/Rhone/Rhone%282012%29.pdf.

[34] J. Parajka, S. Kohnová, G. Bálint et al., "Seasonal characteristics of flood regimes across the Alpine-Carpathian range," *Journal of Hydrology*, vol. 394, no. 1-2, pp. 78–89, 2010.

[35] A. E. Harding, J. Palutikof, and T. Holt, "The climate system," in *The physical geography of the Mediterranean*, pp. 69–88, Oxford University Press, Oxford, UK, 2009.

[36] V. Homar, A. Jansà, J. Campins, A. Genovês, and C. Ramis, "Towards a systematic climatology of sensitivities of Mediterranean high impact weather: a contribution based on intense cyclones," *Natural Hazards and Earth System Science*, vol. 7, no. 4, pp. 445–454, 2007.

[37] K. Tolika, P. Maheras, M. Vafiadis, H. A. Flocas, and A. Arseni-Papadimitriou, "Simulation of seasonal precipitation and raindays over Greece: a statistical downscaling technique based on artificial neural networks (ANNs)," *International Journal of Climatology*, vol. 27, no. 7, pp. 861–881, 2007.

[38] G. Bellocchi and N. Diodato, "Storm-erosivity model for addressing hydrological effectiveness in France," in *Storminess and Environmental Change*, vol. 39 of *Advances in Natural and Technological Hazards Research*, pp. 131–147, Springer, Dordrecht, The Netherlands, 2014.

[39] A. Barrera, M. Barriendos, and M. C. Llasat, "Extreme flash floods in Barcelona County," *Advances in Geosciences*, vol. 2, pp. 111–116, 2005.

[40] N. Diodato and G. Bellocchi, "Decadal modelling of rainfall-runoff erosivity in the Euro-Mediterranean region using extreme precipitation indices," *Global and Planetary Change*, vol. 86-87, pp. 79–91, 2012.

[41] G. Bellocchi and N. Diodato, "Storm-erosivity model for addressing hydrological effectiveness in France," in *Storminess and Environmental Change*, pp. 131–147, Springer, Dordrecht, The Netherlands, 2014.

[42] K. Johnston, J. M. Ver Hoef, K. Krivoruchko, and N. Lucas, *Using ArcGis Geostatistical Analyst*, ESRI, New York, NY, USA, 2001.

[43] C. V. Deutsch and A. G. Journel, *GSLIB: Geostatistical Software Library and User's Guide*, Oxford University Press, New York, NY, USA, 2nd edition, 1998.

[44] N. Diodato and G. Bellocchi, "MedREM, a rainfall erosivity model for the Mediterranean region," *Journal of Hydrology*, vol. 387, no. 1-2, pp. 119–127, 2010.

[45] R. Twardosz, "Diurnal variation of precipitation frequency in the warm half of the year according to circulation types in Kraków, South Poland," *Theoretical and Applied Climatology*, vol. 89, no. 3-4, pp. 229–238, 2007.

[46] P. Panagos, C. Ballabio, P. Borrelli et al., "Rainfall erosivity in Europe," *Science of the Total Environment*, vol. 511, pp. 801–814, 2015.

[47] N. Diodato and C. Bosco, "Spatial pattern probabilities exceeding critical threshold of annual mean storm-erosivity in Euro-Mediterranean areas," in *Storminess and Environmental Change*, pp. 79–99, Springer, Dordrecht, The Netherlands, 2014.

[48] N. Diodato, G. Bellocchi, N. Romano, and G. B. Chirico, "How the aggressiveness of rainfalls in the Mediterranean lands is enhanced by climate change," *Climatic Change*, vol. 108, no. 3, pp. 591–599, 2011.

[49] O. Nuissier, V. Ducrocq, D. Ricard, C. Lebeaupin, and S. Anquetin, "A numerical study of three catastrophic precipitating events over southern France. I: numerical framework and synoptic ingredients," *Quarterly Journal of the Royal Meteorological Society*, vol. 134, no. 630, pp. 111–130, 2008.

[50] F. Vinet, "Geographical analysis of damage due to flash floods in southern France: the cases of 12-13 November 1999 and 8-9 September 2002," *Applied Geography*, vol. 28, no. 4, pp. 323–336, 2008.

[51] M. I. Vousdoukas, R. Verney, F. Dufois et al., "Sediment dynamics in the Bay of Marseille, Gulf of Lions (France): hydrodynamic forcing vs. bed erodibility," *Journal of Coastal Research*, vol. 27, no. 5, pp. 942–958, 2011.

[52] M. Delmas, O. Cerdan, B. Cheviron, J.-M. Mouchel, and F. Eyrolle, "Sediment export from French rivers to the sea," *Earth Surface Processes and Landforms*, vol. 37, no. 7, pp. 754–762, 2012.

[53] C. Antonelli, F. Eyrolle, B. Rolland, M. Provansal, and F. Sabatier, "Suspended sediment and *137*Cs fluxes during the exceptional December 2003 flood in the Rhone River, southeast France," *Geomorphology*, vol. 95, no. 3-4, pp. 350–360, 2008.

[54] I. Braud, S. Anquetin, H. Roux et al., "A regional distributed hydrological modelling approach for flash-flood understanding and experimental design," in *Proceedings of the 7th EGU General Assembly*, pp. 51–54, Vienna, Austria, May 2010.

[55] K. Meusburger, A. Steel, P. Panagos, L. Montanarella, and C. Alewell, "Spatial and temporal variability of rainfall erosivity factor for Switzerland," *Hydrology and Earth System Sciences*, vol. 16, no. 1, pp. 167–177, 2012.

[56] V. Naipal, C. Reick, J. Pongratz, and K. Van Oost, "Improving the global applicability of the RUSLE model—adjustment of the topographical and rainfall erosivity factors," *Geoscientific Model Development Discussions*, vol. 8, no. 3, pp. 2991–3035, 2015.

[57] G. J. van Oldenborgh, S. Drijfhout, A. van Ulden et al., "Western Europe is warming much faster than expected," *Climate of the Past*, vol. 5, no. 1, pp. 1–12, 2009.

[58] R. Romero, J. A. Guijarro, C. Ramis, and S. Alonso, "A 30-year (1964–1993) daily rainfall data base for the spanish mediterranean regions: first exploratory study," *International Journal of Climatology*, vol. 18, no. 5, pp. 541–560, 1998.

[59] N. Diodato, "Predicting RUSLE (Revised Universal Soil Loss Equation) monthly erosivity index from readily available rainfall data in Mediterranean area," *The Environmentalist*, vol. 26, no. 1, pp. 63–70, 2006.

Hindawi Publishing Corporation
Advances in Meteorology
Volume 2016, Article ID 1393241, 9 pages
http://dx.doi.org/10.1155/2016/1393241

Research Article

Variability of Hydrological Parameters and Water Balance Components in Small Catchment in Croatia

Lidija Tadić,[1] Tamara Dadić,[1] and Marija Leko-Kos[2]

[1] *Faculty of Civil Engineering, University of Osijek, Crkvena 21, 31000 Osijek, Croatia*
[2] *SIRRAH-PROJEKT, Ribarska 4, 31000 Osijek, Croatia*

Correspondence should be addressed to Lidija Tadić; ltadic@gfos.hr

Received 2 October 2015; Accepted 29 November 2015

Academic Editor: Milan Gocic

Analysis of small catchment area in Croatian lowland with its hydrological characteristics in the period between 1981 and 2014 was carried out in order to define significance of change in hydrological and meteorological parameters (precipitation, air temperatures, and discharges) and water balance components (deep percolation and potential evapotranspiration). There was no significant land use change in the observed period, so all changes in hydrological processes can be considered to be without human impact in the last 35 years. Application of RAPS (Rescaled Adjusted Partial Sums) on all data series distinguished two subperiods with different length but the same behaviour. The first subperiod was a period characterised by the decrease, starting in 1980 and finishing between 1991 and 1995, while the second one was a period characterised by the increase of parameters in all analyses, starting between 1991 and 1995 and finishing in 2001. In comparison to the analysis of climate change impacts per decade, this approach is much more appropriate and gives insight into variations throughout the entire observed period. The most variable but not significant parameters are precipitation and discharges, especially in the second subperiod which has a major impact on occurrence of hydrological hazards such as droughts and floods and makes great pressure and responsibility on water management system.

1. Introduction

Climate and human induced changes on catchment hydrological processes are major concerns for scientists, water decision-makers, and politicians. Different scenarios of climate change and its impact on water balance directly and on ecological, chemical, and geomorphological processes indirectly are the main issues of many studies in the last ten years all over the world. Most of them were dealing with different climate scenarios and their impact on global ecosystem, water management, or economy. Global modelling with simulating global water cycle and in that context analysing hydrological extremes and water balance components is the most common approach, as Corzo Perez et al. stated [1]. Droughts are global hydrological phenomena found to increase in duration, area, and severity, according to Lloyd-Hughes et al. [2]. But validation of global models had to be done by observations on smaller scale, on the number of catchment areas of different characteristics, as it was studied by Stahl et al. [3], Gudmundsson et al. [4], and Prudhomme et al. [5]. For example, research of 44 catchments made by Van Loon and Laaha [6] and based on long data series in Austria proved that droughts are strongly governed by combination of climate characteristics, increase of temperature and change of precipitation pattern, and catchment control. One of the most important climate elements is precipitation, strongly affecting water balance and quality of water resources. There are many uncertainties in prediction of precipitation amount, intensity, and seasonal and spatial distribution in the future, presented by De Luis et al. [7], Orlowsky and Seneviratne [8], and Nunes and Lourenço [9]. In the report of IPCC-2007 [10], there is an increase of precipitation in the period 1900–2005 north of the 30° latitude, but it is also stressed that regional and subregional variabilities are frequent and must be carefully analysed. In Northern Germany, a significant precipitation increase and consequently discharge are expected in the coming decades, starting around 2030 with the assumption that all natural features remain stable, apart from climate [11]. There are several scenarios which predict climate change impacts on water resources and water balance components over different regions and throughout all seasons. Spatial distribution of much affected areas is relatively well described, according to authors Blöschl and Sivapalan [12] and Kundzewicz et al. [13]. At the seasonal to interannual timescale, the influence of climate variability on hydrological data (and the occurrence of extreme hydrological events such as floods and droughts) is less recognized. These influences can generate seasonal distortions in the statistical data of hydrological variables, thus threatening the validity of the operational rules applied to water management systems. There is also increasing awareness that the strength of important fluctuations in the global climate may vary at the decadal timescale. Moreover, model studies suggest and observational evidence confirms that an intensified hydrological cycle is likely to be an important consequence of global climate change [14]. However, relationship between physical characteristics and temporary trends of annual precipitation, potential evapotranspiration, and runoff is very important and unique for each catchment area [15]. Future climate scenarios predict higher evapotranspiration rates, lower discharge rates, and groundwater levels. It means that, in the mostly agricultural areas, irrigation rates will increase, but the water resources could be questionable [16]. As a consequence, serious water scarcity could be expected on the regional levels, meso and macro scale [17]. Most researches are oriented to the large river basins (macro scale), but small catchment areas (meso and micro scale) seem to be more vulnerable. By definition of Sivapalan et al. [14], these are fundamental landscape units for the water cycle, sediment, and dissolved geochemical and biogeochemical constituents. As such, they integrate all aspects of the hydrological cycle (surface water, runoff, evapotranspiration, groundwater, etc.) within a defined area that can be studied, quantified, and acted upon. The hydrological processes develop faster; increasing of urbanization and other land uses and land cover change have more significant influence on the landscape and environment. Relationship between soil moisture and temperature and soil moisture and precipitation and their possible modification with climate change can have a tremendous impact on water balance [18]. Huntington [19] wrote that potential acceleration of hydrological cycle under recent and future global warming is of considerable interest in terms of changes and regional variability and extremes. According to the analysis of small catchments made by Tesaŕ et al. [20] and Varis et al. [21], small catchments are very vulnerable from the hydrological point of view. Their size is the main characteristic which defines their hydrological features and water balance in general. Large catchments with areas exceeding 1000 km^2 have well defined relationship between the actual discharge in the closing profile and the total precipitation for a given antecedent period. Gradually, it became evident that models conceived in this way are unable to describe the reality of runoff formation from small catchments with areas up to 100 km^2. Their topographical characteristics, vegetation cover, shape and slope of the catchment, and density of watercourse network have a strong influence on hydrological and geochemical processes. As a result, soil moisture and water balance patterns are very patchy, leading to large spatial variations in evapotranspiration and stream discharge as stated by Ruch and Harum, [22]. Human activities in the form of settlements, infrastructure, and hydraulic structures also have significant impacts on the small scale, even more pronounced than on a large scale [23]. Besides, small catchments usually have shorter series of data records and level of their certainty is much lower, which also could be one of the reasons why small catchments are less described from the hydrological point of view [24]. Another problem is definition of small catchment; generally, catchment areas smaller than 100 km^2 are considered to be small, but there is another approach which defines small catchment as an area with stable and uniform hydrological characteristics and the actual area is not important as much as uniformity of hydrological processes over the catchment area [12].

Most of the previous investigations have been carried out on a macro scale, on the national or regional level. Territory of Croatia belongs to the transitional area between Northern Europe with weak positive trend of annual precipitation amounts in the continental part of the country and drying Mediterranean with more pronounced seasonal trends [25]. Potentially, human induced changes and interaction with natural characteristics of terrain, soil, land cover, and meteorological parameters yield specific and unique hydrological characteristics which might have a great influence on water management. In macro scale, it is very difficult to separate influences induced by human activities from climate change impacts, but in small catchment areas it could be possible. This paper is going to present changes in hydrological parameters on small catchment area in Croatian lowland with no significant human interventions, so all potential changes in hydrological processes must be related to climate change.

2. Materials and Methods

2.1. Study Area. Catchment area of Karašica and Vučica Rivers is located in Danube River basin, part of the Drava River catchment, and its location in the Croatian lowland together with meteorological and hydrological stations and groundwater observation wells relevant for the research area is given in Figure 1. It is small catchment with two different parts. The larger part is typical lowland with altitude between 85 and 125 m a.s.l. (Figure 2(a)). The lowest point is at the mouth of Vučica River into the Drava River. Most of the terrain is higher than the maximum water level of the Drava River, so the area is not affected by high Drava River water levels. The vegetation cover mostly consists of agricultural land, pastures, and forests. Hilly part of the catchment is situated on the southern part, with the altitudes between 125 and 953 m a.s.l. Hilly part is covered by forest, orchards, and vineyards and takes about one-third of the total area. There are many smaller brooks that during high water levels contribute to the discharge of major rivers and cause floods. The whole catchment area has very dense network of natural and artificial watercourses constructed in the last 150 years. Their main purpose was, and still is, flood protection and land drainage studied by Tadić et al. [26].

Table 1: Characteristics of meteorological and hydrological stations.

Meteorological stations		
Name	Elevation (m a.s.l.)	Period of observations
Donji Miholjac	97.00	1981–2014
Valpovo	91.00	1981–2014
Našice	144.00	1981–2014
Slatina	144.00	1981–2014
Orahovica	180.00	1991–2014*

Hydrological stations				
River/station	Location	Distance from the mouth (km)	Catchment area (km^2)	Period of observation
Karašica/Kapelna	45°42′35″	33 + 010	388.8	1987–2012
Vučica/Orahovica	45°32′29″	74 + 950	42.6	1987–2012
Vučica/Beničanci	45°36′47″	48 + 500	750.5	1987–2012

*Only precipitation data.

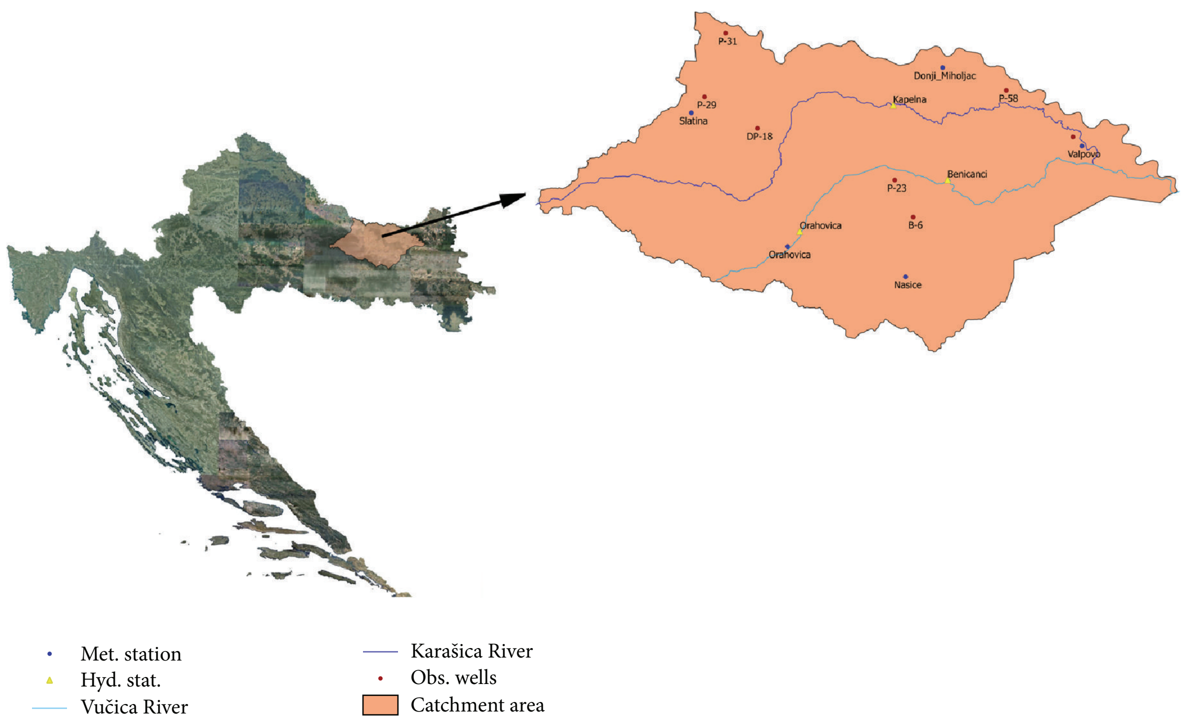

Figure 1: Catchment area with meteorological and hydrological stations.

2.2. Hydrological and Meteorological Characteristics. Data used in the analysis includes monthly and annual precipitation, mean monthly and mean annual precipitation, monthly groundwater levels, and monthly discharges of Karašica and Vučica Rivers. In Table 1, the main characteristics of meteorological and hydrological stations are given.

The catchment of Karašica and Vučica Rivers can be considered as very stable area according to land use change which is important for further analysis; therefore, all other changes in hydrological parameters and processes in the observed period are consequence of climate change. Changes in land use on catchment area were analysed based on Corine Land Cover data which is digital database including changes in land cover and land use for the Republic of Croatia in the period from 1981 to 2012 (Figure 2(b)). There are five different datasets between 1980 and 2012. In this period, change appeared on 13.000 ha but most of it was from unirrigated arable land to irrigable land and from areas of natural vegetation to forest. In total, about 16% of the catchment area land cover has changed, but without significance [27]. It is very important because land use change has significant influence on hydrological processes. For example, Wang et al. [28] and Amirabadizadeh et al. [29] investigated a major influence of land use change, urbanization, and industrialization on water balance change. Data series of monthly and annual precipitation amounts and the mean monthly and annual air temperature are observed on the five meteorological stations in the period between 1981

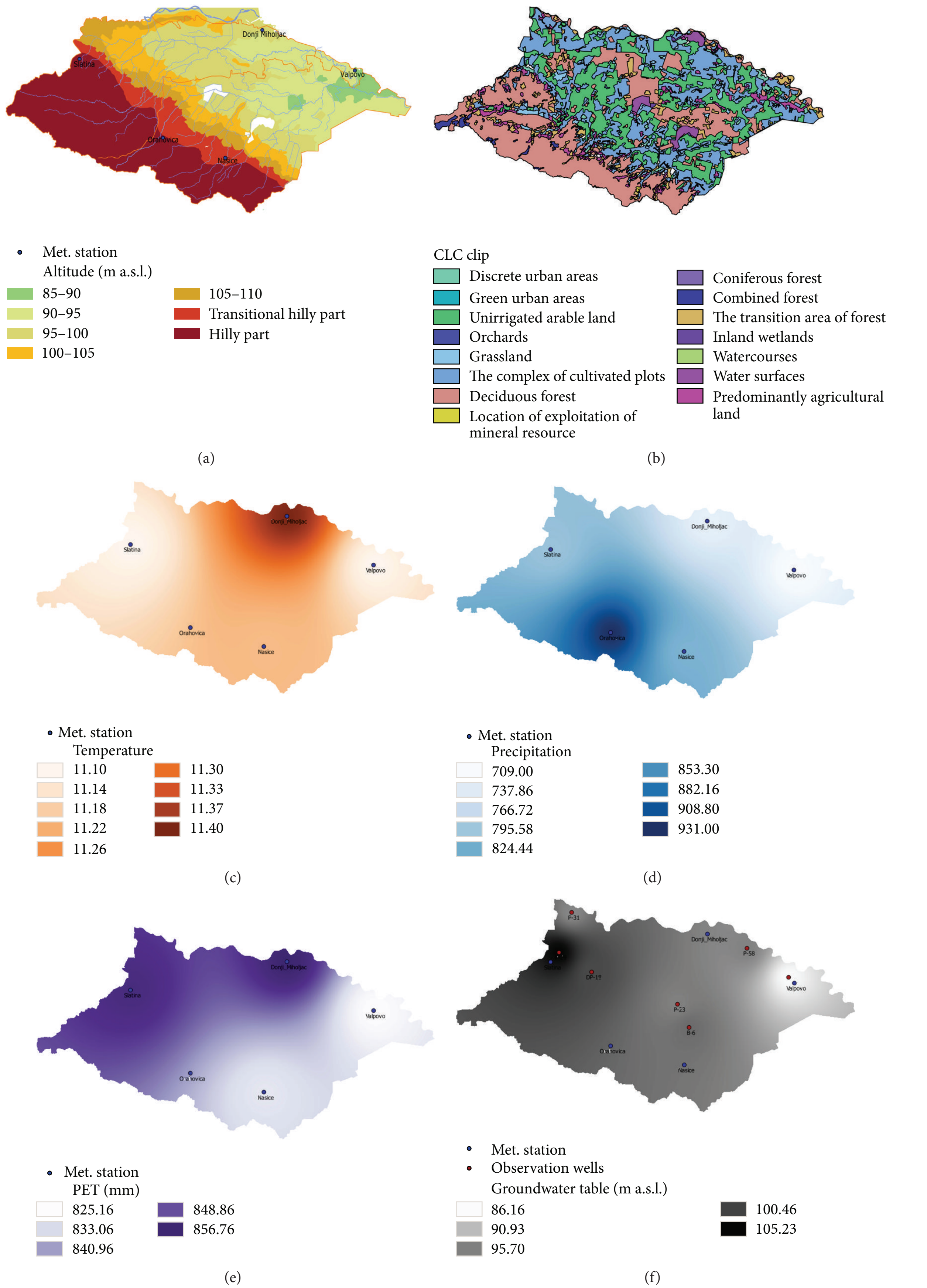

Figure 2: (a) Altitude map of the catchment area, (b) land use map, (c) mean air temperature distribution, (d) annual precipitation distribution, (e) annual potential evapotranspiration distribution, and (f) mean groundwater level.

and 2014. Annual precipitation varies between 710 mm in the lower part and 816 mm in the hilly part of the catchment (Figure 2(d)). Mean annual groundwater level is presented in Figure 2(f), and it is approximately 3.0 m below soil surface. Figures 2(c) and 2(e) present mean air temperature distribution and mean annual potential evapotranspiration. Potential evapotranspiration was calculated by Hargreaves and Samani (HS) [30] equation:

$$\mathrm{ETo} = 0.0135\,\mathrm{Rs}\,(T + 17.8)\,, \tag{1}$$

where Rs is expressed in units of water evaporation in mm/day and T in °C. According to Trajković [31] who studied the HS equation in seven locations in continental Europe, including Croatia, with different altitudes (42–433 m a.s.l.) with RH ranging from 55 to 71%, it is considered to be applicable for the study area.

2.3. Methodology with the Description of RAPS and SPI. In order to demonstrate trends in hydrological parameters and water balance components, RAPS (Rescaled Adjusted Partial Sums) method was used. Random changes, errors, and variability in the analysed time series were overcome with this method. The observed period with this method is divided into several subperiods, based on calculated F-test and t-test at level $p < 0.05$. RAPS are calculated by expression [32, 33]

$$\mathrm{RAPS}_k = \sum_{t=1}^{k} \frac{Y_t - \overline{Y}}{S_y}, \tag{2}$$

where $\overline{Y}$ is the mean value of observed time series; S is the standard deviation; Y_t is the observed parameter (in this case maximum annual discharge and water level in year t); k is the total number of observed years.

Variations of analysed parameters are calculated as a ratio of standard deviation and average value for subject period.

Drought analysis was made by Standardised Precipitation Index (SPI), the method most frequently used in all parts of the world, regardless of climatic or topographical features. The basic advantage of this method lies in the fact that it necessitates only a set of precipitation data for a longer period of time (30 or more years) and that it can be used at various timescales, the most frequent ones being 1, 3, 6, 12, and 24 months. The SPI has defined limit values dependent on the relative frequency; according to McKee et al. [34], a positive SPI points to a greater quantity of precipitation with respect to the mean multiyear value, while a negative SPI is an indication of lower precipitation compared to mean value.

3. Results and Discussion

In Croatia, which is in the transitional zone, precipitation increase can be expected in the future (Perčec Tadić et al. [35]), but in the observed period (1981–2014) there is no increasing trend in annual precipitation according to the records from five meteorological stations (Figure 3). Annual precipitation and mean air temperature were analysed on five meteorological stations in the period between 1981 and 2014 which is presented in Figure 3.

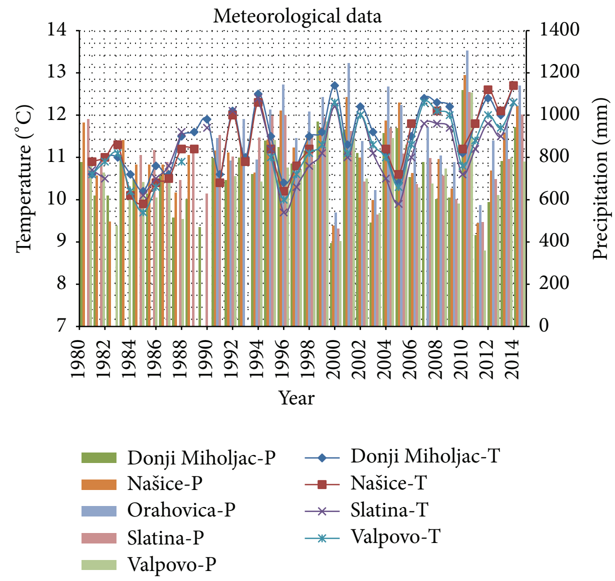

Figure 3: Annual precipitation and mean air temperature.

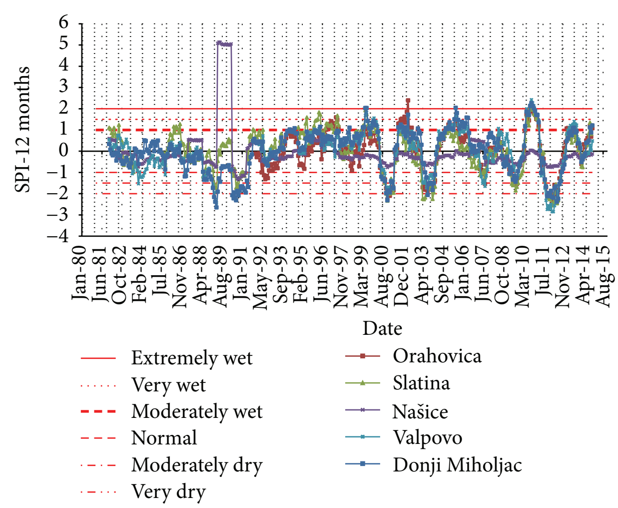

Figure 4: Mean annual SPI for all meteorological stations.

The study area is characterized by extreme hydrological events, droughts, and floods which occur frequently causing great damage. Previous research proved that the most severe droughts have occurred in 2000, 2003, and 2011 in the continental part of Croatia [36].

Annual SPI values did not show any trend (R^2 = 0.0004–0.0032) during the observed period which can be seen in Figure 4, but greater variability can be recognized in the beginning of the 21st century.

Hydrographs of characteristic annual discharges of Karašica and Vučica Rivers are presented in Figure 5. There is no significant trend in maximum, minimum, or mean annual discharges in the period 1981–2012 (R^2 = 0.0008–0.0115).

Floods are another type of extreme hydrological events which are more frequent in the last decades. Similar to the droughts, they also cause great damage to water management,

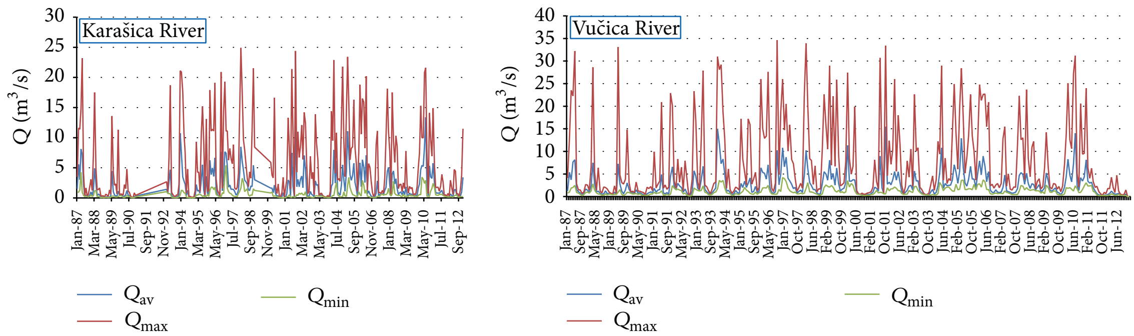

(a) (b)

Figure 5: Characteristic discharges of the Karašica River (a) and the Vučica River (b).

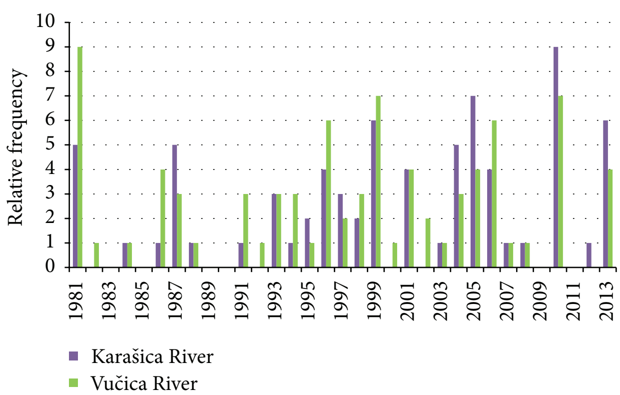

Figure 6: Flood events on the Karašica and Vučica Rivers in the period 1981–2012.

agriculture, and ecosystems. In the observed period between 1981 and 2012, floods have occurred several times (Figure 6).

Spatial distribution of annual groundwater level is presented in Figure 2(b).

Previously described hydrological and meteorological parameters and water balance components did not show any specific trend during the observed period, but there are visible variations in the last decade. Those variations were analysed in more detail in order to achieve a better understanding of hydrological processes in the catchment.

3.1. Precipitation and Air Temperatures. As it was presented previously, there is no increasing precipitation trend in the study area. The application of RAPS on the monthly precipitation data distinguished subperiods with various lengths. The first subperiod, 11 years long, is characterized by decrease of precipitation ending between April 1991 in lower part of the catchment and September 1992 in the hilly part. In the second subperiod, monthly precipitation is increasing (Figure 7(a)). Only in Slatina station are there 3 subperiods; the third one started in December 1999.

The variability of precipitation is one of the predictions of climate change [37] and in the analysed area it is obvious in the observed period even if it is relatively short. Large precipitation variability is beside the amount, main cause of vulnerability to droughts and floods, with a tremendous impact on agriculture, ecosystem, and water management. However, RAPS method applied on annual air temperatures shows more significant change during the whole observed period and subperiods as well. In two meteorological stations, the first subperiod lasted until 1997 and 1998, respectively, with decreasing air temperature trend and the second subperiod with an increasing trend. On the station Našice the breaking point is year 2005, and on meteorological station Slatina there are not any significant changes in the air temperature (Figure 7(b)). These results prove previous conclusions about an average increase of 0.84°C in the period of 50 years or longer obtained on 26 stations in Croatia reached by Bonacci [38].

Calculation of coefficients of variation (CV) of precipitation for these two subperiods and testing of their significance show variations but without statistical significance (0.56–0.62 in the second subperiod, while in the first period significance was between 0.62 and 0.64). Difference of mean air temperatures between the recognized two subperiods is about 1°C. Comparing to the precipitation variability, air temperature coefficients of variation are much smaller and their values are between 0.043 and 0.058.

The same procedure was applied on discharges, groundwater levels, and potential evapotranspiration. RAPS method distinguished two subperiods in each data series but with different duration. Research of Rasouli et al. [39] proved high sensitivity of stream flow to changes in the whole range of hydrological processes in the basin, with particular regard to precipitation. Besides, in relation to extreme fluctuations in precipitation and impact of natural characteristics as far as human activities, water management practice is becoming complex and unreliable. Hydraulic structures are constructed in order to fulfil their purposes including flood protection, irrigation water uptake, and drainage, and their operation in the different conditions makes them unreliable [13]. Their possible adaptation to present and even more significant changes in the future has a lot of uncertainties because there is no accurate projection of future hydrological processes. Most of the research obtained opposite trends of discharges, strongly influenced by natural characteristics of the catchment and their significant variability [40].

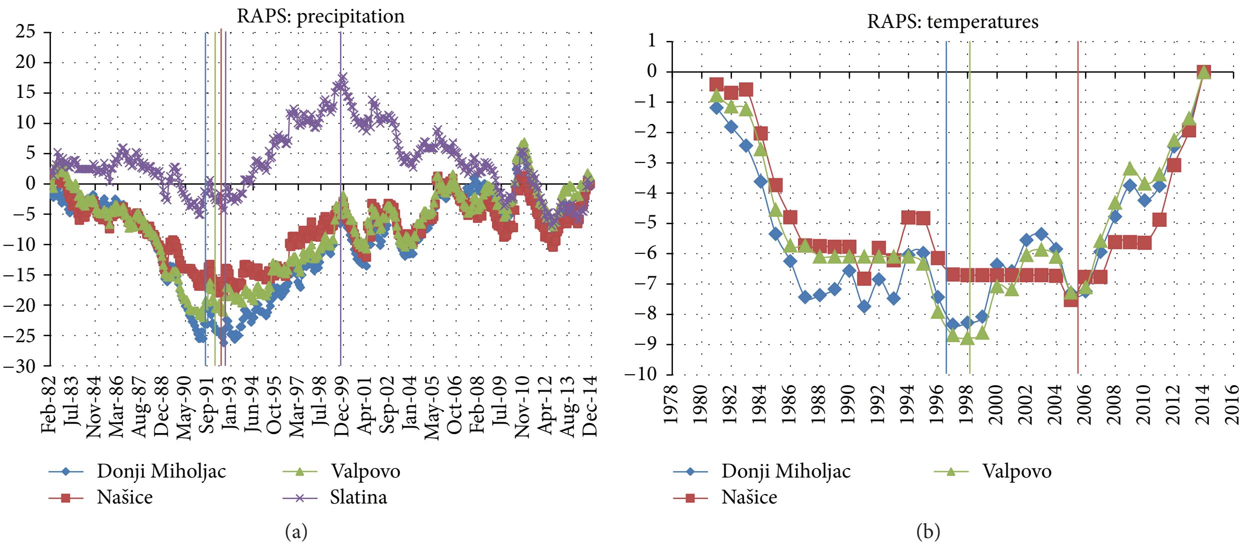

FIGURE 7: (a) RAPS of monthly precipitation data and (b) RAPS of mean annual air temperature data.

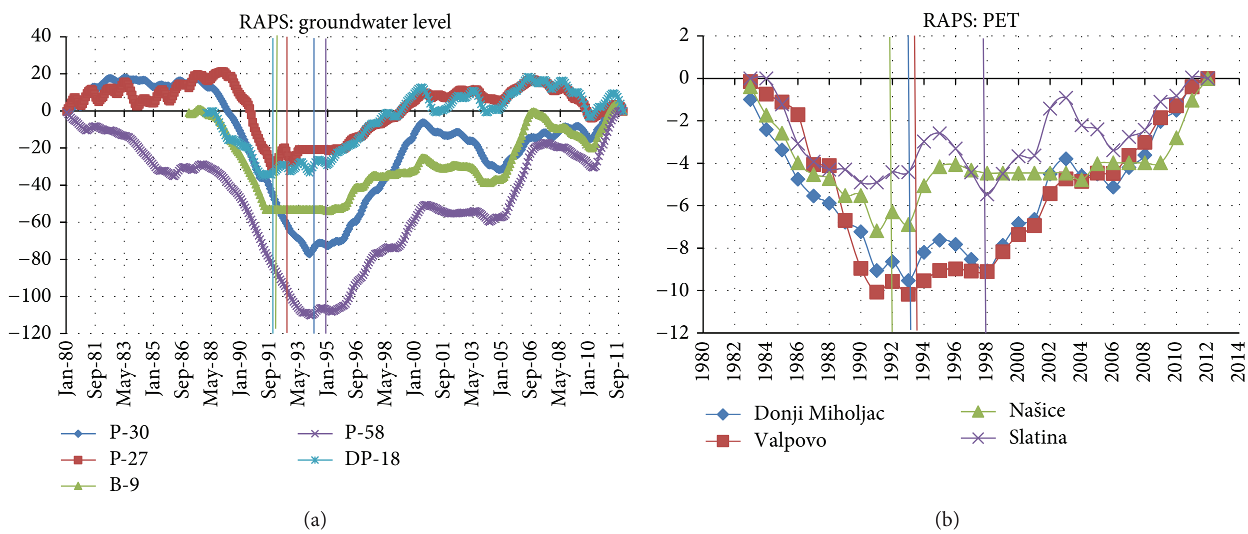

FIGURE 8: (a) RAPS of mean monthly groundwater levels and (b) RAPS of mean annual potential evapotranspiration.

Results obtained in this research confirm previous statement, but subperiods of decreasing and increasing discharges have a delay of 4-5 years comparing to the precipitation, and the coefficients of variations are not significant.

Annual groundwater levels have also two subperiods, the first period of decrease (1991–1993) and the second subperiod of increase of groundwater level. The results of previous Croatian researches on water balance components of much larger areas and longer data series periods (1900–1995) made by Zaninović and Gajić-Čapka [41] recognized a significant increase in potential evapotranspiration and decrease in runoff and soil water content and predicted further development of the analysed processes in the next century. The proposed analysis of small catchment water balance did not completely prove the results. Changes in potential evapotranspiration are present but not significant.

Figure 8 shows application of RAPS method on both, groundwater level and potential evapotranspiration. The first subperiod shows decreasing trend of groundwater level (breaking year is between 1991 and 1995) and the second subperiod of increasing groundwater level. Potential evapotranspiration has a similar behaviour with breaking year between 1991 and 1994, and for one station it is 1998.

All data series show two subperiods with different duration. Decreasing subperiods finish between 1991 (for precipitation and groundwater levels) and 1997 (for air temperature and discharges). They are followed by increasing periods (Figure 9(a)). Different durations of subperiods distinguished by RAPS are partially related to characteristics of catchment area itself. Particularly, trends in runoff processes show a delay of few years. Usually, it is neglected in the trend analysis of climate change impacts. Also, as a complex hydrological

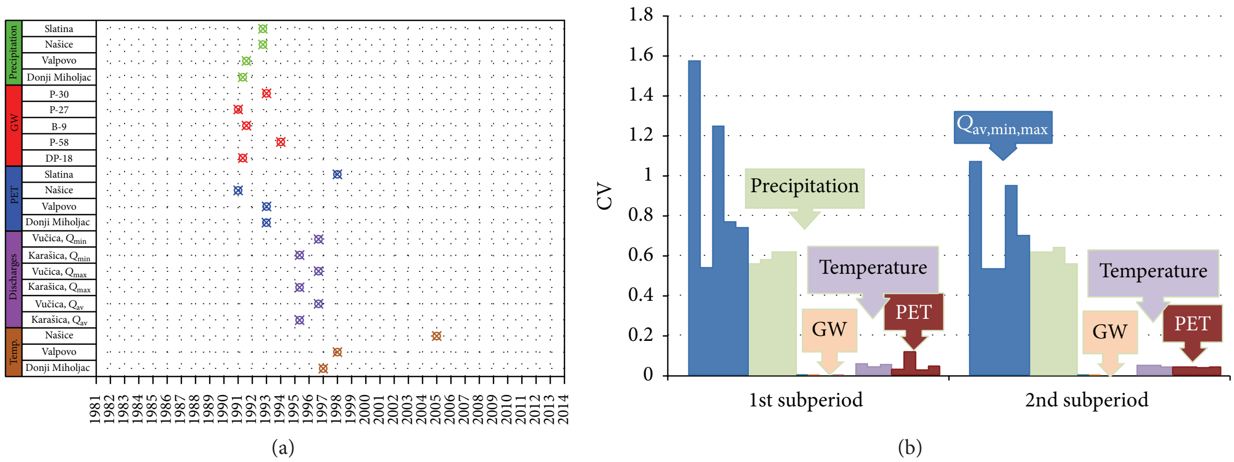

Figure 9: (a) Duration of subperiods distinguished by RAPS and (b) coefficients of variation (CV) of analysed parameters.

process, depending on many parameters, a large variability of characteristic discharges is not surprising. The least variable parameters are air temperatures, potential evapotranspiration, and groundwater levels. There are no statistical differences in significance of CV in the two subperiods (Figure 9(b)).

4. Conclusions

Knowledge of meteorological and hydrological parameters as a driving force of water balance components and their temporal and spatial distribution are essential for water management practice. There are many scenarios of precipitation and air temperature change in the future, but all of them have to be tested on a certain basin with specific geomorphological, hydrological, and vegetation characteristics, and so forth. Each river basin is unique, and small catchment areas especially show significant dependence on shape, slope, land use, and other features, including human structures.

Catchment area of Karašica and Vučica Rivers in Croatia had no significant change in land use since 1980 and all obtained variabilities that occurred in the last period can be considered as a consequence of change in hydrological parameters and processes. Previous research in the area much larger than this study area indicated increase of precipitation, air temperatures, and potential evapotranspiration and decrease of other water balance components, first of all runoff. They are usually given per decade or longer period. This analysis shows opposite results. All analysed parameters in the period of 35 years have two subperiods of different duration related to their hydrological development. The first one is period of decrease, and the second one is period of increase of all parameters, but with time delay of several years, especially in discharges. Also, variability of hydrological parameters is increasing, but without significance. The most variable are discharges and precipitation with consequent occurrence of droughts and floods which make this area and its water management system more vulnerable. Small catchment areas are the basic and unique units of water management, so it is very important to analyse their natural characteristics and processes to be able to cope with water scarcity or sufficiency in the best way.

Conflict of Interests

The authors declare that there is no conflict of interests regarding the publication of this paper.

References

[1] G. A. Corzo Perez, M. H. J. van Huijgevoort, F. Voß, and H. A. J. van Lanen, "On the spatio-temporal analysis of hydrological droughts from global hydrological models," *Hydrology and Earth System Sciences*, vol. 15, no. 9, pp. 2963–2978, 2011.

[2] B. Lloyd-Hughes, L. C. Shaffrey, P. L. Vidale, and N. W. Arnell, "An evaluation of the spatiotemporal structure of large-scale European drought within the HiGEM climate model," *International Journal of Climatology*, vol. 33, no. 8, pp. 2024–2035, 2013.

[3] K. Stahl, H. Hisdal, J. Hannaford et al., "Streamflow trends in Europe: evidence from a dataset of near-natural catchments," *Hydrology and Earth System Sciences*, vol. 14, no. 12, pp. 2367–2382, 2010.

[4] L. Gudmundsson, L. M. Tallaksen, K. Stahl et al., "Comparing large-scale hydrological model simulations to observed runoff percentiles in Europe," *Journal of Hydrometeorology*, vol. 13, no. 2, pp. 604–620, 2012.

[5] C. Prudhomme, S. Parry, J. Hannaford, D. B. Clark, S. Hagemann, and F. Voss, "How well do large-scale models reproduce regional hydrological extremes in Europe?" *Journal of Hydrometeorology*, vol. 12, no. 6, pp. 1181–1204, 2011.

[6] A. F. Van Loon and G. Laaha, "Hydrological drought severity explained by climate and catchment characteristics," *Journal of Hydrology*, vol. 526, pp. 3–14, 2015.

[7] M. De Luis, J. C. González-Hidalgo, M. Brunetti, and L. A. Longares, "Precipitation concentration changes in Spain 1946–2005," *Natural Hazards and Earth System Science*, vol. 11, no. 5, pp. 1259–1265, 2011.

[8] B. Orlowsky and S. I. Seneviratne, "Global changes in extreme events: regional and seasonal dimension," *Climatic Change*, vol. 110, no. 3-4, pp. 669–696, 2012.

[9] A. N. Nunes and L. Lourenço, "Precipitation variability in Portugal from 1960–2011," *Journal of Geographical Sciences*, vol. 25, no. 7, pp. 784–800, 2015.

[10] S. D. Solomon, D. Qin, M. Manning et al., Eds., *Climate Change 2007: The Physical Science Basis*, Cambridge University Press, New York, NY, USA, 2007.

[11] D.-I. Müller-Wohlfeil, G. Bürger, and W. Lahmer, "Response of a river catchment to climatic change: application of expanded downscaling to Northern Germany," *Climatic Change*, vol. 47, no. 1, pp. 61–89, 2000.

[12] G. Blöschl and M. Sivapalan, "Process controls on regional flood frequency: coefficient of variation and basin scale," *Water Resources Research*, vol. 33, no. 12, pp. 2967–2980, 1997.

[13] Z. W. Kundzewicz, L. J. Mata, N. W. Arnell et al., "The implications of projected climate change for freshwater resources and their management," *Hydrological Sciences Journal*, vol. 53, no. 1, pp. 3–10, 2008.

[14] M. Sivapalan, K. Takeuchi, S. W. Franks et al., "IAHS Decade on Predictions in Ungauged Basins (PUB), 2003–2012: shaping an exciting future for the hydrological sciences," *Hydrological Sciences Journal*, vol. 48, no. 6, pp. 857–880, 2003.

[15] D. A. Post and A. J. Jakeman, "Relationships between catchment attributes and hydrological response characteristics in small Australian mountain ash catchments," *Hydrological Processes*, vol. 10, no. 6, pp. 877–892, 1996.

[16] A. Visser, J. Kroes, M. T. H. Van Vliet, S. Blenkinsop, H. J. Fowler, and H. P. Broers, "Climate change impacts on the leaching of a heavy metal contamination in a small lowland catchment," *Journal of Contaminant Hydrology*, vol. 127, no. 1–4, pp. 47–64, 2012.

[17] G. Leng, M. Huang, Q. Tang, and L. R. Leung, "A modeling study of irrigation effects on global surface water and groundwater resources under a changing climate," *Journal of Advances in Modeling Earth Systems*, vol. 7, no. 3, pp. 1285–1304, 2015.

[18] S. I. Seneviratne, T. Corti, E. L. Davin et al., "Investigating soil moisture-climate interactions in a changing climate: a review," *Earth-Science Reviews*, vol. 99, no. 3-4, pp. 125–161, 2010.

[19] T. G. Huntington, "Evidence for intensification of the global water cycle: review and synthesis," *Journal of Hydrology*, vol. 319, no. 1–4, pp. 83–95, 2006.

[20] M. Tesař, M. Šír, and L. Lichner, "Runoff formation in a small catchment," in *Proceedings of the 9th Conference of the European Network of Experimental and Representative Basins (ERB '02)*, pp. 7–12, Demänovská Dolina, Slovakia, September 2002.

[21] O. Varis, T. Kajander, and R. Lemmelä, "Climate and water: from climate models to water resources management and vice versa," *Climatic Change*, vol. 66, no. 3, pp. 321–344, 2004.

[22] C. A. Ruch and T. Harum, "Water balance components for forest and meadow land use systems in a crystalline catchment," in *Proceedings of the 9th Conference of the European Network of Experimental and Representative Basins (ERB '02)*, pp. 26–32, Demänovská Dolina, Slovakia, September 2002.

[23] B. Moldan and J. Černy, "Biogeochemistry of small catchments: a tool for environmental research," *Environmental Science and Pollution Research*, vol. 1, no. 4, pp. 284–285, 1994.

[24] V. U. Smakhtin, "Low flow hydrology: a review," *Journal of Hydrology*, vol. 240, no. 3-4, pp. 147–186, 2001.

[25] M. Gajić-Čapka, K. Cindrić, and Z. Pasarić, "Trends in precipitation indices in Croatia 1961–2010," *Theoretical and Applied Climatology*, vol. 121, no. 1-2, pp. 167–177, 2015.

[26] L. Tadić, Z. Tadić, I. Crnčan, and J. Korov, "Analysis of flood frequency on the area of Drava river basin," in *Proceedings of the 21st Conference of Danube Countries on the Hydrological Forecasting and Hydrological Bases of Water Management (Proceedings on CD)*, Bucharest, Romania, September 2002.

[27] T. Dadić and L. Tadić, "Climate and land use changes impacts on small catchment areas," in *Proceedings of the 14th International Symposium Water Management and Hydraulic Engineering*, pp. 171–180, Brno, Czech Republic, September 2015.

[28] W. Wang, Q. Shao, T. Yang et al., "Quantitative assessment of the impact of climate variability and human activities on runoff changes: a case study in four catchments of the Haihe River basin, China," *Hydrological Processes*, vol. 27, no. 8, pp. 1158–1174, 2013.

[29] M. Amirabadizadeh, Y. F. Huang, and T. S. Lee, "Recent trends in temperature and precipitation in the Langat River basin, Malaysia," *Advances in Meteorology*, vol. 2015, Article ID 579437, 16 pages, 2015.

[30] G. H. Hargreaves and Z. A. Samani, "Estimating potential evapotranspiration," *Journal of the Irrigation and Drainage Division*, vol. 108, no. 3, pp. 225–230, 1982.

[31] S. Trajković, "Hargreaves versus Penman-Monteith under humid conditions," *Journal of Irrigation and Drainage Engineering*, vol. 133, no. 1, pp. 38–42, 2007.

[32] J. Garbrecht and G. P. Fernandez, "Visualization of trends and fluctuations in climatic records," *Water Resources Bulletin*, vol. 30, no. 2, pp. 297–306, 1994.

[33] O. Bonacci, D. Trninić, and T. Roje-Bonacci, "Analysis of the water temperature regime of the Danube and its tributaries in Croatia," *Hydrological Processes*, vol. 22, no. 7, pp. 1014–1021, 2008.

[34] T. B. McKee, N. J. Doeskin, and J. Kleist, "Drought monitoring with multiple time scales," in *Proceedings of the 9th Conference on Applied Climatology*, pp. 179–184, American Meteorological Society, Dallas, Tex, USA, January 1995.

[35] M. Perčec Tadić, M. Gajić-Čapka, K. Zaninović, and K. Cindrić, "Drought vulnerability in Croatia," *Agriculturae Conspectus Scientificus*, vol. 79, no. 1, pp. 31–38, 2014.

[36] L. Tadić, T. Dadić, and M. Bosak, "Comparison of different drought assessment methods in continental Croatia," *Građevinar*, vol. 67, no. 1, pp. 11–22, 2015.

[37] B. Nijssen, G. M. O'Donnell, A. F. Hamlet, and D. P. Lettenmaier, "Hydrologic sensitivity of global rivers to climate change," *Climatic Change*, vol. 50, no. 1-2, pp. 143–175, 2001.

[38] O. Bonacci, "Analiza nizova srednjih godišnjih temperatura zraka u Hrvatskoj," *Građevinar*, vol. 62, no. 9, pp. 781–791, 2010.

[39] K. Rasouli, J. W. Pomeroy, J. R. Janowicz, S. K. Carey, and T. J. Williams, "Hydrological sensitivity of a northern mountain basin to climate change," *Hydrological Processes*, vol. 28, no. 14, pp. 4191–4208, 2014.

[40] H. Hisdal, K. Stahl, L. M. Tallaksen, and S. Demuth, "Have streamflow droughts in Europe become more severe or frequent?" *International Journal of Climatology*, vol. 21, no. 3, pp. 317–333, 2001.

[41] K. Zaninović and M. Gajić-Čapka, "Changes in components of the water balance in the Croatian lowlands," *Theoretical and Applied Climatology*, vol. 65, no. 1-2, pp. 111–117, 2000.

Hindawi Publishing Corporation
Advances in Meteorology
Volume 2016, Article ID 1579415, 10 pages
http://dx.doi.org/10.1155/2016/1579415

Research Article

Drought Risk Assessment in Yunnan Province of China Based on Wavelet Analysis

HuiCong Jia[1] and DongHua Pan[2]

[1]*Key Laboratory of Digital Earth Science, Institute of Remote Sensing and Digital Earth, Chinese Academy of Sciences, Beijing 100094, China*
[2]*National Disaster Reduction Center of China, Ministry of Civil Affairs of the People's Republic of China, Beijing 100124, China*

Correspondence should be addressed to DongHua Pan; eliteast@mail.bnu.edu.cn

Received 13 July 2015; Revised 26 September 2015; Accepted 12 October 2015

Academic Editor: Milan Gocic

A wavelet transform technique was used to analyze the precipitation data for nearly 60 years (1954–2012) in Yunnan Province of China. The wavelet coefficients and the variance yield of wavelet were calculated. The results showed that, in nearly 60 years, the spring precipitation increased slightly; however, the linear trend of other seasonal and annual precipitations showed a reducing trend. Seasonal and annual precipitation had the characteristics of multiple time scales. Different time scales showed the different cyclic alternating patterns. Overall, in the next period of time, different seasons and the annual precipitation will be in the periods of precipitation-reduced oscillation; high drought disaster risks may occur in Yunnan province. Particularly, by analyzing large area of severe drought of Yunnan province in 2009–2012, the predicted results of wavelet were verified. The results may provide a scientific basis for guiding agricultural production and the drought prevention work for Yunnan Province and other places of China.

1. Introduction

China is a typical monsoon climate country and is an agricultural country. The instability of monsoon climate leads to frequent flood and drought, causing 55% of total natural disasters loss in China [1, 2]. Drought has become the key obstacle factor constraining China's agriculture and sustainable development. During the last decade, the severe drought in southwest China has resulted in tremendous losses, including crop failure, a lack of drinking water, and ecosystem destruction [3]. From July 2009, Yunnan Province of China has been hit with the worst droughts in a century. The drought has affected about 2.1 million hectares of farmland or about 85 percent of wheat producing areas of Yunnan province until March 2010 [4]. From 2009 to 2012, Yunnan province has suffered a continuous severe drought. Most parts of China's Yunnan Province have been gripped by drought since early December 2011 as rainfall has been 50%–80% less than the long-term average [5]. Some attempts have been made to explore the causes and variability of drought in southwest China [6–10]. However, it is unclear and even disputable as to what and how precipitations and circulation oscillation patterns affect the drought risk.

Droughts are caused by a depletion of precipitation over time [11]. It is well known that precipitation is one of the most important aspects related to climate change and, in recent years, droughts and also floods have been experienced with higher peaks and severity levels [12]. The wavelet transform is a mathematical tool that provides a time scale representation of a signal in the time domain [13]. It could be applied to meteorological data to bring up distinct patterns that might be hidden within the original data [14]. It also could be used to identify the location of the mutation point in nonstationary signals. Currently, wavelet analysis research mainly focused on the multiple time scales characteristics of temperature and precipitation [15–17]: connections' definition between hydrometeorological variables [18–21], short-term climate prediction [22–24], and so on. In China, based on statistical methods, some scholars have studied the relationship between precipitation and drought in Yunnan Province [25–27].

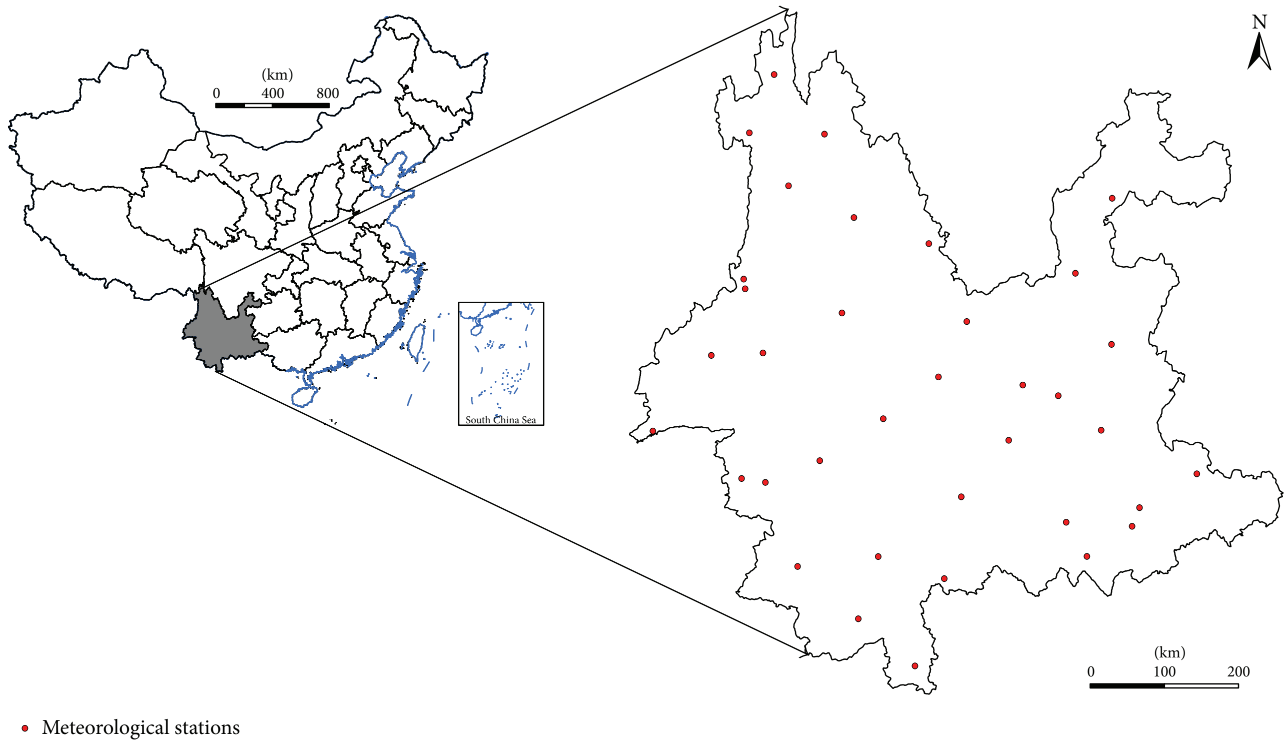

Figure 1: Study area and the distribution of meteorological stations in Yunnan Province.

The continuous wavelet analysis on Yunnan meteorological data is a new research for studying periodicities and long-term variability. Different temporal levels of precipitation (such as the seasonal and annual levels) in the structure and characteristics of abnormal variation should be revealed. In this study, based on Yunnan meteorological data, the precipitation characteristics in long-term drought and interdecadal changes were analyzed. Decreasing trends found in previous studies of precipitation were also clarified by using wavelet transforms. The objective of this study is twofold: (1) to explore the periodical fluctuations and the relationship between precipitation and drought risk in Yunnan Province and (2) to predict the seasonal precipitation in Yunnan Province and the trend of the annual precipitation. The results from this study will be of important reference value and significance to understand the precipitations characteristics, agricultural production, and the drought prevention work in Yunnan Province.

2. Data and Methods

2.1. Study Area. Yunnan, located in the southwest China (Figure 1), has a vast territory, magnificent mountains and rivers, and abundant natural resources. With an area of 390,000 square kilometers, Yunnan is the eighth largest province in China. It is an inland province, with Guizhou Province and Guangxi Zhuang Autonomous Region in the east, Tibet Autonomous Region in the northwest, and the Qinghai-Tibet Plateau in the southwest. The regional climate is classified as subtropical monsoonal, with annual average precipitation of 1100 mm and mean annual temperature between 5°C and 24°C from north to south.

Daily precipitation records of 36 stations in Yunnan Province from 1954 to 2012 were provided by the National Climate Centre of China Meteorological Administration (CMA). Based on the daily records, we calculated annual, monthly, and seasonal data series to assess responses of precipitation to drought disaster. We use the wavelet transform technique to analyze the precipitation data for nearly 60 years in Yunnan Province. The wavelet coefficients and the variance yield of wavelet were calculated to study the characteristics of abnormal variation. From the precipitation-reduced oscillation information, we can judge the trend of precipitation in different seasons and local drought disaster may occur in some areas.

2.2. Methods. The wavelet transform is a useful mathematical tool that can provide information about both time and frequency simultaneously and enable a separation to be made between features associated with different characteristic length scales, so they have some advantages over traditional Fourier transforms. At present, there are a large number of wavelet transforms available for various applications. In this study, we selected the Morlet wavelet [28] to analyze the multiple time scales inherent in our data series; it is a complex nonorthogonal continuous wavelet; the basis of a Morlet wavelet (ψ) consisting of a plane wave modulated by a Gaussian function can be defined as

$$\psi(\eta) = \pi^{-1/4} e^{i\omega\eta - \eta^2/2}, \tag{1}$$

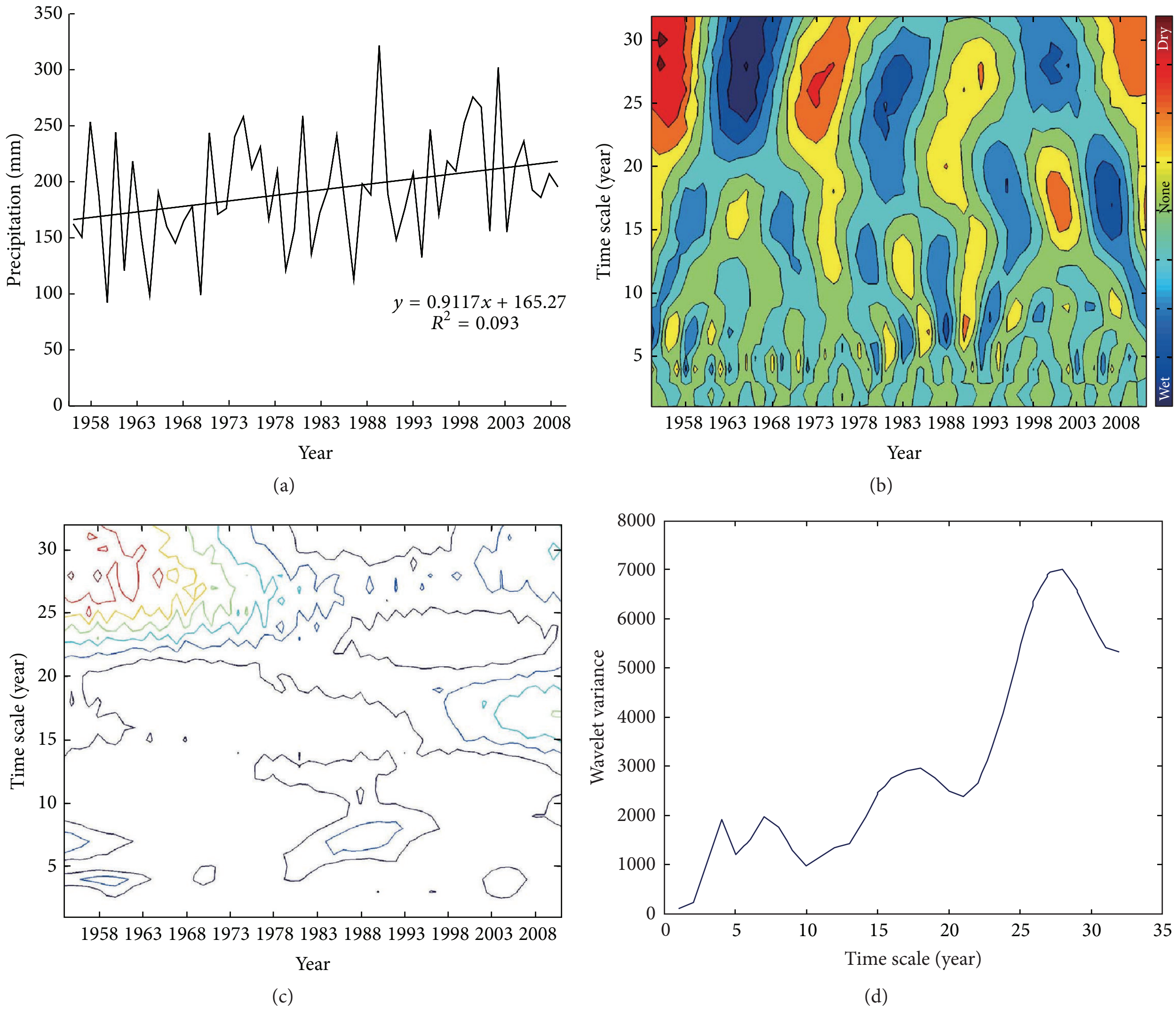

Figure 2: (a) Spring precipitation interannual change of Yunnan. (b) Spring precipitation wavelet transform of Yunnan. (c) Spring precipitation wavelet coefficients contour of Yunnan. (d) Spring precipitation wavelet variance of Yunnan.

where ω is the dimensionless frequency and η is the dimensionless time parameter. The continuous wavelet transform (CWT) has an ability to detect significant cycles and their occurrence time in the observation period. The CWT is defined as

$$W(a,b) = \frac{1}{\sqrt{a}} \int f(t) \cdot \psi^{*}\left(\frac{t-b}{a}\right) dt, \qquad (2)$$

where a and b are scale and translation parameters, respectively, and ψ^{*} is the complex conjugate of ψ.

The wavelet variance ($W(a)$) used to detect the main periods contributing to a signal can be expressed as

$$W(a) = \frac{1}{\sqrt{a}} \int \left|W_x(b,a)\right|^2 db. \qquad (3)$$

Since the precipitation data sets used in this paper are of finite length and the Morlet wavelet is not completely localized in time, errors will occur at the beginning and at the end of the wavelet power spectrum. To reduce the edge effects, we carried out a symmetry extension at both ends of the precipitation time series before undertaking the wavelet transform and then removed them.

3. Results and Analysis

3.1. Analysis of Spring Precipitation Variation Characteristics. As seen from Figure 2(a), the spring precipitation of Yunnan Province presented an upward trend in recent 60 years. The annual precipitation increased in the linear inclined rate which was 9.117 mm/10 years, but in recent five years it presented a downward trend. Figure 2(b) showed that a periodic oscillation is obvious under the scale of 18 years. With the increase of time scale, above the scale of 18 years, a gentle periodic oscillation was indicated for 7 cycles. Until year 2012, the contours of decreased precipitation were still not closed, indicating that spring drought may occur within the next

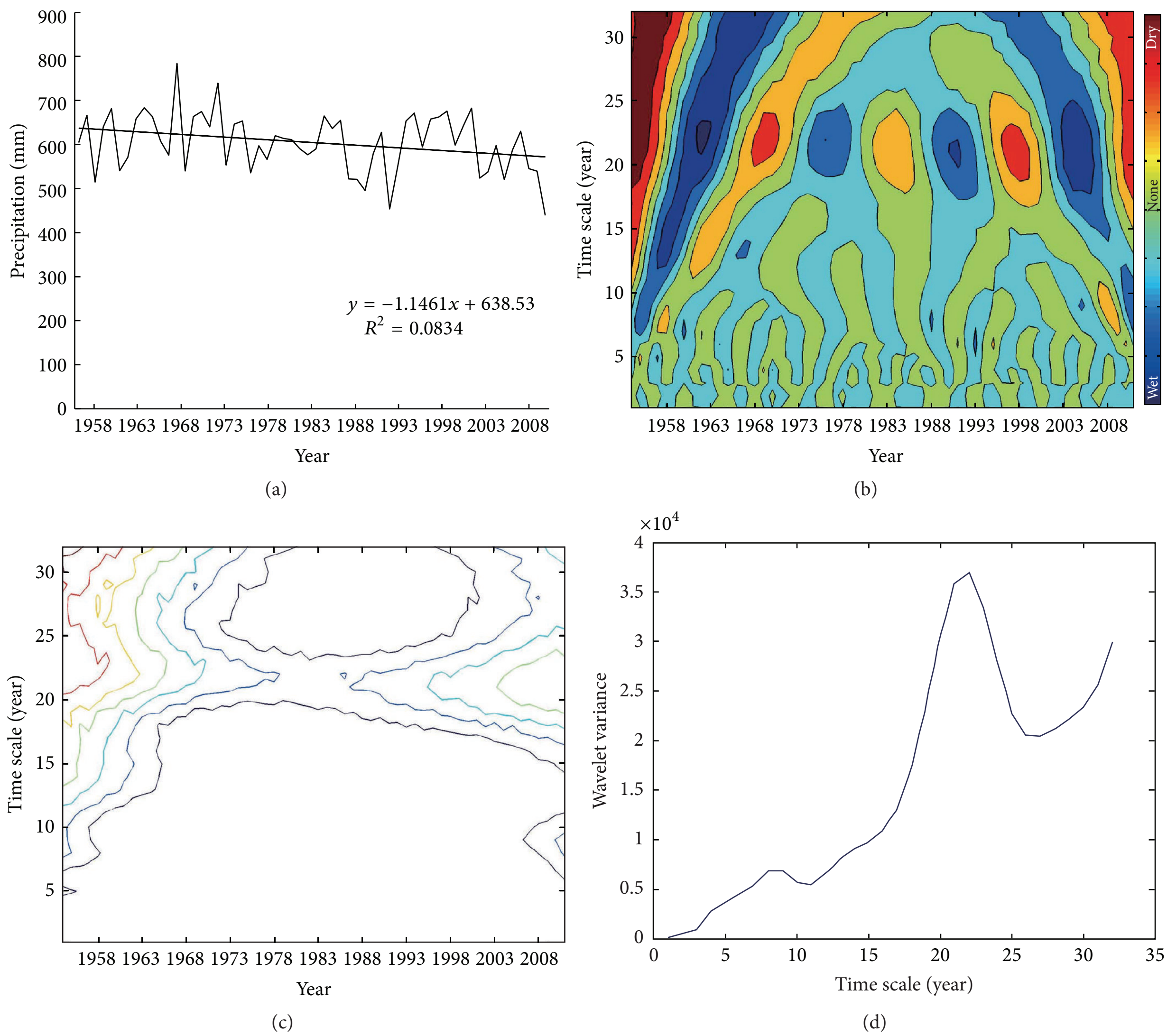

Figure 3: (a) Summer precipitation interannual change of Yunnan. (b) Summer precipitation wavelet transform of Yunnan. (c) Summer precipitation wavelet coefficients contour of Yunnan. (d) Summer precipitation wavelet variance of Yunnan.

few years. The fact of spring Yunnan drought event in 2009, 2011, and 2012 has proved the results of the analysis. From Figure 2(c) we can see that a precipitation wavelet energy spectrum is strong at time scale of 25~32 years, but the cycle changes have a localization characteristic (before 1980). The wavelet energy spectrum is weaker at time scale of 10~22 years, but more obvious cycle distribution occupies the entire study time domain (1954~2012). Figure 2(d) showed that wavelet variance of spring rainfall has four peaks, corresponding to time scales of 28 years, 18 years, 7 years, and 4 years (correlation coefficient is 0.82 and coefficient is significant at 0.05 level). The largest peak value corresponds to the time scale of 28 years indicating that the period oscillation of 28 years fluctuated most; it could be considered as the first major period in spring precipitation change.

3.2. Analysis of Summer Precipitation Variation Characteristics. From Figure 3(a) we can see that the summer precipitation of Yunnan Province presented a downward trend in recent 60 years. The annual precipitation decreased in the linear inclined rate which was −11.461 mm/10 years. Figure 3(b) showed that a periodic oscillation is gentle at the scale of above 22 years; the regular pattern is obvious. Until 2012, the contour of decreased precipitation has not closed, indicating that summer drought may continue to occur. As seen from Figure 3(c), we can see that a precipitation wavelet energy spectrum is strong at time scale of 20~32 years, but the cycle changes have a localization characteristic (before 1970). The wavelet energy spectrum is weaker at time scale of 6~18 years, but more obvious cycle distribution occupies the entire study time domain (1954~2012). Figure 3(d) showed that wavelet variance of summer rainfall has two peaks, corresponding to time scales of 22 years and 8 years (correlation coefficient is 0.85 and coefficient is significant at 0.05 level).

3.3. Analysis of Autumn Precipitation Variation Characteristics. From Figure 4(a) we can see that the autumn precipitation of Yunnan Province presented a nondistinct fluctuation

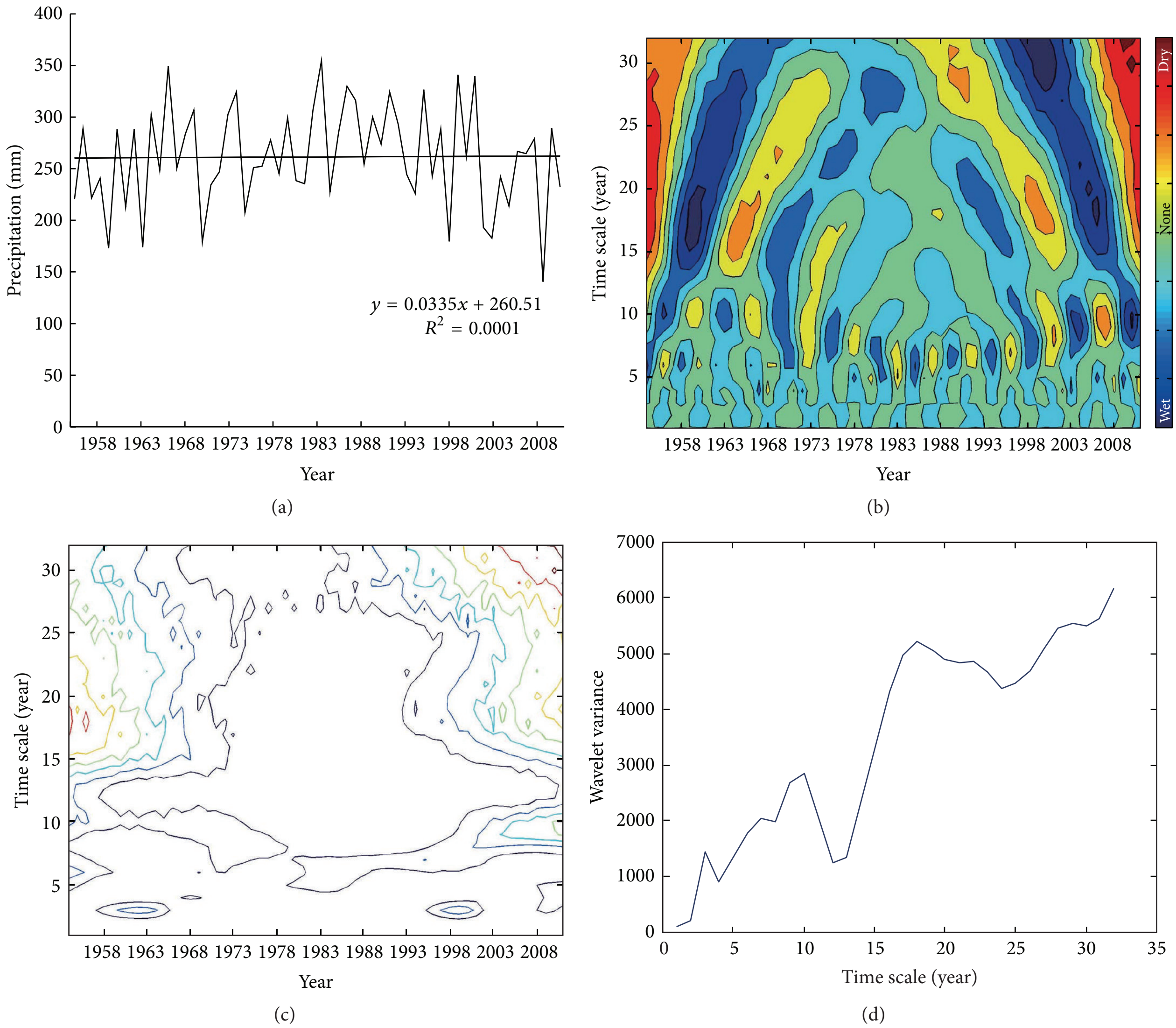

Figure 4: (a) Autumn precipitation interannual change of Yunnan. (b) Autumn precipitation wavelet transform of Yunnan. (c) Autumn precipitation wavelet coefficients contour of Yunnan. (d) Autumn precipitation wavelet variance of Yunnan.

in general. The linear inclined rate was 0.335 mm/10 years. Figure 4(b) showed that a periodic oscillation is obvious under the scale of 15 years, performing no obvious law. With the increase of time scale, above the scale of 15 years, a gentle periodic oscillation was distinct and represented 7 cycles. Precipitation was relatively more in the period of 1970–2000. Autumn rainfall went into the dry season after 2003. The year of 2012 located in the middle of reduction period of oscillation; autumn drought may continue within the next few years. From Figure 4(c) we can see that a precipitation wavelet energy spectrum is strong at time scale of 15~32 years, but the cycle changes have a localization characteristic (before 1960 and after 2000). The wavelet energy spectrum is weaker at time scale of 8~13 years, but more obvious cycle distribution occupies the entire study time domain (1954~2012). Figure 4(d) showed that wavelet variance of autumn rainfall has three peaks, corresponding to time scales of 18 years, 10 years, and 3 years (correlation coefficient is 0.90 and coefficient is significant at 0.05 level).

3.4. Analysis of Winter Precipitation Variation Characteristics. Figure 5(a) showed that the winter precipitation of Yunnan Province presented a little downward trend in recent 60 years. The annual precipitation decreased in the linear inclined rate which was −0.929 mm/10 years. Figure 5(b) showed that a periodic oscillation is obvious under the scale of 17 years. With the increase of time scale, above the scale of 17 years, a gentle periodic oscillation represented 10 cycles. Until 2012, the contour of increased precipitation has not closed, indicating that the trend of precipitation increase in winter will continue within the next few years. From Figure 5(c) we can see that a precipitation wavelet energy spectrum is strong at time scale of 15~20 years, but the cycle changes have a localization characteristic (1985–1995). The wavelet energy spectrum is

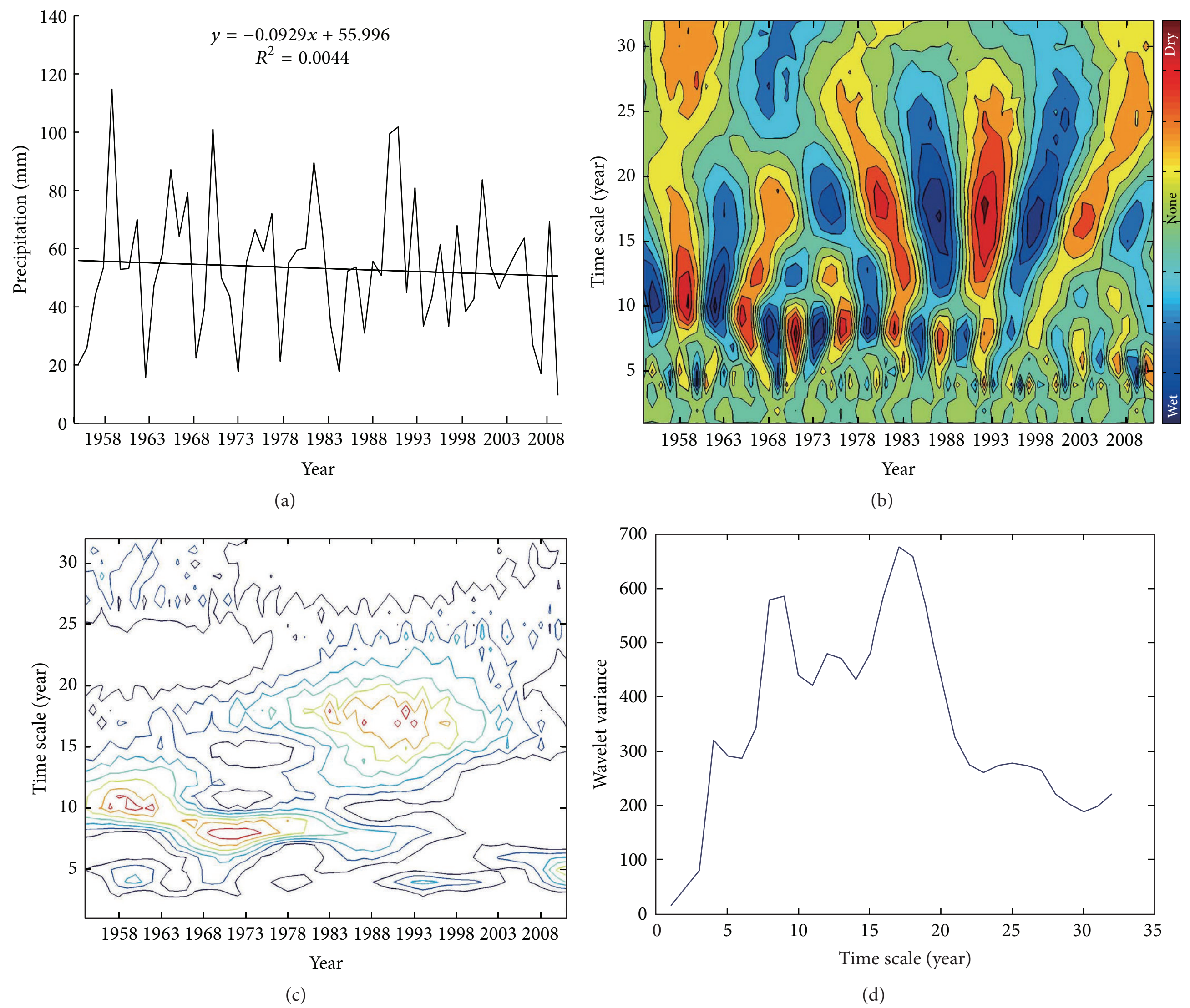

Figure 5: (a) Winter precipitation interannual change of Yunnan. (b) Winter precipitation wavelet transform of Yunnan. (c) Winter precipitation wavelet coefficients contour of Yunnan. (d) Winter precipitation wavelet variance of Yunnan.

weaker at time scale of 10~22 years, but more obvious cycle distribution occupies the entire study time domain (1954~2012). Figure 5(d) showed that wavelet variance of winter rainfall has three peaks, corresponding to time scales of 17 years, 9 years, and 4 years (correlation coefficient is 0.88 and coefficient is significant at 0.05 level).

3.5. Analysis of Annual Precipitation Variation Characteristics. Figure 6(a) showed that the annual precipitation of Yunnan Province presented a little downward trend in recent 60 years. The annual precipitation decreased in the linear inclined rate which was −3.323 mm/10 years. The descending trend of recent 5 years is obvious. Figure 6(b) showed that a periodic oscillation has a nondistinct law under the scale of 22 years. With the increase of time scale, above the scale of 22 years, a gentle periodic oscillation represented 7 cycles. The year of 2012 located in the middle of reduction period of oscillation; annual precipitation reduction may continue within the next few years. From Figure 6(c) we can see that a precipitation wavelet energy spectrum is strong at time scale of 20~32 years but mainly before 1960. The wavelet energy spectrum is weaker at time scale of 7~22 years, but more obvious cycle distribution occupies the entire study time domain (1954~2012). Figure 6(d) showed that wavelet variance of annual rainfall has two peaks, corresponding to time scales of 22 years and 10 years (correlation coefficient is 0.76 and coefficient is significant at 0.05 level).

3.6. Case Verification. Water scarcity and bad water quality are the basic reasons which lead to drinking difficulties (hereafter referred to as "PDWDD"). Severe drought has led to problems of difficulty in accessing drinking water. In China,

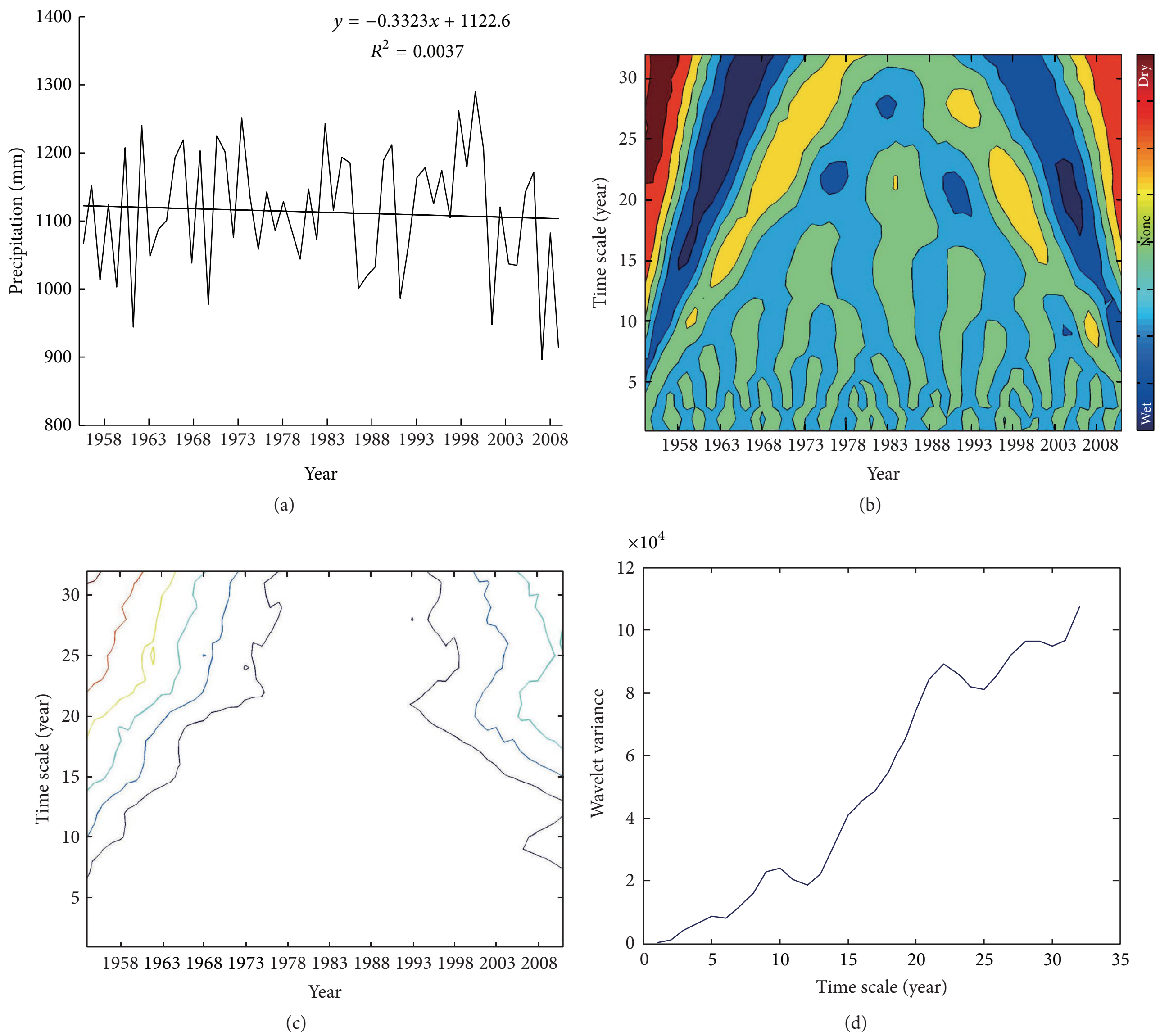

Figure 6: (a) Annual precipitation interannual change of Yunnan. (b) Annual precipitation wavelet transform of Yunnan. (c) Annual precipitation wavelet coefficients contour of Yunnan. (d) Annual precipitation wavelet variance of Yunnan.

PDWDD is an important indicator of drought disaster. The reported drought disaster statistic data [29] in 2009–2013 of Yunnan province was selected as basis for a case validation.

From the point of view of meteorological precipitation statistics, since the year of 2009, drought has occurred four times in Yunnan Province [30]: from September 2009 to May 2010, across autumn, winter, and spring seasons; from June to September 2011, lasting for 4 months, from December 2011 to May 2012, lasting for 6 months, and from October 2012 to May 2013, lasting for 8 months. The four processes have significant correspondence with the four wavelet seasonal changes (Figures 7(a), 7(b), 7(c), and 7(d)).

From the perspective of disaster statistics, the four consecutive occurrences of drought, continuous heavy drought across autumn, winter, and spring seasons in 2009-2010, continuous drought from summer to autumn in 2011, continuous drought from winter to spring in 2012, and continuous drought from winter to spring in 2013, the cumulative effects of the disaster were very obvious. Under a comparative analysis of PDWDD of the four processes of Yunnan Province, the drought process in 2013 was a light drought, the counties' (cities and districts) number of heavier drinking population problems (>50,000) is 17. Respectively, it accounted for 10% and 37% of the total heavier county numbers of the 2009-2010 drought process and the 2012 drought process. Severely affected counties of PDWDD (>100,000) were least for the past four years. Currently Yunnan province is in a dry period of precipitation wavelet analysis, with the likelihood of frequent droughts occurrence being greater.

4. Conclusions

Based on the Morlet wavelet method, this paper used the precipitation data for nearly 60 years (1954–2012) to study

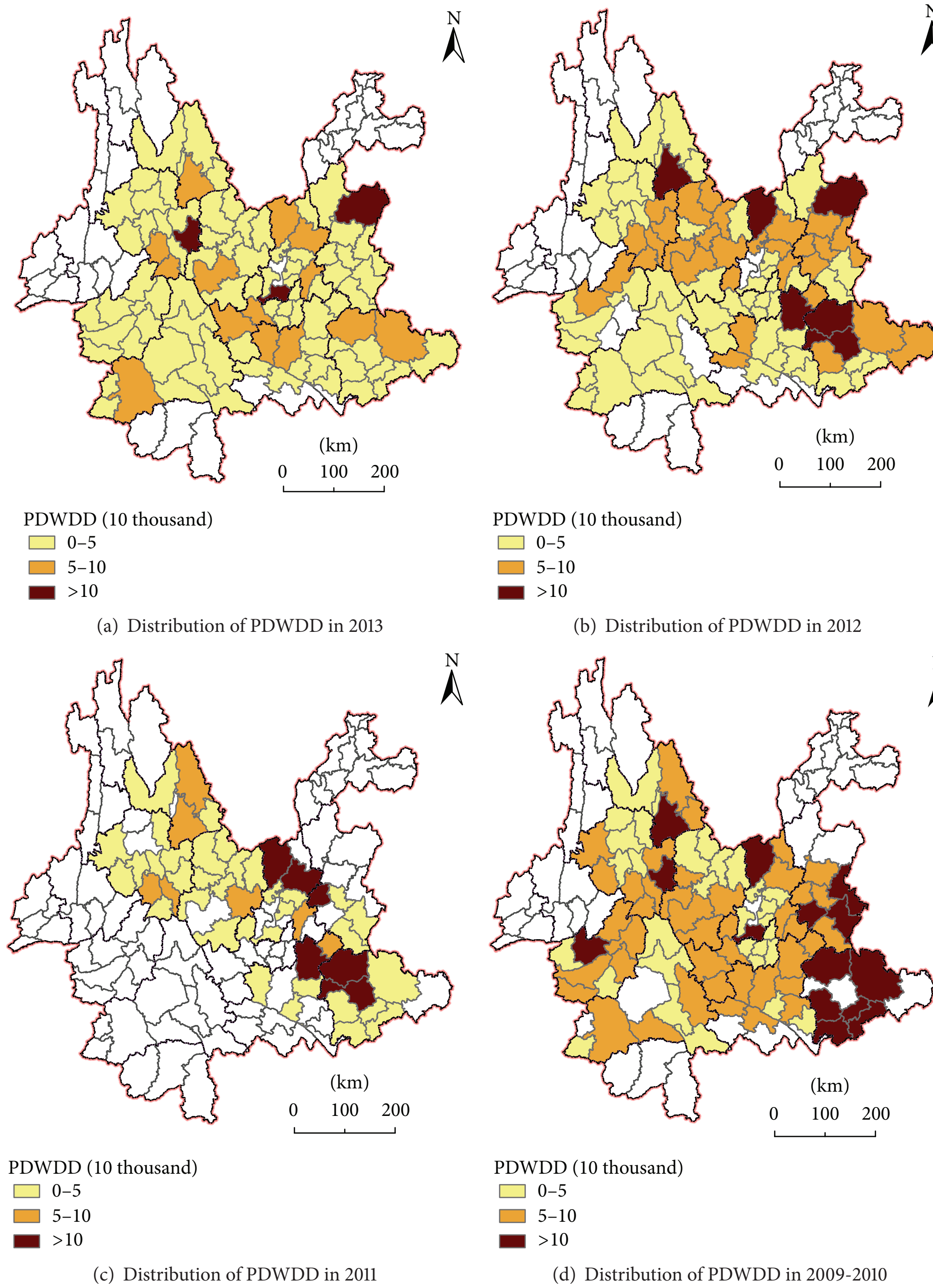

FIGURE 7: Distribution of populations in drinking water access difficulties because of drought of Yunnan province in 2009–2013.

the characteristics of the periodic variation of precipitation in Yunnan Province. The results showed some conclusions which are given as follows.

In the recent 60 years, all the seasons except for spring and annual precipitation showed a decreasing trend. Seasonal and annual precipitation had a characteristic of multiple time scales. A periodic oscillation is significant at the scale of 17~28 years. Secondly, oscillations of time scale of 7~10 years are obvious. The periodic variation on a large scale contains the periodic variation on a small scale.

Wavelet and energy spectrum in summer is the closest to that of annual. It indicated that annual precipitation is mainly affected by summer precipitation. From perspective of multiple time scales, summer precipitation has a similar trend and phase to annual precipitation; that is, when there is more summer rainfall, annual precipitation is greater.

According to the main cycle of summer and the annual rainfall, precipitation of Yunnan is in the decreased oscillation period; local drought may also occur in the next future times.

Time-frequency localization properties of wavelet analysis can show the fine structure of precipitation time series not only to dig out information hidden in the sequence of periodic oscillations over time but also to determine the approximate location of the mutation point of precipitation and qualitatively estimate the time sequence evolution trend. These results can provide a new way for the analysis of multiple time scale climate variations and short-term climate prediction.

Disclosure

This work was completed in Key Laboratory of Digital Earth Science, Institute of Remote Sensing and Digital Earth, Chinese Academy of Sciences, China.

Conflict of Interests

The authors declare that there is no conflict of interests regarding the publication of this paper.

Acknowledgments

This research was supported by National Natural Science Foundation of China (Grant. nos. 41301593 and 41471428), the Arid Meteorology Science Foundation, CMA (IAM201407), and the State Key Development Program for Basic Research of China (Grant no. 2012CB955402).

References

[1] J.-A. Wang, P.-J. Shi, X.-S. Yi, H.-C. Jia, and L.-Y. Zhu, "The regionalization of urban natural disasters in China," *Natural Hazards*, vol. 44, no. 2, pp. 169–179, 2008.

[2] H. C. Jia and D. H. Pan, "On the spatial and temporal patterns of flood and drought hazards of China," *Disaster Advances*, vol. 6, no. 3, pp. 12–18, 2013.

[3] R. Huang, Y. Liu, L. Wang et al., "Analysis of the causes of severe drought occurring in Southwest China from the fall of 2009 to the spring of 2010," *Chinese Journal of Atmospheric Sciences*, vol. 3, pp. 443–457, 2012.

[4] D.-D. Zhang, D.-H. Yan, F. Lu, Y.-C. Wang, and J. Feng, "Copula-based risk assessment of drought in Yunnan province, China," *Natural Hazards*, vol. 75, no. 3, pp. 2199–2220, 2014.

[5] China Daily, "Six-month-long drought set to end in Yunnan," April 2013, http://www.chinadaily.com.cn/china/2013-04/10/content_16391011.htm.

[6] G. F. Peng, E. X. Zhao, and G. L. Zhou, "Analysis on trend and causes of Spring-Summer consecutive drought in Yunnan province," *Journal of Yunnan University*, vol. 32, no. 4, pp. 443–448, 2010.

[7] J. He, M. Zhang, P. Wang, S. Wang, and X. Wang, "Climate characteristics of the extreme drought events in Southwest China during recent 50 years," *Acta Geographica Sinica*, vol. 66, no. 9, pp. 1179–1190, 2011.

[8] H. Yu, L. Wang, L. Tian et al., "Analysis on trend of time series of drought composite index in Yunnan," *Journal of Anhui Agricultural Sciences*, vol. 4, pp. 2090–2092, 2012.

[9] Y. Li, F. Ren, Y. Li, P. Wang, and H. Yan, "Characteristics of the regional meteorological drought events in Southwest China during 1960–2010," *Journal of Meteorological Research*, vol. 28, no. 3, pp. 381–392, 2014.

[10] Y. Ji, G. Zhou, S. Wang, and L. Wang, "Increase in flood and drought disasters during 1500–2000 in Southwest China," *Natural Hazards*, vol. 77, no. 3, pp. 1853–1861, 2015.

[11] UN (United Nations), "Risk awareness and assessment," in *Living with Risk*, pp. 39–78, UN/ISDR, Geneva, Switzerland, 2002.

[12] A. K. Mishra and V. P. Singh, "A review of drought concepts," *Journal of Hydrology*, vol. 391, no. 1-2, pp. 202–216, 2010.

[13] R. Polikar, "The story of wavelets," in *Physics and Modern Topics in Mechanical and Electrical Engineering*, N. Mastorakis, Ed., pp. 192–197, World Scientific and Engineering Society Press, Stevens Point, Wis, USA, 1999.

[14] T. Partal, "Wavelet analysis and multi-scale characteristics of the runoff and precipitation series of the Aegean region (Turkey)," *International Journal of Climatology*, vol. 32, no. 1, pp. 108–120, 2012.

[15] X. G. Dai, P. Wang, and J. F. Chou, "Multiscale characteristics of the rainy season rainfall and interdecadal decaying of summer monsoon in North China," *Chinese Science Bulletin*, vol. 48, no. 24, pp. 2730–2734, 2003.

[16] O. C. Penalba and W. M. Vargas, "Interdecadal and interannual variations of annual and extreme precipitation over central-northeastern Argentina," *International Journal of Climatology*, vol. 24, no. 12, pp. 1565–1580, 2004.

[17] X. Y. Jiang, S. H. Liu, and M. M. Ma, "Wavelet analysis of the precipitation time series in Northeast China during the last 100 years," *Geographical Research*, vol. 2, pp. 354–361, 2009.

[18] M. Nakken, "Wavelet analysis of rainfall-runoff variability isolating climatic from anthropogenic patterns," *Environmental Modelling and Software*, vol. 14, no. 4, pp. 283–295, 1999.

[19] A. F. Drago and S. R. Boxall, "Use of the wavelet transform on hydro-meteorological data," *Physics and Chemistry of the Earth*, vol. 27, no. 32–34, pp. 1387–1399, 2002.

[20] X. M. Shao, Y. Q. Xu, and C. R. Yan, "Wavelet analysis of rainfall variation in the Yellow River Basin," *Acta Scientiarum Naturalium Universitatis Pekinensis*, vol. 42, no. 4, pp. 503–504, 2006.

[21] X. Lana, M. D. Martínez, A. Burgueño, C. Serra, J. Martín-Vide, and L. Gómez, "Spatial and temporal patterns of dry spell lengths in the Iberian Peninsula for the second half of the twentieth century," *Theoretical and Applied Climatology*, vol. 91, no. 1–4, pp. 99–116, 2008.

[22] E. H. Taleb and L. M. Druyan, "Relationships between rainfall and West African wave disturbances in station observations," *International Journal of Climatology*, vol. 23, no. 3, pp. 305–313, 2003.

[23] Y. M. Zhu, X. G. Sun, and X. Y. Chen, "Application of wavelet analysis to climate prediction on drought and flood along the middle to lower reaches of Yangtze River," *Journal of PLA University of Science and Technology*, vol. 6, pp. 90–93, 2003.

[24] M. Özger, A. K. Mishra, and V. P. Singh, "Low frequency drought variability associated with climate indices," *Journal of Hydrology*, vol. 364, no. 1-2, pp. 152–162, 2009.

[25] H. C. Jia, J. A. Wang, C. X. Cao, D. Pan, and P. Shi, "Maize drought disaster risk assessment of China based on EPIC

model," *International Journal of Digital Earth*, vol. 5, no. 6, pp. 488–515, 2012.

[26] H. C. Jia, Y. Yuan, C. X. Cao, D. H. Pan, H. J. Zhou, and Y. L. Ma, "Geographical factor based rapid assessment model of population in drinking water access difficulties because of drought—a case study of 2012 Yunnan extreme drought," *Journal of Catastrophology*, vol. 1, pp. 92–97, 2013.

[27] H. C. Jia, D. H. Pan, Y. Yuan, and W. Zhang, "Using a BP neural network for rapid assessment of populations with difficulties accessing drinking water because of drought," *Human and Ecological Risk Assessment*, vol. 21, no. 1, 2015.

[28] D. L. Liu, X. Z. Liu, B. C. Li, S. Zhao, and X. Li, "Multiple time scale analysis of river runoff using wavelet transform for Dagujia River Basin, Yantai, China," *Chinese Geographical Science*, vol. 19, no. 2, pp. 158–167, 2009.

[29] Yunnan Provincial Bureau of Statistics, *Yunnan Statistical Yearbook*, China Statistics Press, Beijing, China, 2013.

[30] China Meteorological Administration & National Climate Committee, *China Climate Bulletin*, China Meteorological Press, Beijing, China, 2015.

Hindawi Publishing Corporation
Advances in Meteorology
Volume 2016, Article ID 9125219, 14 pages
http://dx.doi.org/10.1155/2016/9125219

Research Article

Methodology for Developing Hydrological Models Based on an Artificial Neural Network to Establish an Early Warning System in Small Catchments

Ivana Sušanj,[1] Nevenka Ožanić,[1] and Ivan Marović[2]

[1]*Department of Hydrology and Geology, Faculty of Civil Engineering, University of Rijeka, 51000 Rijeka, Croatia*
[2]*Department of Construction Management, Technology & Architecture, Faculty of Civil Engineering, University of Rijeka, 51000 Rijeka, Croatia*

Correspondence should be addressed to Ivana Sušanj; isusanj@uniri.hr

Received 29 September 2015; Accepted 10 November 2015

Academic Editor: Slavisa Trajkovic

In some situations, there is no possibility of hazard mitigation, especially if the hazard is induced by water. Thus, it is important to prevent consequences via an early warning system (EWS) to announce the possible occurrence of a hazard. The aim and objective of this paper are to investigate the possibility of implementing an EWS in a small-scale catchment and to develop a methodology for developing a hydrological prediction model based on an artificial neural network (ANN) as an essential part of the EWS. The methodology is implemented in the case study of the Slani Potok catchment, which is historically recognized as a hazard-prone area, by establishing continuous monitoring of meteorological and hydrological parameters to collect data for the training, validation, and evaluation of the prediction capabilities of the ANN model. The model is validated and evaluated by visual and common calculation approaches and a new evaluation for the assessment. This new evaluation is proposed based on the separation of the observed data into classes based on the mean data value and the percentages of classes above or below the mean data value as well as on the performance of the mean absolute error.

1. Introduction

Natural events, phenomena that occur in urban areas, with consequences such as loss of human life and/or significant material and infrastructure damage, are considered hazards. The same events in uninhabited areas and areas of no interest to people are not considered disasters, and they are rarely of interest in terms of detailed research and the implementation of hazard mitigation processes, such as early warning systems (EWSs) [1]. In populated areas, it is difficult to separate events as solely natural events in a manner that excludes the impact of human activities. The occurrence of hazard phenomena cannot be prevented by humans, but its consequences can be minimized or even intensified depending on the human activities in the hazard-prone area. Debris flow, expansive soils, landslides, rock falls, drought, erosion, sedimentation, river flooding, flash floods, and mud flows are all considered hazard events.

This paper focuses on hazards that are caused by the activity of water, such as flash floods, mud flows, and debris flows.

Flash floods can be described as floods caused by a storm event in a short period of time. The term “flash” reflects a fast response, with water levels in the water bed reaching a peak within minutes to a few hours after the onset of the rain event, leaving an extremely short time for warning [2]. Flash floods can also become filled with small particles from terrestrial deposits that were saturated with rain; in that case, they are defined as mud flows [3]. A debris flow is a flow, typically torrential, that is a mixture of mud flows and debris that suddenly comes down the slope, preceded by huge boulders that pose a severe hazard [4].

Prediction of flash floods, mud flows, and debris flows, as a part of the EWS in areas where there is no possibility of minimizing human activities or mitigating risk, becomes a crucial tool for preventing the consequences caused by the

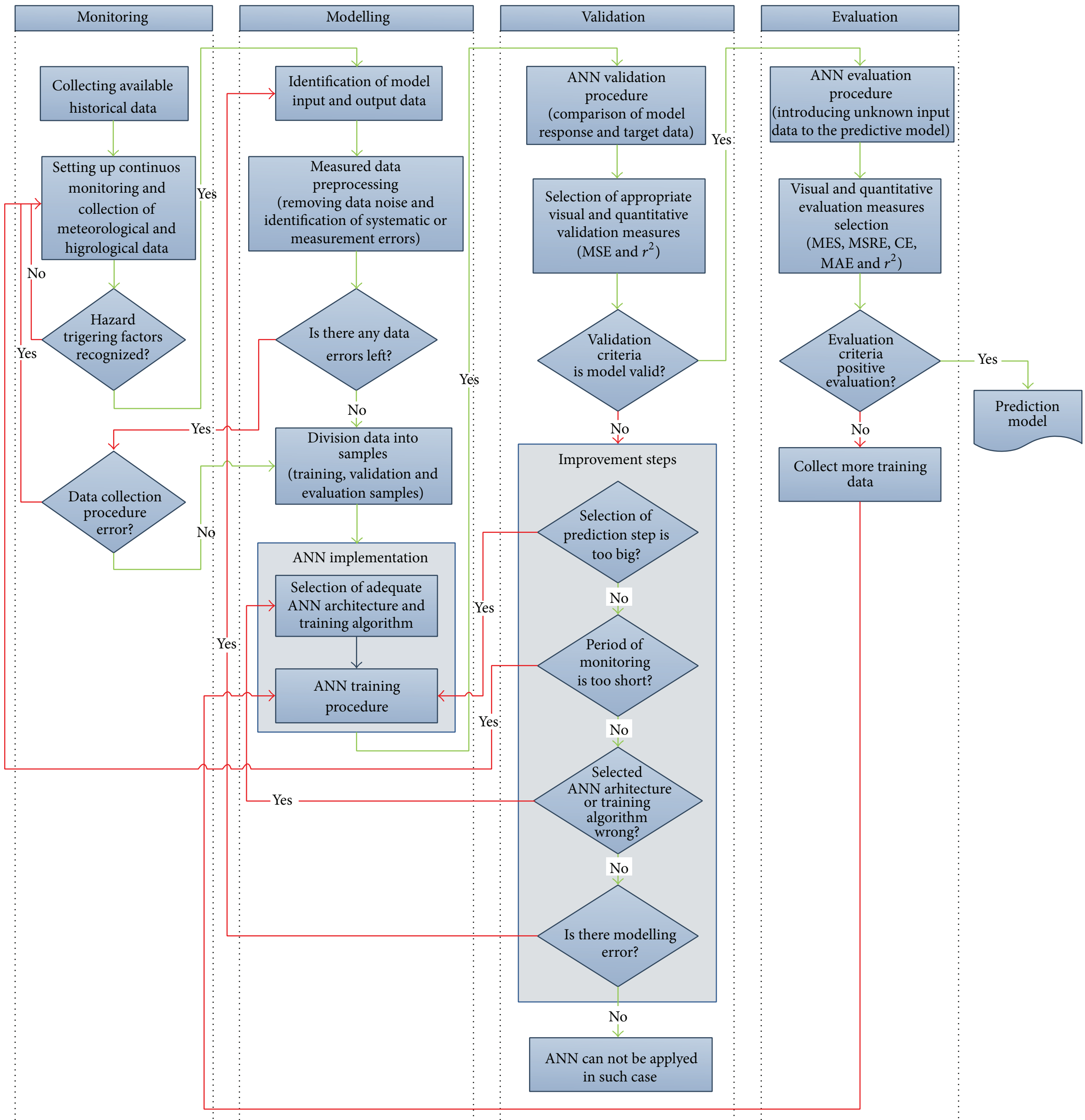

Figure 1: ANN predictive model development flowchart for the small catchments (green direction: forward movement in procedure; red direction: backward movement in procedure).

aforementioned hazards. As a result, there are currently many projects aimed at the development and implementation of EWSs. One such project is the bilateral Croatian-Japanese project "Risk Identification and Land-Use Planning for Disaster Mitigation of Landslides and Floods in Croatia," in which Japanese scientists transferred their knowledge of the development of EWSs to Croatian researchers because EWSs are still in the development stage in the Republic of Croatia.

As the aforementioned hazards are initiated by many natural and anthropogenic factors, which can become triggering factors when combined, it is critical to establish the monitoring of areas that are known as existing or potentially hazardous areas. Natural triggering factors can be extreme meteorological events (e.g., rainfall, snow melt, or wind) or hydrogeological conditions, such as high water levels and poor soil.

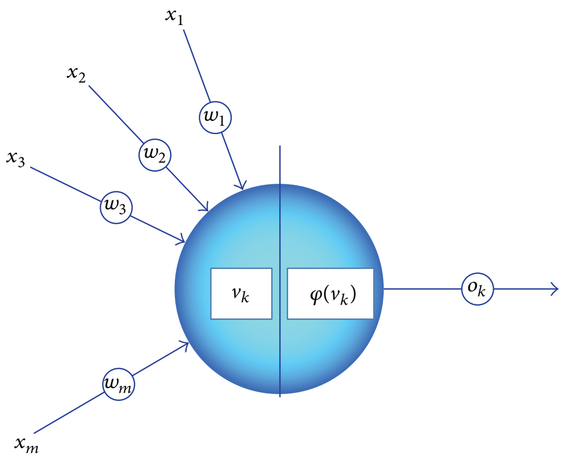

FIGURE 2: Artificial neuron node model ($x_1, x_2, \ldots, x_m$: input data; $w_1, w_2, \ldots, w_m$: weight coefficient; v_k is the sum of products of the weight coefficients; φ is the activation function of the neuron node; o_k is the response of the neuron node in the kth epoch of the calculation) [8].

According to the United Nations International Strategy for Disaster Reduction (UN/ISDR, 2009), a complete and effective EWS includes four related elements: (i) risk knowledge, (ii) a monitoring and warning system service, (iii) dissemination and communication, and (iv) response capability. The hazard prediction model is developed under the monitoring and warning system service. It requires a number of technologies and areas of expertise that consist of several elements, such as long-term monitoring and collection of existing data on the potential hazard area, real-time and remote monitoring of triggering factors, data analysis, development, validation, and evaluation of the predictive hydrological model, and development of a decision support system that will assist public authorities and citizens in choosing the appropriate protection measures [5].

In the last few decades, predictive hydrological models for establishing EWSs have been developed with the growth of computational capabilities. Most of the prediction models are formed as rainfall-runoff models that can be assigned to one of three broad categories: (i) deterministic (physical), (ii) conceptual, or (iii) parametric (also known as analytic or empirical). Deterministic models use physical laws of mass and energy transfer to describe rainfall-runoff processes, whereas conceptual models use perceived systems to simplify the processes, and parametric models use mathematical transfer functions to connect meteorological parameters to runoff. Hydrological models can also be classified as lumped, which means that the model treats a catchment as a single unit or as distributed, where the catchment is divided into connected subsystems [6].

Hydrological prediction models are typically extremely complex, which inhibits their widespread implementation. Furthermore, there is a lack of objectivity and consistency in the way that models are assessed, evaluated, and compared [7]. The models are typically prepared for specific large catchments, and they cannot be used anywhere else. Such models

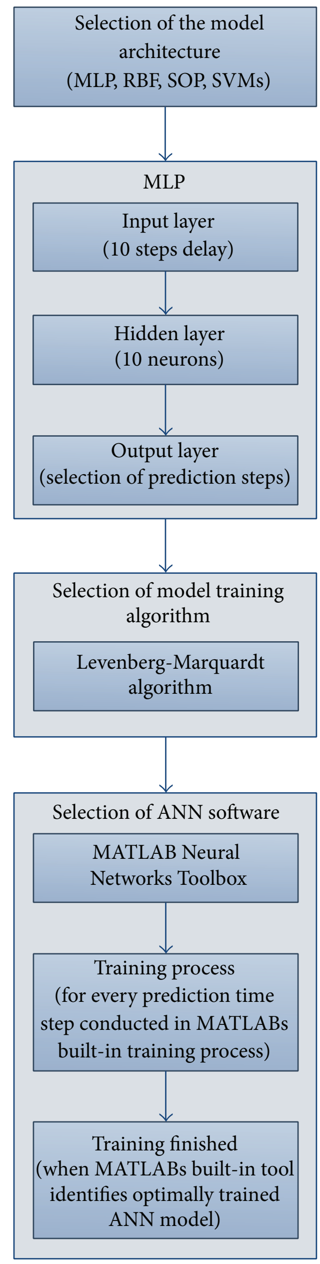

FIGURE 3: ANN implementation procedure.

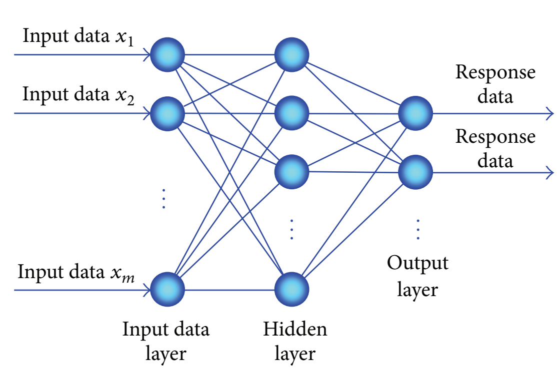

FIGURE 4: Multilayer perceptron (MLP) model [8].

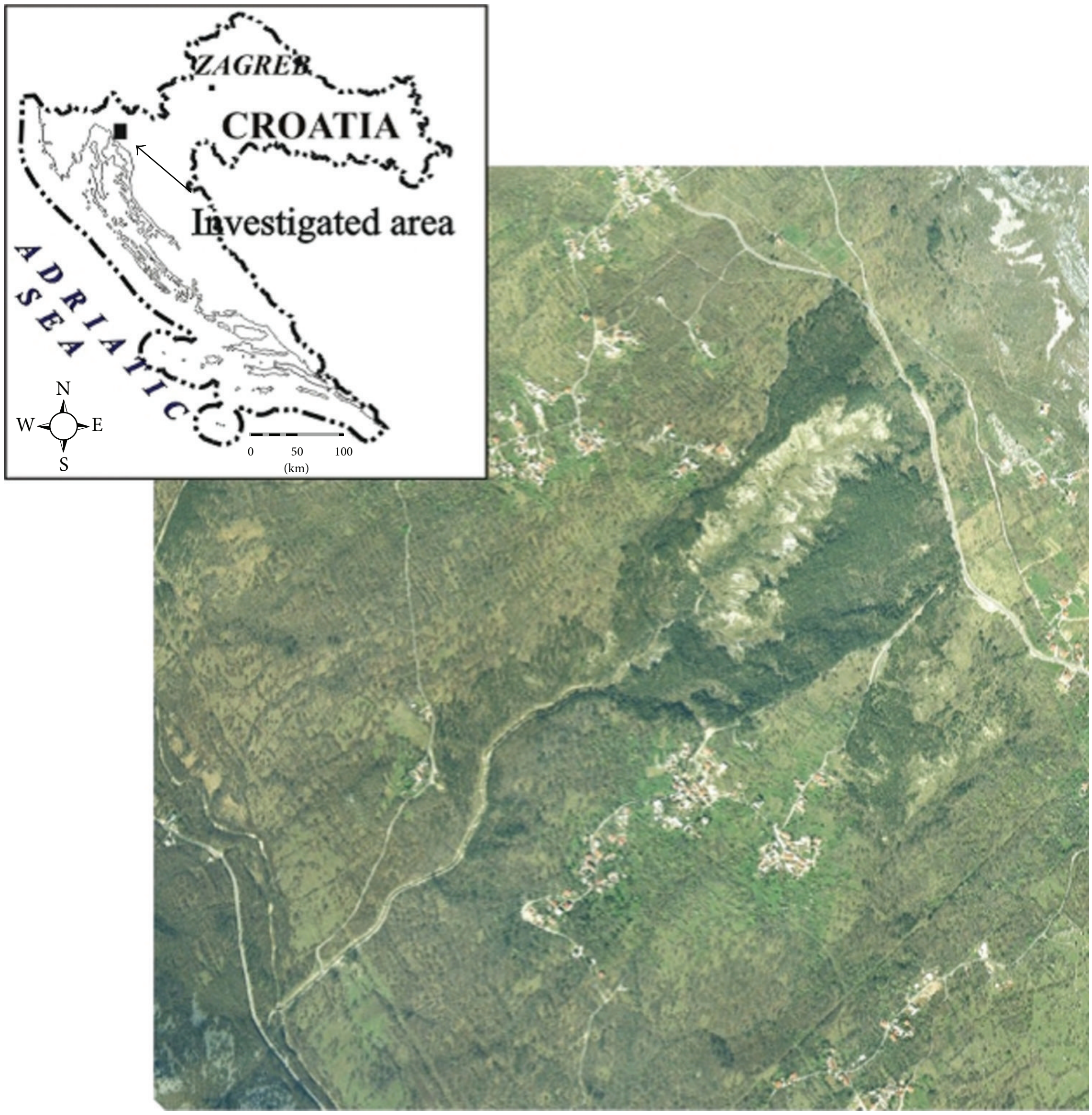

Figure 5: Location of the investigated area according to the Republic of Croatia map, with an aerial photograph of the Slani Potok catchment area [33].

cannot be applied to small catchments, whose resolution and time of prediction are more sensitive.

Therefore, in this paper, the methodology for developing data-driven predictive models, as well as its application and predictive ability as a function of the time step, is based on an artificial neural network (ANN) and is developed for small catchments (less than 5 km^2) as a basis for the establishment of an EWS.

An ANN can be classified as a parametric model that is generally lumped because rainfall-runoff processes are treated as a "black box" with inputs and outputs [6, 8, 9]. Additionally, ANNs are often less expensive and simpler to implement than other types of models [6, 8].

Recently, many studies have been conducted with the aim of predicting hydrogeological parameters with the help of an ANN, such as river discharge [6, 10, 11], flood prediction [12], pore-water pressure [13], lake water levels [14], ground water levels [15], water resources prediction [16], peak flow estimates [17], evaporation estimation [18], river water temperature [19], and water quality modelling [20].

All of these studies were prepared for large catchments, whereas few studies consider small catchments, perhaps because they do not represent an enormous hazard risk compared to large ones or because it is widely accepted that it is difficult to predict flash floods, mud flows, or debris flows for catchments that are small and have short rainfall response periods [21]. However, although hazards associated with small catchments do not seem intimidating, they still exist and can cause the same hazards as large areas.

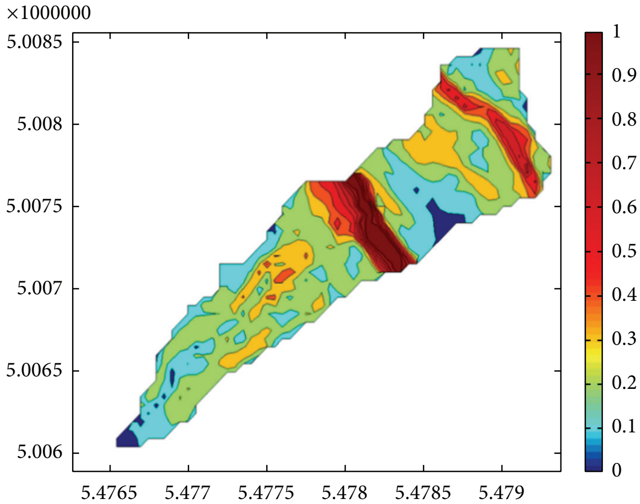

FIGURE 6: Slope map of the Slani Potok catchment area.

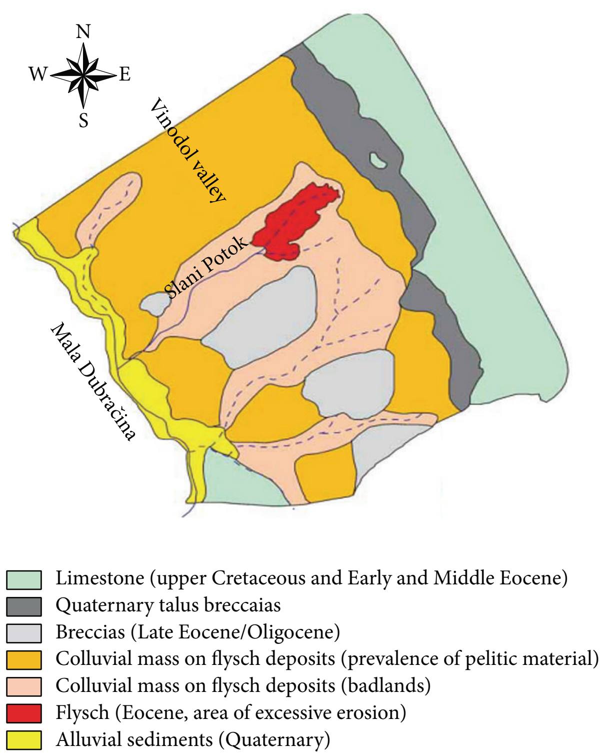

FIGURE 7: Schematized geologic map of the Vinodol valley with the Slani Potok catchment area [33].

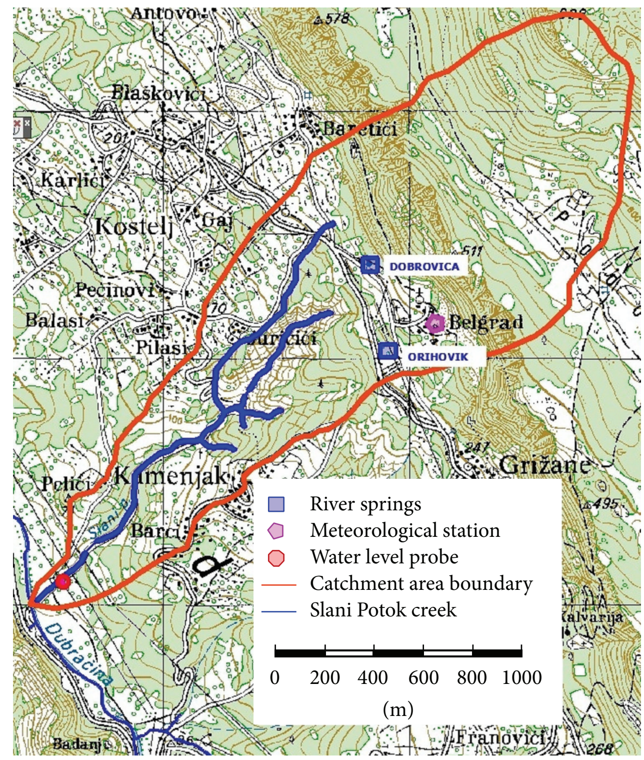

FIGURE 8: Location of the monitoring points in the Slani Potok catchment.

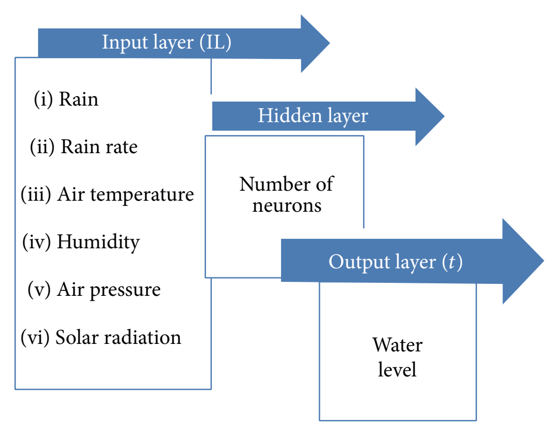

FIGURE 9: Schematized ANN model structure.

2. Methodology for the Development of Data-Driven ANN Predictive Models for Small Catchments

There are already many existing guidelines and methodologies for the development of rainfall-runoff data-driven models [22, 23], and all of them are generally based on three main steps: (i) monitoring, (ii) modelling, and (iii) evaluation. Those steps can also be scaled for predictive ANN modelling in small catchments, whose development flowchart is shown in Figure 1.

2.1. Monitoring. As shown in Figure 1, before monitoring points in the research area are established, it is important to collect all of the available historical data, such as information on constructed hydraulic structures (e.g., river network, river regulation), geology (e.g., soil type, erosion, and landslide-affected areas), land use (e.g., types of vegetation coverage, areas used for agriculture), and anthropology (e.g., urban areas, traffic infrastructures, and illegal waste disposals),

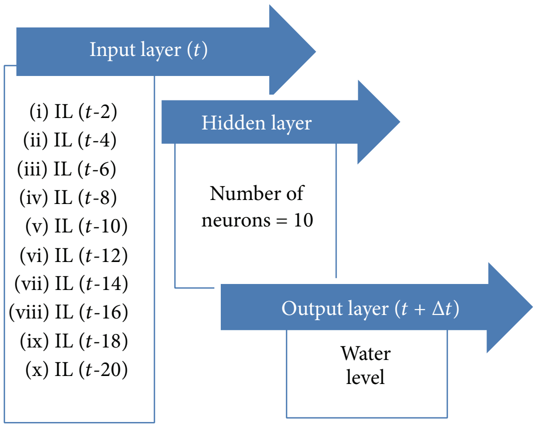

Figure 10: Schematized ANN prediction model.

Table 1: Boundary scale for validation and evaluation criteria.

Validation/evaluation boundary and scale criteria	CE ⟨−∞, +1]	r^2 [−1, +1]
Very good	⟨0.75, 1.00]	⟨—0.75—, —1—]
Good	⟨0.65, 0.75]	/
Poor	⟨0.5, 0.65]	⟨—0.50—, —0.75—]
Very poor	≤0.5	<—0.5—

as well as historical data (e.g., affected areas in the past, implemented structural and nonstructural measures).

After the available data are collected, continuous monitoring of meteorological and hydrological parameters should be set to recognize triggering factors that can lead to the hazard events and to represent the basis of every model. The establishment of monitoring with at least one metrological station and water level monitoring point is highly recommended.

Before developing the model, small catchments should be monitored for a sufficiently long period to have a range of several heavy rain events in different periods of the year, with a minimum period of two years. Additionally, the time step of meteorological and hydrological measurements should not be longer than five minutes.

2.2. Modelling. After collecting a sufficient amount of measured data, the model development can begin by identifying model inputs and outputs. For the purpose of modelling the small catchment using the ANN model with a small time step, the measured data must be processed to remove data noise and to identify possible systematic errors because they can lead to appreciable model prediction errors. If data processing did not remove all errors, data collection procedure must be verified until the problem is resolved. The entire procedure of data processing is shown in Figure 1.

The ANN model is chosen to apply the predictive model to the small catchment because it is a fast and efficient model that can rapidly predict hazards caused by the activity of water, thus leaving sufficient time to announce a hazard notification.

An ANN is a massively parallel distributed processor that has a natural propensity for storing experiential knowledge and making it available for use. It resembles the brain in two respects: (i) knowledge is acquired by the network through a learning process and (ii) interneuron connection strengths, known as synaptic weights, are used to store the knowledge [24].

The main microstructural component of the ANN is the artificial neuron node, whose model is shown in Figure 2.

An artificial neuron node can also be defined by the following mathematical expressions:

$$o_k = \varphi(v_k), \qquad v_k = \sum_{n=0}^{m} (w_k \times x_k)_n, \tag{1}$$

where o_k is the response of the neuron node in the kth epoch of the calculation, v_k is the sum of products of the weight coefficients w_k, x_k is the input data in the kth epoch of the calculation, and φ is the activation function of the neuron node.

As shown in Figure 1, ANN implementation consists of (i) selection of the adequate ANN architecture and training algorithm and (ii) ANN training procedure. ANN implementation procedure is shown in Figure 3.

ANN implementation in prediction model according to Figure 3 starts with the selection of the ANN mesostructure, which refer to the type of network (architecture) with which the model will be built. This structure can in turn be generally divided into static and dynamic ones; this is followed by the selection of the activation function [8, 9]. The most common types of networks used in the development of rainfall-runoff models are (i) multilayer perceptron (MLP), (ii) radial basis function (RBF), (iii) self-organizing map (SOP), and (iv) support vector machines (SVMs) [9]. The MLP architecture is the best choice for data-driven prediction model development [8]. The MLP architecture can be described as a static feed forward neuron network that consists of a minimum of three layers: (i) input, (ii) hidden, and (iii) output, as shown in Figure 4. Every layer consists of neurons that are connected by activation functions. Activation functions can be (i) linear, (ii) limited linear, (iii) unipolar sigmoid, (iv) bipolar sigmoid, or (v) hyperbolic tangent, among others [9, 12]. Their purpose is to direct data through the layers of the network from the input layer to the output layer. The numbers of neurons in the input and output layers are defined by the number of selected data, whereas the number of neurons in the hidden layer should be optimized to avoid overfitting the model, defined as the loss of predictive ability [9].

The MLP architecture was introduced by Werbos in 1974 in his Ph.D. thesis [25]. Its final form was introduced by Rumelhart, Hinton, and Williams in 1986 [26], who also presented applications of the MLP architecture and a description of its success in prediction, classification, and association related to real problems.

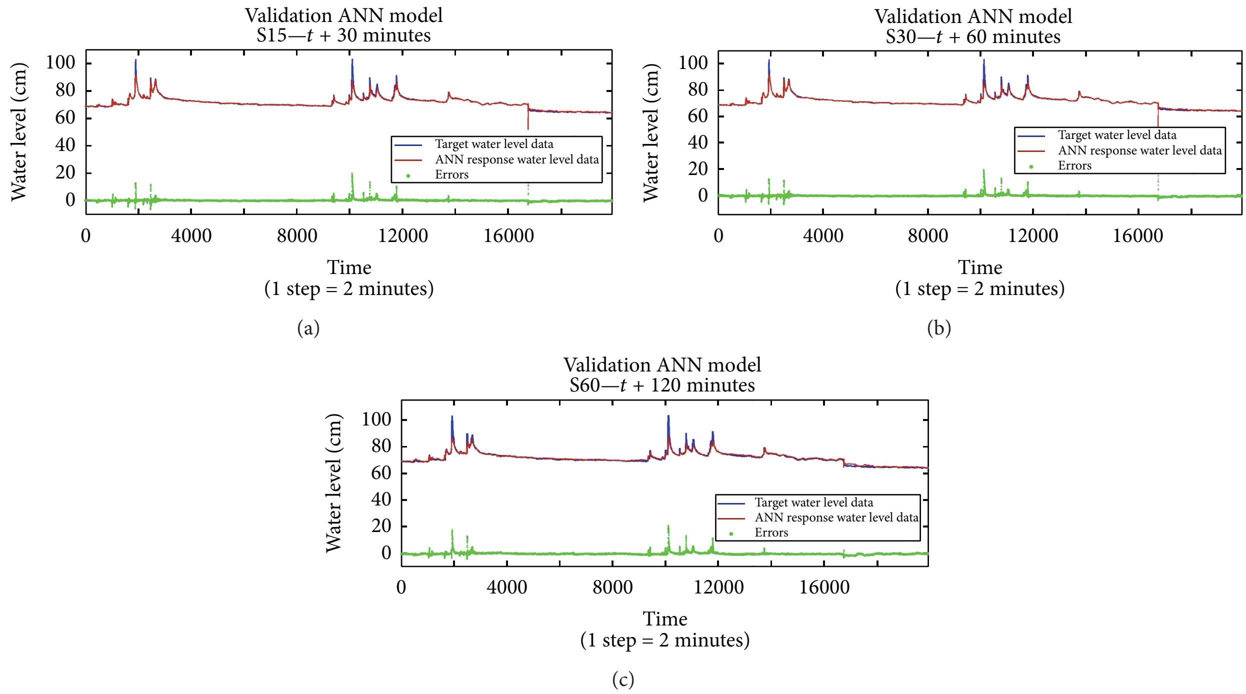

FIGURE 11: Graphical presentation of the target water level data and response water level data for the ANN model during validation: (a) S15, (b) S30, and (c) S60.

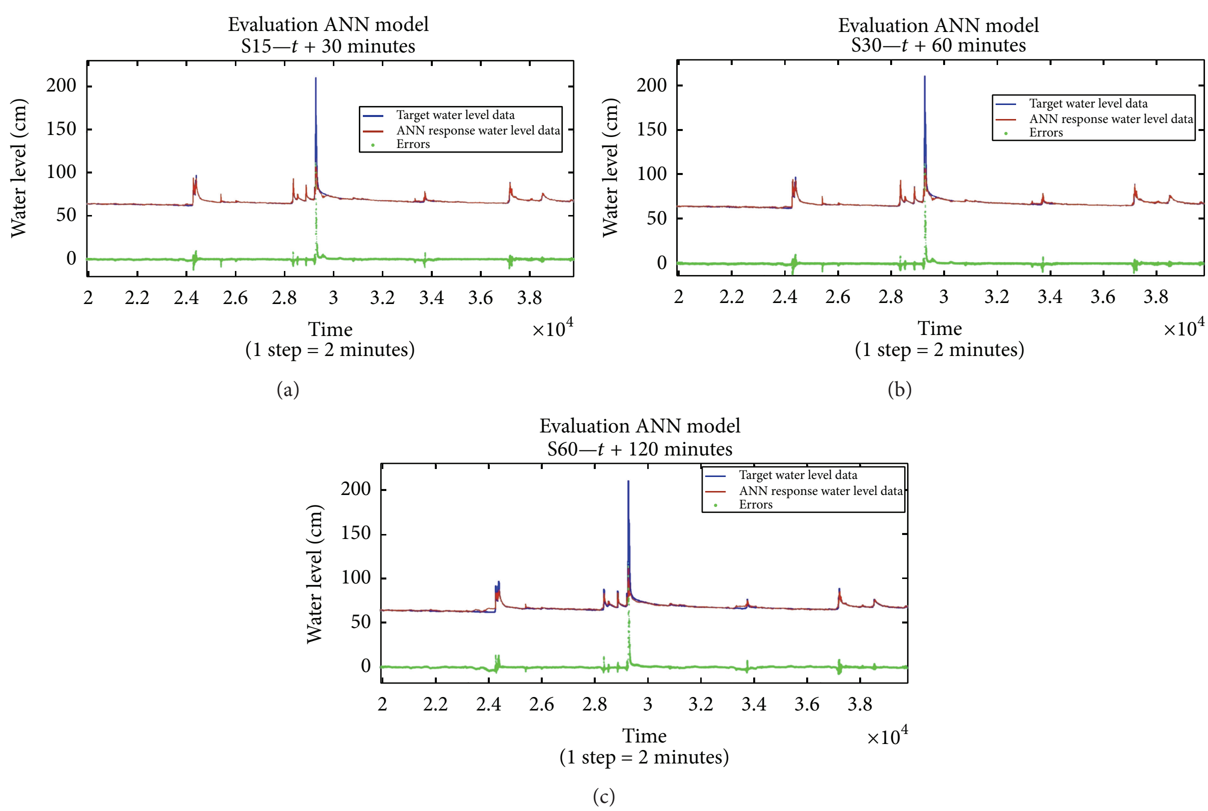

FIGURE 12: Graphical presentation of the target data and response of the ANN prediction model during evaluation: (a) S15, (b) S30, and (c) S60.

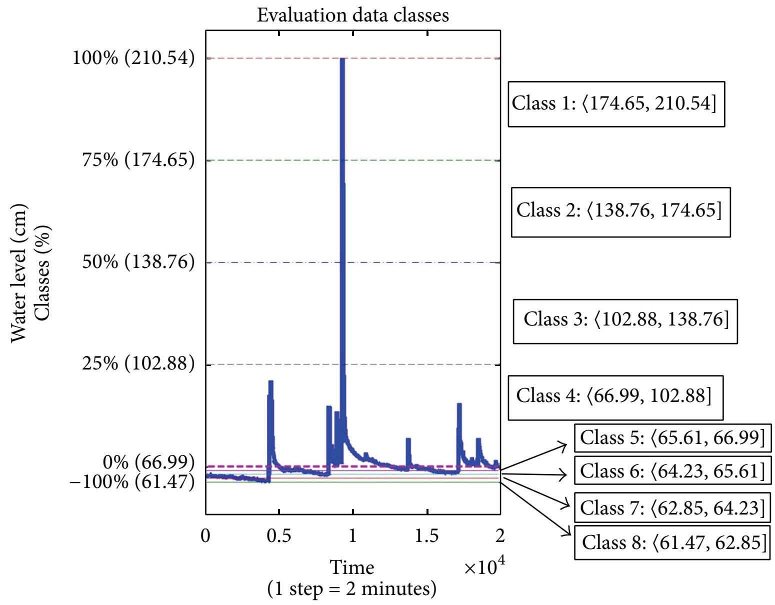

Figure 13: Evaluation classes of the target water level data.

Table 2: Statistics of data used for training and evaluation of the ANN model.

Statistics*	Input layer Rain [mm]	Rain rate [mm/h]	Air temperature [°C]	Humidity [%]	Air pressure [hPa]	Solar radiation [W/m^2]	Output layer Water level [cm]
Model training data							
n	92948	92948	92948	92948	92948	92948	92948
Max.	7.68	230.4	33.3	96	773	1092	156.7
Min.	0	0	5.8	32	750.2	0	8.1
μ	0.0066	0.20	16.78	68.68	762.42	113.25	64.90
σ	0.0955	2.86	4.58	14.88	3.86	214.69	7.79
Model validation data							
n	19912	19912	19912	19912	19912	19912	19912
Max.	2.85	85.4	27.5	96	772.1	860.0	104.0
Min.	0	0	6.20	47.0	753.7	0	63.3
μ	0.0053	0.158	12.78	76.03	762.43	60.20	70.88
σ	0.0558	1.6744	4.89	10.81	4.41	131.85	4.47
Model evaluation data							
n	19912	19912	19912	19912	19912	19912	19912
Max.	10.11	303.2	29.8	95	764.80	938	210.54
Min.	0	0	14.1	38	752.6	0	61.47
μ	0.0166	0.499	21.14	69.80	760.66	151.77	66.99
Σ	0.218	6.525	3.37	12.76	2.25	229.973	5.86

*n: number of observation; Max.: maximum; Min.: minimum; μ: sample mean; σ: standard deviation.

For the purpose of predictive hydrological ANN model development it is important that input layer consist of the data with minimum ten delay steps and output layer with prediction time step as presented in Figure 3. Delay steps can be defined as input data from previous time steps.

Because the output data from the network in one epoch of calculation will have errors, which are a function of the target output and model response in the output layer, an algorithm for determining the change Δw_k of the weight coefficient w_k is needed. These algorithms are known as training algorithms because they optimize input data in each following epoch, which reduces the error in the output layer with respect to the target output. The optimization of the weight coefficient can be defined as

$$w_{k+1} = w_k + \Delta w_k, \tag{2}$$

Table 3: Performance statistics of the ANN model during validation.

Validation prediction step	MSE	r^2
S15 (t + 30 minutes)	0.603	0.960
S30 (t + 60 minutes)	1.150	0.940
S60 (t + 120 minutes)	1.391	0.932

Table 4: Performance statistics of the ANN model during evaluation.

Evaluation prediction step	MSE	MSRE	CE	r^2
S15	5.737	0.0003	0.833	0.902
S30	9.359	0.0005	0.728	0.849
S60	11.656	0.0007	0.661	0.809

where w_{k+1} is the weight coefficient in the $k+1$th epoch and Δw_k is the change determined by the training algorithm.

Training algorithms can be divided into three groups: (i) first-order local algorithms (error backpropagation, generalized delta rule), (ii) second-order local algorithms (Newton algorithm, quasi-Newton algorithm, and Levenberg-Marquardt (LM) algorithm), and (iii) global algorithms (genetic algorithm, simulated annealing, and evolutionary programming) [9, 27].

The LM algorithm is the fastest and most appropriate for training simpler structures [28] under the MLP architecture, and it was specially developed for the training of ANNs. Because of those characteristics, this algorithm is proposed for the development of data-driven ANN models for small catchments as shown in ANN implementation procedure flowchart (Figure 3).

Using the second-order local algorithms, the change measure Δw_k is obtained from the squared approximation of the error function, which is represented by the Hessian matrix. Because the Hessian matrix typically cannot be used in ANN training and because it is not in compliance with appropriate conditions and is thus unsolvable, algorithms that avoid solving the Hessian matrix, such as the LM algorithm, are used.

The LM algorithm [29], which is a special combination of the Gauss-Newton and error backpropagation algorithms, uses a conjugate gradient method by introducing the Jacobian matrix instead of the Hessian matrix. The change measure Δw_k can be defined as

$$\Delta w_k = -\left(\mathbf{J}^T * \mathbf{J} + \mu * \mathbf{I}\right)^{-1} \times \mathbf{J}^T * \mathbf{e}, \quad (3)$$

where $\mathbf{J}$ is the Jacobian matrix of the error vector e with respect to the weight coefficients in the kth epoch of the calculation, $\mathbf{J}^T$ is the transpose of the Jacobian matrix, and μ is a scalar representing the learning rate.

The Jacobian matrix of networks errors can be written as

$$\mathbf{J} = \frac{\partial \mathbf{e}}{\partial w} = \begin{bmatrix} \frac{\partial \mathbf{e}_1}{\partial w_1} & \frac{\partial \mathbf{e}_1}{\partial w_2} & \cdots & \frac{\partial \mathbf{e}_1}{\partial w_n} \\ \frac{\partial \mathbf{e}_2}{\partial w_1} & \frac{\partial \mathbf{e}_2}{\partial w_2} & \cdots & \frac{\partial \mathbf{e}_2}{\partial w_n} \\ \vdots & \vdots & & \vdots \\ \frac{\partial \mathbf{e}_n}{\partial w_1} & \frac{\partial \mathbf{e}_n}{\partial w_2} & \cdots & \frac{\partial \mathbf{e}_n}{\partial w_n} \end{bmatrix}, \quad (4)$$

where $\mathbf{J}$ is the Jacobian matrix of the network errors, $\mathbf{e}_1, \mathbf{e}_2, \ldots, \mathbf{e}_n$ are the errors, and $w_1, w_2, \ldots, w_n$ are the weight coefficients.

At the end of every calculating epoch, the sum squared error $E(e)$ is calculated as follows:

$$E(e) = \sum_{k=1}^{n} (e_k)^2 = \sum_{k=1}^{n} (d_k - o_k)^2, \quad (5)$$

where e_k is the error in kth epoch of the calculation, d_k is the target value, and o_k is the response model value in kth epoch of the calculation.

Depending on the increase or decrease in the sum squared error $E(e)$, the learning rate scalar μ changes through every epoch of the calculation by dividing or multiplying by a constant factor (e.g., β in the range $[0, 1]$) to control the LM algorithm to be more similar to the Gauss-Newton error backpropagation algorithm and also to increase the training speed. If the sum of squared errors increases, the learning rate scalar μ will be multiplied by a constant amount β, and the LM algorithm will be more similar to the Gauss-Newton algorithm; otherwise, it will be more similar to the backpropagation algorithm.

After the architecture of the ANN and the training algorithm are determined, the software should be chosen in order to conduct ANN training process as shown in Figure 3. There is a variety of prepared software programs available for ANN modelling, such as Brainmaker Professional, NeuralWorks Professional II/Plus, Explorer from Neural Ware Inc., WEKA, MATLAB Neural Network Toolbox, and Statistica [8, 9]. For the purpose of this study, MATLAB Neural Network Toolbox is proposed because it provides built-in training process that stops when the ANN is adequately trained. ANN model should be trained for every time prediction step and, after training process, validated and evaluated as presented in model development flowchart (Figure 1).

2.3. Validation and Evaluation. Assessment of the model during the training period is considered the model validation, and it cannot be used as criteria with which to evaluate the predictive abilities of the ANN model. Validation is defined as an assessment of the errors between the ANN model response and the target training data, and it can be represented by the same measures as the evaluation, the most common being the mean square error (MSE) and the coefficient of determination (r^2), which are defined by (6) and (9), respectively.

Validation boundary and scale criteria according to validation measures are presented in Table 1. If validation process

Table 5: Performance statistics of the ANN model during evaluation: mean absolute error (MAE) for the data classes.

	Target data versus output data [cm]		S15	S30	S60
	Maximum absolute error [cm]		98.24	111.34	117.37
Class	Percentage [%]	Water level class limits [cm]		MAE	
1	[100, 75⟩	[210.5, 174.65⟩	82.54	100.47	101.32
2	[75, 50⟩	[174.65, 138.76⟩	38.7	53.30	59.80
3	[50, 25⟩	[138.76, 102.88⟩	13.55	24.94	34.39
4	[25, 0⟩	[102.88, 66.99⟩	0.56	0.74	0.84
5	[0, −25⟩	[66.99, 65.61⟩	0.29	0.44	0.71
6	[−25, −50⟩	[65.61, 64.23⟩	0.23	0.67	1.35
7	[−50, −75⟩	[64.23, 62.85⟩	0.23	0.41	0.44
8	[−75, −100]	[62.85, 61.47]	0.21	0.28	0.45

has indicated that the model is “poor” or “very poor,” the model should be improved. Figure 1 shows four possible steps for the model improvement: (i) reduction of the prediction time step, (ii) increase of the data monitoring collection period, (iii) selection of the different ANN architecture and/or training algorithm, or (iv) identification of the error in modelling process. If model improvement did not result in problem solving, then ANN is not appropriate for predictive purposes of small catchments.

The evaluation of the model, as shown in Figure 1, is considered to be an assessment of the predictive ability of the time step of the ANN model. As mentioned before, evaluation of ANN models and of predictive models in general is problematic. There are a large number of evaluative measures that are widely used, and they can be divided into visual and quantitative measures. Visual evaluation measures are considered to be graphical representations of the ANN model response and target data in the form of the graph, which provides insight into errors in the model output. The most commonly used calculation evaluation measures are the MSE, the mean square relative error (MSRE), the Nash-Sutcliffe coefficient (CE), and coefficient of determination (r^2) [8, 30]. The MSE and MSRE are measures that indicate error in the units (or squared units) of the model, and CE and r^2 describe the degree of collinearity between modelled and measured data [29]. The described measures can be defined by the following equations:

$$\mathrm{MSE} = \frac{1}{n}\sum_{k=1}^{n}\left(d_k - o_k\right)^2, \tag{6}$$

$$\mathrm{MSRE} = \frac{1}{n}\sum_{k=1}^{n}\left(\frac{d_k - o_k}{d_k}\right)^2, \tag{7}$$

$$\mathrm{CE} = 1 - \frac{\sum_{k=1}^{n}\left(d_k - o_k\right)^2}{\sum_{k=1}^{n}\left(d_k - \overline{d}\right)^2}, \tag{8}$$

$$r^2 = \left[\frac{\sum_{k=1}^{n}\left(d_k - \overline{d}\right)\left(o_k - \overline{o}\right)}{\sqrt{\sum_{k=1}^{n}\left(d_k - \overline{d}\right)^2\sum_{k=1}^{n}\left(o_k - \overline{o}\right)^2}}\right]^2, \tag{9}$$

where n is the number of data points in the input layer, d_k is the target value, o_k is the model response value in the kth epoch of the calculation, $\overline{d}$ is the mean value of the target data, and $\overline{o}$ is the mean value of the network response data.

These measures provide insight into the global model errors, but it is impossible to determine the distribution of the errors from those measures. Many studies have been published on classification approaches to model evaluation, such as seasonal weather data classification [31], classification of the predictions according to the percentage of observed data, or measurement of the mean absolute error (MAE) and root mean squared error (RMSE) for all predicted peak flood events in a data set [32]. Thus, for ANN model evaluation in small catchments, the classification of the errors is proposed in this paper. This evaluation consists of separating the data into evaluation classes considering the mean value of the data and the percentage classes above or below the mean value in the range of −100% below the mean value to 100% above the mean value, as well as performance of the MAE of every class. This evaluation measure ensures the visibility of error clustering. The mean absolute error can be defined as

$$\mathrm{MAE} = \frac{1}{n}\sum_{k=1}^{n}\left|d_k - o_k\right|, \tag{10}$$

where d_k is the target value and o_k is the model response value in the kth epoch of calculation.

The model quality boundary criteria of the validation and evaluation measures for the MSE, MSRE, and MAE are not strictly defined, but it is preferred that they be as small as possible, with a value of 0 indicating a perfect fit. Quality boundaries of the CE and r^2 measures are shown in Table 1 [7, 8].

Because ANN models operate as universal optimizers and are able to replicate any input data to output data, evaluations must be performed with data that are not used during the training process. In this manner, generalization properties can be evaluated. In other words, it is possible to determine whether the ANN model is able to produce good responses according to learned similar events from the training process.

3. Implementation of the Model

3.1. Location of the Research Area and Geological and Hydrological Characteristics. The Slani Potok catchment is a part of the Dubračina River catchment area, located in the central part of the Vinodol valley, as shown in Figure 5. The Vinodol valley is a separated geographical entity of the eastern Kvarner area in the Republic of Croatia, and it is a unique spatial unit between the Križišće village to the northwest, the city of Novi Vinodolski to southeast, and the Vinodol channel.

The Slani Potok catchment area can be considered an example of combined erosion. Excessive surface erosion occurs in an area that is 600 m in length and 250 m in width. Side effects around the erosion centre include local landslides, which result from weathering of the flysch rock mass. This affected area is approximately 3 km^2 large, and the surrounding settlements of Belgrade, Baretići, Grižane, and Kamenjak, as well as the surrounding roads, are at risk. Because of mentioned hazard risk, this area was chosen as the case study area under the bilateral Croatian-Japanese project "Risk Identification and Land-Use Planning for Disaster Mitigation of Landslides and Floods in Croatia" coordinated by the Research Centre for Natural Hazards and Disaster Recovery of the Niigata University in Japan. Within this project's timeframe (from 2009 to 2014) monitoring of the meteorological and hydrological parameters was established. The same case study area research continued, financed by the University of Rijeka in the Republic of Croatia, as part of the scientific project "Water Resources Hydrology and Floods and Mud Flow Risks Identification in the Karstic Area." Results of aforementioned research became the foundation for the hydrological model development based on ANN methodology.

The Slani Potok catchment has an area of approximately 2 km^2, and its altitude extends from 50 to 700 m a.s.l. The average slope of the catchment area is 22%, and the slopes range from 5% to 100%, as shown in Figure 6. Therefore, this catchment area is characterized as being very steep. The lower part of the catchment area (0.9 km^2) is formed in flysch sediments (mainly siltstone), and it contributes the majority of the surface runoff. The upper part of the catchment area is a karstic plateau from which the runoff is insignificant. A schematized geologic map of the area is shown in Figure 7. In the karstic and flysch contact zone, several overflow springs are placed, contributing the majority of the water balance in the dry season.

As noted in Figure 7, the Slani Potok catchment area is known as an example where erosion is combined with local landslides. Together with water activity, these landslides have resulted in an increasing occurrence of flash floods, mud flows, and debris flows in the last 100 years.

The main problem with this surface erosion area is the impossibility of reconstruction or mitigation of erosion processes or human activity. Therefore, it is essential to establish EWSs to notify residents about the possibility of occurrence of a hazard in a timely manner. The study catchment is small, with a large coefficient of runoff, distinct steep slopes, and a short response time of the rain event, which means that the time period from the beginning of the rain event until the maximum hydrograph peak can be measured in minutes. Therefore, it is essential to develop a model with the capability for fast response, such as a data-driven ANN model.

3.2. Data Collection. Continuous data monitoring points of the hydrological and meteorological parameters have been established since 2012. Water levels in the Slani Potok creek waterbed are measured by a Mini Diver pressure probe (manufactured by Schlumberger Water Services) at the mouth of the Slani Potok creek as it enters the Dubračina River. Meteorological parameters were measured using a Vantage Pro 2 meteorological station (manufactured by Davis Instruments Corporation) near Belgrade with a measurement frequency interval of two minutes. The position of the installed equipment is presented in Figure 8. After three years of data collection, rain events from 2013 were selected as the representative data set.

3.3. Data Processing and Model Implementation. Because this area is known as a hazard area, the impact of the rainfall on the erosion base was recognized many years ago. An immediate hazard is possible when the rainfall starts to erode the surface, causing local landslides, which bring mud and debris mixed with water downstream.

Selection of the input layer data and output layer data was conducted to develop the ANN model. In this case study, the following meteorological parameters were selected as input data: (i) rain, (ii) rain rate, (iii) air temperature, (iv) humidity, (v) air pressure, and (vi) solar radiation. River water levels were used as output data (target data), as shown in Figure 9. Those meteorological parameters were selected because they directly or indirectly influence the prediction of the rain event or because they define the hydrometeorological conditions of the catchment.

Using the software MATLAB 2012a (MathWorks, Natick, Massachusetts, US), selected data were processed to recognize errors and then locally smoothed by using locally weighted polynomial regression (LOESS method) [34] to eliminate data noise, and then the time between input and output layers was synchronized. After data processing, data were divided into training, validation, and evaluation data in a proportion of 70% for training, 15% for validation, and 15% for evaluation. Statistics of the data used for the model are shown in Table 2.

The training data included 92,948 samples, with over ten large rain events that caused a maximum water level of 156.7 cm. The validation data included 19,912 samples with six rain events, with a maximum water level of 104.0 cm. The evaluation data set included 19,912 samples with five rain events, one of which resulted in a water level of 210.54 cm and induced debris flow and infrastructure damage; thus, this data set is excellent for evaluating the predictive ability of the model.

As described in the methodology of this paper, an MLP mesostructure is used to develop the data-driven ANN model for small catchments, with sigmoid and linear activation functions trained by the LM algorithm. The model is conducted with the help of the software MATLAB 2012a Neural Network Toolbox (MathWorks, Natick, Massachusetts, US).

To test the predictive capability of the model, ten steps of delay were used in the input layer. In other words, meteorological parameters from the last ten measured parameters (twenty minutes) were used in every step of the calculation. In the output layer, future steps for prediction at the fifteenth step (S15; $t + 30$ minutes), thirtieth step (S30; $t + 60$ minutes), and sixtieth step (S60; $t + 120$ minutes) were selected. The schematized structure of the prediction model is shown in Figure 10.

Furthermore, 10 neurons are chosen to provide calculation in the hidden layer.

Validation of the developed model, after the training process and according to the proposed measures, is presented visually by comparing the water level targets with the ANN model response in Figure 11, as well as by calculations according to (6) and (9) for all prediction steps, as shown in Table 3.

The validation results have shown that each of three prediction steps can be used, but their prediction quality must be evaluated. The validation measures presented in Table 3 for the MSE are small in all prediction steps, which means that the models do not have many global errors. r^2 indicates that the models can be categorized as "very good" according to the model quality criteria in Table 1. Additionally, by visual comparison of the target data with the response of the ANN model in Figure 11, a good match with the data is visible, with some deviations in the maximum water levels.

3.4. Water Level Prediction Capability: Model Results and Discussion. The predictive ability of the model is tested by visual and quantitative evaluation measures for prediction steps S15, S30, and S60. A graphical presentation of the water level target data and the ANN model response is shown in Figure 12. The performance of the model is quantitatively evaluated according to (6), (7), (8), and (9), as shown in Table 4.

Because the model was evaluated using a data set that consists of data that were not used in the training process and the data set included one large rain event that caused a hazard, it is visibly apparent in Figure 12 that errors in the prediction of the maximum water levels increase at every prediction step. Additionally, prediction of the other water levels did not result in large errors at all of the prediction steps. Although the visual evaluation indicates errors in the high water level prediction, the models still have a good time response to increases in water level.

The results of the quantitative evaluation measures (see Table 4) indicate an increase in the errors at every step of the prediction, as expected. The MSE and MSRE measures indicate small global errors in the models. The evaluation measure CE, according to the model quality criteria boundaries presented in Table 1, categorized prediction model S15 as "very good" and models S30 and S60 as "good," whereas evaluation measure r^2 categorized all prediction steps in the models as "very good." The calculation evaluation measures show that all prediction models are usable for the prediction and do not reproduce large global model errors. Visual evaluation errors are recognized in predictions of high water levels. Therefore, to evaluate the predictive models using target water level data, data must be categorized into classes to recognize error clustering.

Error clustering of the prediction models was evaluated by categorizing the target data into classes and solving (10) on every class. The data classes are presented in Figure 13, and the results of the class evaluation are presented in Table 5.

The error clustering evaluation performed by the MAE shows that, for all prediction steps, the majority of the errors are placed in classes 1, 2, and 3. In other words, the values of evaluation measure MAE are larger if the predicted water level is in the range above 25% of the mean water level. In the data range between −100% and 25% of the data set, the MAE value is small aside from model S60, which showed large errors for all visual and quantitative evaluation measures. Therefore, the S15 and S30 models can be used for prediction purposes.

The conducted evaluation indicates that, for all prediction steps, errors in maximum water levels occurred and increased at each time prediction step. The majority of errors are clustered near maximum water level predictions, which can be explained by the use of a data set, for the training process, that did not have a sufficient variety in water levels to predict the maximum water level, which was not used in the training process.

For the development of the EWS, the main objective is to obtain a model that is able to predict the time when the water level will start to increase according to meteorological parameters; this objective has been fulfilled. After the evaluation data set is implemented in the training process, the errors in maximum water level are expected to decrease, and, thus, the models will have better water level prediction performance.

According to the visual and calculated evaluation measures, it is difficult to determine which prediction step is optimal for use because all of the measures (apart from MAE) categorized model S15 as "very good" and models S30 and S60 as "good." As noted above, there is a significant problem in evaluation of the models. In this case, it is the best to exclude model S60 because visual evaluation and the MAE indicated large clustering errors.

4. Conclusions

In this paper, the methodology for a data-driven ANN model for the prediction of river water levels conducted from meteorological parameters as a basis for EWS development in a small catchment is proposed. The model is implemented for the case study of the Slani Potok catchment in the Republic of Croatia, and its predictive ability is evaluated. An MLP mesostructure, with sigmoid and linear activation functions trained by the LM algorithm, is used in the ANN model development. The developed model was trained, validated, and evaluated on data set with 132,772 monitored meteorological and hydrological parameter samples that were divided in the proportions of 70% for training, 15% for validation, and 15% for verification. The predictive ability of the model was tested for time steps of thirty minutes (S15), sixty minutes (S30), and one hundred and twenty minutes (S60).

The validation of the models resulted in their classification as "very good" (with small global error) for all prediction steps.

Common quantitative evaluation measures (MSE, MSRE, CE, and r^2) of the developed models showed that the predictive abilities of the models are classified as "very good" for model S15 and as "good" for models S30 and S60. The evaluation measure r^2 categorized all model prediction steps as "very good." Visual evaluation indicated errors in the prediction of high water levels. Thus, new measures for evaluating prediction error clustering in the small catchment were proposed. The error clustering evaluation was based on the MAE for the target data set and divided into percentage classes according to the mean data value. This showed substantial clustering of the errors in the prediction of the maximum water levels, which are 25% to 100% larger than the mean value of the water level in the Slani Potok river bed for the S30 and S60 models. Those models were developed based on the observed data sets, implying that a data set with larger variety in the training process will yield an improved prediction performance.

Overall, the evaluation also showed that all models accurately predict the time when the water level starts increasing. Additionally, the evaluation showed that the model's response is more important for the development of the EWS than precise water level prediction when considering the short time of the response of water level to rainfall in the small catchments.

The conducted evaluation demonstrates that the models S15 and S30 can be used for the prediction. For EWS development, the prediction time for a small catchment does not have to be long, so a prediction time based on a maximum time step of sixty minutes (S30) can be considered sufficiently long to announce a hazard.

The proposed methodology for the development, validation, and evaluation of predictive models for a small catchment can serve as the basis for the implementation of the EWS if continuous meteorological and hydrological monitoring, measured on a short time frequency, is established.

Conflict of Interests

The authors declare that there is no conflict of interests regarding the publication of this paper.

Acknowledgments

The research for this paper was conducted within the bilateral international Croatian-Japanese project "Risk Identification and Land-Use Planning for Disaster Mitigation of Landslides and Floods in Croatia," as well as a part of the scientific project "Water Resources Hydrology and Floods and Mud Flow Risks Identification in the Karstic Area" financed by the University of Rijeka.

References

[1] K. Smith, *Environmental Hazards: Assessing Risk and Reducing Disaster*, Routledge, New York, NY, USA, 6th edition, 2013.

[2] D. Norbiato, M. Borga, S. Degli Esposti, E. Gaume, and S. Anquetin, "Flash flood warning based on rainfall thresholds and soil moisture conditions: an assessment for gauged and ungauged basins," *Journal of Hydrology*, vol. 362, no. 3-4, pp. 274–290, 2008.

[3] K. Yano and A. Daido, "Fundamental study on mud-flow," *Bulletin of the Disaster Prevention Research Institute*, vol. 14, no. 2, pp. 69–83, 1965.

[4] T. Takahashi, *Debris Flow: Mechanics, Prediction and Countermeasures*, Taylor & Francis, London, UK, 2014.

[5] V. V. Krzhizhanovskaya, G. S. Shirshov, N. B. Melnikova et al., "Flood early warning system: design, implementation and computational modules," *Procedia Computer Science*, vol. 4, pp. 106–115, 2011.

[6] C. W. Dawson and R. L. Wilby, "Hydrological modelling using artificial neural networks," *Progress in Physical Geography*, vol. 25, no. 1, pp. 80–108, 2001.

[7] D. R. Legates and G. J. McCabe Jr., "Evaluating the use of 'goodness-of-fit' measures in hydrologic and hydroclimatic model validation," *Water Resources Research*, vol. 35, no. 1, pp. 233–241, 1999.

[8] R. J. Abrahart, P. E. Kneale, and L. M. See, *Neural Networks for Hydrological Modelling*, Taylor & Francis, London, UK, 2004.

[9] S. O. Haykin, *Neural Networks and Learning Machines*, Pearson Education, Upper Saddle River, NJ, USA, 3rd edition, 2009.

[10] M. Campolo, A. Soldati, and P. Andreussi, "Artificial neural network approach to flood forecasting in the river Arno," *Hydrological Sciences Journal*, vol. 48, no. 3, pp. 381–398, 2003.

[11] R. J. Abrahart and L. M. See, "Neural network modelling of non-linear hydrological relationships," *Hydrology and Earth System Sciences*, vol. 11, no. 5, pp. 1563–1579, 2007.

[12] N. Do Hoai, K. Udo, and A. Mano, "Downscaling global weather forecast outputs using ANN for flood prediction," *Journal of Applied Mathematics*, vol. 2011, Article ID 246286, 14 pages, 2011.

[13] M. R. Mustafa, R. B. Rezaur, H. Rahardjo, M. H. Isa, and A. Arif, "Artificial neural network modeling for spatial and temporal variations of pore-water pressure responses to rainfall," *Advances in Meteorology*, vol. 2015, Article ID 273730, 12 pages, 2015.

[14] C.-C. Young, W.-C. Liu, and W.-L. Hsieh, "Predicting the water level fluctuation in an Alpine lake using physically based, artificial neural network, and time series forecasting models," *Mathematical Problems in Engineering*, vol. 2015, Article ID 708204, 11 pages, 2015.

[15] I. N. Daliakopoulos, P. Coulibaly, and I. K. Tsanis, "Groundwater level forecasting using artificial neural networks," *Journal of Hydrology*, vol. 309, no. 1–4, pp. 229–240, 2005.

[16] H. R. Maier and G. C. Dandy, "Neural networks for the prediction and forecasting of water resources variables: a review of modelling issues and applications," *Environmental Modelling and Software*, vol. 15, no. 1, pp. 101–124, 2000.

[17] K. P. Sudheer, P. C. Nayak, and K. S. Ramasastri, "Improving peak flow estimates in artificial neural network river flow models," *Hydrological Processes*, vol. 17, no. 3, pp. 677–686, 2003.

[18] S. Trajkovic, B. Todorović, and M. Stanković, "Forecasting of reference evapotranspiration by artificial neural networks," *Journal of Irrigation and Drainage Engineering*, vol. 129, no. 6, pp. 454–457, 2003.

[19] A. Rabi, M. Hadzima-Nyarko, and M. Šperac, "Modelling river temperature from air temperature in the river Drava (Croatia)," *Hydrological Sciences Journal*, vol. 60, no. 9, pp. 1490–1507, 2015.

[20] W. B. Chen and W. C. Liu, "Water quality modelling in reservoirs using multivariate linear regression and two neural network models," *Advances in Artificial Neural Systems*, vol. 2015, Article ID 521721, 12 pages, 2015.

[21] C. G. Collier, "Flash flood forecasting: what are the limits of predictability?" *Quarterly Journal of the Royal Meteorological Society*, vol. 133, no. 622, pp. 3–23, 2007.

[22] D. C. Black, P. J. Wallbrink, and P. W. Jordan, "Towards best practice implementation and application of models for analysis of water resources management scenarios," *Environmental Modelling and Software*, vol. 52, pp. 136–148, 2014.

[23] A. M. Kaleth, "Rainfal-runoff modelling using artificial neural networks (ANNs): modelling and understanding," *Caspian Journal of Environmental Sciences*, vol. 6, no. 1, pp. 53–58, 2008.

[24] S. O. Haykin, *Neural Networks: A Comprehensive Foundation*, MacMillan, New York, NY, USA, 1994.

[25] P. J. Werbos, *Beyond regression: new tools for prediction and analysis in the behavioural sciences [Ph.D. thesis]*, Harvard University, Cambridge, Mass, USA, 1974.

[26] D. E. Rumelhart, G. E. Hinton, and R. J. Williams, "Learning representations by back-propagating errors," *Nature*, vol. 323, no. 6088, pp. 533–536, 1986.

[27] K. Madsen, N. B. Nielsen, and O. Tingleff, *Methods for Nonlinear Least Squares Problems*, Technical Report, Informatics and Mathematical Modelling, Technical University of Denmark, 2nd edition, 2004.

[28] H. B. Demuth and M. H. Beale, *Neural Network Toolbox, User's Guide*, MathWorks, Natick, Mass, USA, 2004.

[29] D. W. Marquardt, "An algorithm for least-squares estimation of nonlinear parameters," *Journal of the Society for Industrial and Applied Mathematics*, vol. 11, no. 2, pp. 431–441, 1963.

[30] D. N. Moriasi, J. G. Arnold, M. W. Van Liew, R. L. Bingner, R. D. Harmel, and T. L. Veith, "Model evaluation guidelines for systematic quantification of accuracy in watershed simulations," *American Society of Agricultural and Biological Engineers*, vol. 50, no. 3, pp. 885–900, 2007.

[31] A. Colman and M. Davey, "Prediction of summer temperature, rainfall and pressure in Europe from preceding winter North Atlantic Ocean temperature," *International Journal of Climatology*, vol. 19, no. 5, pp. 513–536, 1999.

[32] R. J. Abrahart and L. See, "Comparing neural network and autoregressive moving average techniques for the provision of continuous river flow forecasts in two contrasting catchments," *Hydrological Processes*, vol. 14, no. 11-12, pp. 2157–2172, 2000.

[33] D. Aljinović, V. Jurak, M. Mileusnić, D. Slovenec, and F. Presečki, "The origin and composition of flysch deposits as an attribute to the excessive erosion of the Slani Potok valley ('Salty Creek'), Croatia," *Geologia Croatica*, vol. 63, no. 3, pp. 313–322, 2010.

[34] W. S. Cleveland, "Robust locally weighted regression and smoothing scatterplots," *Journal of the American Statistical Association*, vol. 74, no. 368, pp. 829–836, 1979.

Hindawi Publishing Corporation
Advances in Meteorology
Volume 2016, Article ID 8364134, 13 pages
http://dx.doi.org/10.1155/2016/8364134

Research Article

Severe Weather Caused by Heat Island and Sea Breeze Effects in the Metropolitan Area of São Paulo, Brazil

Felipe Vemado and Augusto José Pereira Filho

Departamento de Ciências Atmosféricas, Instituto de Astronomia, Geofísica e Ciências Atmosféricas, Universidade de São Paulo, 05508–090 São Paulo, SP, Brazil

Correspondence should be addressed to Felipe Vemado; vemado@model.iag.usp.br

Received 18 June 2015; Revised 21 August 2015; Accepted 3 September 2015

Academic Editor: Shahaboddin Shamshirband

The Metropolitan Area of São Paulo (MASP) is one of the most populated regions of the planet with one of the largest impervious regions as well. This research work aims to characterize MASP heat island (HI) effect and its interaction with the local sea breeze (SB) inflow in rainfall amounts and deep convection. The combined SB-HI produces direct circulation over the MASP and produces severe weather and socioeconomic impacts. All SB-HI episodes between 2005 and 2008 are identified and analyzed with surface and upper air measurements, weather radar, and satellite data. The current work indicates that intense SB-HI episodes are related to air and dew point temperatures above 30°C and 20°C, respectively, right after the passage of the SB front over MASP. Results indicate that the precipitation related to SB-HI episodes is up to 600 mm or about four times higher than that in rural or less urbanized areas in its surroundings. Measurements indicate that 74% of SB-HI episodes are related to NW winds in earlier afternoon hours. Moving cold fronts in southern Brazil tend to intensify the SB-HI circulation in MASP. A conceptual model of these patterns is presented in this paper.

1. Introduction

The Metropolitan Area of São Paulo has 39 municipalities with São Paulo city being the largest one with an area of 8051 km^2 with a 20 million population according to Brazilian Geography Institute, 2010. Frequently, severe weather systems cause major socioeconomic impacts in the São Paulo megacity such as the ones related to cold fronts, sea breeze circulation, mesoscale convective systems, and isolated convection [1–3] with heavy rainfall, wind gusts, hailstones, and lightning. SB circulation reaches MASP more than half of the days throughout the year. Oliveira and Dias [4] analyzed several instances of sea breeze (SB) and indicated wind veering from NE to SE, backing from NW to SE, and intensification of the SE wind. Pereira Filho et al. [5] studied the SB and HI effects on rainfall accumulation in the Metropolitan Area of São Paulo (MASP) and found that weak synoptic conditions, air temperature, and dew point above 30°C, respectively, in the afternoon hours tended to result in heavy precipitation. Oliveira and Dias [4] reported many instances of summer convection in the MASP preceded by changes in wind direction from NW to SE associated with temperature drop and dew point temperature increase. The SB intensifies as it moves across Serra do Mar ridge and injects Atlantic Ocean moisture in the MASP. The SB intensity and inland displacement are modulated by the HI effect in the MASP [6, 7], and the distance propagated over landmass [8], topography, and atmospheric stability [9]. The differential heating in the Serra do Mar ridge induces vertical motion along its steep scarp (Figure 1) and intensifies the SB circulation along the mountain range [10, 11]. Pereira Filho et al. [1] analyzed 18 episodes of floods in MASP associated with SB (Figure 2). Vertical mixing of relative warmer and drier urban boundary layer air with relatively cooler and moister SB air at its frontal region turns the air unstable and updrafts develop to deep convection driven by latent heat release. The effect of large urban areas on rainfall is an issue of several research works. Shepherd et al. [12] used the Tropical Rainfall Measurement Mission (TRMM) satellite to confirm the increase of rainfall downwind urban areas

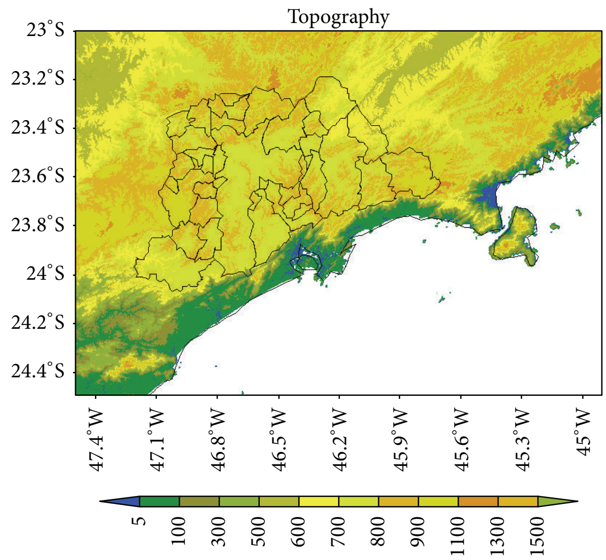

Figure 1: Topography of Eastern São Paulo State. Contours, geographic coordinates, and political boundaries are indicated. Color bar indicates altitudes (m).

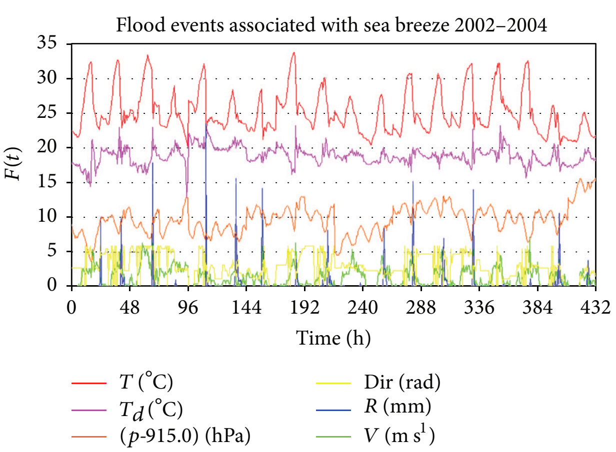

Figure 2: Temporal evolution of air temperature (red), dew point (pink), atmospheric pressure (orange), rainfall accumulated (blue), wind direction (yellow), and wind intensity (green) of 18 floods events. Font: Pereira Filho et al. [1].

of USA. Accumulated and rainfall rate increases with the increase of the city area. Kusaka et al. [13] showed that urbanization caused an increase in precipitation in Tokyo metropolitan area and less precipitation in inland areas.

The SB circulation in Eastern São Paulo State is so regular that it can be clearly seen in the numerical modeling climatology of hourly winds between 2005 and 2007 as an inertial circulation (Figure 3). Surface winds back NW to SE between 1500 UTC and 1600 UTC over MASP similar to those observed by Oliveira and Dias [4].

This work analyzes all SB events between 2005 and 2008 associated with thunderstorms in MASP as well as synoptic conditions that enhance local circulation and intensity of thunderstorms. SB and synoptic scale timing for maximizing deep convection efficiency is also investigated in the present work. Many studies have characterized the effect of urban areas in precipitation and its spatial distribution but less emphasize on temporal and spatial phase looking at different systems scales. The results of this research can be a useful nowcasting rule for MASP and other similar metropolitan areas of the planet.

Urban Heat Island. The temperature gradient between urban areas and their surrounding areas is called urban heat island (UHI) [14]. The average annual temperature in the inner city is higher than in the surroundings. In dry winter days, the temperature gradient can reach 10°C or more in the late afternoon and early evening [15, 16]. The temperature difference between urban and rural New York City is 5°C during nighttime in summer [17]. The UHI is characterized by anthropic sources of heat within urban areas that absorbs short wave irradiation and converts it into sensible heat [18]. Under clear sky conditions and during the night, the temperature is more dependent on microscale urban features [19].

The UHI is a microclimate change of anthropic nature, changing rural surfaces to urban ones altering energy fluxes of latent heat (less) and sensible heat (more). The irradiance is used for evapotranspiration in a rural area, but, in an urban area, it is stored up and increases the sensible heat flux to the atmospheric boundary layer [14, 20]. A thermal low forms and induces convergence and vertical mixing of relatively warmer and drier air near surface with cooler and drier air aloft, so the boundary layer becomes deeper and even drier as surface air temperature increases and dew point decreases until the inflow of SB front. So, UHI environments are in general warmer and drier in relation to rural ones [21].

The MASP topography is complex and varies from 650 m to 1200 m. It is 50 km from the coast of São Paulo State. The SB circulation in MASP is intensified by the Serra do Mar scarps resulting in higher precipitation over it. Since MASP is at tropical latitudes, differential heating tends to induce more intense and persistent direct circulations [22]. The MASP UHI becomes even more intense under weak synoptic conditions [23] and amplifies rural-urban temperature gradients resulting in stronger and deeper thermal circulation between morning and midafternoon when the advection of moisture by the SB increases moist static instability and deep convection develops with subsequent heavy rainfall [1, 2]. Moreover, Han et al. [24] showed that higher aerosol concentration in urban areas results in increased concentration of smaller cloud drops and higher condensational heating that yields stronger updrafts, larger liquid water content, enhanced higher level riming and melting, and, consequently, enhancement of precipitation downwind of the urban area.

Freitas et al. [25] suggested that UHI accelerates the SB front thus yielding longer and intense updrafts. Farias et al. [26] observed higher frequency of negative cloud-to-ground (CG) lightning flashes and lower for positive CG ones over MASP. Their results are similar to other megacities where air pollution and UHI are suggested as main factors [26].

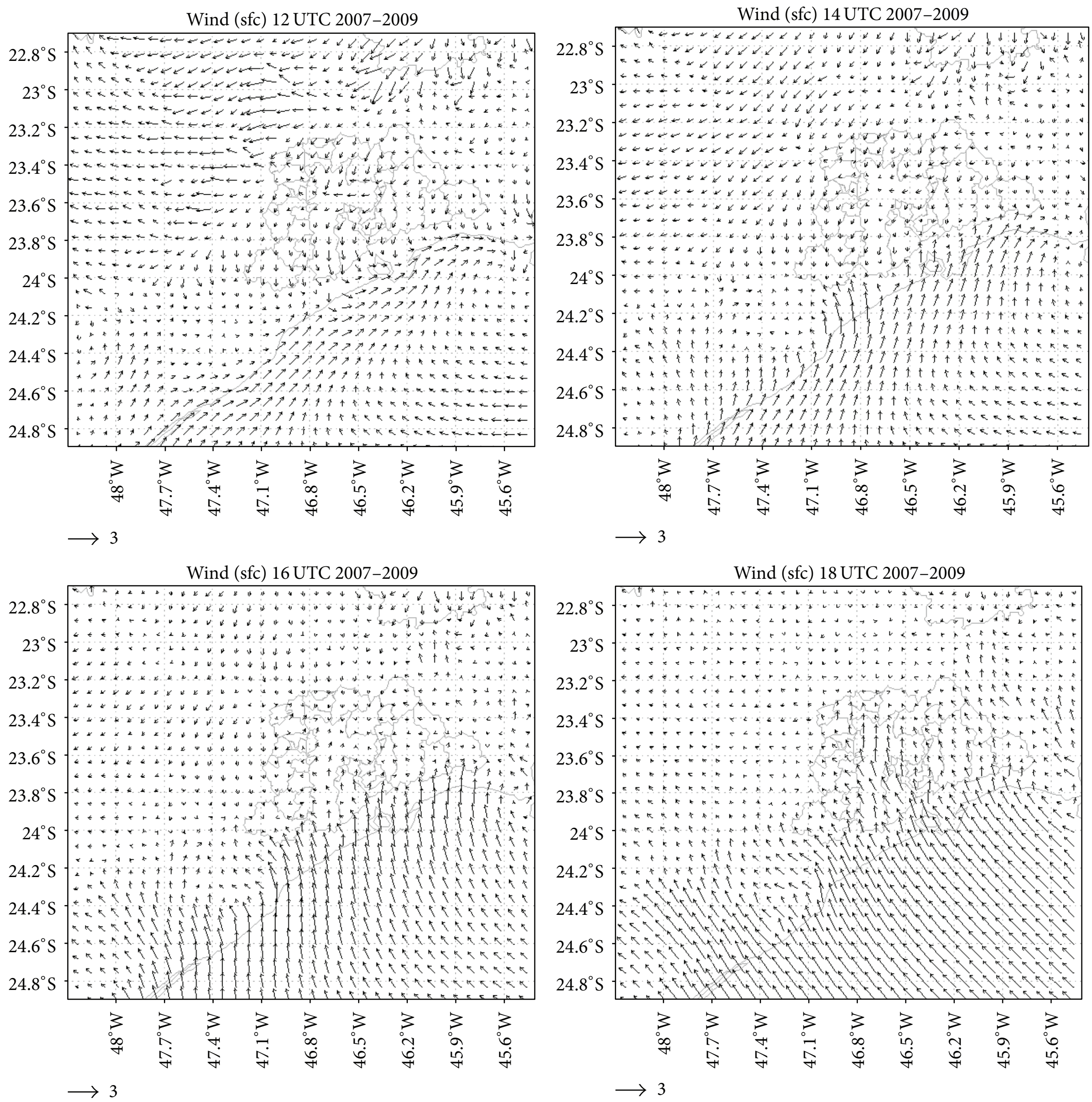

Figure 3: Hourly mean wind (m s^{-1}) climatology between January 2007 and December 2009 obtained with ARPS simulations. Contours, geographic coordinates, and political boundaries are indicated.

Storms. Storms develop in response to the convective available potential energy (CAPE) in the atmosphere. The storms have been linked to radiative, thermodynamic, and dynamic processes that regularly produce atmospheric instability. These physical processes trigger new dynamic and thermodynamic conditions in a well-defined cycle of events [27]. Convection ceases when CAPE is dissipated or when heat and moist fluxes are interrupted. Convective cells are produced at the local scale under such thermodynamics conditions and influenced by synoptic scale dynamics [28]. Convective forecasting depends on complex thermodynamic, dynamic, and microphysical processes at cloud scale. Thunderstorms develop in a matter of minutes where near-the-surface warm and most air is underlying cold and dry air aloft in association with a lifting mechanism [29]. Atmospheric model performance is limited by unknown triggering mechanisms of convection [30].

Figure 4 shows convective events associated with SB. Vicente et al. [31] indicate that 36% of storms in East São Paulo State between 1990 and 1995 occurred in the afternoon hours. In general, model circulation and precipitation have high and low performance, respectively [32]. Thunderstorms simulated with the Advanced Regional Prediction System (ARPS) [33–36] in MASP indicate that even little changes in boundary and initial conditions can drastically displace the convective cells. However, the ARPS system is able to simulate

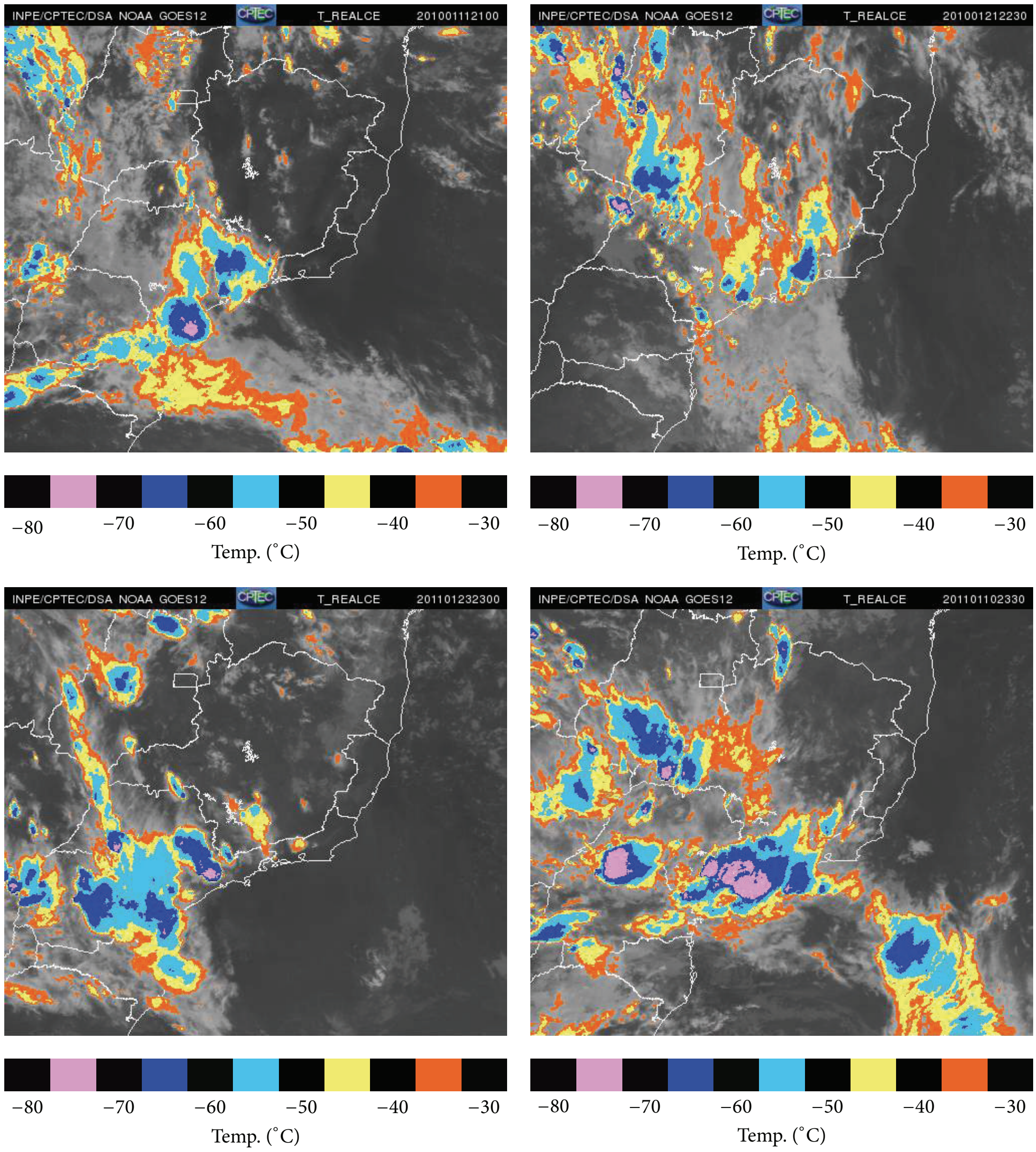

Figure 4: GOES-12 enhanced IR images of cloudiness associated with sea breeze related deep convection events. Contours, geographic coordinates, and political boundaries are indicated. Colors indicated the brightness temperatures. Source: INPE.

the strength of convective cells as well as the interaction between the SB and gust fronts [37, 38] where horizontal vorticity resulting from the SB front and thunderstorm gust fronts result in stronger upward motion [39].

2. Materials and Methods

A total of 125 SB events related to heavy rainfall were selected in three and half years of observations. GOES-8 and GOES-12 Satellites infrared images with 4-km resolution have been used in association with weather station measurements, upper air soundings, the São Paulo weather radar (SPWR), rainfall rate estimates at 3-km altitude, polarimetric variables of the mobile X-POL weather [40], the Global Forecast System (GFS) of National Centers for Environmental Prediction (NCEP), and ARPS. These measurements are briefly described below.

2.1. The São Paulo Weather Radar. The São Paulo S-band weather radar is located at Ponte Nova City near a Serra do Mar ridge at 916 m altitude. It has been operational since 1988. Volume scans are obtained every 5 minutes to estimate rainfall rates [41] at a constant altitude with 2-km × 2-km horizontal resolution. Figure 5 shows an instance of thunderstorms caused by the SB within the surveillance area of the SPWR. Episodes with rainfall rates above 30 mm h^{-1} that lasted for more than 10 minutes related to SB were

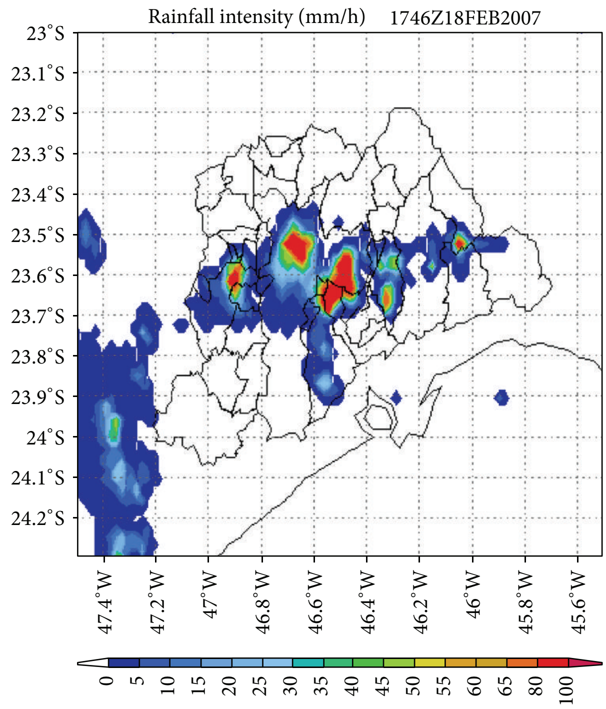

Figure 5: SPRW rainfall rate CAPPI showing thunderstorms at 1746 UTC on February 18, 2007. Color bar indicates rainfall rates (mm hr^{-1}).

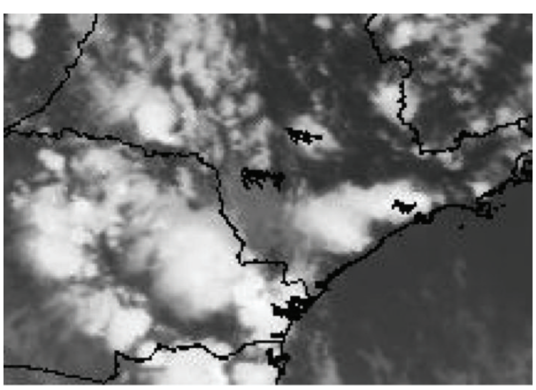

Figure 6: GOES-12 IR image over Eastern São Paulo State at 1800 UTC on January 11, 2010.

selected. Figure 6 shows the respective GOES-12 IR image of the SB episode.

2.2. Satellite GOES-12. GOES-12 IR images provided by CPTEC-INPE were analyzed at 30-minute time intervals. Cloud brightness temperatures below −30°C were enhanced. Figure 4 shows the inset of storms developed by the SB and the UHI circulation.

2.3. Surface Measurement. Temperature (°C), relative humidity (%), air pressure (hPa), wind speed (m s^{-1}) and direction (°), precipitation (mm), and cloud cover fraction are regularly measured at Congonhas and Campo de Marte Airports and by the IAG-USP weather station. The datasets were used to select SB episodes between January 2005 and April 2008, using the identification method developed by Oliveira and Dias [4]. These events were identified by changes in wind direction and intensity, air temperature decrease, and dew point temperature increase [4] for days with convective activity in the MASP. Figure 5 shows the estimated rainfall rate field by the SPWR at 1746 UTC February 18, 2007, associated with NW winds that backed to SE after 1500 UTC when the SB front moved into MASP (not shown). Constant SSE winds after the SB front passage were used to select the episodes. Satellite images were also used to verify cloudiness and its depth along the coast of São Paulo State.

2.4. MXPOL Weather Radar. The mobile weather radar X-band Doppler termed MXPOL is a multifunctional system that provides polarimetric data with high spatial resolution [40]. It measures raw and adjusted reflectivity (Z), radial velocity (V_r), spectral width (W), differential reflectivity (Z_{DR}), propagation differential phase (φ_{DP}), specific differential phase (K_{DP}), and correlation coefficient lag zero of the signal co-pol and cross-pol H V ($\rho_{0\mathrm{HV}}$). Its software produces constant elevation (PPI) and altitude (CAPPI) maps, vertical cross-sections (RH), and echo tops (ECHOTOP) of the above variables as well as fields of rainfall accumulation, vertically integrated liquid water (VIL), and others. MXPOL was positioned West of the MASP in Barueri City (Figure 7) at 23° 29′ 59.6″S and 46° 54′ 18.6″W [40]. PPI products at elevations 0.6° and 1.2° were used to identify moving boundaries detected by targets such as shaft, insects, and small cumulus droplets forming in the SB front. Figure 7 shows an episode of SB in late afternoon on January 11, 2010, that produced deep thunderstorms with reflectivity above 55 dBZ (hail).

2.5. Soundings. Radiosounding measurements made at Campo de Marte Airport at 0000 UTC and 1200 UTC were used. The variables are air temperature (°C), dew point (°C), wind speed (m s^{-1}) and direction (°), air pressure (hPa), geopotential height (m), water vapour mixing ratio (g kg^{-1}), potential temperature (K), virtual potential temperature (K) and equivalent potential temperature (K), convective available potential energy (CAPE) (J kg^{-1}), convective inhibition (CINI) (J kg^{-1}), and precipitable water (mm). The CAPE (1) and IL index (2) obtained with the soundings were compared to the ones simulated with ARPS system (Section 2.6):

$$\mathrm{CAPE} = g\int_{\mathrm{NCL}}^{\mathrm{NE}} \left(\frac{\theta_{ep(\mathrm{NCL})} - \theta_{esa}}{\theta_{esa}}\right) dZ, \quad (1)$$

where NCL is lifting condensation level (m); NE is equilibrium level (m); θ_{ep} is equivalent potential temperature of an air parcel (K); and θ_{esa} is saturated equivalent environment potential temperature (K);

$$\mathrm{IL} = T_{500} - T'_{500}, \quad (2)$$

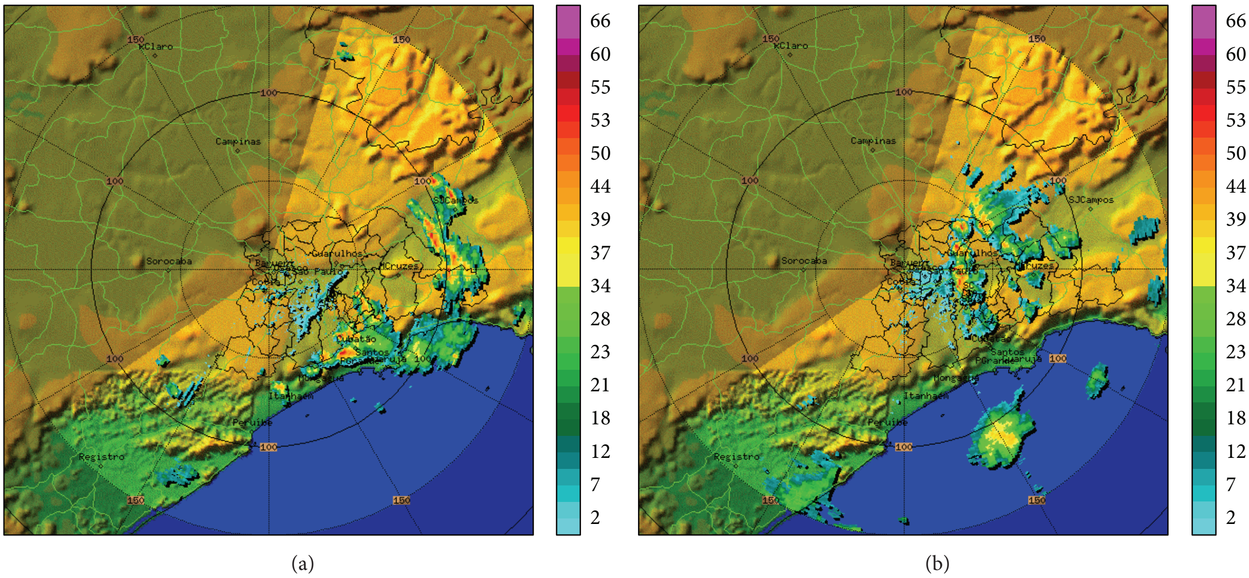

Figure 7: MXPOL PPI of reflectivities (dBZ) at 1800 UTC (a) and 2030 UTC (b) on January 11, 2010. Colors indicate reflectivities (dBZ). Contours, geographic boundaries, radial and azimuthal distances, and political boundaries are indicated.

where T_{500} is air temperature (°C) at 500 hPa and T'_{500} is air temperature (°C) by lifting an air parcel with the mean mixing ratio from 500 hPa.

2.6. The ARPS System. The ARPS system was described by Xue et al. [35, 42]. It runs twice daily since 2005 at the computing facility of Laboratório de Hidrometeorologia (LABHIDRO) at IAG-USP. The domain has two nested grids at 12 km and 2 km resolution. The latter is centered in the MASP region but the former is used in the present work. The boundary and initial conditions were provided by GFS model outputs in the domain shown in Figure 10.

2.7. Global Forecast System (GFS). GFS is a spectral weather forecast model with 64 vertical levels running four times a day by the National Centers for Environmental Prediction (NCEP). It covers the whole globe at a 28-km horizontal resolution. GFS results at 1° resolution were input as boundary and initial conditions to ARPS runs at 12-km spatial resolution. The GFS predicts weather up to 16 days in advance. Its complete documentation can be found at http://www.emc.ncep.noaa.gov/GFS.

3. Results

All SB and UHI heavy rainfall episodes measured with the SPWR were analyzed between 2005 and 2008. The respective synoptic features were obtained with the GFS and the local circulation and instability indexes with the ARPS simulations at 12-km grid resolution.

3.1. Characteristics of SB Episodes. 125 SB episodes were selected with deep thunderstorms in MASP. It was obtained with weather stations that episodes of surface wind veering from NW to SE made up 74% of all of them, 11% from NE to SE, and 15% due to intensification of SE winds during the day. The frequency of storms due to NW winds days agrees with that obtained by Rodriguez et al. [43]. The average dew point temperatures before and after the SB front inflow at IAG's weather station were 17.9°C and 20.7°C, respectively. Similarly, average air temperatures before and after the SB front inflow were 28.6°C and 24.9°C, respectively. At Campo de Marte Airport average air temperatures were 29.7°C and 25.8°C. Noteworthily, the estimates were obtained with data one hour before and one hour after the SB front passage at both weather station locations.

The average SB front speed between both weather stations was 9 m s^{-1}. There have been just four episodes where the SB front did not reach Campo de Marte Airport. Winds were from N to W between 2 and 3 m s^{-1}. The maximum air temperature was less than 27°C and temperature gradients between MASP and Serra do Mar scarp seemed to be considerably lower, consequently the SB dissipated before moving across MASP.

Episodes with dew point temperature less than 15°C before the SB front incoming yielded weak ordinary convective cells and friction quickly dissipates the SB front. However, higher dew point temperatures yielded frequent deeper and stronger convective cells. Downdrafts and gusts near the rear flank induced its faster displacement by cooling downdrafts resulting from higher temperature gradients near the surface about the SB front. Under clear air condition and low dew point, the UHI intensifies [19] and so to produce convective cells over MASP the SB circulation needs to be deeper and stronger.

Most episodes of heavy precipitation associated with SB occur between October and April. Table 1 shows our results about the mean time of SB front passage at IAG's weather station estimated with Oliveira and Dias [4] method.

Table 1: Mean time of SB incoming in each weather station. LT indicates local time.

Year	Campo de Marte airport (SBMT)	Congonhas airport (SBSP)	IAG-USP (Cientec)
2005	1936 UTC (17:36 LT)	1827 UTC (16:27 LT)	1817 UTC (16:17 LT)
2006	1912 UTC (17:12 LT)	1815 UTC (16:15 LT)	1809 UTC (16:09 LT)
2007	1918 UTC (17:18 LT)	1818 UTC (16:18 LT)	1814 UTC (16:17 LT)

The average SB displacement time between IAG and Campo de Marte Airport was 1 hour. In general, heavy precipitation cells over MASP have been triggered at 1800 UTC. Noteworthily, earlier or later times episodes were weaker, probably due to near surface colder air temperatures and little or no precipitation occurs [1].

The time of the SB front inset allows the nowcasting of heavy rain. The SB front can be monitored by reflectivity MXPOL measurements on clear air mode (Figure 7) together with air and dew point temperatures at the weather stations providing a good tool to predict storms over MASP.

3.2. Rainfall Analysis. Figure 8 shows the spatial distribution of precipitation accumulation within the SPWR surveillance area for all SB episodes. The maximum accumulation was 600 mm downstream from the maximum urbanization in MASP. It agrees with previous studies [12, 24] that indicate downstream sensible heat advection associated with the UHI. Similar rainfall distribution was obtained for all episodes in a given year between 2005 and 2008. A secondary maximum has been observed in Vale do Paraíba (West of MASP) due to valley-mountain differential heating [44].

Figure 9 shows the spatial distribution of the normalized difference vegetation index (NDVI). Lower NDVIs are associated with urban areas [45] and are close to maximum precipitation region over MASP. The current study indicated that 74% of all SB episodes were related to NW winds early afternoon and the maximum rainfall accumulation was downwind of urbanization with lower NDVIs or SE of MASP due to prevailing winds from NW. Baik and Chun [46] and Shepherd et al. [12] found similar results about the advection of HI in other cities. Other rainfall maxima in Figure 8 are related to topography effects.

3.3. Synoptic Patterns and Instability. Hourly mean fields of wind, temperature, and relative humidity at 1000 hPa, 850 hPa, 500 hPa, and 200 hPa pressure levels have been obtained from ARPS runs at 12 km resolution for the 125 SB episodes. Figure 10 shows the 1000-hPa wind field. The results of this research show that ARPS simulation of the time in which the SB has reached IAG's weather station perfectly matches observations (1800 UTC). The wind field direction is from N to NE in early morning and from N to NW in early afternoon and then shifts to SE after 1800 UTC. Figure 11 shows the 1000-hPa mean divergence field with main positive and negative lines of divergence along the coast of São Paulo associated with updrafts (sea breeze) and downdrafts (land breeze), respectively. Figure 14 shows our estimated conceptual model for synoptic conditions for a typical SB episode over MASP. In general, a cold front is moving through over South Brazil, which tends to intensify NW circulation and convergence against the SB front midafternoon.

Vale do Ribeira region is to the SW of MASP about 50-km from the Coastline forming a valley with warmer temperature that induces upward motion and the SB front push earlier than in MASP region. Indeed, we noted that CAPE is generally higher in Vale do Ribeira that accelerates SB front (Figure 12). CAPE values simulated with the ARPS model vary between 1750 J kg^{-1} and 2000 J kg^{-1} over MASP. Results indicate that all SB episodes trigger thunderstorms only under moist unstable environments over MASP. In several SB episodes high CAPE with no CINI inhibit vigorous thunderstorms since CAPE is reduced by generalized convection. Emanuel [47] suggested that under CINI only some convective cells are formed and so updrafts are stronger and induce stronger downdrafts in the nearby environment of the thunderstorms. The mean CINI is −40 J kg^{-1} in MASP so that it hinders convection and CAPE dissipation [47]. The local circulation induced by the UHI yields updrafts over MASP added to the one by the SB front circulation. Figure 15 shows a conceptual model of such circulation with a 2-km deep SB circulation. Since CAPE is only one index of thunderstorm potential, the lifting index, IL [48], was also used. The ARPS mean IL varied between −1.5°C to −2.0°C and −3.5°C to −4.0°C at 1200 UTC and 1600 UTC, respectively. Higher IL has been observed in West and Vale do Ribeira in São Paulo and Mato Grosso do Sul State. They well agree with the warming observed in these regions. The mean CAPE obtained from soundings at Campo de Marte Airport at 1200 UTC was 616 J kg^{-1} against ARPS 559 J kg^{-1} and IL −2.2°C (observed) and −1.5°C (ARPS), respectively. In general, ARPS is in good agreement with observation, though it tends to underestimate IL and properly estimates CAPE.

Synoptic conditions associated with SB episodes show the Bolivian High circulation over Brazil and the South Atlantic subtropical high at low levels with Northerly winds over São Paulo State in the morning. The SB circulation stretches itself throughout the Coastline of Brazil in the afternoon with an average depth of 2-km. In general, a moving cold front in Southern South America is also present. The circulation patterns at 500 hPa and 200 hPa levels are shown in Figure 13. Anticyclonic circulation is over Mato Grosso do Sul and zonal winds are over the São Paulo State (500 hPa) and the circulation is due to Bolivia's high at 200 hPa.

4. Conclusions

The MASP is prone to severe weather with major impacts on society given its steady urban growth in the past decades with microclimate changes induced by anthropic sources that produced the urban heat island effect. It tends to increase precipitation over MASP especially in summer. The warmer urban environment intensifies thunderstorms and

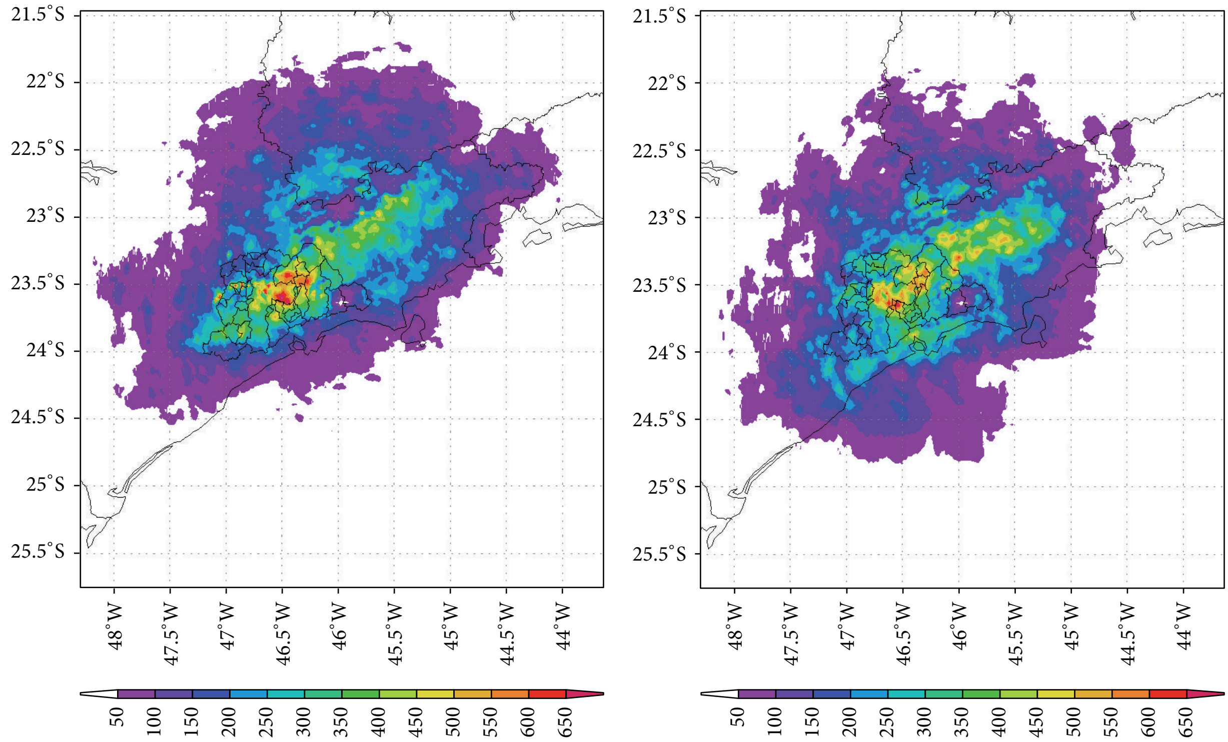

(a) (b)

Figure 8: SPWR estimated rainfall accumulation (mm) within its surveillance area in Eastern São Paulo State of all sea breeze events in 2005 (a) and 2007 (b). Contours, geographic boundaries, and political boundaries are indicated.

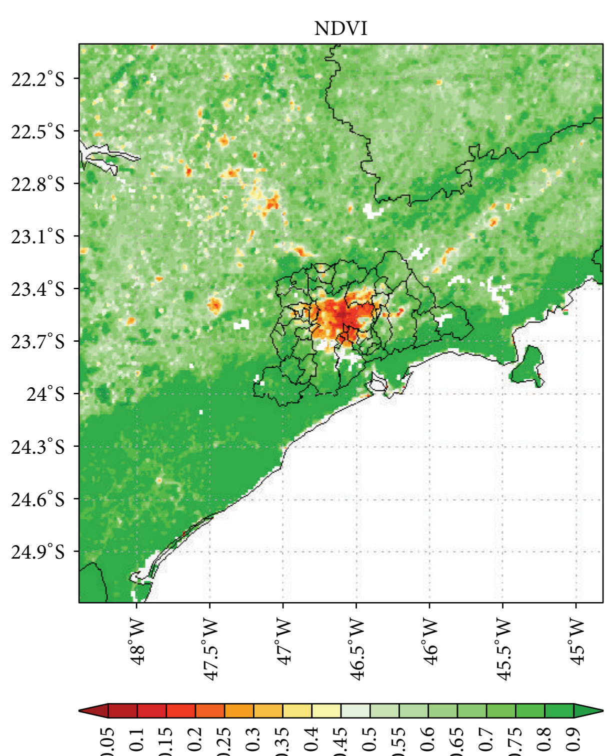

Figure 9: Normalized difference vegetation index (NDVI) within the surveillance area of the SPWR in Eastern São Paulo State. Colors indicate NDVI levels. Contours, geographic boundaries, and political boundaries are indicated.

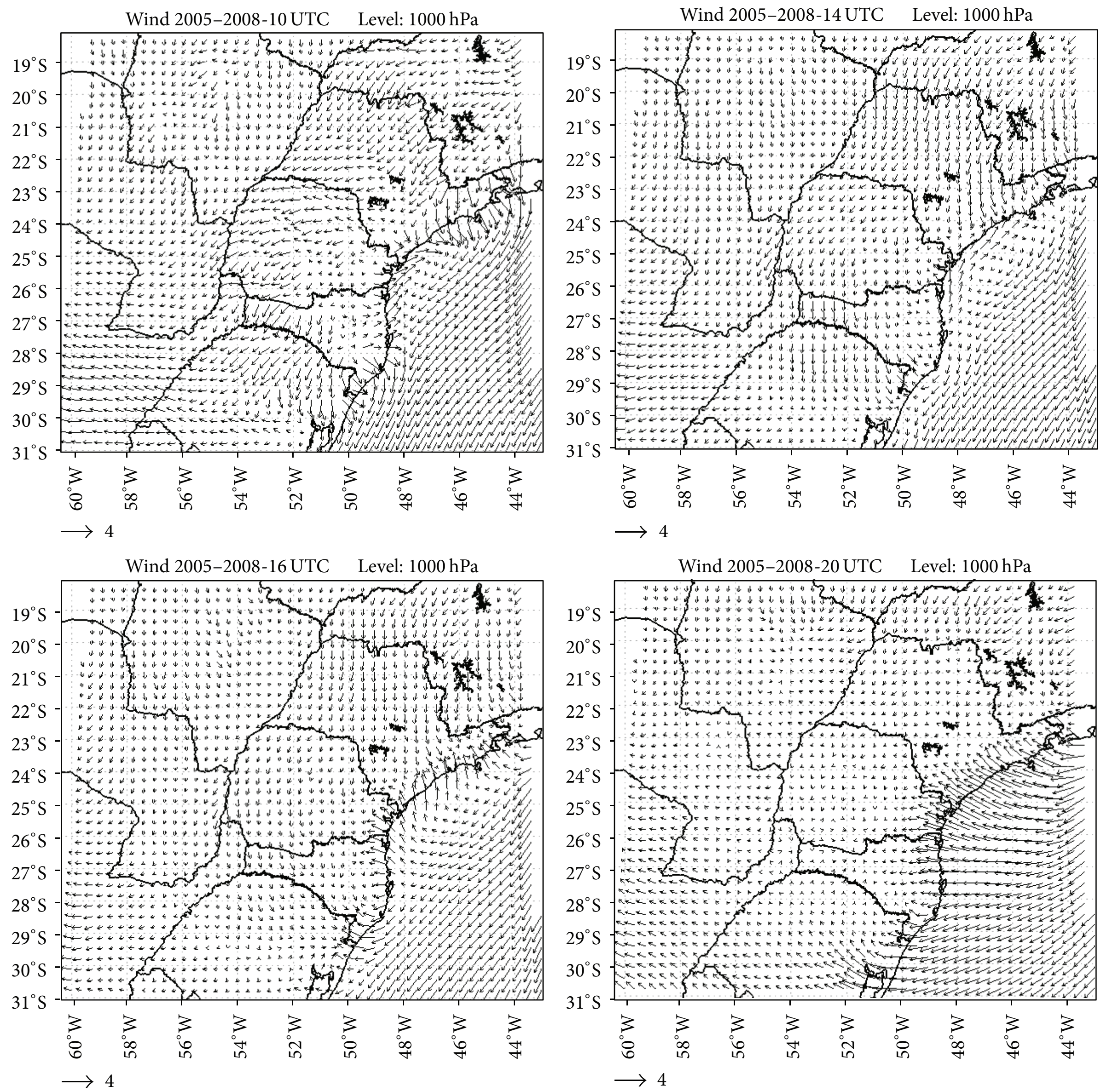

Figure 10: Hourly mean wind field at 1000-hPa between 2005 and 2008 associated with sea breeze and heat island episodes obtained with the ARPS system. Hour, level, contours, and geographic boundaries are indicated.

given impervious urban soil conditions, flash floods, high wind gusts, and other impacts are common. Thunderstorms have been preceded by NW winds in 74% episodes. The SB reaches MASP at about 1800 UTC at IAG weather station and at 1900 UTC at Campo de Marte Airport. At that time, SB circulation had produced very deep thunderstorms over MASP.

The total rainfall field estimated with SPWR has a core of 600 mm over MASP slightly shifted to SE more heavily urbanized. The total rainfall accumulation due to SB episodes is close to half of the annual average at IAG weather station. The Vale do Paraíba region shows a secondary maximum rainfall accumulation as well associated with greater warming and temperature gradients between the mountains and the valley.

The statistics obtained with ARPS simulations well reproduced the diurnal cycle of all days of the year [49]. Maximum CAPE and IL estimated for the afternoon hours were $1750\,\mathrm{J\,kg^{-1}}$ and -3.5°C to -4.0°C, respectively. They are good indicators of conditions favorable to thunderstorm development induced by SB fronts.

Noteworthily, the cold front over southern Brazil plays an important part in intensifying vertical vorticity together with the SB front circulation. In the upper levels under typical summer conditions an anticyclonic circulation is observed and associated with Bolivia's high [50]. The SB circulation interacts with UHI circulation to produce deep thunderstorms. The MXPOL weather radar [40] has been used in conjunction with the ARPS system to nowcasting thunderstorms triggered by these mesoscale features in MASP. Under

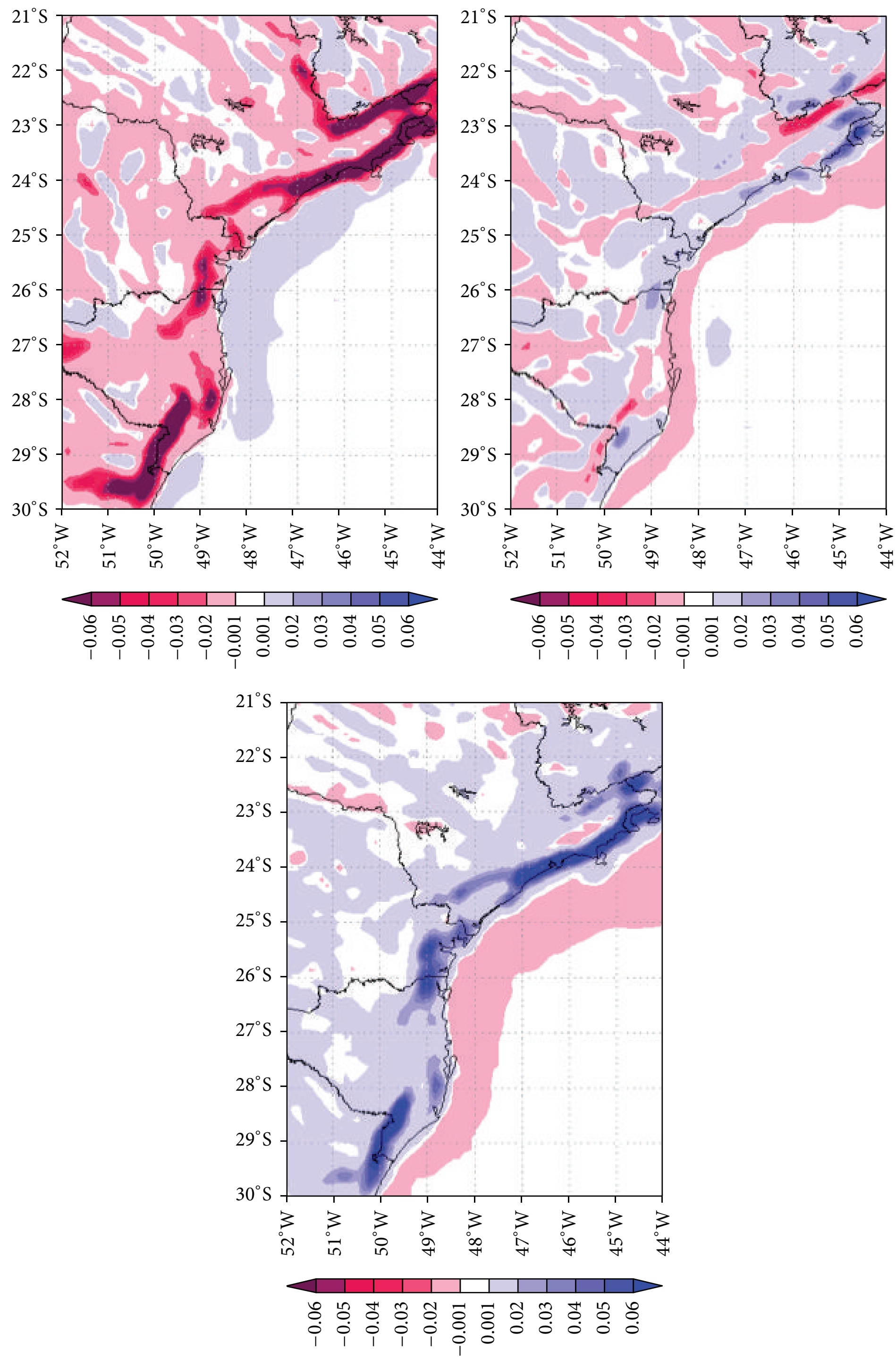

Figure 11: Similar to Figure 10 except for divergence (s^{-1}) at 1000 UTC, 1200 UTC, and 1600 UTC, respectively. Colors indicate divergence (s^{-1}).

certain instability levels and synoptic conditions observed in this research, it is possible to forecast the inset of heavy thunderstorms. These systems are mainly responsible for human and material losses every year. The main findings of this research are useful for nowcasting local and synoptic conditions that will trigger very deep thunderstorms with strong wind gusts, heavy rainfall rates, hail, lightening that in turn will cause damage to urban structures, injuries and casualties, economic losses, and social problems. So, mitigating these anthropic related impacts can be achieved by incorporating local and synoptic features and meteorological variable thresholds such as air and dew point temperatures, wind direction and intensity, and boundaries observed by weather radar and satellite.

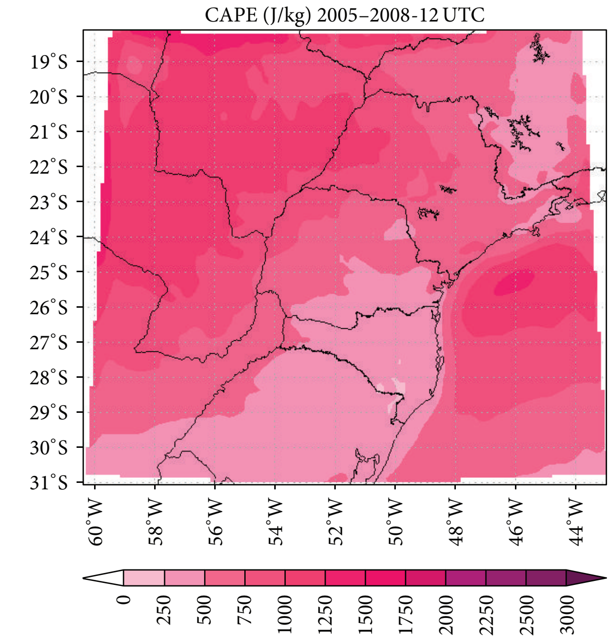

FIGURE 12: Similar to Figure 10 except for CAPE. Colors indicate CAPE (J kg^{-1}).

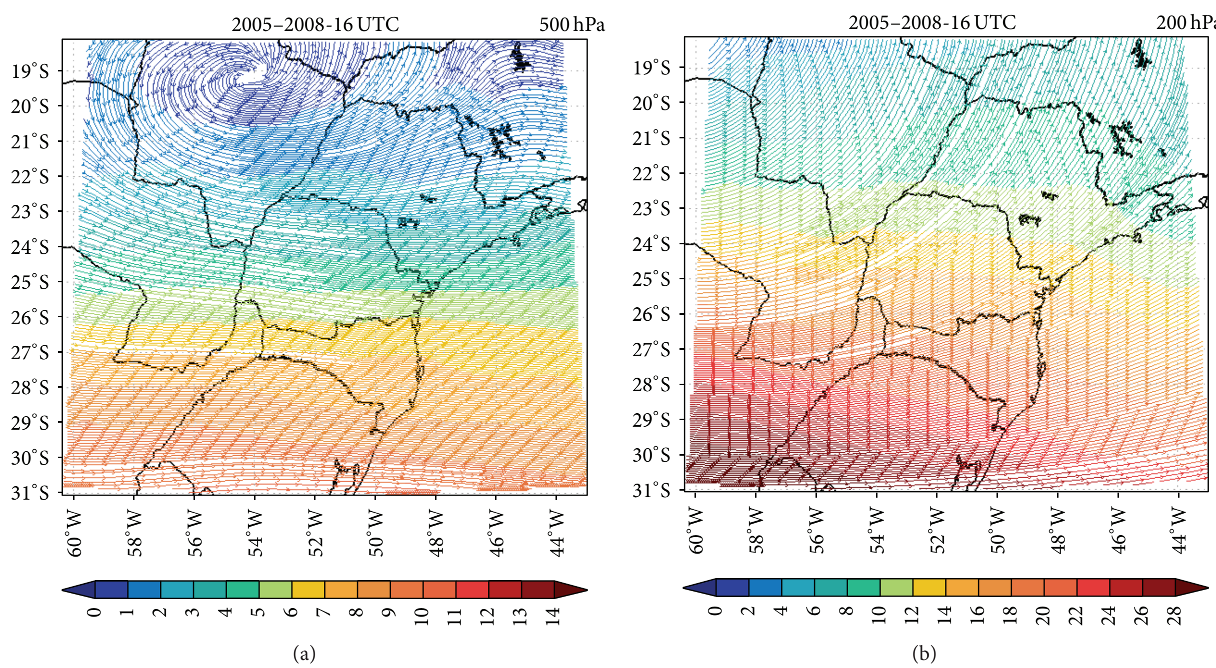

FIGURE 13: Similar to Figure 10 except for mean wind streamlines at 500 hPa (a) and 200 hPa (b) at 1600 UTC. Colors indicate wind speeds (m s^{-1}).

Conflict of Interests

The authors declare that there is no conflict of interests regarding the publication of this paper.

Acknowledgments

The authors would like to thank IAG, Guarulhos (SBGR), and Congonhas Airports (SBSP) for providing datasets used in this work. The airports data are available in "http://www.redemet.aer.mil.br/index.php?i=produtos&p=plotagem-metar" and IAG data can be obtained from "http://www.estacao.iag.usp.br/sol_dados.php." The CPTEC/INPE provided satellite images that can be obtained from "http://satelite.cptec.inpe.br/." The ARPS system was developed by CAPS and can be downloaded from "http://www.caps.ou.edu/ARPS/arpsdown.html." The data from São Paulo weather radar can be obtained by sending an email to radar@saisp.br. The authors

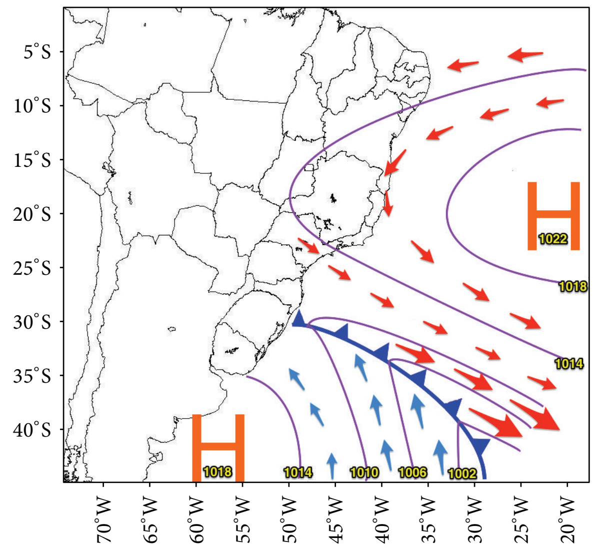

FIGURE 14: Schematics of a typical synoptic condition associated with deep convection development over MASP caused by intense sea breeze and heat island circulation. Isobars (hPa) and winds and frontal boundaries are indicated.

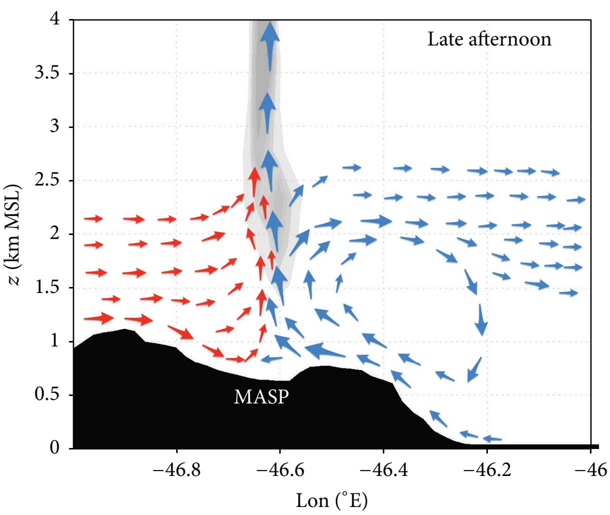

FIGURE 15: Schematics of a late afternoon cross-section of local winds and cloudiness observed for a typical deep convection development over MASP caused by sea breeze and local heat island.

can provide data from MXPOL weather radar that was generated according to description in Pereira Filho [40]. The sounding data are available in "http://weather.uwyo.edu/upperair/sounding.html." This research is supported by CAPES and CNPq.

References

[1] A. J. Pereira Filho, M. T. L. Barros, R. Hallak, and A. W. Gandu, "Enchentes na região metropolitana de São Paulo: aspectos de mesoescala e avaliação de impactos," in *Proceedings of the 13th Congresso Brasileiro de Meteorologia*, pp. 28–93, Fortaleza, Brazil, September 2004, (Portuguese).

[2] A. J. Pereira Filho, R. Haas, and T. Ambrizzi, "Caracterização dos eventos de cnchente na Bacia do Alto Tietê por meio do radar meteorológico e da modelagem numérica de mesoescala," in *XII Congresso Brasileiro de Meteorologia*, Foz do Iguaçu, Brazil, August 2002 (Portuguese).

[3] A. J. Pereira Filho, "Chuvas de verão e as enchentes na grande São Paulo: el niño, brisa marítima e ilha de calor," in *I Seminário Brasileiro de Hidrometeorologia and XI Congresso Brasileiro de Meteorologia*, Rio de Janeiro, Brazil, 2000 (Portuguese).

[4] A. P. Oliveira and P. L. S. Dias, "Aspectos observacionais da brisa marítima em São Paulo," in *II Congresso Brasileiro de Meteorologia*, vol. 2, pp. 129–161, Pelotas, Brazil, October 1982 (Portuguese).

[5] A. J. Pereira Filho, O. Massambani, R. Hallak, and H. Karam, "A hidrometeorological forecast system for the Metropolitana Area of São Paulo," in *Proceedings of the World Weather Research Programme's Symposium on Nowcasting and Very Short Range Forecasting (WSN '05)*, Toulouse, France, 2005.

[6] W. T. Thompson, T. Holt, and J. Pullen, "Investigation of a sea breeze front in an urban environment," *Quarterly Journal of the Royal Meteorological Society*, vol. 133, no. 624, pp. 579–594, 2007.

[7] A. Dandou, M. Tombrou, and N. Soulakellis, "The influence of the City of Athens on the evolution of the sea-breeze front," *Boundary-Layer Meteorology*, vol. 131, no. 1, pp. 35–51, 2009.

[8] F. J. Robinson, M. D. Patterson, and S. C. Sherwood, "A numerical modeling study of the propagation of idealized sea-breeze density currents," *Journal of the Atmospheric Sciences*, vol. 70, no. 2, pp. 653–668, 2013.

[9] A. N. F. Porson, D. G. Steyn, and G. Schayes, "Formulation of an index for sea breezes in opposing winds," *Journal of Applied Meteorology and Climatology*, vol. 46, no. 8, pp. 1257–1263, 2007.

[10] B. W. Atkinson, *Meso-Scale Atmospheric Circulation*, vol. 495, Academic Press, London, UK, 1981.

[11] G. Ganbat, J. M. Seo, J.-Y. Han, and J.-J. Baik, "A theoretical study of the interactions of urban breeze circulation with mountain slope winds," *Theoretical and Applied Climatology*, vol. 121, no. 3, pp. 545–555, 2015.

[12] J. M. Shepherd, H. Pierce, and A. J. Negri, "Rainfall modification by major urban areas: Observations from spaceborne rain radar on the TRMM satellite," *Journal of Applied Meteorology*, vol. 41, no. 7, pp. 689–701, 2002.

[13] H. Kusaka, K. Nawata, A. Suzuki-Parker, Y. Takane, and N. Furuhashi, "Mechanism of precipitation increase with urbanization in Tokyo as revealed by ensemble climate simulations," *Journal of Applied Meteorology and Climatology*, vol. 53, no. 4, pp. 824–839, 2014.

[14] E. Marques Filho, H. Karam, A. Miranda, and A. França Junior, "Rio de Janeiro's tropical urban climate," *News Letter of the Internation Association of Urban Climate*, vol. 32, pp. 5–9, 2009.

[15] E. D. Freitas and P. L. S. Dias, "Alguns efeitos de áreas urbanas na geração de uma ilha de calor," *Revista Brasileira de Meteorologia*, vol. 20, no. 3, pp. 355–366, 2005.

[16] T. R. Oke, *Boundary Layer Climates*, Routledge, London, UK, 1978.

[17] T. Meir, P. M. Orton, J. Pullen, T. Holt, and W. T. Thompson, "Forecasting the New York City urban heat island and sea breeze during extreme heat events," *Weather and Forecasting*, vol. 28, no. 6, pp. 1460–1477, 2013.

[18] M. J. Ferreira, *Estudo do balanço de energia na superfície aplicado a cidade de São Paulo [Ph.D. thesis]*, Department of Atmospheric Science, University of São Paulo, São Paulo, Brazil, 2010.

[19] I. Eliasson, "Urban nocturnal temperatures, street geometry and land use," *Atmospheric Environment*, vol. 30, no. 3, pp. 379–392, 1996.

[20] J. L. Flores, H. A. Karam, E. P. M. Filho, and A. J. P. Filho, "Estimation of atmospheric turbidity and surface radiative parameters using broadband clear sky solar irradiance models in Rio de Janeiro-Brasil," *Theoretical and Applied Climatology*, 2015.

[21] H. E. Landsberg, *The Urban Climate*, Academic Press, New York, NY, USA, 1981.

[22] J. D. Fast and M. D. McCorcle, "A two-dimensional numerical sensitivity study of the great plains low-level jet," *Monthly Weather Review*, vol. 118, no. 1, pp. 151–163, 1990.

[23] G.-X. He, C. W. F. Yu, C. Lu, and Q.-H. Deng, "The influence of synoptic pattern and atmospheric boundary layer on PM10 and urban heat island," *Indoor and Built Environment*, vol. 22, no. 5, pp. 796–807, 2013.

[24] J.-Y. Han, J.-J. Baik, and H. Lee, "Urban impacts on precipitation," *Asia-Pacific Journal of Atmospheric Sciences*, vol. 50, no. 1, pp. 17–30, 2014.

[25] E. D. Freitas, C. M. Rozoff, W. R. Cotton, and P. L. Silva Dias, "Interactions of an urban heat island and sea-breeze circulations during winter over the metropolitan area of São Paulo, Brazil," *Boundary-Layer Meteorology*, vol. 122, no. 1, pp. 43–65, 2007.

[26] W. R. G. Farias, O. Pinto Jr., K. P. Naccarato, and I. R. C. A. Pinto, "Anomalous lightning activity over the Metropolitan Region of São Paulo due to urban effects," *Atmospheric Research*, vol. 91, no. 2–4, pp. 485–490, 2009.

[27] H. B. Blueinstein, *Synoptic-Dynamic Meteorology in Midlatitudes. Volume II: Observations and Theory of Weather Systems*, Oxford University Press, New York, NY, USA, 1993.

[28] R. A. Anthes, "Numerical prediction of severe storms—certainty, possibility or dream?" *Bulletin of the American Meteorological Society*, vol. 57, pp. 423–430, 1976.

[29] W. R. Cotton and R. A. Anthes, *Storm and Cloud Dynamics*, Academic Press, EUA, San Diego, Calif, USA, 1989.

[30] R. H. Johnson and B. E. Mapes, "Mesoescale processes and severe convective weather," in *Severe Convective Storms*, C. A. D. Doswell III, Ed., vol. 28 of *Meteorological Monographs*, American Meteorological Society, 2001.

[31] E. C. Vicente, C. A. Sangiolo, and A. J. Pereira Filho, "Características das precipitações convectivas intensas na area do radar meteorológico de São Paulo," in *XII Congresso Brasileiro de Meteorologia*, Poços de Caldas, Brazil, August 2002.

[32] P. J. Roebber, D. M. Schultz, B. A. Colle, and D. J. Stensrud, "Toward improved prediction: high-resolution and ensemble modeling systems in operations," *Weather and Forecasting*, vol. 19, no. 5, pp. 936–949, 2004.

[33] M. Xue, K. K. Droegemeier, and V. Wong, "The Advanced Regional Prediction System (ARPS)—a multi-scale nonhydrostatic atmospheric simulation and prediction model. Part I: model dynamics and verification," *Meteorology and Atmospheric Physics*, vol. 75, no. 3-4, pp. 161–193, 2000.

[34] M. Xue, K. K. Droegemeier, V. Wong et al., "The Advanced Regional Prediction System (ARPS)—a multi-scale nonhydrostatic atmospheric simulation and prediction tool. Part II: model physics and applications," *Meteorology and Atmospheric Physics*, vol. 76, no. 3-4, pp. 143–165, 2001.

[35] M. Xue, D. Wang, J. Gao, K. Brewster, and K. K. Droegemeier, "The Advanced Regional Prediction System (ARPS), storm-scale numerical weather prediction and data assimilation," *Meteorology and Atmospheric Physics*, vol. 82, pp. 139–170, 2003.

[36] M. Xue and W. J. Martin, "A high-resolution modeling study of the 24 May 2002 dryline case during IHOP. Part II: horizontal convective rolls and convective initiation," *Monthly Weather Review*, vol. 134, no. 1, pp. 172–191, 2006.

[37] R. Hallak, A. J. Pereira Filho, A. W. Gandu, and M. T. Barros, "Simulação numérica de precipitação intense na Região Metropolitana de São Paulo com o modelo de mesoescala ARPS," in *Proceedings of the 13th Congresso Brasileiro de Meteorologia*, Fortaleza, Brazil, September 2004.

[38] R. Hallak, *Simulações numéricas de tempestades severas na RMSP [Ph.D. thesis]*, Department of Atmospheric Science, University of São Paulo, São Paulo, Brazil, 2007.

[39] F. W. Menezes, *Tempestades severas: um modelo para latitudes subtropicais [Ph.D. thesis]*, Department of Atmospheric Science, University of São Paulo, São Paulo, Brazil, 1998.

[40] A. J. Pereira Filho, "A mobile X-POL weather radar for hydrometeorological applications in the metropolitan area of São Paulo, Brazil," *Geoscientific Instrumentation, Methods and Data Systems*, vol. 1, no. 2, pp. 169–183, 2012.

[41] J. S. Marshall and W. M. K. Palmer, "The distribution of raindrops with size," *Journal of Atmospheric Sciences*, vol. 5, no. 4, pp. 165–166, 1948.

[42] M. Xue, K. K. Droegemeier, W. Wong, A. Shapiro, and K. Brewster, *Advanced Regional Prediction System Users Guide*, University of Oklahoma, Norman, Okla, USA, 1995.

[43] C. A. M. Rodriguez, R. P. da Rocha, and R. J. Bombardi, "On the development of summer thunderstorms in the city of São Paulo: mean meteorological characteristics and pollution effect," *Atmospheric Research*, vol. 96, no. 2-3, pp. 477–488, 2010.

[44] H. Tong, A. Walton, J. Sang, and J. C. L. Chan, "Numerical simulation of the urban boundary layer over the complex terrain of Hong Kong," *Atmospheric Environment*, vol. 39, no. 19, pp. 3549–3563, 2005.

[45] T. N. Carlson and D. A. Ripley, "On the relation between NDVI, fractional vegetation cover, and leaf area index," *Remote Sensing of Environment*, vol. 62, no. 3, pp. 241–252, 1997.

[46] J.-J. Baik and H.-Y. Chun, "A dynamical model for urban heat islands," *Boundary-Layer Meteorology*, vol. 83, no. 3, pp. 463–477, 1997.

[47] K. Emanuel, *Atmospheric Convection*, Oxford University Press, 1994.

[48] J. G. Galway, "The lifted index as a predictor of latent instability," *Bulletin of the American Meteorological Society*, vol. 37, pp. 528–529, 1956.

[49] A. P. Oliveira, R. D. Bornstein, and J. Soares, "Annual and diurnal wind patterns in the city of São Paulo," *Water, Air, and Soil Pollution: Focus (Prelo)*, vol. 3, no. 5, pp. 3–15, 2003.

[50] P. L. Silva Dias, W. H. Schubert, and M. DeMaria, "Large-scale response of the tropical atmosphere to transient convection," *Journal of the Atmospheric Sciences*, vol. 40, no. 11, pp. 2689–2707, 1983.